IDENTIFYING ESSENTIAL MECHANISMS FOR CORTICAL ACTOMYOSIN CONTRACTIONS WITH COMPUTATIONAL MODELING

by

Callie Johnson Miller

BS, James Madison University, 2008

MA, University of Pittsburgh, 2009

Submitted to the Graduate Faculty of

the Swanson School of Engineering in partial fulfillment

of the requirements for the degree of

Doctor of Philosophy

University of Pittsburgh

2014

UNIVERSITY OF PITTSBURGH

SWANSON SCHOOL OF ENGINEERING

This dissertation was presented

by

Callie Johnson Miller

It was defended on

July 11, 2014

and approved by

Lance A Davidson, Ph.D., Associate Professor, Department of Bioengineering

Steve Abramowitch, Ph.D., Assistant Professor, Department of Bioengineering

G Bard Ermentrout, Ph.D., Professor, Department of Mathematics

Sanjeev Shroff, Ph.D., Chair, Department of Bioengineering

Dissertation Director: Lance A Davidson, Ph.D., Associate Professor, Department of Bioengineering

IDENTIFYING ESSENTIAL MECHANISMS FOR CORTICAL ACTOMYOSIN CONTRACTIONS WITH COMPUTATIONAL MODELING

Callie Johnson Miller, PhD

University of Pittsburgh, 2014

The success of embryogenesis requires coordinated cell-cell signaling, tissue patterning, and morphogenetic movements. In order to understand how birth defects such as spina bifida occur, we must understand how signaling and patterning integrate mechanically to drive morphogenetic movements. Although there are many different scales to consider (molecular, cellular, or tissue), this dissertation is unique in its attempt to bridge molecular biophysics to cell- and tissue-scale biomechanics. On the molecular level, filamentous actin (F-actin) and non-muscle myosin II (NMM II) motors are cytoskeletal proteins responsible for cell motility and shape change. Currently, there are no techniques for measuring *in vivo* forces generated by cortical actomyosin. In order to gain a better understanding of the behavior of actomyosin *in vivo*, we have developed theoretical models, beginning with a simple rotational model for actomyosin, and extended the theory to a simple sliding filament system. Based on the results and intuition gained from these simple models, we developed a 2D model where we can study the emergent morphology of the filaments and motors. *In vivo*, we observe actomyosin punctuated contractions which initiate from a quiescent background of F-actin to flow into a region of high intensity and disassemble, returning to baseline levels. Previous research showed the correlation between the locations of these punctuated contractions and the resultant cell shape change during development. The 2D model allows us to explore the kinematics of F-actin arrays and the dynamics of their force production as we vary biophysical parameters. We can also test the model results against *in vitro* observations of purified actin and myosin. Although still simplified, our model has set the groundwork

for future studies on the role of actin binding proteins in actomyosin dynamics, simulating the role of actomyosin in cell shape change, and making comparative measurements for experimental studies of purified cytoskeletal actomyosin.

TABLE OF CONTENTS

LIST OF TABLES

LIST OF FIGURES

PREFACE

Dr. Shroff- Thank you for challenging me to think about my research in a broader aspect than just the little niche of development.

Dr. Abramowitch- Thank you for always believing in and challenging me to reach beyond what I thought my abilities were. Your advice on the process and intellectual discussions helped me push through the times when I wanted to give up.

Dr. Ermentrout- You were there from the very beginning when I started graduate school in the math department. I took your classes in the fall and the spring that year, and you challenged me to think about biologic problems in a whole new way. Beginning the collaboration with you led to this work and I am immensely grateful. You have taught me to always pursue what I find interesting and greatness will follow.

Dr. Davidson- Words can't begin to express my thanks. You took a chance on me when no one else would. Even though you didn't have funding for me, you met with me and quickly sold me on your mission of understanding developmental defects. You challenged me to learn the intricacies and difficulties of biology research, in addition to bolstering my confidence in mathematical modeling. I am constantly in awe of your breadth and depth of knowledge and strive to achieve a similar knowledge base in order to be worthy of being considered a colleague. I also appreciate your candid conversations and encouragement for handling "life" and finding balance. You have been a mentor in many different capacities and I hope to continue our relationship. Additional thanks to your wife, Laura, and daughter, Rosie, who have been so accepting of my family.

Davidson lab- So many of you have been integral to my success. Thank you, Hye Young and Sagar for guiding me in the beginning; Lin, Carsten, and Noah for your help "behind the scenes;" Steve for your guidance and openness; Demetrius for trusting my vision during the summer we worked together; and Deepthi, Joe, and Tim for our stimulating discussions, shared ideas, and your unfailing confidence in my abilities.

My parents- Thank you for always encouraging me to strive for greatness, never settling for adequate. The stubbornness that I have found necessary to complete this journey comes from those traits and the support and encouragement you have always offered. Thank goodness for cell phones and being within driving distance because you are my "rechargers," and I know I wouldn't have been able to complete this without you both.

Brian- Thanks for your continual encouragement and support during this journey. I'm sure you found me crazy at times, but somehow you've managed to still keep pushing me through to the finish line. I'm excited to find out what the next part of our journey will entail, and hope you never forget how integral you were to helping me achieve and complete this portion.

To my sister, my daughter, and the rest of my friends and family- Thank you, thank you, thank you. Thank you for understanding when I was distracted or forgetful. Thank you for believing in me always and encouraging me when I was discouraged.

Table 0.1: Abbreviations Reference

Abbreviation	Definition
NMM II	Non-muscle myosin II
ECM	Extracellular matrix
AS	Amnioserosa
MDCK	Madin-Darby Canine Kidney Epithelial Cells
FRET	Forster Resonance Energy Transfer

1.0 INTRODUCTION

The aim of this dissertation seeks to investigate force production and morphology in the actomyosin cytoskeleton in cells. The actomyosin cytoskeleton is responsible for cell movement and shape change, as well as structure, and intracellular trafficking. At the molecular scale, we seek to understand how cells generate the force needed to drive their large scale movements. Understanding cellular forces helps to know how cells act within a healing tissue, and move to generate tissue layers and organs in development. The primary goal of this project is to understand how cortical actomyosin dynamics play a role in coordinating cell motility and shape change with tissue-level mechanics during morphogenesis.

Actomyosin is a general reference to a complex of cytoskeletal proteins including filamentous actin, its associated motor myosin, and various actin binding proteins. Filamentous actin or F-actin, is a polymer composed of G-actin monomer subunits. The F-actin polymer has an inherent polarity with a "plus" end (sometimes called "barbed" end), where assembly or polymerization dominates, and a "minus" end (sometimes called "pointy" end), where disassembly or depolymerization dominates. F-actin arrays take on different morphologies in cells depending on the cell's location in a tissue (e.g. [Feroze et al., tted]), and to some extent, the external mechanics (e.g. [Zemel et al., 2010]; fig 1.1A). There are 6 gene isoforms for actin in birds and mammals[Perrin and Ervasti, 2010], 139 myosin motors which act on actin (phylogenetic tree, [Hodge et al., 2000]), and 162 distinct and separate actin binding proteins, not including synonyms or isoforms [Dos Remedios et al., 2003]. Myosin motors are the motor protein associated with F-actin and are responsible for producing forces that drive cell shape change and contractility. The 139 myosin motors are conserved with a "head" domain that binds to F-actin and categorized based on the structure of their "tail" domain and binding motif (fig 1.1B).

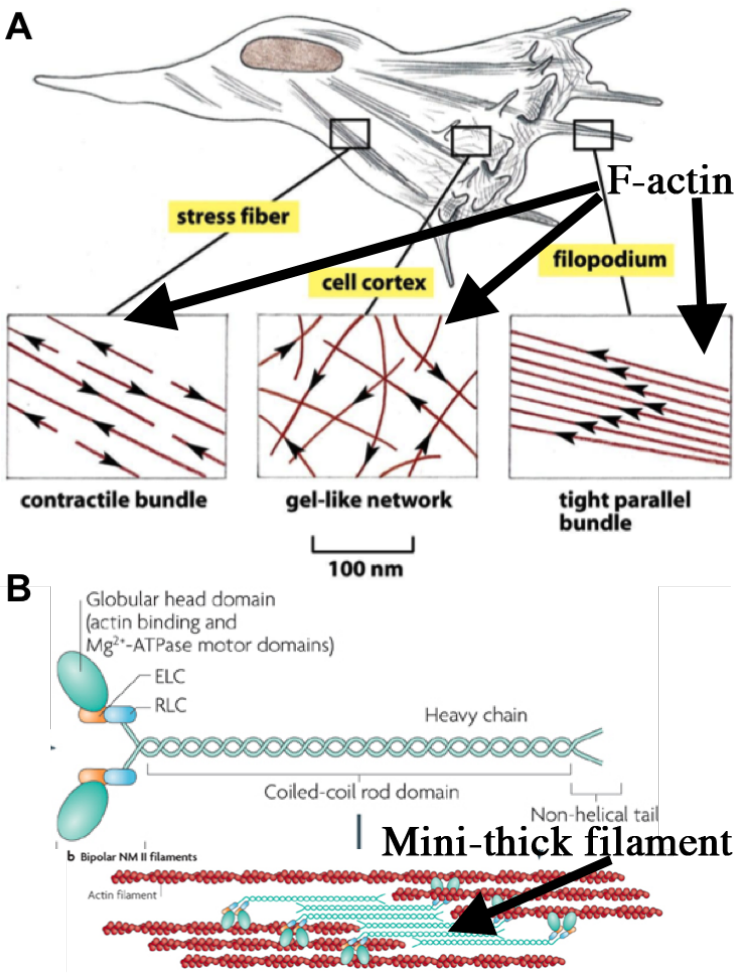

Figure 1.1: **Actomyosin:** (A) Example of 3 different arrangements of actin filaments (red) in a crawling fibroblast (Fig. 16-47, p.1006 [Alberts, 2008]). (B) Cartoon depiction of a single non muscle myosin II molecule (top) and a bundled, processive mini-thick filament comprised of multiple non-muscle myosin II molecules (Figure 1, [Vicente-Manzanares et al., 2009]).

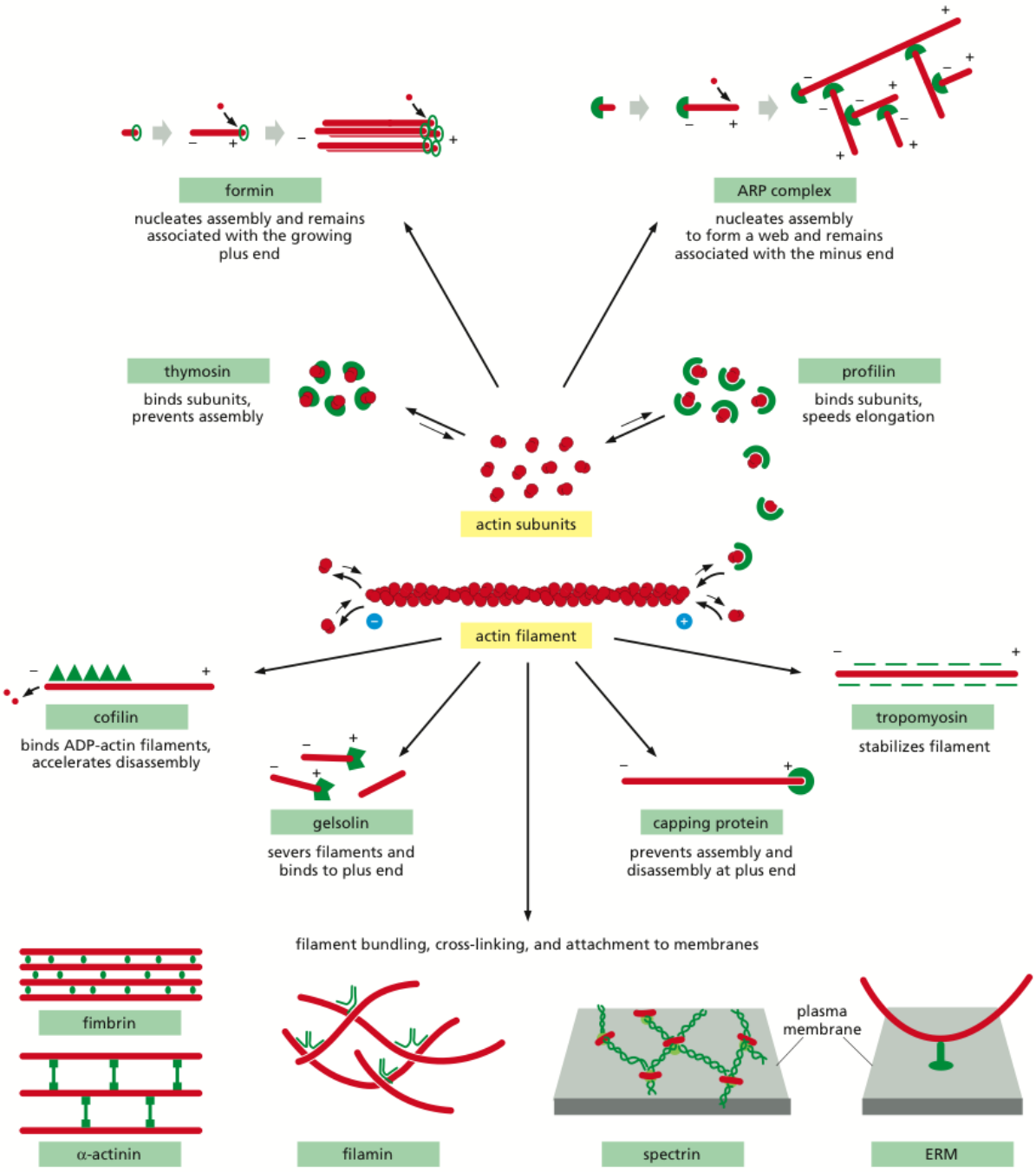

Figure 1.2: **Actin filament associated proteins.** Illustrating the many fundamental roles and proteins affecting actin dynamics which make the actomyosin system complex (Panel 16-3 in [Alberts, 2008]).

Additional proteins to be considered with actomyosin are actin binding proteins which are categorized based on structure and function [Pollard and Cooper, 1986] (see examples in fig 1.2). Because actin binding proteins are essential to normal development, they are often considered to be highly redundant, suggesting overlapping biophysical functions [Ponte et al., 2000]. There are model systems for mutations in actin binding proteins, for example, mouse where more than 1/3 of mutations causing neural tube defects are in actin binding proteins and signaling pathways that regulate actomyosin dynamics [Zohn et al., 2005].

There are multiple roles of actomyosin in the cell including lamellipodial protrusions, and vesicle and organelle trafficking. The lamellipodia is a thin actin protrusion at the edge of a cell and is used for cell migration [Ponti et al., 2004a]. Vesicle and organelle trafficking are seen with the intracellular transport of pigment granules in *Xenopus* [Snider et al., 2004], or vacuole transport for cell division [Hill et al., 1996]. Actomyosin also enables cell motility [Ghosh et al., 2004], muscle contraction [Reisler, 1993], and creation and maintenance of cell junctions [Howard et al., 1993].

Most research concerning the mechanics of actomyosin focus on the protrusion of lamellipodia at the leading edge of migrating cells and a region dense with F-actin but little myosin [Lauffenburger and Horwitz, 1996, Rafelski et al., 2009, Burnette et al., 2011]. Recently, however, observations of actomyosin in the cortical layer of embryonic cells have raised many questions about the mechanics and role of these punctuated actomyosin contractions during morphogenesis [Martin et al., 2009, Solon et al., 2009, Wozniak and Chen, 2009, Kim and Davidson, 2011]. Punctuated actomyosin contractions have been observed during morphogenesis in *C. elegans, Drosophila,* and *Xenopus laevis* (fig 1.3) and show remarkable similarities in the time scale and geometry of actomyosin contractions [Martin, 2010, Solon et al., 2009, Gorfinkiel and Blanchard, 2011b].

Actomyosin not only affects the shape of single cells, but also regulates macroscopic properties, such as the viscoelasticity of embryos [Davidson et al., 2009]. Dorsal tissue stiffness in the *Xenopus* embryo has been shown to decrease in stiffness with a reduction in actomyosin contractility [Davidson et al., 2009, Zhou et al., 2009]. The underlying mechanics of actomyosin contractions and how they contribute to essential aspects of morphogenesis, such as convergent extension [Keller et al., 2000, Davidson et al., 2010], are unknown.

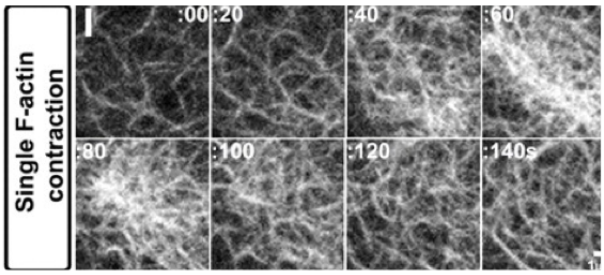

Figure 1.3: **Punctuated actin contraction:** Time-lapse images of a single actin contraction in *Xenopus laevis* (fig 3I, [Kim and Davidson, 2011]).

Through the use of high resolution live cell confocal imaging and image analysis, our lab has shown that during the process of convergent extension in the *Xenopus laevis* embryo, punctuated actomyosin contractions (fig 1.1) increase in frequency and are aligned in the direction of the axis of elongation for mesodermal cells [Kim and Davidson, 2011] (fig1.4). Even though these data demonstrate a relationship between actomyosin dynamics and cell shape change, what remains unanswered are the biophysical mechanisms actomyosin uses to drive cell shape changes.

Actomyosin biochemistry and the biophysical intricacies of the complex are well characterized. Experimental studies have given estimates for actin assembly/disassembly and myosin processivity rates [Kouyama and Mihashi, 1980, Cooper et al., 1983, Amann and Pollard, 2001, Lecuit et al., 2011] and rules for their interaction[Schaub et al., 2007, Burnette et al., 2011]. Studies on actomyosin dynamics and cell motility describe the crawling motion of single cells as a process involving protrusion of the leading edge (from actin polymerization), adhesion to the surface (through focal adhesion complexes), retraction of the rear of the cell (disassembly of actin filaments), and finally breaking focal adhesions at the rear [Pollard and Borisy, 2003].

The current modeling approaches used to investigate the role or function of actomyosin can be divided into three general categories: (i) understanding actomyosin organization and force generation in the lamellipodia, (ii) simulating actomyosin sorting and alignment, and (iii) understanding the mechanics of the network. Theory of actomyosin organization and

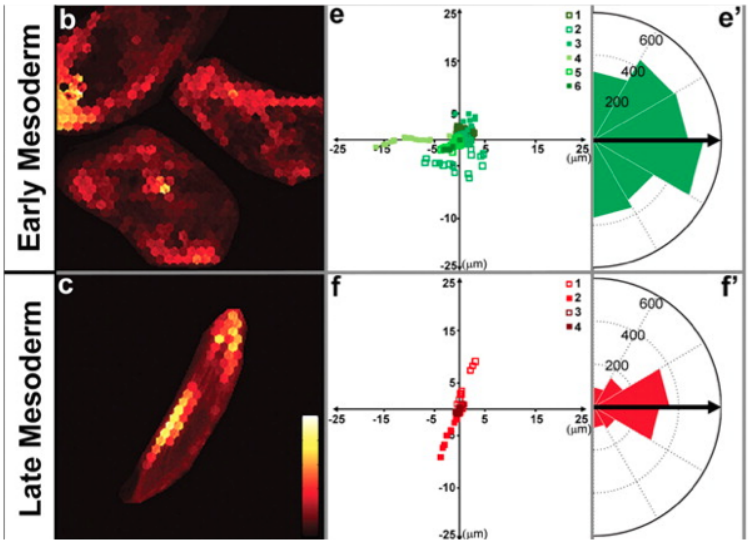

Figure 1.4: **Frequency and orientation of actin contractions:** A frequency and orientation map shows where punctuated actin contractions occur compared to the major axis of the cell (Figure 4H (b,c,e,e',f,f') [Kim and Davidson, 2011]).

force generation in the lamellipodial regions of the cell are very well documented and closely match experimental observations for various cell culture systems [Schaub et al., 2007, Burnette et al., 2011, Waterman-Storer and Salmon, 1997, Mogilner and Oster, 1996, Chan and Odde, 2008]. The hypothesized mechanisms for actomyosin force generation and organization in the cortical region of the cell, however, are thought to be different than actomyosin organization in the lamellipodial region. It is believed that the expression of actin genes and actin binding proteins are locally different within the cell and thus change the architecture of the network of local populations of actomyosin.

There have been many theoretical studies on the sorting and organization of F-actin for cellular events such as the contractile ring of the cleavage furrow during cell division [Zemel and Mogilner, 2009, Zumdieck et al., 2007], and the organization of cytoskeletal components for spindle separation during prophase [Sommi et al., 2011, Loughlin et al., 2010, Burbank et al., 2007]. There have even been studies on the sorting of the "disorganized," aster-like, filament clusters, but these models assume that the filament network is stabilized and myosin

are added to exert a localized force and bring neighboring asters together without allowing the network morphology to emerge [Smith et al., 2007, Ziebert et al., 2009]. These models are somewhat related to experimental observations of filament location and dynamics, but the models were designed to capture properties of the static network, not the dynamics of the network.

One approach to understand the mechanics of the actomyosin network, is to consider reconstituted F-actin gels. These models consider a fixed network of actin filaments that are then acted upon by crosslinking proteins and myosin motors to generate a change in the network which can then be mechanically quantified [Spiros and Edlestein-Keshet, 1998, Kruse et al., 2004, Murrell and Gardel, 2012, Dasanayake et al., 2011]. These approaches assume a linear interaction between network architecture and resulting force changes, but *in vivo* the F-actin is dynamically remodeled as a result of mechanical and chemical cues, which then leads to dramatic changes in F-actin organization.

In order to implement a dynamic model of actomyosin contractions, we have chosen to use the Monte Carlo method. The Monte Carlo method uses random sampling with assigned properties and probabilities [Sobol, 1994]. With a finite number of motors and filaments there are interactions and processes which are inherently stochastic, e.g. attachment or detachment of a motor or the turnover of an actin filament. Monte Carlo techniques allow us to properly include these random processes. To implement the stochasticity, we generate a random number at each stochastic event and compare it to the rate or probability of the event occurring. Even with the randomness, we find that the models have a steady state morphology that emerges. For example when filaments form an aster (Chapter 5), how it is formed is different every time, but the end morphology is the same.

To understand the complex non-linearities of actomyosin dynamics we developed quantitative tools to quantify the actomyosin network and the forces generated while cells change their shape and move. In addition we identified a few essential components of the actomyosin system that help it to act in an optimal manner for cell shape change and motility. Once the essential mechanisms for actomyosin dynamics are thoroughly understood through our models, future research will be able to model specific actomyosin network morphologies. They

will be able to vary parameter values in order to achieve the desired network morphology, and then use the identification of the parameter to target experimental studies appropriately.

1.1 SPECIFIC AIMS

1.1.1 *AIM 1: Identify how rates of F-actin polymerization and myosin generated forces affect actomyosin dynamic morphology*

Introduction. Even though the composition of actomyosin system is potentially very complex, we hypothesize that the ability of myosin to exert forces on actin filaments, and the turnover rates of actin filaments through polymerization are the two essential mechanisms through which actomyosin contraction dynamics and F-actin morphology are regulated. In order to address this, we will investigate actin polymerization rates, calculate generated forces and parameters that affect this force, and identify characteristic contraction morphologies.

AIM 1.1: Investigate the role of actin polymerization rates in creating or deconstructing actomyosin contractions. We will use a range of models from a simple model of rotation, to a more complex 2D model for F-actin (Chapters 3, 4, and 5).

AIM 1.2: Calculate forces generated by actomyosin contractions and how these forces vary with filament morphology, polymerization, and motor contractility. Utilizing our 2D model, we will calculate the spring force generated by the myosin II motors at every time step of a Monte Carlo simulation to determine the forces present to induce actomyosin contractile morphologies. We are also able to calculate the force of the myosin II motors for any continuum model extension of the discrete model. We consider "force" as the forces produced by myosin motors on individual filaments. We will use our quantity representing "order" or morphology of our actomyosin system to establish any correlations between the morphology and the forces generated by the myosin motors. We will be able to vary parameters of the model very simply and then use our order parameter in order to deduce how polymerization rates, or starting geometry affect the resulting forces generated by the myosin motors.

AIM 1.3: Identify characteristic actomyosin contraction morphologies and their associated "rules". Through the use of our 2D model, we will run multiple simulations of actomyoisn contractions with different initial geometric configurations and then identify what morphologies emerge. Once we identify the characteristic actomyosin contraction geometries, we can compare them to the characteristic morphologies from *Xenopus laevis* embryonic tissue.

The development of our models will help us to understand how specific biophysical processes contribute to actomyosin contraction morphology. Correlating these models to the experimental data will strengthen the validity of our models and modeling approach, as well as help us understand the in vivo actomyosin contraction dynamics.

1.1.2 *AIM 2: Test the role of actin crosslinking proteins on dynamic morphology*

Introduction. The main objective of this aim is to increase the physiological relevance of our models by including actin crosslinking proteins. Our working hypothesis is that crosslinking proteins change the geometry of actomyosin contractions.

AIM 2.1: Determine how crosslinkers will affect actomyosin morphology. We will build upon our previously established model for actomyosin dynamics by including actin crosslinking proteins. Actin crosslinking proteins are extremely diverse with some serving to bundle filaments into parallel arrays, bundle filaments into orthogonal arrays, or create branching morphologies. Specifically, we will consider the role of a "universal" actin crosslinking protein, to bundle actin filaments together. Our assumptions for modeling the actin cross linker will include binding to a filament pair within a certain angle difference of and spatial distances from each other. This way we can use the cross linker to represent any class of actin bundling proteins. aim 1.1.2

1.2 OUTLINE OF THE DISSERTATION

Since understanding the molecular biology and cell mechanics is extremely important when building models, I co-authored a review on mechanosensing proteins and their roles during development in Chapter 2. The review points to the importance of understanding the molecular roles of force generation and reaction to forces, and how to relate force at this level to the cellular level.

Our modeling efforts began by developing an actomyosin model that focused on rotational movements of actin filaments driven by myosin II motors (Chapter 3). Since we focused solely on the rotation of pinned filament-type rods about a point, the model geometry was non-physiological, but the mathematics was tractable and we were able to develop continuum theory to validate our computational simulations. Although the geometry and physics are extremely simple, we found that without actin turnover, filaments reach a state of permanent alignment. We also found that once filament polymerization was introduced into the model, there exists a steady state solution for the morphology of the filaments.

We built upon the simple rotational model to consider translational sliding of filaments (Chapter 4) and found similar dependencies and existences of steady states of morphology that depended on polymerization. This model is more physiological for aligned actin arrays, but the continuum analysis is difficult to determine. To create a simple, physiologically relevant model of actomyosin, we extended our rotational and sliding models into two dimensions (Chapter 5). We found that an aster geometry was the steady state morphology for the 2D network and was dependent on the rate of polymerization, as were the previous models. We were able to take this model a step further, though, and simulated *in vitro* experimental results from purified actin and myosin, in addition to building the model's complexity by considering actin crosslinking proteins.

As an example of the types of experimental questions we are addressing, Chapter 6 describes a study on the role of temperature in the mechanics of the developing embryo. I contributed to the study by investigating how temperature affects *in vivo* actomyosin contractions. I was able to image live actomyosin contractions and develop an analysis technique for determining the duration of actomyosin contractions. In the conclusions chapter (Chap-

ter 7), we describe ideas for how to use the models to investigate the role of temperature in development to complement this experimental study.

We outline future directions of this research in the conclusion (Chapter 7). We have also taken the opportunity to begin to address the role of actin binding proteins from Aim 2 (1.1.2). At the conclusion of this research, we have a physiologically relevant theoretical model that is closely correlated to experimental data. Through the use of the model and experiment we are able to explore the biophysical basis of *in vivo* mechanics and dynamics. Our model is a tool to help other researchers determine factors that affect the force generating capacities of the actomyosin system, and to understand how these factors may be applied to achieve desired dynamics in stem cell differentiation or cancer metastasis research. We hope to provide our code through the lab website so other researchers can easily use to simulate and analyze their data using our methods.

2.0 THE INTERPLAY BETWEEN CELL SIGNALING AND MECHANICS IN DEVELOPMENTAL PROCESSES

In this paper Dr. Davidson and I wanted to reach an audience of geneticists who would be unfamiliar with biomechanics and communicate the need for examining complex feedbacks between mechanical signals/response and genetic signals/response. We reviewed the literature for known mechanically active gene transcription and protein activation, and, in most cases, hypothesized the role of these factors in developmental systems. This examination of proteins and the complexity of interaction and signaling to actomyosin further motivates my research trying to understand the basic mechanics of actomyosin contractions before adding in all the additional *in vivo* complexities. This paper was published in Nature Reviews Genetics in October 2013 [Miller and Davidson, 2013].

2.1 INTRODUCTION

Behind the motions of cells and tissues in the early embryo lie forces and mechanics. Universal principles of mechanics reveal how forces shape the early embryo and drive tissues to move, strain, and deform (see Box A.3 - Terminology of Mechanics - for a brief introduction to engineering terms and principles). The spatial and temporal regulation of gene expression and protein activity that guide cell physiology and behavior regulate the production of force and the mechanical response of embryonic cells and tissues to those forces. New findings suggest that mechanical cues may also directly alter gene expression and protein activity which in turn play a role in deciding cell fates and cell behaviors. Thus the developing

form of the embryo and the phenotype of the organism are the direct consequence of these biomechanical processes and are constrained by the physical laws of mechanics.

Early studies of the physical and mechanical constraints on development [His, 1888, Rhumbler, 1902, Morgan, 1927] included the construction of physical analog models of morphogenesis to test hypotheses on the origin of forces and role of tissue architecture in guiding movements. For example, assemblies of physical analogs consisting of elastic rubber bands, and brass bars allowed embryologists to simulate gastrulation and other examples of morphogenesis in the amphibian *Amphioxus maculatum* and to test their ideas about the cellular production of mechanical bending moments [Lewis, 1947]. The goal of these early studies was to test the plausibility of the application of physical laws to morphogenesis.

Recent experimental biomechanics studies have exposed previously concealed forces and the roles of mechanics in cell and developmental biology. Additional experiments consider the capacity of cells to sense physical force and mechanical cues, similar to how they sense chemical gradients and guidance cues. From these initial studies, several broader roles have been identified for mechanics in development, such as force generation from actomyosin contractions that 'pull' tissue edges. To serve such functions, cells must first be able to evaluate or measure mechanical 'signals' from their environment, as well as their own internal mechanical state. Second, cells must be able to transduce those signals into changes in gene expression and cell behaviors. Third, the cell must be able to generate and transmit mechanical forces to others.

However, one of the greatest challenges to understanding the role of mechanics in development is that the physics of mechanical structures cannot be 'knocked out' in the same sense as individual genes can be mutated. Instead, mechanics must be investigated on the systems level, where the role of mechanics is studied through perturbation. The general experimental design of these studies is to introduce a molecular perturbation (such as by knockdown or using an acute-acting inhibitor) or through mechanical perturbations (such as by laser cutting or other micro mechanical manipulations) and to identify the most proximal consequences of that perturbation on the cell or tissue scales. Molecular-scale biochemistry and biophysics is the final arbiter of these perturbations, but their action at the molecular

scale is beyond the scope of this Review (see [Howard, 2001], for example, for an introduction the biophysics of motor proteins and the cytoskeleton).

In this Review we discuss recent studies in developmental biology, cell biology and biophysics and how they are revitalizing the field of developmental biomechanics. These examples illustrate the classical, direct role of physical mechanics in shaping tissues, as well as the potential role of mechanics in cell signaling and in patterning cell identity. We then turn to reviewing several examples of the sensory and signaling pathways that may play a part in these processes. Along the way we introduce engineering principles that can be used to describe the important physical mechanics that shape tissues and we conclude with a discussion of the challenges that remain in connecting molecular mechanisms to developmental mechanics.

2.2 THE ROLE OF MECHANICS IN SCULPTING TISSUES

Cell-shape change: cause or effect?

Embryologists studying the role of mechanics in shaping tissues, such as the vertebrate neural tube [Selman, 1955, Selman, 1958, Smith and Schoenwolf, 1991, Smith et al., 1994, Alvarez and Schoenwolf, 1992, Smith and Schoenwolf, 1997] and the echinoderm archenteron [Ettensohn, 1985, Gustafson and Wolpert, 1963], recognized that the establishment of geometric patterns of cell shapes in tissues can either indicate programmed active cell-shape changes, such as cells adopting wedge shapes in order to bend the tissue, or can reflect passive shape changes in the tissue in response to forces applied outside the field; for example, when a tissue is folded by the action of cells outside the folded region. In genetic terms, the passively shaped cell is responding to non-cell-autonomous processes, whereas the processes directly shaping the cell are cell-autonomous processes. To distinguish between these two cases, embryologists have micro surgically isolated specific layers to determine which tissue contains the 'motor' that drives tissue shape change (box A.4). For example, they have isolated the vegetal plate of the blastula from the surrounding ectoderm in the starfish *Dendraster eccentrics* [Moore and Burt, 1939]. The modern genetic approach to the

same question relies on localized expression of a mutant protein or on mosaically knocking out a protein in a specific tissue.

The interaction of forces during tissue movement The transmission of force through a tissue integrates the activities of multiple cells and tissues, enabling otherwise disconnected cellular processes to contribute to the same morphogenetic movement (box A.3). An elegant series of papers on dorsal closure in *Drosophila melanogaster* demonstrates this principle [Hutson et al., 2003, Peralta et al., 2007, Toyoma et al., 2008, Kiehart et al., 2000]. Using biophysical modeling, laser microdissection and high-resolution live time-lapse confocal imaging of embryos (box A.4) in which key morphogenetically active proteins were mutated, it was shown that dorsal closure relies on multiple discrete motors. Large-scale tissue movements in the whole embryo are coordinated by long-range stresses generated by: pulsatile actomyosin contractions within the amnioserosa (an epithelium that covers a transient hole in the early dorsal epidermis) [Solon et al., 2009, Gorfinkiel et al., 2009, David et al., 2010]; a contractile actin purse-string at the margin of the lateral epidermis [Young et al., 1993, Edwards et al., 1997, Jacinto et al., 2002]; and the fusion of epidermis at the anterior and posterior ends [Millard and Martin, 2008], or acanthi, of the amnioserosa (figure 2.1). Large laser cuts across many cells were used to isolate and identify force-generating tissues within target tissues (box A.4). Local recoil from smaller laser-induced wounds on single cell-cell junctions were used to quantify the relative contribution of each motor to the global movements. Together with genetic manipulation, these biophysical studies demonstrate how multiple sources of force combine to shape a complex structure and how none of these individual motors acting in isolation can reliably seal the dorsal epidermis. Thus, to understand the role of mechanics in driving morphogenesis, it is crucial to describe the molecular mechanisms that generate force as well as those mechanisms that transmit and coordinate forces within complex tissues.

Mechanical equivalency of cellular processes. A range of different cellular and molecular mechanisms are capable of driving nearly identical morphogenetic movements. Two or more cellular or molecular mechanisms are capable of driving nearly identical morphogenetic movements. Two or more cellular or molecular mechanisms could be mechanically equivalent in that they contribute similar forces or maintain equivalent mechanical proper-

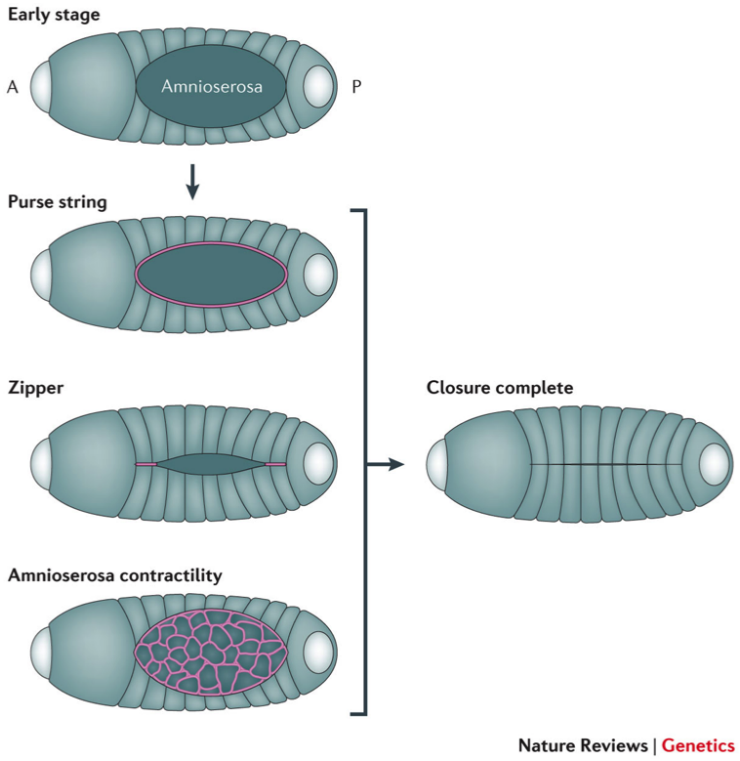

Figure 2.1: **Forces contributing to tissue movements in development.** The process of *Drosophila melanogaster* dorsal closure is shown and the individual mechanical components that help to complete closure are illustrated. In the early-stage embryo, the amnioserosa cells are located in the 'hole' that prospective epidermal cells will cover. The embryo is already polarized into an anterior (A) section, where the head will form, and a posterior (P) section. Closure is driven to completion by three distinct cellular processes that contribute to global tissue movements. First, the actomyosin purse string (shown in pink) forms at the boundary between the epithelial cells and amnioserosa cells. Second, as the epidermal cells meet at the anterior and posterior ends of the amnioserosa, they fuse and create a zipper (pink) that progressively seals the epidermal sheet over the amnioserosa. Third, cells in the amnioserosa undergo cycles of actomyosin contractions (amnioserosa contractility) to narrow their exposed apical faces and draw the epidermal margins of the AS together.

ties in the embryo. Similar patterns of force or stress may not necessarily be attributed to the same molecular mechanism. For example, a computer simulation used to study the invagination of a simple, single-cell-layered epithelial sheet in the sea urchin demonstrated how this movement could be driven by five distinctly different cellular mechanisms [Davidson et al., 1995] (box A.5). First apical constriction within the vegetal plate can drive cytoplasm to move in the basal direction. Second, cells lateral to the vegetal plate fracturing towards the centre of the plate can cause buckling. Third, contraction of a multicellular actomyosin ring or purse-string surrounding the vegetal plate can cause buckling. Fourth, apical-basal contraction in the cytoskeleton shortens the height of vegetal plate cells and can generate a compressive force within the vegetal plate cells, resulting in buckling. Fifth, differential swelling by localized secretion of a hydrophilic chondroitin sulphate proteoglycan can cause a swelling in the apical lamina that causes buckling of the vegetal plate [Davidson et al., 1995]. Subsequent experimental measurement of the mechanical properties of the embryo (box A.4), separating the contributions of the extracellular matrix (ECM) from those of the cytoskeleton, were then used to rule out the plausibility of theories requiring a compliant ECM, leaving those requiring a stiff ECM to be tested further [Davidson et al., 1999].

Another example can be found in the biomechanics analysis of gastrulation movements in ascidian embryos [Sherrard et al., 2010]. This study tested the contributing role of different tissues and different cellular programs of mechanical contractility in driving the large epithelial in-folding of mesoderm progenitors. Detailed immunofluorescence studies of the location and activation of myosin regulatory light chain allowed the construction of a computer simulation of the process (box A.5). These computer simulations provided testable predictions of the 'trajectory' of both cell- and tissue- shape changes in the embryo as the program me of force production was altered. The predicted shapes were then compared with those found within gastrulating embryos subjected to inhibitors of actomyosin contractility. Studies such as these involving whole embryos provide a basic framework for investigating the biomechanics of morphogenesis [Koehl, 1990] and have been inspired by advances in biophysics and cell mechanics. These examples suggest that different cellular processes may be mechanically equivalent because they can drive the same movement.

2.3 BIOMECHANICAL CUES AND CELL FATE AND BEHAVIOR

May of the early studies of cell mechanics were motivated by a desire to understand the cellular basis of morphogenesis (see [Trinkaus, 1984] for a classic and still relevant monograph). Qualitative measurements of the forces generated by individual cells [Harris et al., 1980] have given way to precise measurements collected using traction force microscopy [Dembo and Wang, 1990]. The application of traction force microscopy, sophisticated micro fabrication methods and advanced imaging tools have revealed a central role for focal adhesions in both guiding cell movement [Wang et al., 2001] and signaling [Chen et al., 1997]. For example, cultured cells can 'sense' the mechanical properties of their microenvironment through focal adhesions and can use these cues to guide movements.

To investigate the role of force in directing stem cell fate, a key study cultured muscle-derived stem cells on stiffness-tunable elastic substrates in the physiological ranges of 100 Pa to more than 100 kPa [Engler et al., 2006]. The authors were able to direct these cells into osteogenic fates with stiff substrates, neurogenic fates with soft substrates and myogenic fates with intermediate substrates; substrate stiffnesses were tuned to mimic the stiffness of the endogenous microenvironment for each of these cell types. Thus, information from the mechanical microenvironment of a cell can complement information from growth factor signaling in the patterning of cell identities. In these studies, cell-fate decisions seem to take several days to progress through the stages of commitment, specification and differentiation, analogous to developmental programs. This leads to further questions concerning the specific signaling factors that mediate these choices, how cells integrate mechanical and chemical signaling, and whether cells sense bulk stiffness or fine-scale features of ECM compliance [Trappmann et al., 2012]. It is unclear whether the biological principles of cell mechanics in cultured cells, many of which have evolved to provide physiological adaptation or to allow cells to thrive on tissue-culture plastic, behave similarly to cells during normal development. Another study has shown that substrate geometry can regulate human mesenchymal stem cell differentiation [McBeath et al., 2004]. However, microfabricated geometry clues might not reflect endogenous geometry cues present during development. In terms of the role of biomechanics during development and the nature of these potential cues in the embryo,

numerous questions remain, such as where and when these cues operate, whether these are hidden patterns of mechanical cues, and how the mechanical cues might be regulated by gene expression and protein activity (figure 2.2a).

In vivo studies in developing amphibian [Brodland et al., 1994, Beloussov et al., 1990, Beloussov et al., 2006] and *D. melanogaster* [Desprat et al., 2008, Farge, 2003, Kumar and Shivashankar, 2012] embryos suggest that differentiation can be triggered by high levels of mechanical strain. These are opportunities to investigate the role of mechanics in the model systems of *D. melanogaster* epithelial morphogenesis [Lecuit et al., 2011] and the early stages of development in *Xenopus laevis* [Keller et al., 2003]. Because one of the primary roles of mechanical strain is to drive tissue movement, it is often difficult to distinguish the direct or immediate roles of mechanical cues in differentiation from the classical secondary inductions, as these movements bring new contacts between signaling and responding tissues. For example, mechanical processes that drive the extension of the anterior mesoderm into the forming head result in novel signaling between these cells and the overlying neural tissues [Sampath et al., 1998]. The forces driving the mesoderm into contact with new ectodermal cells enable a new round of nodal signaling; this new round of signaling then divides a single domain of gene expression that drives eye formation into separate left and right domains. Force and mechanics are clearly necessary for this secondary induction, but mechanical signaling events are not directly controlling gene expression within the prospective eye field.

Several *in vivo* studies in which exogenously applied strains have produced changes in gene expression have suggested that mechanical signals could create auto regulatory feedback loops. Such feedback would be triggered as an endogenous mechanical cue initiates a cell signaling pathway, which then drives force production and a morphogenetic movement. Such a mechanism might operate in *D. melanogaster* ventral furrow formation or in midgut invagination during gastrulation, in which high levels of exogenously applied mechanical strain can trigger Twist (Twi) expression and can activate myosin II contractility [Farge, 2003, Pouille et al., 2009]. Temporal control of myosin II contractility [Martin et al., 2009] and the restriction of actomyosin to the apical caps of these epithelial cells drive folding and gastrulation [Mason et al., 2013]. Mechanically induced Twi expression can drive ectopic invagination and can redirect the cell fates of induced cells. Whether the redirection of cell-

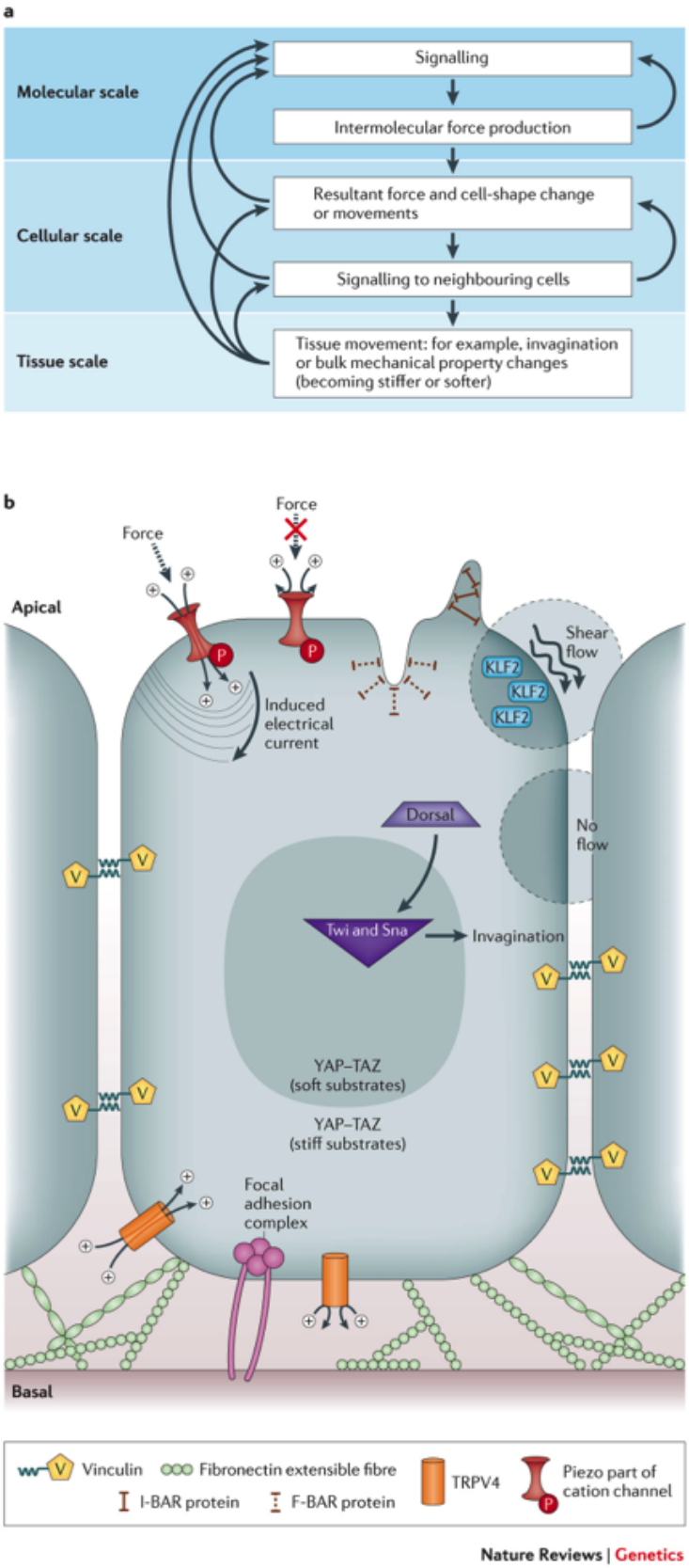

Figure 2.2: **Information flow and molecular origins of mechanics**

Figure 2.2: **Information flow and molecular origins of mechanics** a) This flow chart shows the intricacies involved with connecting molecular-, cellular- and tissue-scale behaviors and mechanisms. At the molecular scale, there is molecular signaling that causes intermolecular force production. This force production feeds back into more molecular signaling and also translates into cell-shape changes or movements at the cellular scale that induce signaling to neighboring cells. The cellular scale can then feedback into molecular-scale dynamics or can result in tissue-scale movements or bulk mechanical property changes. Isolating any portion of this intricate feedback look is extremely difficult without considering all upstream and downstream effects. b) Different molecules involved in sensing and signaling force are shown. Vinculin is located inside the cell at sites of focal adhesions and is also a candidate for sensing forces during development. Fibronectin is an extensible extracellular matrix fiber that might sense tension within the tissue. Transient receptor potential cation channel subfamily V member 4 (TRPV4) is a membrane mechanosensitive ion channel that is believed to open in response to tension in the cell membrane. Piezo is a protein part of a cation channel that induces an electrical current in response to force. I-BAR (inverse-Bin-Amphiphysin-Rvs) proteins are located at protrusions of the cell membrane, and F-BAR (Fes/CIP4 homology-BAR) proteins are located at invaginations of the cell membrane. Kruppel-like factor 2 (KF2) is a transcription factor that becomes transcribed when the cell experiences shear flow. Yes-associated protein-transcriptional co-activator with PDZ-binding motif (YAP-TAZ) is activated when the cell is on stiff substrates. Dorsal is a transcription factor upstream of Twist (Twi) and Snail (Sna) that is responsible for mesoderm invagination in *Drosophila melangaster*

fate decisions is due to mechanical cues or is the product of more conventional downstream signaling pathways, such as secondary induction, is an active area of invagination [Somogyi and Rorth, 2004].

2.4 SENSING MECHANICAL SIGNALS

One of the difficulties in understanding the molecular biology of cell mechanics is that molecular factors that generate and transmit forces may also sense forces and mediate cellular responses. We consider below a set of candidate molecular mechanosensors (figure 2.2b) capable of detecting mechanical conditions both outside and inside cells and transducing that information to intracellular signaling pathways that regulate cell fate and behaviors. Distinguishing between factors that transmit mechanical information and factors that are involved in sensing and transducing mechanical information is difficult: for example, classical knockdown or knockout of factors responsible for maintaining the mechanical integrity of a tissue might produce the same effect as removing a factor that senses biomechanics cues conveyed by a tissue. Below, we describe the role that each candidate mechanosensor has in cultured cells and, where possible, in developmental model systems.

Sensing mechanical signals from the microenvironment of a cell. Elements of the ECM such as fibronectin and proteins within the focal adhesion complex such as vinculin have been implicated as key components of mechanosensing signaling pathways, but they also transmit force and maintain tissue integrity. The ECM may have roles in providing mechanical stiffness, serving as a scaffold for migration or cell rearrangement, and providing polarity cues for tissue architecture. Fibronectin is an ECM fiber that is extremely extensible, experiences large strain and contains cryptic cell-binding sties [Garcia et al., 1999] that open with increased molecular strain [Krammer et al., 1999]. Furthermore, fibronectin fibril assembly requires the mechanical action of cells. Fluorescence resonance energy transfer analysis has shown that fibril assembly occurs only after cryptic sites in the molecule, which are kept in a partially unfolded state, are opened at the cell surface [Klotzsch et al., 2009]; these sites refold when cell tension is reduced [Baneyx et al., 2002]. This suggests that fibronectin may sense tension within the tissue. Antisense morpholino knockdown and genetic mutations reveal that fibronection is essential to both early development and later organogenesis. For example, fibronectin is required for *X. laevis* gastrulation [Marsden and DeSimone, 2001, Davidson et al., 2006], zebrafish heart development [Trinh and Stainier, 2004], endothelial invasion or migration in the developing kidney [Chiu et al., 2012], and the

establishment of left-right asymmetry [Pulina et al., 2011]. The requirement of fibronectin during development and its tension-dependent assembly into fibrils make it a key candidate in mechanosensing pathways.

Several candidates for mechanosensing during development can be found at sites of cell-cell adhesion, such as adherents junctions or desmosomes. Plakoglobin [Weber et al., 2012], β-catenin [Farge, 2003], α-catenin [Raich et al., 1999, Yonemura et al., 2010] and vinculin [Kong et al., 2013] have all been implicated as potential sites where physical cues are transducer into intracellular signaling pathways. Another candidate for mechanosensing in development is vinculin, a cytoskeletal protein found in focal adhesions and cell-cell adherents junctions [Kong et al., 2013]. Vinculin is also required for normal development. During mouse development, vinculin mutants show a lack of midline fusion of the neural tube and have delayed heart development accompanied by structural defects; such defects are probably due to the function of vinculin in regulating cell adhesion and motility [Xu et al., 1998]. Beyond the adhesion complex, these factors transmit and might sense tension between the ECM and intracellular actomyosin contractile structures. Vinculin also seems to play a part in sensing tension at cell-cell junctions. For example, the mechanosensing role of vinculin within E-cadherin complexes has been observed with magneto twisting cytometry, a tool that allows the application of force to a cell through adherent micro-beads, applied to MDCK or F9 cells [le Duc et al., 2010]. The role of vinculin in F9 cells has been further dissected by direct determination of the adhesion forces and creep modulus (the tendency of a material to deform) using magnetic tweezers (another tool for applying force to cells). This finding suggests that vinculin contributes to the mechanical properties of the cell under large external forces through the regulation of contractile stresses in actomyosin [Mierke et al., 2008]. Using magnetic tweezers, total internal reflection fluorescence microscopy and atomic force microscopy, another study revealed that forces transmitted by talon (another scaffold protein linking ECM integrin receptors to the cytoskeleton) to vinculin altered cytoskeletal reorganization by exposing cryptic binding sties on vinculin [del Rio et al., 2009]. It is important to recognize that the principles of cell mechanics have mostly been explored in cultured cells, with only a few rigorous studies carried out in developing embryos or in intact embryonic tissues.

Sensing mechanical signals from the plasma membrane and cell cortex. Mechanical cues may be sensed along the apical or basolateral faces of cells by stretch-sensitive channels, such as transient receptor potential cation channel subfamily V member 4 (TRPV4), Bin-Amphiphysin-Rvs (BAR) proteins, or Piezo proteins. Whereas the ability of a cell to sense forces exerted on it is discussed above, we discuss below the ability of a cell to sense intracellular mechanical conditions. These sensors might still reflect external cues but might also detect stresses and forces produced inside the cell. A role for stretch-sensitive channels in transducing mechanical cues at the membrane can be seen in the ability of mammalian endothelial cells to reorient when exposed to, for example, fluid shear or to cyclic stretch; when TRPV4 channels are knocked down, the cells fail to reorient to flow [Ho et al., 2012]. TRPV4 triggers reorientation by activating phosphoinositide 3-kinase (PI3K), which then activates $\beta 1$ integrins [Thodeti et al., 2009]. In addition to the role of TRPV4 in transducing fluid shear forces, its more general role in mecahnotransduction has been studied in single muscle fibers [Ho et al., 2012]. In zebrafish, TRPV4 channels within renal cilia are throughout to sense mechanical stimuli and are also thermosensitive [Kottgen et al., 2008]. In *D. melanogaster*, TRPV4 homologues have a role in photo-transduction mechanical sensing [Cosens and Manning, 1969], and in *Caenorhabditis elegan*, TRPV4 homologues have a role in olfactory cue sensing mechanotransduction [Liedtke et al., 2003]. Piezo proteins are another family of channel proteins that are thought to be responsible for converting mechanical forces into electrophysiological signals. Patch clamp studies of the *D. melanogaster* homologue Piezo expressed in human embryonic kidney cells demonstrated that Piezo channels can open in response to mechanical forces applied by a fine glass pipette [Coste et al., 2012]. *In vivo*, Piezo mediates noxious response to high temperature and is essential for sensing noxious mechanical stimulus [Kim et al., 2012]. In zebrafish, Piezo1 regulates cell extrusion in order to maintain homeostatic epithelial cell numbers in the growing tail fin [Eisenhoffer et al., 2012], a function that may parallel its role in regulating cell density within confluent MDCK cultures. In mice, PIEZO1 is required for the initiation of mechanically activated currents in neuroblastoma cells [Coste et al., 2010]. These examples have been identified in mechanosensing pathways in cultured cells and physiology studies, and are likely to have important roles in mechanical feedback signaling during development.

How these endogenous biosensors trigger behavioral or cell-shape changes in cells is mostly unknown.

It has long been recognized that cell protrusive activity can be triggered by mechanical events at the cell membrane and cell cortex; for example, during contact inhibition of cell migration or tension-induced protrusion [Weber et al., 2012]. Recent examples of responses to applied tension include the response of *X. laevis* embryonic mesendoderm cells [Weber et al., 2012] and single neutrophils [Houk et al., 2012]. One candidate family of proteins that might mediate the sensing of these types of mechanical events in the cortex are the BAR family of proteins. BAR proteins are membrane-deforming or membrane curvature-sensing proteins that connect F-actin structures to the plasma membrane [Itoh et al., 2005] and have been suggested to sense mechanical cues. Owing to their conformation, F-BAR (Fes/CIP4-homology BAR) proteins accumulate within intracellular invaginations or concave-shaped membrane structures, whereas I-BAR (inverse-BAR) proteins accumulate within cellular protrusions or convex-shaped membrane structures. Deformed membranes also correlate with positive or negative membrane strains [Suetsugu, 2010]. Signaling to the actin cytoskeleton can occur via the I-BAR domain because it can induce strong phosphatidylinositol-4,5-bisphosphate clustering [Saarikangas et al., 2009]. In zebrafish, loss-of-function studies also found defects in ciliary structures that are directly related to BAR protein function [Schler et al., 2013]. These proteins have not yet been shown to have a role in early development or morphogenesis.

2.5 FROM MECHANICAL CUES TO GENE EXPRESSION

After a mechanical cue has been converted into a conventional intracellular signal, cell fate choices are made through the activation of mechanically responsive transcription factors, such as TWI [Desprat et al., 2008, Farge, 2003], Kruppel-like factor 2 (KLF2) [Parmar et al., 2013, Lee et al., 2006, Groenendijk et al., 2004, Wang et al., 2006] and the newly identified Yes-associated protein-transcriptional co-activator with PDZ-binding motif (YAP-TAZ) complex [Dupont et al., 2011, Gee et al., 2011, Morin-Kensicki et al., 2006]. The

downstream targets of KLF2 and YAP-TAZ are being elucidated, but the targets of the transcription factor TWI have been subjected to detailed analysis [Sandmann et al., 2007].

TWI initiate a broad range of developmental modules, including differentiation, the cell cycle, cell migration and morphogenesis [Sandmann et al., 2007]. The following example highlights the prospective role of Twi in the mechanics of mesoderm invagination, apical constriction and anterior endoderm compression by germ-band extension in *D. melanogaster* [Farge, 2003]. Conventional signaling pathways that are active during mesoderm patterning that turn on the Dorsal transcription factor turn on overlapping expression of the transcription factors Twi and Snail (Sna). It has been hypothesized that Sna expression over a broad region activates myosin II and drives pulsatile contractions in the mesoderm [Martin et al., 2009]. This first wave of contractility activates the pathway downstream of the gene folded gastrulation (Fog). Cells with an activated Fog signaling pathway and that express Sna-induced genes then initiate Twi expression; this stabilizes actomyosin in the apical cap and results in a second contraction wave that drives cell-shape changes and the formation of the ventral furrow [Pouille et al., 2009, Mason et al., 2013]. Twi mutants revealed these two phases of furrowing, in which the forces produced by the first wave of actomyosin contractions activate signaling pathways to produce the next wave of stable contractions that drive the furrow to deepen. In Twi mutants, the second constriction wave is defective, whereas in Sna mutants with Fog still expressed, both the first and second waves are defective. This suggests that Sna directs the expresso of factors that control the first contraction wave, whereas Twi targets, including Fog are necessary for the second wave. In Sna homozygous mutants, applying a local deformation with a micromanipulated needle succeeds in inducing furrowing in nearly 70% of the embryos [Pouille et al., 2009]. In Sna and Twi double mutants, mechanical indentation does not rescue the defect but activates Fog signaling in the mesoderm, suggesting that Twi directs the expression of mechanical force sensors required for the mechanical rescue of Sna mutants [Pouille et al., 2009] (figure 2.3. Further studies of apical constriction in ventral furrow formation have found that activated myosin II no longer accumulates at the apical cortex in Twi and Sna mutants and that myosin II remains in cell-cell junctions, suggesting that mechanical cues may reorganize the apical cortex, reinforcing it as ventral furrow format progresses [Martin et al., 2009].

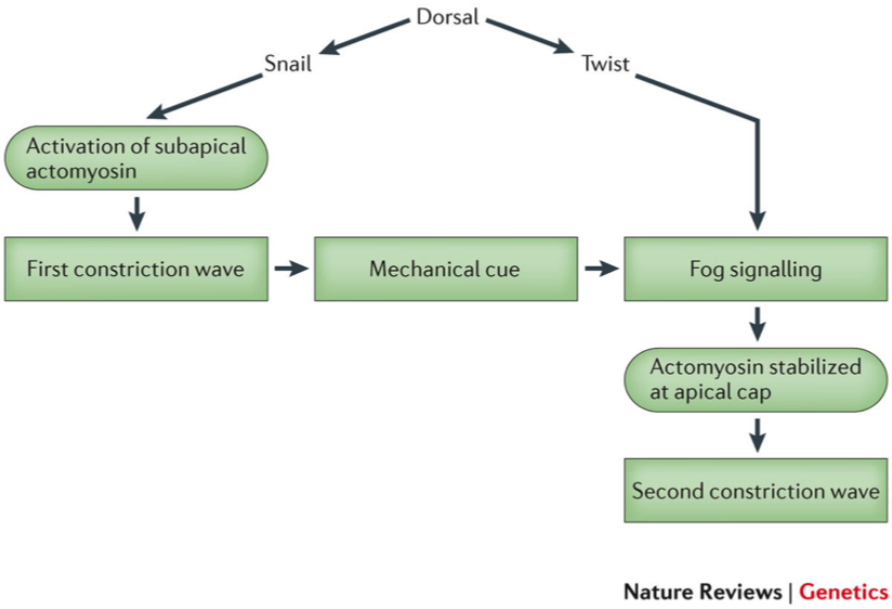

Figure 2.3: **Mechanical feedback during morphogenesis.** A pathway depicting the genetic control of ventral furrow formation and anterior midgut invagination in *Drosophila melanogaster* and a role in that network for mechanical cues. Snail expression is responsible for the mechanical cues produced by the first phase of myosin II contraction. Strain within the epithelium might redirect actomyosin to the apical cap and activate folded gastrulation (Fog) signaling, and strain and Fog signaling act during the second, Twist-dependent phase to stabilize actomyosin contractions and to drive epithelial folding. Furrowing and invagination in Twist mutants can be rescued by exogenously applied strain either by laser ablation or by physical indentation. After the rescue of invagination, larval development was reported to proceed as normal.

A similar role for Twi in a mechanotransduction pathway has been proposed during invagination of the anterior midgut primordial in *D. melanogaster*. Magnetic tweezers were used in conjunction with laser ablation to rescue the differentiation of the stomodeal primordium. Twi expression in stomodeal primordia could be blocked by the ablation of nearby cells and restored after magnetically controlled compressive forces were applied to the primordial [Desprat et al., 2008]. Mechanical perturbations of ventral furrow formation and anterior midgut invagination in *D. melanogaster* have been conducted at the tissue scale, where forces must be transmitted and integrated before being sensed.

Another transcription factor, KLF2, is expressed in response to shear strains resulting from fluid flow. For example, artery, vein and capillary formation depends on KLF2 signaling in response to blood flow. KLF2 is a member of the Kruppel-like factor family of zinc finger-containing transcription factors with homology to the *D. melanogaster* segmentation gene product Kruppel [Pearson et al., 2008]. *In vitro* studies have been used to refine the nature of the mechanical cues that trigger KLF2 expression. Cultured human umbilical vein endothelial cells have increased KLF2 expression when subjected to pulsatile shear flow and decreased KLF2 expression after exposure to reciprocating oscillatory shear flow [Wang et al., 2006]. *In vivo*, KLF2 expression correlates with disturbed patterns of local fluid flow. KLF2 expression in chick embryonic vasculature is found in regions of high shear stress [Groenendijk et al., 2004]. Similar studies in mice also suggest that KLF2 expression correlates with the rise in fluid shear forces during development [Lee et al., 2006]. Studies of zebrafish silent heart mutants (in which the heart does not beat) revealed highly altered vascular expression of Klf2a, suggesting a direct dependence of Klf2a expression on blood flow *in vivo* [Parmar et al., 2013].

The role of mechanics in driving gene expression has been quantified more thoroughly *in vitro* with the application of defined shear forces [Wang et al., 2006]. These studies demonstrate that cell fate and behavioral decisions can be responsive to mechanical cues, but the molecular mechanisms for sensing biomechanical conditions and triggering signaling pathways have been difficult to identify. A direct connection between mechanical stimulation and transcriptional response has been made int he case of the transcription factor YAP and its transcriptional co-activator TAZ. YAP and TAZ are unregulated in mammary epithelial

cells cultured on high stiffness substrates [Fu et al., 2010]. Most work with YAP has been in cell culture; however, knockout and knockdown studies have implicated this transcription factor in vascularization and anterior-posterior axis elongation [Morin-Kensicki et al., 2006]. YAP knockdown studies in both fish and frogs have implicated that YAP may have a role in axis formation, as well as in epiboly during gastrulation [Gee et al., 2011]. The strongest cases for a correlation between mechanics and YAP-TAZ activation are found when cells are cultured under well-defined mechanical conditions [Fu et al., 2010]. In order to determine whether YAP-TAZ transcription activation reports ECM stiffness, transcriptional activity was measured in various cell types (mammary epithelial cells, MDA-MB-231 cells and HeLa cells) cultured on stiff and soft fibronecyin-coated hydrogels [Fu et al., 2010]. Stiff substrates had YAP-TAZ transcriptional activity that was comparable to that in cells grown on plastic, whereas on soft substrates YAP-TAZ activity was reduced to levels comparable to those in YAP-TAZ knockdowns [Fu et al., 2010]. Furthermore, on soft substrates YAP-TAZ is found in the cytoplasm, but on hard substrates it moves into the nucleus. Micropatterned fibronectin substrates could also drive YAP-TAZ from the cytoplasm into the nucleus as cells adopt a spread-out morphology. To determine whether YAP-TAZ was reacting to the cell spreading or the ECM contacts, both the stiffness of the substrate and the density of fibronectin were controlled by culturing cells on micropillars- elastomeric moulded microposts the height of which corresponds to the rigidity of individual pillars [Fu et al., 2010]. On shorter or stiffer micropillars, YAP-TAZ remained int he nucleus, even though the spreading area of the cell was the same. YAP-TAZ activation is also regulated by intracellular actomyosin contractility, as inhibition of RHO or reduced F-actin assembly also inhibits YAP-TAZ transcriptional activity. Similar responses of YAP-TAZ to reduced RHO kinase (ROCK) and non-muscle myosin activity suggest that cytoskeletal tension drives YAP-TAZ nuclear location. YAP-TAZ may have a key role in stem cell differentiation because YAP-TAZ depletion prevents stem cells from responding to changes in ECM stiffness [Dupont et al., 2011]. In *D. melanogaster*, increasing the activity of the YAP homologue, Yorkie, increases F-actin assembly [del Rio et al., 2009].

2.6 MECHANICS, FEEDBACK AND ROBUST DEVELOPMENT

The ability of the embryo to develop amid genetic, maternal and environmental variation has puzzled developmental biologists for decades. Considerable experimental evidence suggests that cells and embryos must be able to modulate cell signaling networks, gene expression patterns and cell behaviors to accommodate variation (for example, [Manu et al., 2009]). Still, even with these robust programs, there remains considerable phenotypic variation [Tyszka et al., 2005]. Several factors might provide feedback between the mechanical environment and signaling networks as part of these programs. On the molecular scale, the motor complex of myosin II can adjust force production based on the mechanical loading [Howard, 2001]. At the cell scale, the shape of a cell can dictate its protrusive activity [Jiang et al., 2005], as well as its commitment to specific cell lineages [McBeath et al., 2004]. Finally, at the tissue scale, the classical processes of secondary induction might serve to signal the success of a particular tissue movement or elicit further morphogenetic movements. The molecular scale and cellular scale processes that provide feedback from the mechanical processes of morphogenesis are poly understood, and their resolution will provide deeper insights into many larger questions in evolution, as well as the nature of disease liability and birth defects [Farge, 2003, von Dassow and Davidson, 2011, Farge, 2011, Shook and Keller, 2008].

2.7 FUTURE CHALLENGES

Advances in developmental mechanics are revealing the hidden contribution of biomechanics to patterning, morphogenesis and organogenesis and are extending our understanding of the origin of structural birth defects. These advances are being accomplished by unifying the efforts of geneticist, cell biologists, physicists, and engineers. One of the crucial challenges to progress is that one cannot simply knock out a mechanical process in the same way as one knocks out a gene. Furthermore, there are no one-to-one correspondence principles between gene functions and the mechanical events that they affect. It is clear that mechanical processes have a polygenic origin and that dozens if not hundreds of genes are responsible for

physical processes operating on a range of scales from molecular to cellular to the tissue level. There are many ways for mechanical processes to influence development, including through a direct and immediate effect on gene expression, through guiding cell behaviors and through the long-term consequences of tissue movements. The challenges of characterizing these roles for mechanics, and in particular distinguishing between what are causes and what are effects, are well understood by geneticists. To overcome these challenges, developmental biologists are turning to systems biology with principles borrowed from control theory and computer simulation.

A systems or theoretical approach to studying morphogenesis involves breaking down the biochemical and biological processes of force generation, transmission and sensing into multiple separate processes operating on different scales and then recombining those processes in a mathematical or computational framework. Processes that are difficult to isolate experimentally *in vivo* are easily controlled in a computer model. For example, motor proteins such as myosin II have roles in force generation, transmission and coordination within the tissue. Furthermore, single-molecular studies have shown that myosin II can directly 'sense' levels of applied force and can adjust their own force production to compensate so it seems likely that this might occur universally during morphogenesis. Alternatively, another report suggests that cells directly sense force *in vivo* and trigger the recruitment of myosin II to the site where applied forces were sensed [Fernandez-Gonzalez et al., 2009]. This is an attractive hypothesis, but it is unclear what stresses are present *in vivo* and whether the magnitude or range of those forces are physiologically relevant at the scale of the cell or are relevant to physical demands of morphogenesis. Efforts to understand the role of myosin II feedback *in vivo* in either a cell or a tissue setting will require sophisticated experimental designs that parallel earlier *in vitro* single-molecule studies in which the loads and processivity of myosin II were controlled [Sweeney and Houdusse, 2010]. Such future studies will require laser ablation and photoactivation, methods for applying controlled forces, and loss-of-function mutants.

Future progress in developmental biomechanics will require new experimental techniques and theories for controlling mechanical loads on tissues [von Dassow et al., 2010], assessing changes in gene expression, protein activity and signaling, and evaluating their effects on the

rates of morphogenesis and phenotypic variation. Experiments that rigorously evaluate the role of mechanics in directing cell fate or in providing feedback to improve the robustness of developmental programs are difficult to design. The long time-lag between a mechanical stimulus and cell differentiation and the difficulty in ruling out a role for secondary induction are only two challenges. Falsifying hypotheses involving both mechanical and chemical signaling pathways requires testing tissue or cellular responses to well-defined mechanical stimuli. Advances in cell mechanics, tunable elastic substrates and micro fabrication provide increasingly sophisticated tools for controlling the mechanical microenvironment of cells and tissues. Advances in cell biology and imaging are providing tools for interrogating the cell signaling pathways that are needed to report the status of mechanically stimulated cells. Together with theoretical and systems biology, these experimental biomechanics approaches are leading to more complete, integrated views of developmental mechanics that will provide lasting insights into development and the self-organizing processes that assemble organs and lay the foundation for physiological function.

3.0 ROTATIONAL MODEL FOR ACTIN ALIGNMENT BY MYOSIN

To begin our examination of Aim 1 (1.1.1; Identify how rates of F-actin polymerization and myosin generated forces affect actomyosin dynamic morphology), we decided to start with an extremely simplified model of F-actin and non-muscle myosin II. The physics of the system only considered the rotation of F-actin and made even more non-biological simplifying assumptions for how the actomyosin interactions would occur. Dr. Ermentrout helped us develop the model and derive the continuum equations to further analyze the model and system. I developed the code to simulate the rotational model and performed subsequent analysis in Matlab 2011a. In addressing Aim 1 (1.1.1), this study allowed us to address how actin polymerization rate affected morphology, perform a parametric analysis of model parameters, and quantify how these parameters affected force and morphology. This paper was published in the Journal of Theoretical Biology in May 2012 [Miller et al., 2012].

3.1 INTRODUCTION

Filamentous actin or F-Actin and its associated motor protein myosin II are fundamental cytoskeletal proteins essential to the physiological function of cells, establishment and maintenance of cell shape, and enabling cell motility. Actomyosin regulates cell shape and cell motility by restricting contractility to specialized regions in the cell such as the apical cell cortex [Martin, 2010], or the trailing edge of migrating cells [Yam et al., 2007, Kim and Davidson, 2011]. In these cases the role of actomyosin is experimentally tested by perturbing either the assembly of F-actin or the cross-linking and contractility of myosin II. However, given the ubiquity of actomyosin within non-muscle cells it has been difficult to resolve

the specific role of actomyosin and related regulatory proteins within multicellular tissues. Actin rotation is believed to play a role in stress fiber formation, formation of the cytokinetic actin ring, initiation of filopodia, and podosome extension[Condeelis, 1993, Yamaguchi et al., 2006].

Recent advances in mathematical and biophysical models of cytoskeletal filaments and motors have provided an important framework in which to analyze the dynamic properties of the cytoskeleton. Theoretical studies of cytoskeletal dynamics of microtubules and their associated motor protein kinesin [Karsenti et al., 2006, Nedelec et al., 2003] have been used to elucidate the formation and function of spindles during mitosis. In vitro studies of the rheology of purified protein have found a multiple stage aggregation process by which myosin motors organize actin filaments into contracted states [Soares e Silva et al., 2011]. Similar models of the actin cytoskeleton have been used to study the role of actin polymerization in powering intracellular movement of *Listeria monocytogenes* [Alberts and Odell, 2004]. Although there are many theoretical models for actomyosin dynamics [Sommi et al., 2011, Kruse and Jülicher, 2006, Kruse et al., 2004, Spiros and Edlestein-Keshet, 1998], these analyses have used "agent-based" computer simulations in which discrete elements, individual filaments, and structural elements are modeled within a complex geometry. Such models create a virtual assembly of "agents" with association rules and biochemical rates describing all interactions mediated by simple physics of diffusion, chemistry, and mechanics. To simplify the physically and biochemically complex cytoskeleton a range of alternative theoretical approaches have been adopted to break the complex biology of actomyosin into simpler systems whose behaviors can be explored analytically rather than computationally [Mogilner and Oster, 1996, Chan and Odde, 2008, Zemel and Mogilner, 2009]. However, few of these studies have investigated the role of polymerization and motor contractility in aligning filaments. Given that filament alignment may be involved in diverse processes that reorganize F-actin, we developed theoretical models to directly explore these processes.

We hold the filaments pinned at their minus ends in order to prevent translational movements of filaments and expose mechanisms which play a role in aligning filaments. The polarity of the actin filament and its motor protein myosin II is a critical property and distinguishes the cytoskeleton from more generic types of polymer gels. In order to understand

the complex behavior of actomyosin in complex morphologies we must consider the polarity and assembly of actin filaments, actin filament bending, the dual role of myosin motors as cross- linkers, and how motors shape and contribute to the mechanical properties of solid-like multi-filament structures. Through our simulations and analysis we found that filaments will always align and the time needed for alignment to occur depends on an optimal velocity for the myosin motors. We also investigated what mechanisms would inhibit alignment, and found that actin polymerization is a natural source of noise to destabilize alignment. We found that a phase transition to strong alignment occurs when either polymerization rates are reduced or the velocity for the myosin motor is changed toward an optimum.

3.2 MODEL AND METHODS

3.2.1 Simple geometry of actin-myosin interaction

Within the cell cortex actin filaments are present with arbitrary orientations and myosin motors attach to the filaments, move toward filament plus-ends exerting a force which acts to align the filaments. If confined to a two dimensional plane each actin filament has three degrees of freedom: the position of its center of mass in the plane, and its orientation with respect to that center of mass. We first consider a simplified actomyosin array of one motor and two filaments (Figure 3.1A). In the cell, myosin II is organized into anti parallel arrays of bundled motors [Pollard and Borisy, 2003]. In our model we represent a single bundle as a mini thick filament and refer to such a bundle as a single "motor." Filaments are only allowed to change their orientation. Minus ends which remained pinned at a fixed location we call the "origin." Motors first attach at the pinned minus ends of a pair of filaments move toward the plus end, exerting a spring-like force on the filament pair (Figure 3.1B). We can define the angle of orientation for each filament (θ_1 and θ_2), and the distance from the minus-end to the attached motor (s_1 and s_2). The position of the two motors can be written in a Cartesian frame of reference as $(s_1 \cos\theta_1, s_1 \sin\theta_1)$ and $(s_2 \cos\theta_2, s_2 \sin\theta_2)$. As motors move to filament plus-ends, we assume they move with a constant velocity, v. As the two

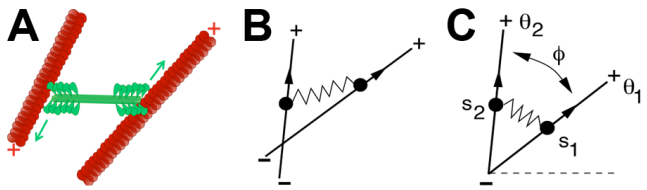

Figure 3.1: **Description of geometry, method, parameters, and variables.** (A) Cartoon depicting the biological interaction between actin filaments (red) and myosin II motors (green). (B) Simplified depiction of interaction between two actin filaments and one motor. (C) Idealized geometry for the motor-filament configuration used in our models. We refer interested readers to the supplementary material for simulation details.

ends of the myosin motor move apart toward the plus-ends of their respective filaments the myosin acts as a dynamic spring exerting forces on each filament in the pair [Dunaway et al., 2002, Neumann et al., 1998, Nagornyak et al., 2005], resulting in movement and rotation of both filaments.

From this biophysical description of motors, actin filaments, and their interactions we can describe the life-cycle of a myosin motor. The motor begins its life-cycle unattached to any filaments, waiting at the origin until it chooses to attach to a random pair of filaments. Once the motor attaches to a pair of filaments, the motor walks toward the plus-ends of the filament pair, generating force which pulls the filaments towards each other. The motor can detach from the filament pair as a result of a random stochastic process, and if the motor detaches, returns to the pool of unattached motors at the origin. On the other hand, if the motor reaches the end of the filament pair, it will fall off and return to the origin.

We have also simulated actin filament polymerization and depolymerization by allowing randomly selected filaments to disappear and be replaced by polymerization at the same time at a new angle. Polymerization rates represented by a rate per filament which allows the random, stochastic removal of a filament and placement of a new filament during our Monte Carlo simulations. In the event that a motor is attached to a depolymerizing filament, the motor will detach.

3.2.2 Equations of motion for the myosin motor and filament pair

Based on these rules we derive and compute the equations of angular motion for the filament pair as a myosin motor draws them into alignment. To extend the equations to the N filaments and M motors case, we only need to consider that the forces sum linearly. We derive the equations of motion for two filaments and one motor (Equation 3.1), where k is the spring constant, μ is a viscous damping term, and s is the distance between the filament's plus end and the attachment of the motor.

$$\begin{aligned} \dot{\theta}_1 &= \frac{k}{\mu} s^2 \sin(\theta_2 - \theta_1) \\ \dot{\theta}_2 &= \frac{k}{\mu} s^2 \sin(\theta_1 - \theta_2). \end{aligned} \tag{3.1}$$

More generally, we can define the change in angle for filament i from N total filaments as the sum of forces exerted by each motor m from the pool of motors (M) which are all attached to filament i (Equation 3.2).

$$\dot{\theta}_i = \frac{k}{\mu} \sum_{m \in M} s_m^2 \sin(\theta_{p(m,i)} - \theta_i) \tag{3.2}$$

Since we have to calculate the change in angle between the filament pair to which the motor, m, is attached, we define the index for one filament to be i and the other filament's index to be $p(m, i)$.

From these equations of motion we can evaluate the mean of the distance the motor travels along the filament, s, squared. This term can be related to the mean rate of alignment and the average force exerted by the system (Equation 3.3).

$$\langle s^2 \rangle = \frac{k}{\mu} \frac{1}{T} \int_0^T s^2(t)\ dt. \tag{3.3}$$

We can also describe the morphology of the resulting actin array with an order parameter (Z), a measure of alignment of the filaments in our system. Z is defined as follows:

$$\begin{aligned} S(t) &:= \frac{1}{N}\sum_{i=1}^{N}\sin(\theta_i(t)) \\ C(t) &:= \frac{1}{N}\sum_{i=1}^{N}\cos(\theta_i(t)) \\ Z &:= \lim_{T\to\infty}\frac{1}{T}\int_0^T \sqrt{S^2(t)+C^2(t)}\; dt. \end{aligned} \tag{3.4}$$

In the statistics of circular or periodic distributions $(1 - Z)$ is often called the *circular variance* [Zar, 1999]. The order parameter can be determined explicitly in the case of two filaments (Equation 3.5), where the difference in the angle between the filament pair, $\phi(t)$, is defined for $-\pi$ to π.

$$Z = \lim_{T\to\infty}\frac{1}{T}\int_0^T \left|\cos\frac{\phi(t)}{2}\right| dt \tag{3.5}$$

The order parameter as it relates to our Monte Carlo simulations describes the degree to which a set of filaments is co-aligned. For instance, in the case where the order parameter is one ($Z = 1$), all filaments are perfectly co-aligned with the same orientation angle. Alternatively, when the order parameter is zero ($Z = 0$), the filaments will have orientation angles uniformly distributed around the circle.

3.2.3 Biophysical properties of actin filaments and myosin motors

All of the parameters and their associated most commonly used value for the Monte Carlo simulations are found in table form with the supplementary information (TableB1), along with all of the variables (TableB2). The Monte Carlo simulations were carried out using MATLAB and the algorithm, represented as a simple flow chart (FigureB3), has been included in the supplementary information.

Actin filament polarity and length (L) – Actin microfilaments or F-actin vary from minimal lengths of a few G-actin subunits to more than 10 μm with a distinct polarity of plus- and minus- ends. For the majority of our simulations and continuum analyses we set

filament length to 1 μm. This may be considered either the fixed length of a stable filament or the dynamic length of a tread-milling filament.

Myosin motor geometry and velocity *(v)* – Each functional myosin II subunit is assembled from two heavy chains, two essential light chains, and two regulatory light chains. Myosin II mini thick filaments are assembled from multiple subunits into an antiparallel array with the globular ATPase head domains at the opposite ends of the filament and the rod-like domain of the subunits bound in antiparallel arrays in the center bare region of the mini-filament. The composition and length of mini thick filaments vary from cell type to cell type of ∼20 myosin II complexes and are approximately ∼350 nm in length [Niederman and Pollard, 1975]. Little is known experimentally about the force-producing capabilities of mini thick filaments but they can stretch and act like springs [Neumann et al., 1998, Nagornyak et al., 2005, Dunaway et al., 2002, Smith et al., 2007].
We assume that ATP levels are high and myosin II motor ATPase activity is maximized.

Model time *(t)* – Model time is reported in seconds and the Monte Carlo simulations are advanced with individual time-steps of 0.01 seconds.

Myosin motor attachment rate *(r_0)* – In the cell, the rate of motor attachment would reflect several factors including the rate of diffusion of myosin mini-filaments, the volume each mini-filament can search, and the relative density of F-actin binding sites. In our unique geometry the situation is considerably simplified since all unbound motors are held within binding range of F-actin at their minus-end. Thus, for a majority of our simulations we fix the motor attachment rate at 0.7 per second.

Myosin motor detachment rate *(r_1)* – Myosin motors are highly processive but do occasionally dissociate from filaments before reaching the plus-end. Since these rates are poorly characterized *in vivo* we choose detachment rates that range from 0.1 to 0.8 per second. This rate may also vary based on the amount that the motor is stretched; e.g. load (Section 3.5).

Depolymerization rate *(r_2)* – Actin filaments within cells are constantly being turned over so we introduce a depolymerization rate per filament. This rate may be dependent on the length of the filament and may be controlled within the cell. Polymerization rates are allowed to vary from 0.01 to 0.2 per second. *In vivo*, the polymerization / depolymerization rates may control actin abundance, however, within our simulations we enforce constant F-actin density and promptly polymerize a new filament when one filament depolymerizes.

Viscosity *(μ)* – In the cell, filaments experience viscous drag forces as they rotate through the cytoplasm. By contrast, myosin mini thick filaments, due to their smaller size, do not experience such drag forces. In our model, we only consider the viscous drag of water and explicitly simulate filament-filament interactions that would contribute to cytoplasmic viscosity. If we increase the viscosity parameter, we would see that the time it would take to align would increase since the increase in viscosity would make it more difficult for the filaments to rotate through the space. The viscosity of water is defined as 1×10^{-3} Pa s.

Motor stiffness *(k)* – As the two ends of the myosin II motor mini-filaments move apart on pairs of actin filaments the mini-filament exerts spring-like forces on the two filaments. Thus, our simulations include a motor spring stiffness term k. Myosin mini-filament stiffness has been measured from 1.7 to 5.0 pN/nm [Kaya and Higuchi, 2010, Neumann et al., 1998, Nagornyak et al., 2005, Dunaway et al., 2002].

(μ/k) – For our equations of motion and continuum analysis, we do not use separate values of μ and k but instead use the ratio of stiffness to viscosity. Due to uncertainty in the exact value of this term, ranging from 0.2 to 0.6 (s/m^2) we set this ratio to 1.

3.3 RESULTS

3.3.1 Two filaments, one motor

For simplicity, we first consider two filaments and one motor. The two filaments lie at specific angles (θ_1 and θ_2) and may be bound together at a distance, s, from their origin by a motor. We found it advantageous to consider the angle between the two filaments ($\phi := \theta_2 - \theta_1$) rather than the orientation angle of each filament. We found a single equation of motion could replace the two equations defined previously (see Section 3.2.2, Equation 3.1):

$$\dot{\phi} = -2s^2 \frac{k}{\mu} \sin \phi. \tag{3.6}$$

For the case of two filaments and one motor, we used this equation of motion to follow events that occurred during a typical simulation (Figure 3.2A): (a) the motor attached to the filament pair and started to pull filaments together as the motor traveled down the filament at a fixed velocity, (b) the motor fell off the filaments before it reached the ends of the filament pair, (c) the motor spent time waiting to attach to the filament pair, (d) the motor reached the plus-end of the filament and fell off. For all simulations perfect alignment is guaranteed since there were no other processes which could cause the difference in filament angle (ϕ) to increase. Thus, the changing morphology of the system could be followed as the order parameter (Equation 3.5) increased to a value of one and force-generated by the motor decreased to zero (Figures 3.2B-F).

However, actomyosin in cells rarely assumes the form of static bundles and we turned to investigate processes that could destabilize or prevent formation of aligned bundles. Since actin filaments are constantly turning over in the cell we introduced the processes of polymerization and depolymerization. These processes introduced a form of noise into our simulations; by contrast, thermal noise could also prevent perfect alignment, but for filaments in a viscous media this source of noise is negligible.

Allowing filaments to undergo depolymerization and polymerization resulted in more complex dynamics for the two filament case. We considered the events along a typical time course (Figure 3.2F): (a) the motor attached to the filament pair and pulled filaments

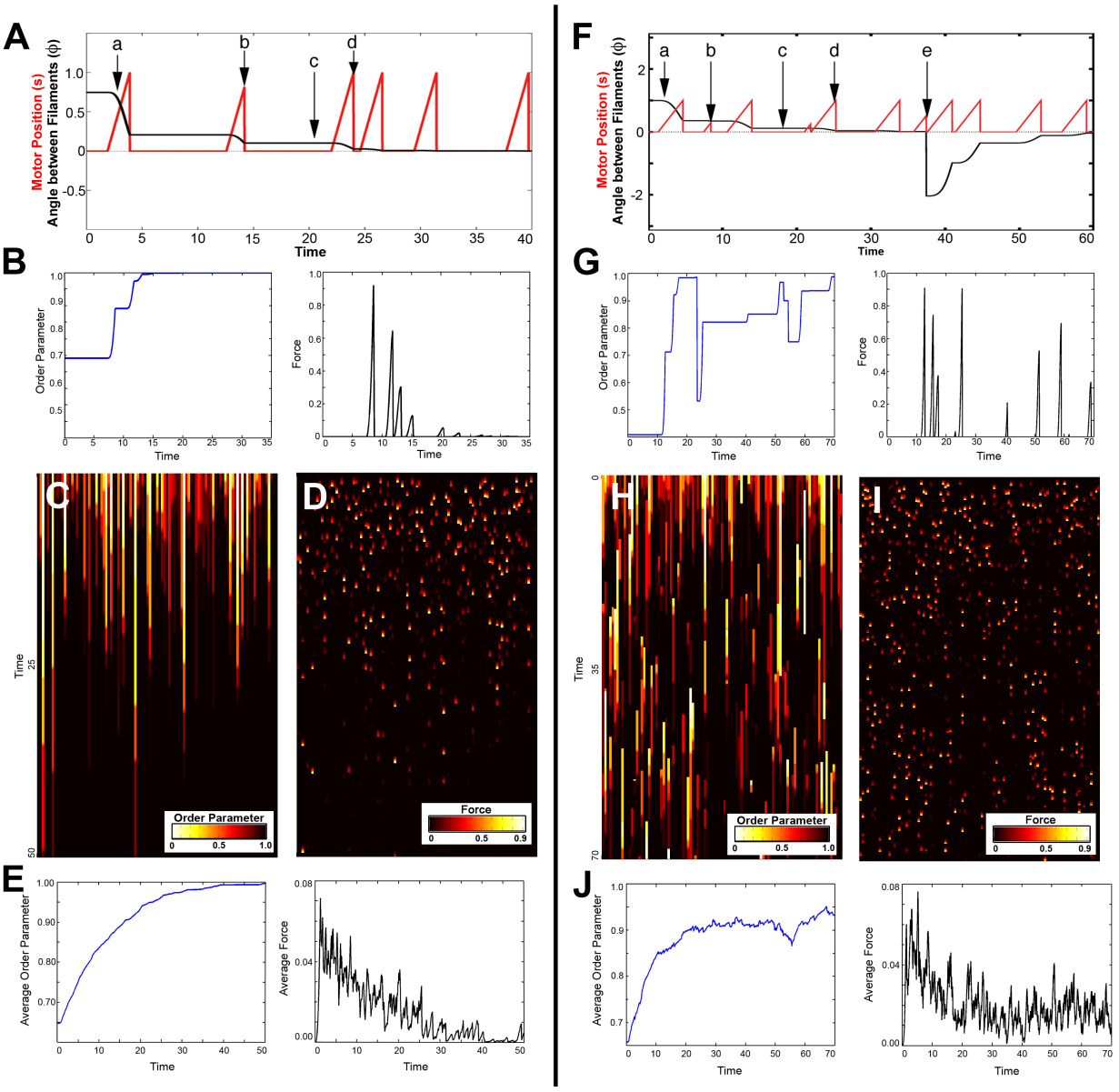

Figure 3.2: **Monte Carlo Simulations for two filaments and one motor.**(A) Visual of one Monte Carlo simulation time course for motor movement (red) and the resulting change in angle of the filament pair (black) without polymerization: (a) motor attaches to the filament pair, (b) motor falls off before it reaches the end of the filaments, (c) motor waits to attach, (d) motor falls off when it reaches the end of the filaments. *Continued on next page*

Figure 3.2: *Continued from previous page* (B) Plots of order parameter (blue), and force generated (black) for one Monte Carlo simulation. (C) Color evolution plot of the order parameter for 100 Monte Carlo simulations. Given enough time, the two filaments become aligned by the motor. (D) Color evolution plot for the force generated by the motor for the 100 Monte Carlo simulations in C. (E) Average order parameter (blue) and average force generated (black) for the 100 Monte Carlo simulations shown in C and D. (F) One Monte Carlo simulation time course for motor movement (red) and the change in angle of the filament pair (black) with polymerization: (a) motor attaches to the filament pair, (b) motor falls off before it reaches the end of the filaments, (c) motor waits to attach, (d) motor falls off when it reaches the end of the filaments, (e) one filament depolymerizes and a new filament instantaneously polymerizes at a new angle. (G) Plots of order parameter (blue), and force generated (black) for one Monte Carlo simulation with polymerization. (H) Color evolution plot of the order parameter for 100 Monte Carlo simulations. In contrast to C, the addition of polymerization impedes long term alignment of the two filaments. (I) Color evolution plot for the force generated for the 100 Monte Carlo simulations in H. (J) Average order parameter (blue) and average force generated (black) for the 100 Monte Carlo simulations shown in H and I.

together as the motor traveled down the filament at a fixed velocity, (b) the motor spontaneously fell off the filaments, (c) the motor spent time waiting to attach, (d) the motor fell off once it reached the end of the filaments, (e) a filament depolymerized while a new filament polymerized at a new angle, discontinuously changing the value of the angle difference (ϕ). The motor worked to reduce the angle difference between filaments only to have that angle reset by a depolymerization and polymerization event. By including polymerization, perfect alignment is no longer possible. We described the degree of imperfect alignment through the time-evolution of the order parameter and the forces generated (Figures 3.2G-J). During the course of a single representative simulation run, the order parameter could rise to one and

forces generated by a shared motor dropped to zero as filaments were completely aligned. However, once a filament depolymerized, the order parameter decreased and the motor again generated force.

Even though depolymerization destabilizes the actomyosin system, we found that the angle difference between filaments in a population was still reduced over time. To understand this effect, we considered a histogram for the angle difference between filaments (ϕ). The distribution of angles for a long Monte Carlo simulation for two-filaments, one-motor showed a large number of perfectly aligned filament pairs and that depended on motor function (Figure 3.3A). As the rate of depolymerization increased, however, the angle distribution in the population became flatter with more filament pairs having larger filament angles.

When we varied the motor velocity instead of the rate of depolymerization, we also observed a non- monotonic dependence of filament alignment on motor velocity (Figure 3.3B). In this case, both low and high motor velocities acted to flatten the distribution of angle differences. In order to understand the relationship between motor velocity and the difference in filament angles, we considered the average force generated ($\langle s^2 \rangle$) for a large number of simulations as we varied motor velocity (Figure 3.3C). We found that average force reaches a maximum value at a unique motor velocity and this velocity in turn depends on the rates of motor attachment and detachment.

These effects could be understood if one took the perspective of a myosin motor. For any given set of motor filament interactions, e.g. rates of attachment and detachment, the most rapid alignment occurred when the motor spent the largest fraction of its life-cycle bound to the filament pair. For example, if the rate at which an unbound motor attached was reduced (that is, it took longer for the motor to attach), then the percent of the motor's life-cycle devoted to aligning the filament pair was also reduced (compare red and black curves in Figure 3.3C). In order to increase the time devoted to aligning the filament pair the motor needed to slow down so it would not reach the end of the filament and fall off. As a correlate, if the rate of the motor spontaneously falling off was increased, then the velocity required for optimal alignment increased (compare red and green curves in Figure 3.3C). Thus, the ability of myosin motors to align filaments depended on both its velocity as well as its rates of attachment and detachment.

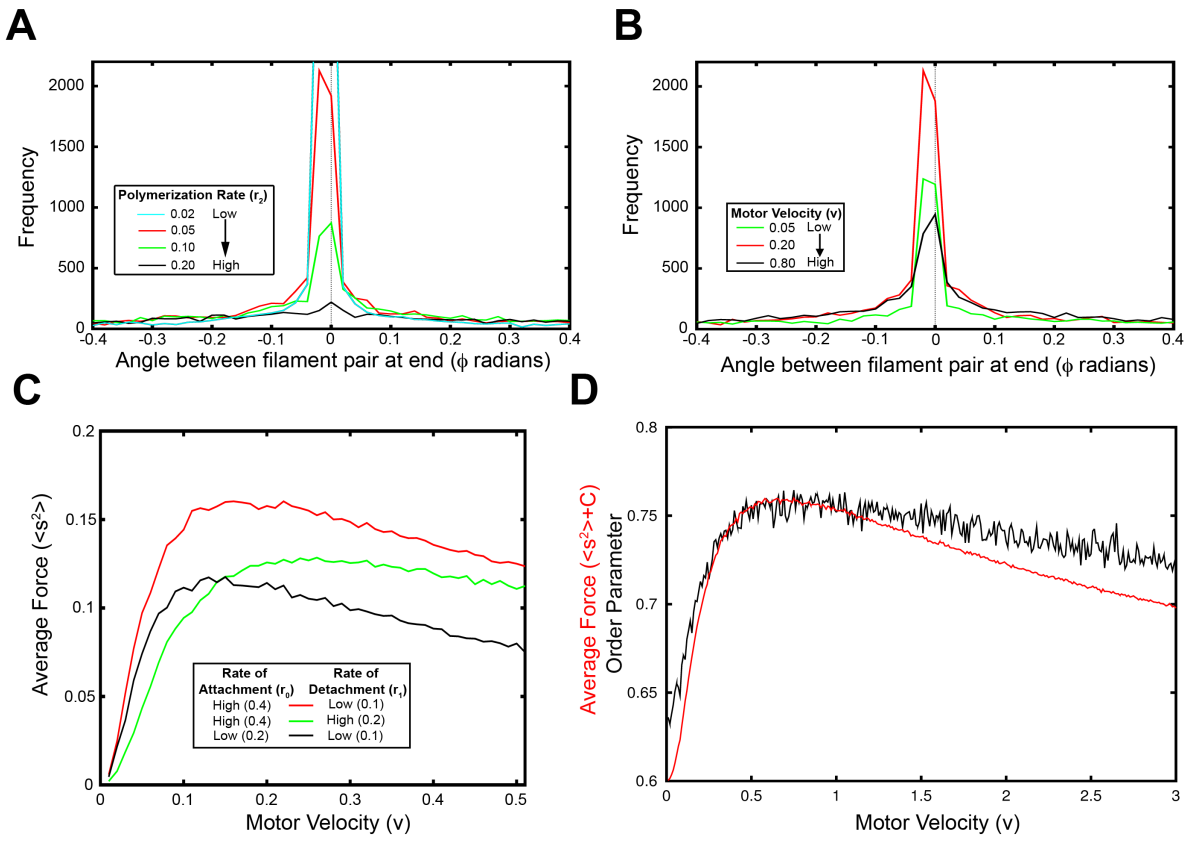

Figure 3.3: **Comparing effects of parameters on order with Monte Carlo simulations for two filaments, one motor.** (A) Distribution of the angle between the two filaments, ϕ, as the polymerization rate, r_2, increased. (B) Distribution of the angle between filaments as motor velocity increased. (C) Average force as a function of velocity for different rates of attachment, r_0, and detachment, r_1. (D) Order parameter (black) and average force (red) for the Monte Carlo simulations as motor velocity varied. $r_0 = 0.4$, $r_1 = 0.1$, $r_2 = 0.05$.

Intriguingly, motor velocities that produced maximal average force generation ($\langle s^2 \rangle$) also produced the most aligned filament pairs (Figure 3.3D). The functional dependence of morphology and force production on motor velocity suggested we might be able to analytically derive these functions from a continuum representation of the dynamics of the two filament, one motor system.

3.3.2 Recasting the stochastic model of two filaments and one motor as a continuum model

In order to understand the relationship between actin filament alignment and forces generated by the motor we derived continuum equations which described the two filament, one motor dynamical system. Motor activity within a two filament network could be thought of as an example of a 'two-state process': either the motor was detached and waiting to attach to a filament at the minus end (P_0), or the motor was moving toward the plus ends of the two filaments and pulling the pair into alignment (P_1). We considered the time evolution of populations of motors in each of these two states:

$$\frac{\partial P_0(\phi,t)}{\partial t} = \underbrace{vP_1(\phi,L,t)}_{\text{Lost from plus-end}} + \underbrace{r_1 \int_0^L P_1(\phi,s,t)\, ds}_{\text{Randomly detach}} - \underbrace{r_0 P_0(\phi,t)}_{\text{Attach}}$$

$$+ \underbrace{\frac{r_2}{2\pi} \int_{-\pi}^{\pi} \int_0^L P_1(\psi,s,t)\, ds\, d\psi}_{\text{Detach after depolymerization}} \tag{3.7}$$

The population or density of motors not bound to any filaments (P_0, Equation 3.7) changed by: 1) motors falling off the plus-end of any filament (from the group of filaments with attached motors, P_1), 2) motors randomly detached as they moved toward the filament's plus-end, 3) motors bind to filament minus-ends, and 4) motors fell off filaments that depolymerized. Since motors could detach at any distance, s, along a filament's length (defined from 0 to L), the second term in Equation 3.7 was integrated over all possible motor positions. We noticed that the first three terms in Equation 3.7, the loss and gain of motors, were

independent of the filament pair's orientation; only the last term depended explicitly on the rate of depolymerization. It was important to note that while filaments without attached motors could depolymerize, the last term of this equation only considered depolymerization of filaments with bound motors. The time evolution of motors bound to filament pairs was similar but we needed to include the density of motors at various positions along the length of the filament pairs:

$$\underbrace{\frac{\partial P_1(s,\phi,t)}{\partial t}}_{} = \underbrace{-\, v\frac{\partial P_1(s,\phi,t)}{\partial s}}_{\text{Motor movement}} \underbrace{+\, \frac{k}{\mu}s^2\frac{\partial}{\partial \phi}(\sin\phi P_1(s,\phi,t))}_{\text{Filament movement}}$$

$$\underbrace{-\, r_1 P_1(s,\phi,t)}_{\text{Randomly detach}} \underbrace{-r_2 P_1(s,\phi,t)}_{\text{Detach after depolymerization}} \tag{3.8}$$

The density of motors attached to filaments must include movement of motors: 1) as motors moved toward the plus-ends of the filament pair, 2) as motors moved with the angular movement of filaments, 3) as motors randomly detached from filaments, and 4) as motors detached when filaments depolymerized.

We investigated solutions which led to stable assemblies of filament systems, i.e. the steady state solution which yielded the stationary distribution of filaments over filament angles, ϕ, and motor positions, s. We began by defining a distribution, Q, which denoted the stationary solution and obtained expressions for force and the order parameter:

$$\langle s^2 \rangle = \int_{-\pi}^{\pi}\int_{0}^{L} Q_1(\phi, s)s^2 \; ds \; d\phi$$

Furthermore, we were able to derive an equation for the steady state marginal distribution of the distance along the filaments, $\int_{-\pi}^{\pi} Q_1(\phi, s)d\phi$ and thus compute $\langle s^2 \rangle$ (Equation 3.9; see Appendix B.2).

$$\langle s^2 \rangle = \frac{r_0}{r_1^2}\frac{2v^2 - e^{-r_1/v}(2v^2 + 2vr_1 + r_1^2)}{r_1 + r_0(1 - e^{-r_1/v})}. \tag{3.9}$$

With this exact solution we calculated analytically how force generation depended on motor velocity, rates of motor attachment and detachment, and rates of filament polymerization (Figures 3.3D and 3.4). We found that our continuum equations were able to exactly replicate

the Monte Carlo simulations for the two filament, one motor actomyosin system (Figure 4). In addition, the continuum solution was able to validate our Monte Carlo simulations of the two filament, one motor actomyosin system. For instance, we previously considered the density of steady state angles from our Monte Carlo simulations (Figures 3.3A and 3.3B) and the continuum equations showed us exactly how these densities depended on the parameters of the model.

Further analysis of these equations and their steady state solutions (see Appendix B.2) allowed us to investigate exact relationships between rates of motor-filament attachment and detachment, motor velocities, polymerization rates, filament morphology, and force generation. For instance, as the rate of attachment decreased, the motor spent more time off the filaments and so the motor velocity must have been chosen so it maximized the amount of time the motor spent attached to the filaments.

3.3.3 Multiple Motors, Multiple Filaments

In order to understand more complex actomyosin networks we investigated the behavior of multiple-motors and multiple-filaments arranged with the same geometry as the simpler two filament, one motor system discussed previously. Initially, we suspected that the competition between multiple motors attached to the same filament might impede the progress of filament alignment. To test this hypothesis we returned to Monte Carlo simulations. These simulations started with multiple filaments randomly distributed around 360° and multiple motors all in an unbound state waiting to attach to the filament minus-ends. Each simulation was run for 400,000 steps with a time step of 0.01s. In order to compare steady state rates of filament alignment in each simulation, we averaged the order parameter over the last 300,000 steps. The reason for this, was that once the simulation started, if given enough time, the filaments would get closer and closer to their natural alignment, e.g. filament dynamics approached steady state.

Interestingly, we found that filaments aligned in a manner analogous to the two filament, one-motor case (Figures 3.5 and 3.6 and Movie C.1) and exhibited the same dependence on parameters that were observed previously. For example, as we allowed the rate at which the

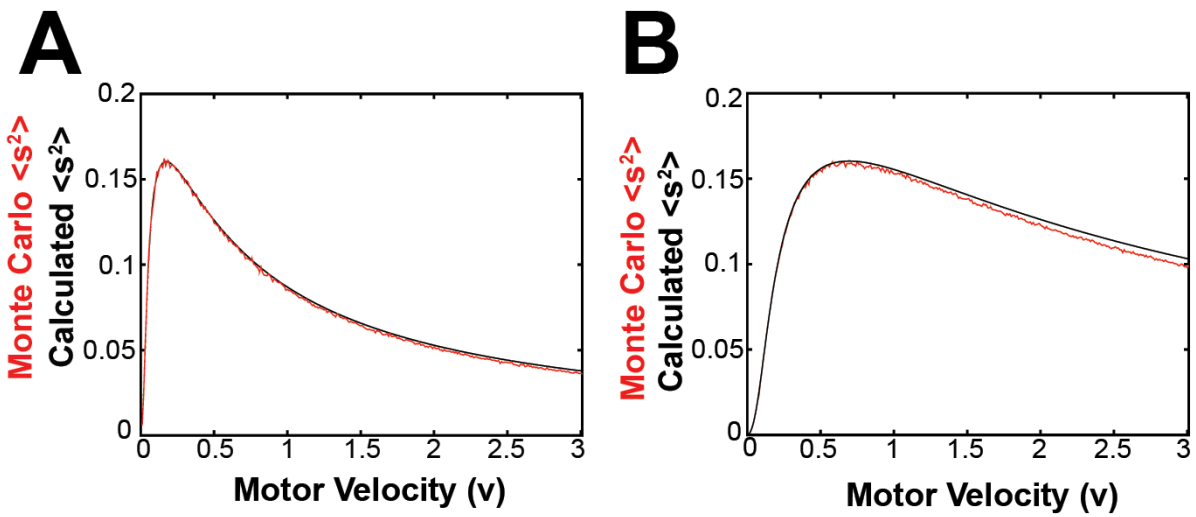

Figure 3.4: **Monte Carlo simulations and continuum solution.** (A) Plot of the continuum solutions calculation of $< s^2 >$ (black) compared to the Monte Carlo simulation calculation of $< s^2 >$ (red) for $r_0 = 0.4$, $r_1 + r_2 = 0.15$. (B) Plot of the continuum solutions calculation of $< s^2 >$ (black) compared to the Monte Carlo simulation calculation of $< s^2 >$ (red) for $r_0 = 1.4$, $r_1 + r_2 = 0.6$.

motors spontaneously fell off the filaments to increase, the velocity at maximal alignment also increased which was accompanied by a decrease in the magnitude of alignment (Figure 3.5A). Thus, the process of filament alignment is slowed as motors spend less time bound to the filaments. Furthermore, we found that the velocity which produced maximal alignment was independent of filament density(Figure 3.5B). When the ratio of filaments to motors had fewer motors, however, the maximal degree of alignment decreased, even though the optimal motor velocity remained the same.

When we considered the rate of depolymerization, we found that the order or alignment of our system was extremely sensitive to the rate of depolymerization (Figure 3.5C and Movie C.2) and that depolymerization is the only stochastic process capable of impeding the progress of filament alignment. Furthermore, the extremely steep decrease in alignment with a small increase in the rate of depolymerization suggested that a phase transition from a completely disordered (in this case a perfectly uniform distribution of filaments) to an ordered or aligned state may occur.

From our parameter analysis, we concluded that the motor velocity and depolymerization rate of filaments are key parameters that control alignment of actin filaments. In order to draw a more descriptive conclusion as to how these two parameters effect the alignment of our system, we next considered the density angles between two filaments (Figure 3.7). In the case where filaments of the system were mostly aligned, the distribution has a tall, sharp peak about the angle difference of zero and flattens after the motor velocity is shifted from this optimal value (Figure 3.7A), or after the rate of depolymerization is increased (Figure 3.7B). To investigate the behavior of our actin network near this phase transition we turned from the Monte Carlo simulations to a continuum representation for our multiple filament, multiple motor system.

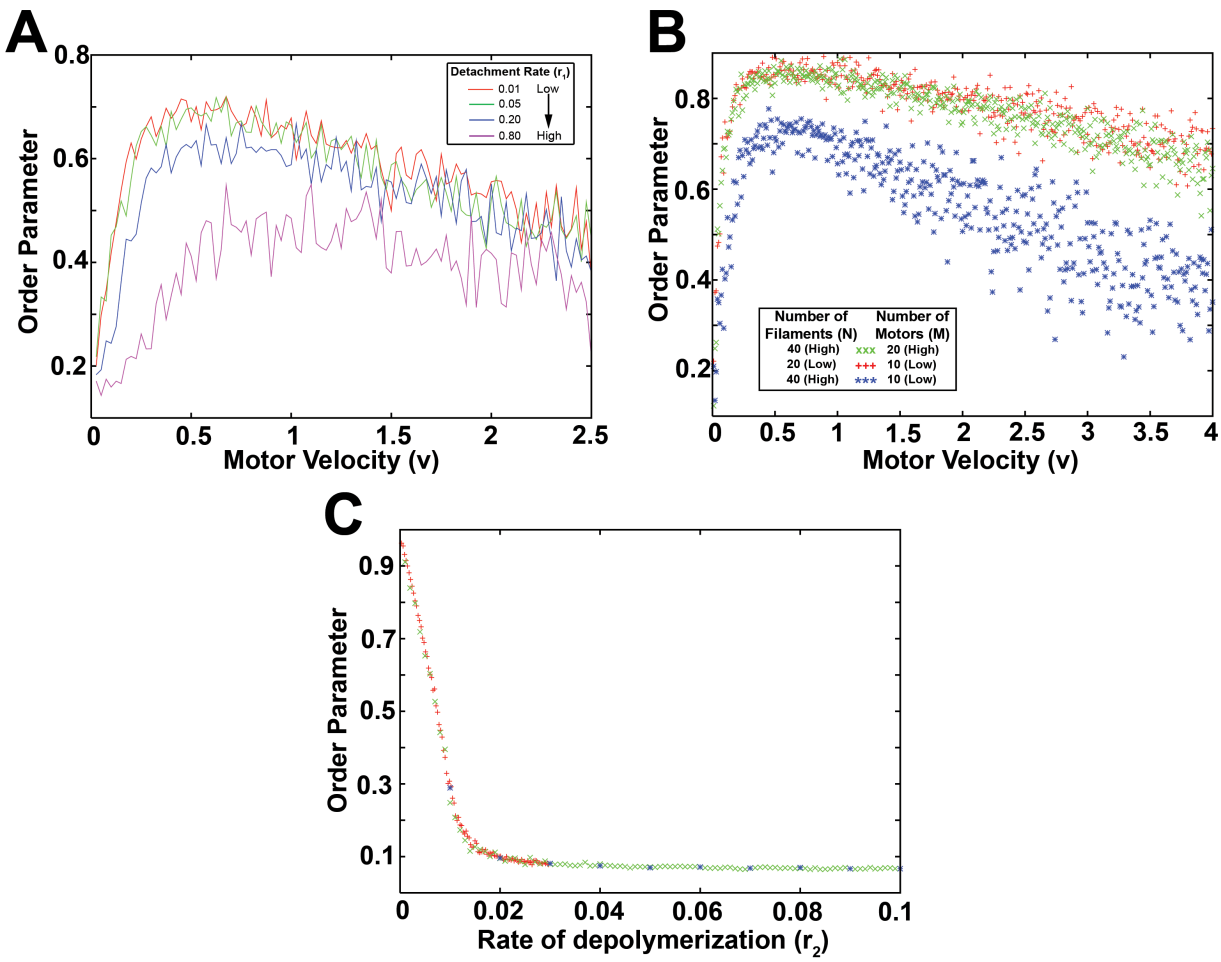

Figure 3.5: **Same behavior for multiple filament, multiple motor case, as previously for two filaments, one motor.** (A) Plot showing the dependence of the order parameter on the rate of detachment (r_0) for 40 filaments and 20 motors. As expected, an increase in detachment resulted in a decrease in order. $r_0 = 0.7$, $r_2 = 0.05$. (B) Plot examining the relationship between the relative densities of motors to filaments. When the ratio of filaments to motors was the same, the same amount of order is expected; however, the optimal motor velocity required to achieve maximum alignment was independent of filament and motor density. $r_0 = 0.7$, $r_1 = 0.1$, $r_2 = 0.05$. (C) Plot showing the sensitivity of the order parameter of the system to the rate of depolymerization (r_2). Blue shows a larger discretization than green, with red being the most fine discretization of sampling order.

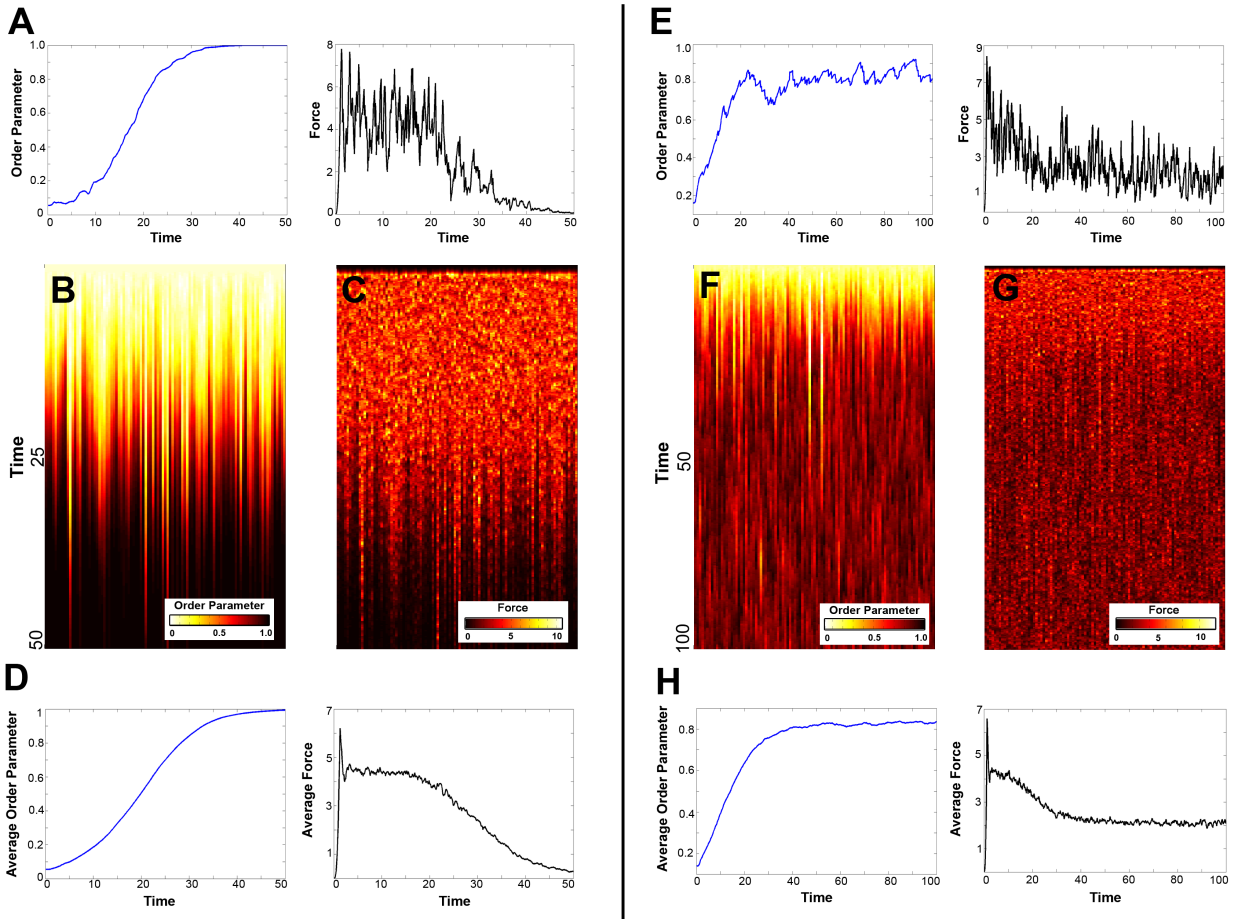

Figure 3.6: **Monte Carlo Simulations: multiple filaments, multiple motors.** (A) Order parameter (blue) and force generated (black) for one Monte Carlo simulation with multiple filaments and multiple motors without polymerization. Note the same characteristics as seen in Figure 3.2B. (B) Color evolution plot of order parameter for 100 Monte Carlo simulations without polymerization. (C) Color evolution plot for force generated by the 100 Monte Carlo simulations shown in B. (D) The average order parameter (blue) and average force generated (black) by the 100 Monte Carlo simulations in B and C. (E) Order parameter (blue) and force generated (black) for one Monte Carlo simulation with polymerization. (F) Color evolution plot of order parameter for 100 Monte Carlo simulations with polymerization. (G) Color evolution plot for force generated by the 100 Monte Carlo simulations shown in F. (H) The average order parameter (blue) and average force generated (black) by the 100 Monte Carlo simulations in F and G.

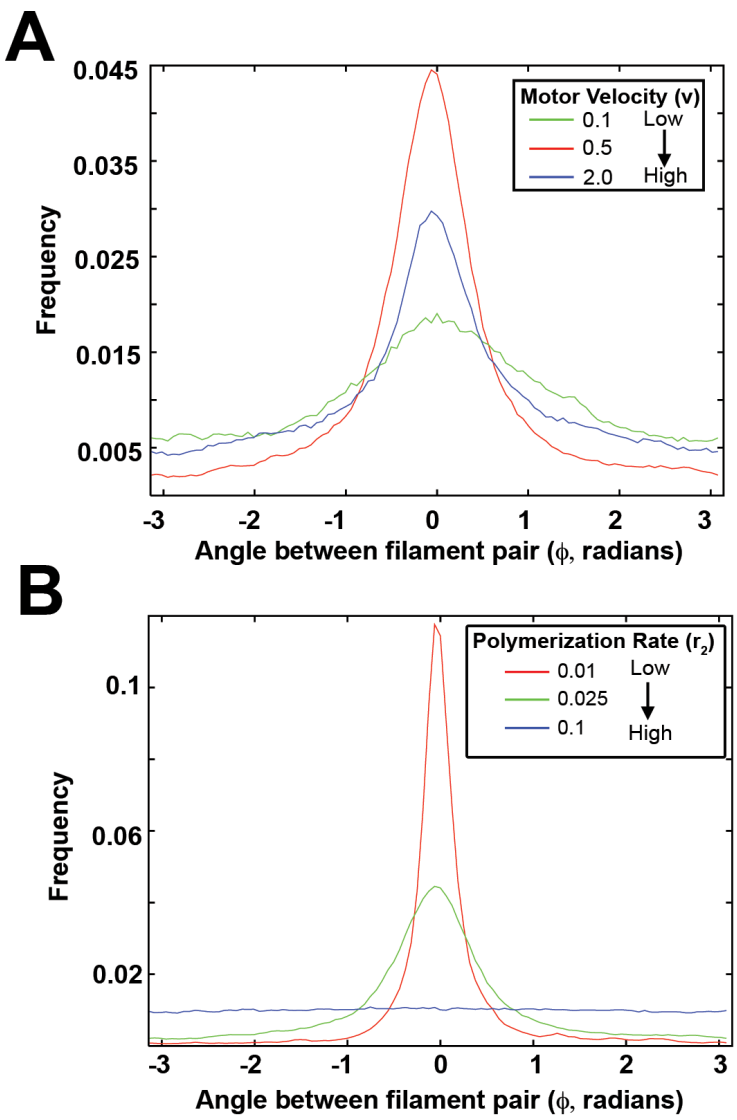

Figure 3.7: **Effects of motor velocity and rate of polymerization (r_2) on multiple filament and multiple motor alignment.** (A) The distribution of the difference in angle between all filaments compared to filament #1. As motor velocity decreased from high (blue) to low (green), there was an intermediary velocity which caused the sharpest peak in the distribution, and thus the most alignment (red). (B) The distribution of the difference in angle between all filaments compared to filament #1. As polymerization rate increased from low (red) to high (blue), note the quick flattening of the distribution peak which suggested a phase transition dependent on the rate of polymerization.

3.3.4 Mean field analysis of multiple filaments and multiple motors

We considered an array of a large number of filaments, N, where each filament was at a discrete angle (θ_i) with a large number of motors, M. From this discrete model we calculated forces experienced by a single filament:

$$f(\theta_i) = \frac{k}{\mu} \sum_{j=1}^{N} \sum_{r=1}^{M} p_{ijr} s_r^2 \sin(\theta_j - \theta_i) \tag{3.10}$$

The average force on a filament was found by linearly summing all the forces exerted by the motors which were attached to that filament. An attached motor, r, connects filament i and j. The term p_{ijr} was the probability that motor r was attached to filaments i and j. Since motors may contact any 2 out of N filaments, and connections are chosen randomly this probability factor was $1/(N(N-1))$.

In order to compute a mean field equation for the network of motors and filaments, we let the number of motors and filaments grow to infinity, keeping the ratio of motors to filaments as a fixed number, c. When we did this, the sum in Equation 3.10 became an integral (Equation 3.11).

$$f(\theta_i, t) = \frac{kc}{\mu} \int_{-\pi}^{\pi} \int_{0}^{L} s'^2 \sin(\theta' - \theta_i) P_1(\theta', s', t) \; ds' \; d\theta'. \tag{3.11}$$

Next, we returned to the two-state model for myosin motors within a much larger F-actin array. Recall the definitions of P_1 and P_0 from the two filament, one motor case before where P_1 was the density of motors attached to filaments, and P_0 was the density of unbound motors. The time-evolution of motor density within these two states was:

$$\frac{\partial P_1(s,\phi,t)}{\partial t} = \underbrace{-v \frac{\partial P_1(s,\phi,t)}{\partial s}}_{\text{Motor movement}} \underbrace{-\frac{\partial}{\partial \theta}\left(P_1(s,\phi,t) f(\theta)\right)}_{\text{Filament movement}}$$

$$\underbrace{-(r_1 + r_2) P_1(s,\phi,t)}_{\text{Detachment}} \tag{3.12}$$

$$\frac{\partial P_0(s,t)}{\partial t} = vP_1(L,\theta,t) \qquad -r_0P_0 \qquad + \int_0^L r_1P_1(s',\theta,t)ds'$$

Lost from plus-end | Attach | Randomly detach

$$+\frac{1}{2\pi}\int_0^L \int_{-\pi}^{\pi} r_2P_1(s',\theta',t)\ d\theta' ds' \tag{3.13}$$

Detach after depolymerization

In contrast to the density functions for the simple case of two filaments and one motor, we considered the actual angle rather than the difference of angles. Since forces depend on the density of motor-bound filaments we found a nonlinear term that represented the movement of motors as filaments moved. Thus, unlike the two filament case, the density equations were nonlinear due to the fact that $f(\theta)$ was itself a function of P_1.

Since motors can only attach to filaments at the minus ends, we enforced a boundary condition that related motors leaving the pool of unbound motors with the motors attached at the minus-end of the filament pairs.

$$P_1(\theta,0,t) \quad = \quad \frac{r_0}{v}P_0(\theta,t). \tag{3.14}$$

Readers familiar with the analysis of coupled oscillators will see a strong similarity between Equation (3.12) and the Kuramoto equation [Kuramoto, 1984] (see Appendix B.5). Because this was a nonlinear equation, there was no simple closed form solution; however, we used these equations to investigate the transition driven by high rates of depolymerization from a completely disordered state to an aligned state (referred to as the "asynchronous state" in coupled oscillators).

When we considered the density distribution of relative filament angles and increasing rates of depolymerization, we concluded that there existed a solution which was uniform in the filament angle, θ (Figure 3.7B; see Appendix B.3). These solutions were the marginal

densities of the distance traveled for attached motors, $W_1(s) = \int_{-\pi}^{\pi} Q_1(\phi, s)\ d\phi$, and the density of unattached motors, $W_0 = \int_{-\pi}^{\pi} Q_0(\phi)\ d\phi$ (see Appendix B.3).

$$\begin{aligned} P_1(\theta, s, t) &= \frac{1}{2\pi} W_1(s) \\ P_0(\theta, t) &= \frac{1}{2\pi} W_0 \end{aligned}$$

Returning with these solutions to our continuum equation for the force on a single filament we found:

$$f(\theta) = \frac{kc}{\mu} \frac{1}{2\pi} \int_0^L s^2 W_1(s) \int_{-\pi}^{\pi} \sin(\theta' - \theta)\ d\theta'\ ds = 0$$

The term $f(\theta)$ represented the angular flux of filaments moving under the influence of bound motors. As the array of filaments approached steady state this term disappeared and we were left with a steady state analogous to that found in our earlier analysis of two filaments and one motor.

This equilibrium solution corresponded to a completely disordered state in which the distribution of the filament angles was uniform. Since the equations for the two filament, one motor case were linear they do not include the integration of angular filament flux, and the completely disordered state was never a solution. The equation which described arrays of multiple filaments and multiple motors was nonlinear, so there may be more than one possible steady state. The most direct method to determine if there were other possible stationary distributions of motors was to examine the stability of the disordered state as parameters, such as the motor velocity, were varied.

We searched for a possible nonlinear phase transition by investigating the stability of different periodic modes of the disordered state (see Appendix B.4). If the fully disordered state was unstable with respect to perturbations to the distribution of filaments, then this mode would grow and the distribution might remodel into a single peak. With this approach we linearized the full equations about the trivial steady state and then solved the resulting linear system.

We discovered that F-actin morphology alone was not a predictive indicator of force production. Whereas a unique filament array morphology that did produce a unique level of maximal force (see asterisk in Figure 3.8B). Force production at even slightly lower levels

produced by two distinct filament morphologies (see "arrow heads" in Figure 3.8B). One, a tightly aligned and another, a disorganized filament arrays produced identical levels of force. Thus, morphology alone was not a sufficient index for the assessment of force production within arrays of actin filaments which were free to rotate.

3.3.5 Biological Complexities: How does the behavior of this simplified system change as more realistic conditions are introduced?

Thus far, our simulations and analysis did not limit the length that myosin motors could stretch between pairs of actin filaments. To test the importance of this assumption, we ran simulations where motors detached once they exceeded a threshold length (Figure 3.9A). This change lowered the motor velocity needed for optimal alignment of the filaments (Figure 3.9A'). Simulations where we introduced a threshold of myosin detachment behaved as if we had simply increased the rate of detachment of the motor (e.g. increased r_1). Alternatively, when we increased the threshold we found that the filaments aligned more strongly and the motor velocities needed for optimal alignment also increased.

Up to this point our simulations used filaments of uniform length (Figure 3.9B); to test the importance of this assumption we ran simulations with filaments having different fixed lengths. With increased filament length, we found that filaments aligned to a greater degree and that the motor velocity needed to optimally align filaments also increased (Figure 3.9B'). If we allowed filaments to have random lengths between 0.75 and 1.25, so their average length would be 1.0. We found almost no change in the velocity needed to optimally align filaments, however, the magnitude of alignment decreased slightly (Figure 3.9B').

3.4 CONCLUDING REMARKS

Actomyosin networks shape a diverse array of cellular structures. Many of these, such as the alignment of actin filaments into the cytokinetic furrow or into the base of dynamic filopodia, are likely to involve filament rotation. To understand the principles that shape

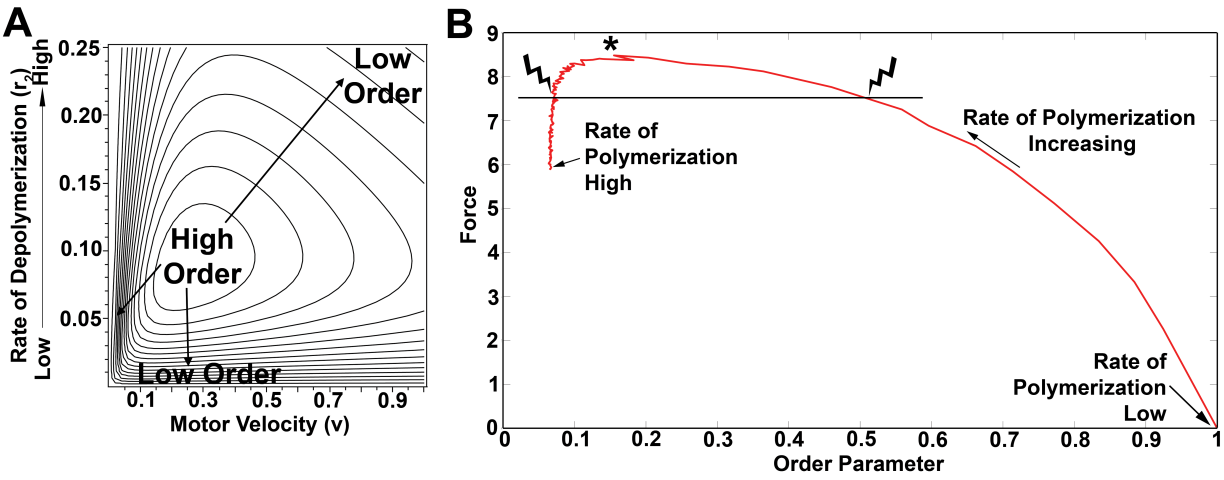

Figure 3.8: **Examining the relationship between polymerization, motor velocity, order, and force with the continuum model.** (A) Contour plot for the continuum equations solutions show the domains of high and low order as a result of the polymerization rate (r_2) and the motor velocity (v). (B) Solutions predicted from the continuum model for force and order as the rate of polymerization increases. We observed that there exists a region where two differently ordered morphologies generate the same force.

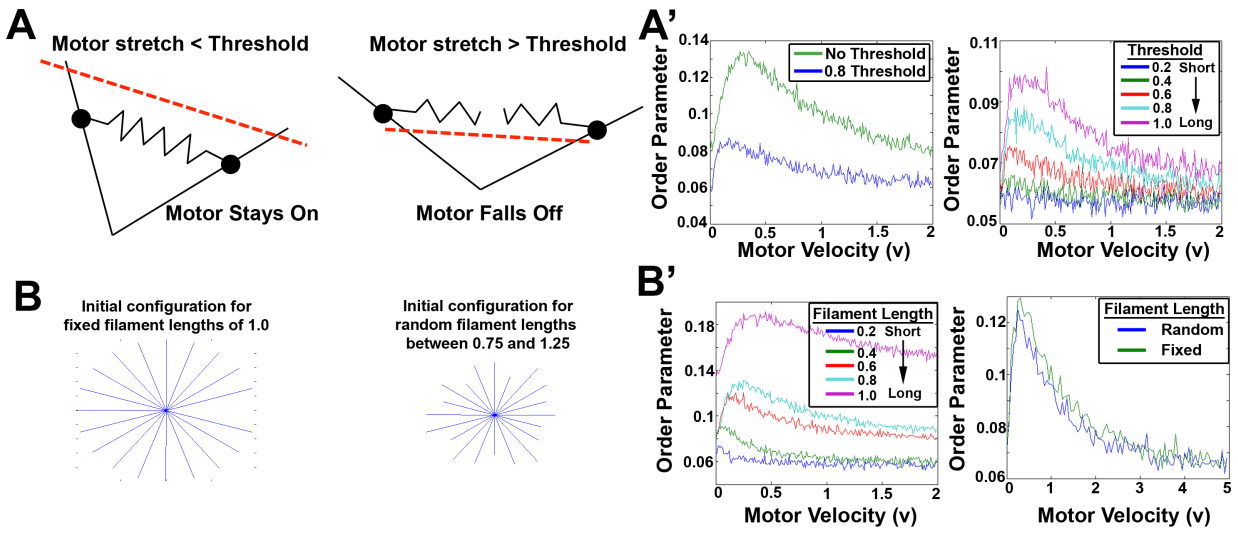

Figure 3.9: **Introducing complexities to the model yields the same results.** (A, A') The model allowed motors to stretch as far as necessary in order to stay attached to the filament pair; however, *in vivo*, it is more likely that the motor is limited in its stretch. We restricted the distance the motors can stretch which reduced the order of the system. (B, B') We assumed filaments had fixed lengths of one for our Monte Carlo simulations. We introduced complexity by varying the fixed length, which resulted in a decrease in order for a shortened filament length. To increase complexity even further, we considered filaments with random lengths that had an average length of one and found both the fixed length of one and random lengths with average length one, had the same order.

these networks we have constructed a set of theoretical models to study the evolution of F-actin morphology and dissected the relative contributions of F-actin polymerization and myosin-motor based alignment to changes in filament morphology and force production. Monte Carlo simulations and continuum models identified regimes where actin filaments are stably bundled and other regimes where actin filament depolymerization leads to an asynchronous state where actomyosin forms a perpetually contractile array. The models suggest biophysical mechanisms through which myosin activity and F-actin polymerization reshape the cytoskeleton and drive cell shape change.

We first derived the equations of motion for a simple system of two filaments and one myosin II motor complex and defined a statistical property of circularly distributed actin filaments, the order parameter, to assess the morphology of arbitrarily large filament-motor arrays. Implementing simple stochastic processes that allow motors to bind or detach from filament-pairs, walk toward filament plus-ends, and pull filaments together, we performed Monte Carlo simulations in order to understand how these processes shape the morphology of filament pairs.

We found that maximal alignment of the filament pair occurred at a unique motor velocity and depended on both the rates of the stochastic processes and the length of the filaments. Motors aligned filaments more rapidly when they spent the largest fraction of their duty-cycle actively contracting the two filaments. At one extreme, if a motor traveled too slowly it would fall off the filament pair before reaching the end; and, at the other extreme, a motor that traveled too rapidly spent too much time waiting to bind to the pair of filaments.

These relationships suggested the existence of an underlying biophysical principle so we simplified the motor-filament interaction slightly and re-cast the problem using continuum equations for a "two-state process and investigated the evolution of the filament-motor system as density functions. These equations were solved explicitly, reproduced the findings from our Monte Carlo simulations and provided a direct link between parameters governing motor-filament interactions, the resultant filament morphology, and contractile strength. Remarkably, this analysis demonstrated that no matter how many motors or filaments there are, the density of motor positions is always the same.

In order to generalize these two-filament one-motor systems to systems with multiple filaments and motors we returned to Monte Carlo simulations. These systems reproduced the same general behaviors seen in the simpler system, namely, that filaments rapidly align over a wide range of model parameters and that the alignment peaks for conditions where motors spend the largest fraction of their duty cycle contracting filament-pairs.

Rapid alignment of filaments underlie a range of cellular processes such as the formation of the cytokinetic furrow in dividing cells and the convergence zone at the rear of lamellipodia in migratory cells. During the initial steps of cytokinesis, myosin II motors bind disordered actin filaments within the cortex and reorient those filaments aligning them within the cytokinetic furrow [Bonder et al., 1988, Vavylonis et al., 2008]. Retrograde flowing actin filaments within lamellipodia first encounter myosin II at the rear of the lamellipodia. In this region, named the convergence-zone, filaments are anisotropically contracted, reoriented perpendicular to the direction of the flow, and are rapidly depolymerized [Ponti et al., 2004b, Vallotton et al., 2004].

However, other cellular processes driven by actomyosin dynamics progress without alignment, for instance actomyosin assemblies at the rear of migrating cells, and a range of processes that direct cell shape change during morphogenesis in embryos [Blanchard et al., 2010, Kim and Davidson, 2011, Martin et al., 2009, Rauzi et al., 2010, Solon et al., 2009]. To investigate processes that might destabilize filament alignment we modified our models to include filament polymerization/depolymerization. Both our two-filament, one-motor and multiple filament, multiple motor models revealed that the rate of depolymerization can alter the speed of alignment but could also produce morphologically stable arrays of permanently contractile filaments.

These models revealed that motor activity and polymerization underlie the ability of F-actin networks to undergo a phase-transition from organized aligned filaments into dynamically disorganized, permanently contractile arrays. This transition could be controlled by both the motor velocity and the frequency or rate of depolymerization. We propose that cells manipulate the state of actomyosin by controlling this phase transition. Actomyosin interactions can result in distinct patterns of force generation in addition to altering the morphology of filament arrays. In the absence of F-actin polymerization, myosin II quickly

align filaments into tight bundles. However, such bundled filaments no longer generate contractile forces. In contrast, once polymerization is introduced, arrays of filaments can achieve some alignment, but instead of forming stable bundles, they form a dynamically disorganized contractile array. Polymerization, or rather depolymerization, allows the actin network to continuously generate contractile force. Thus, actin filament alignment combined with polymerization and depolymerization allows the cytoskeleton to remain continuously contractile even as its morphology is continuously changing.

To build our intuition about the performance of actomyosin we intentionally omitted numerous details of both actin filament and myosin II function. As we explored the behavior of the simple system we extended our models to include many of these omitted details and test their relevance as a more "realistic" biology. For instance, after allowing varying or random length filaments we found we could interpret the results in the context of our simpler model. Our greatest simplification for the model was fixing the minus-ends of filaments together in the center of an array. This simplification allowed us to investigate the complex interactions between polymerization and myosin motor function without the confounding effects of filament translocation or lateral movement. Clearly, more realistic models will require complex geometries of free-associating actin filaments. However these future efforts will to be able to build on both the Monte Carlo models and continuum-level theory that we developed here.

4.0 SIMULATING AND ANALYZING LINEAR MORPHOLOGIES OF ACTOMYOSIN

In Chapter 3, we modeled a simple actomyosin network where filaments rotated as non-muscle myosin II (NMM II) motors remodeled the F-actin array [Miller et al., 2012]. To extend this model to more physiologically relevant conditions, we considered arrays of aligned actin filaments. We also want to continue to address Aim 1 (1.1.1), identifying how rates of F-actin polymerization and myosin generated forces affect actomyosin dynamic morphology. The most common example of aligned actin are in muscle cells where actin and myosin are arranged into parallel, contractile bundles (fig 4.1A; [Littlefield et al., 2001]). The dynamics and mechanics of these contractions are very well understood, but there are additional systems driven by parallel actin arrays. During cell division, the cytokinetic furrow is an organized ring of parallel bundles of actin that contracts based on myosin contractility, eventually pinching the dividing cells into the two daughter cells (fig 4.1B; [Kamasaki et al., 2007]). There have been many models of parallel actin rings to study this phenomenon [Zumdieck et al., 2007, Zemel and Mogilner, 2009].

Another example of parallel bundles of actin filaments is found in stress fibers in cultured cells. The degree of the alignment depends on the stiffness of the substrate (fig 4.1C; [Zemel et al., 2010]), which suggests that aligned actin arrays serve a mechanical role in either sensing external environments, or maintaining cell integrity in different environments. Thus, the current hypothesis is that actin fibers align in response to externally applied stresses.

In development, the classical example of aligned actin is the ring of bundled actin found at the cell-cell junctions below the apical surface of epithelial sheets (fig 4.1D; [Martin et al., 2009]). In order for the tissue to experience the bending of invagination (definition A.1), actin forms into parallel arrays along the cell's boundary and then contracts making the

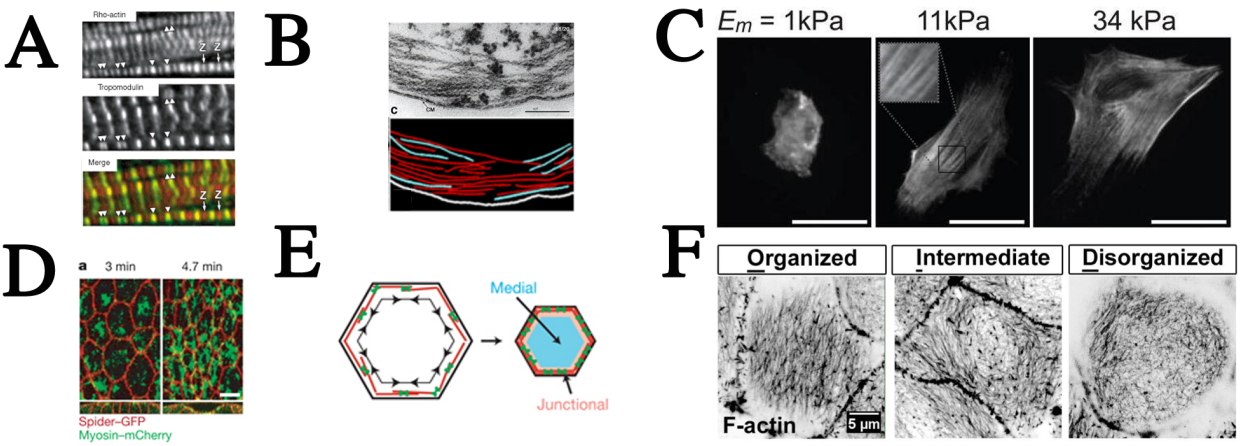

Figure 4.1: **Examples of aligned actin**. (A) Cardiac myocytes stained for F-actin demonstrated highly organized parallel arrays of actin. Arrows indicate pointed ends of filaments, and 'Z' indicates the Z-lines. (Fig 1a from [Littlefield et al., 2001]). (B) cdc25 cells were sectioned longitudinally and examined with transmission electron microscopy to show the parallel arrays of actin beneath the plasma membrane in early anaphase comprising the actin ring for cell division (Fig 2c from [Kamasaki et al., 2007]). The pointed ends of clockwise oriented filaments are in red and counterclockwise filaments are in blue (Fig 2d from [Kamasaki et al., 2007]). (C) hMSCs were cultured on substrates of varying stiffness and the aligned actin arrays were observed (Fig 1a,b,c from [Zemel et al., 2010]). (D) The apical surface of *Drosophila* epithelial experiences convergent extension during development and the cells changed shape accordingly. Spider-GFP (red) marks cell boundaries, and Myosin-mCherry (green) labels actin (Fig 2a from [Martin et al., 2009]). (E) Cartoon model of apical actin rings showing the localization of f-actin (red) and myosin (green) to the cell boundary and how this ring contracts to change cell shape over the course of development (Fig 2f from [Martin et al., 2009]). (F) Utrophin labeled F-actin in *Xenopus laevis* epithelial cells on the apical surface. Cells with organized F-actin arrays were found closest to the blastopore lip, with disorganization increasing the further away cells were from the involuting lip edge (Fig 4a from [Feroze et al., tted]).

boundary shorter (fig 4.1E; [Martin et al., 2009]). Contraction along cell edges and the resulting reduction in cell boundary length often creates "rosette" structures where various numbers of cells share the same apex point [Pohl et al., 2012]. In several, but not all cases, the number of cells in the rosette has been correlated with convergent extension tissue and cell shape changes [Pohl et al., 2012].

Another case of aligned actin in the animal cap has recently been observed during blastopore closure in *Xenopus laevis*. The apical cortex of epithelial cells moving over the lip and joining endodermal epithelial cells lining the archenteron exhibit organized, aligned actin networks (fig 4.1F; [Feroze et al., tted]). This observation suggests that cells exhibiting aligned actin arrays are affected by different mechanical forces than cells further away from the blastopore lip which exhibit more disorganized actin arrays.

In initially constructing a simple model of aligned F-actin, we simulated sliding of F-actin by myosin motors, similar to our purely rotational model published earlier [Miller et al., 2012]. However, earlier models of aligned cytoskeleton considered sliding filament bundles [Zemel and Mogilner, 2009], spindle arrays for microtubules (analogous to actin filaments) [Craig et al., 2011, Mogilner and Rubinstein, 2010], and the filaments within the cytokinetic furrow during cell division [Zumdieck et al., 2007].

Recent work by Thievessen et al [Thievessen et al., 2013] demonstrated that focal adhesion complexes in the lamellipodial and lamellum regions of migrating cells were responsible for transmitting forces from the internal actomyosin cytosekelton to the substrate through a protein of that complex, vinculin. Vinculin transmits forces through its head and tail domains [Grashoff et al., 2010] and also bind with F-actin in the cell cortex [Humphries et al., 2007]. Thus, force transmission occurring at the cell membrane or boundary. Therefore, for our next model, we consider an array of linearly sliding filaments where a limited number of filaments are connected to a defined boundary via a spring (see fig 4.2). Another advantage of our approach is that we can calculate the tension and force directed onto the boundary through a spring connecting the filament array to the boundary.

Since we restrict filament arrays to linear translational movements our f-actin sliding model appears similar to models of muscle actin and myosin in the sarcomere. The dynamics of our model, however, distinguish our sliding model from sarcomere models as we include

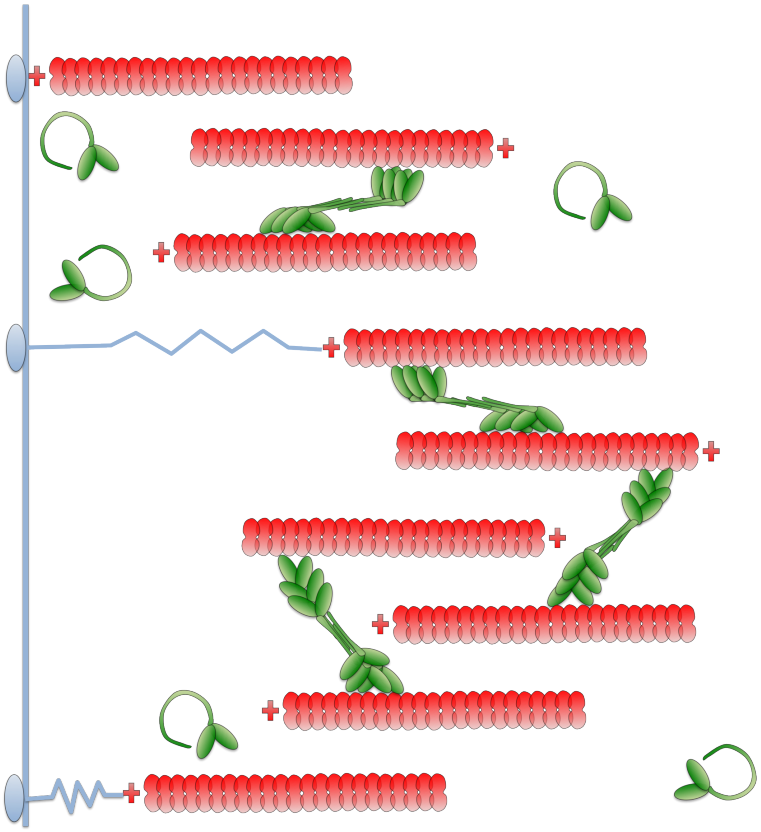

Figure 4.2: **Sliding model:** The boundary of the simulation is shown by the blue line on the left of the figure. Actin filaments are red, and have plus symbols to show their polarity orientation. Some of the filaments are connected by a spring (in blue) to the boundary. The rest of the filaments are considered "free" because they are not connected to the boundary, but can interact with filaments connected to the boundary by the boundary spring. Myosin motors are unattached (2-headed green curls), or bundled into a mini-thick filament, attached to two filaments and walking to the plus ends (green filaments). We make the additional assumption that filaments are on the same "linear track," but are shown in pictures to be separated along the vertical axis.

"free" sliding filaments which are not bound to the boundary. These free filaments are crucial because they allow force transmission through the array to couple spring-bound boundary filaments. By using physiologically relevant geometries and parameters, we are able to estimate forces produced at the boundary, spring bound filaments, and understand how the physics of overlapping filaments, number of laddering free filaments, and contractile motors affect the emergent morphology of the F-actin array.

4.1 MODEL/SIMULATION DESCRIPTION

Constructing a numerical simulation requires the choice of a range of parameters for explicit variables as well as a set of implicit assumptions that guide implementation. In this section we list explicit parameters (Table 4.1) and discuss their implementation in the simulations.

Viscosity- The cytoplasm is a dense aqueous environment comprised of colloidal suspensions of vesicles and organelles, large multi protein complexes, and the cytoskeleton [Luby-Phelps, 2000]. Rather than incorporate the full complexity of the cytoplasm, we use a single value of viscosity (coefficient of viscosity, 1×10^{-3} Pa s).

Filament length- The length of actin filaments is anywhere between 6 nm and 10 μm *in vitro* [Murrell and Gardel, 2012], however it was observed that *in vitro*, with the addition of myosin, the persistence length is approximately 1 μm [Murrell and Gardel, 2012].

Time- In general we ran our simulations for a "long" time, with 20,000 steps equating to 1,000s.

Domain size-We simulated a domain of approximately 2 μm, and for comparison, the 2D actin filament array from Dasanayake, et. al assumed a domain of 5 μm $\times$ 5 μm [Dasanayake et al., 2011].

Motor velocity- Our motors move at a speed of 1 μm/s, which is within the physiological range of 1-3 μm/s [Kron and Spudich, 1986, Murphy et al., 2001].

Motor attach/detach- Myosin motor attachment and detachment rates are not known, however, the affinity of the mini-thick-filament to bind to the actin is much greater than dissociation [Lecuit et al., 2011]. Therefore, we assume that the attachment rate is 5/s while

Table 4.1: Aligned filament model parameter descriptions

Parameter symbol	**Parameter name**	**Coding value**	**Reference**
μ	Viscosity	1×10^{-3} Pa s	[Lang et al., 1986]
l	Length of filament	0.8 μm	[Murrell and Gardel, 2012]
Duration	Time for simulation to stop running	1,000 s, or approx 17 mins	
Domain	Outside boundaries for spring bound filaments	2 μm	[Dasanayake et al., 2011]
dt	Time step size	1/20 s	
v	Motor velocity	1 μm/s	[Kron and Spudich, 1986] [Murphy et al., 2001]
r_1	Rate of motor attachment	5 /s	
r_0	Rate of motor detachment	0.4/s	
r_3	Rate of filament polymerization	0.00006/s - 0.6/s	[Pollard, 1981]
k_1	Stiffness of wall spring	0.1 nN/μm	[Lehenkari and Horton, 1990]
k_2	Stiffness of motor spring	0.6 nN/μm	[Kaya and Higuchi, 2010]

the detachment rate is much smaller, 0.4/s. We assume the detachment rate is dependent on the amount of stretch the myosin experiences (i.e. the probability of detaching is higher the further stretched the myosin becomes).

Filament polymerization- We consider a smaller rate of filament polymerization than what has been observed with *in vitro* actin arrays. The *in vitro* rates of growth/polymerization are in the range of 0.7/s-1.2/s [Pollard, 1981, Amann and Pollard, 2001], and the decay rates range from 9.3×10^{-8}s to 1.77×10^{-7}s [Kouyama and Mihashi, 1980]. Since our filament polymerization rate representing both polymerization and depolymerization, our values of 6×10^{-4}/s to 0.6/s are within this diverse range. Its also worth noting that *in vivo* there are multiple other proteins which interact with actin to advance, inhibit, or decrease filament growth. As an example, ARP 2/3 was shown *in vitro* to slow the overall polymerization of a single actin filament [Amann and Pollard, 2001], because ARP 2/3 allowed for branching of the filament to occur so the G-actin monomeric subunits were quickly recruited to increase filament length in other directions versus having the entire population entirely devoted to increasing a single F-actin filament.

Motor stiffness- Mini thick filaments of non-muscle myosin II (NMM II) *in vitro* have a stiffness between 1.7 to 5.0 nN/μm [Kaya and Higuchi, 2010]. However, the range for individual units of skeletal muscle myosin range from stiffnesses of 0.17-1.79 nN/μm (Table S1 from [Kaya and Higuchi, 2010]), so we are within the order of magnitude range of myosin stiffness.

Boundary springs- The stiffness of the boundary spring to bind the F-actin to the presumed focal adhesion complex, transmembrane bound, is not known. The binding stiffness of integrins of two cells has been approximated to be 26.28 nN/μm [Lehenkari and Horton, 1990], but we would anticipate that the binding stiffness between an integrin and a single F-actin filament to be much smaller. Therefore we assume that the boundary spring represents the connection between an integrin protein complex and a single F-actin filament, so the boundary spring stiffness is smaller than the motor spring stiffness.

F-actin filament implementation- We implement this simulation using the approach we used with our previous model for filament rotation [Miller et al., 2012]. Filaments move in the x direction only. We plot the filaments at different y values so their positions can

be observed, but do not make any assumptions about filaments colliding with each other. We simulate 2 types of filaments, boundary and "free." We can specify the number of filaments attached to the left or right boundaries. In general, we assume that there are two boundary filaments, one each attached to the right and left boundaries. All other filaments are free, meaning they are not bound to the boundary. The free filaments slide left or right based on the forces exerted by the myosin motors. The free filaments can also experience polymerization, which is triggered by a Monte Carlo event (based on the polymerization rate, Table 4.1), or when a filament slides past the boundary. Instead of considering the biological definition of polymerization (the addition and subtraction of G-actin monomers to the F-actin), we consider polymerization as a source of noise, so if polymerization occurs, a "free" filament will disappear and a new one will reappear in a new X location at a random orientation (right or left).

Myosin motor dynamics- The motor dynamics include being in three states at any point in time. The motor can be unattached, at which point it would randomly diffuse right or left. One leg of the motor can attach to a filament if the rate of attachment event occurs, and if a filament is overlapping the X location of the motor. If multiple filaments are overlapping the location, then one filament of the multiple possibilities is randomly selected. Once one "leg" of the motor is attached, then, if the rate of attachment event occurs again, the second leg attaches to a second filament. If one "leg" is only attached to one filament, the motor can walk toward the plus end of the filament, but it will not exert any forces to slide the filament because it is not attached to two filaments.

All variables are in Table 4.2, and we assume that $l < L < 2l$ in order to insure that there is filament overlap of our spring bound filaments ($x_R - x_L \leq l$). We consider motors to be in five fundamental categories of left oriented spring-bound filaments (L), right oriented spring-bound filaments (R), plus oriented filaments without a spring attached (P), negative oriented filaments without a spring attached (N), and unattached motors (0). In the progression of attaching to two filaments, an unattached motor must first pass through one of the four attached states (L,R,P,N), then bind to a second filament (fig 4.3). Motors diffuse along the x-axis while they are unattached, and then will bind to any random filament that crosses its

Table 4.2: Functions for movement and dynamics of aligned filament arrays

Equation symbol	**Equation Definition**
x	real spatial distance
x_L	left boundary
x_R	right boundary
l	length of filament
L	length of domain, such that $0 \leq x_L \leq x \leq x_R \leq L$
r_0	rate of attachment
r_1	rate of detachment
$\rho(x,t)$	unattached motors at position x at time t
$q_L(s_L,t)$	motors with one "leg" attached to the left filament at distance s_L from boundary x_L such that $0 \leq s_L \leq l$
$q_R(s_R,t)$	motors with one "leg" attached to the right filament at distance s_R from boundary x_R such that $0 \leq s_R \leq l$
$q(s_L,s_R,t)$	attached motors with "legs" at s_L on left filament and s_R on right filament

current x-position with a rate of attachment, r_1. All steady state equations of motion are in appendix D.1.

4.2 RESULTS

For our model of aligned actin arrays we assumed the following restrictions: that the filaments are already established in an aligned network, and filaments maintain this parallel alignment throughout the simulation. In addition, we wanted to establish a method for determining how much force the network of filaments was generating so we introduced boundary filaments which are connected to the boundary by a spring (see methods for a description). The general question was what conditions are necessary to pull the boundary filaments together, analogous to an actomyosin contraction. We investigated this question by looking at variations in model parameters.

If we consider 2 boundary filaments located within the domain and long enough that they overlap. We assume that a myosin motor initially binds vertically to a pair of filaments. In the case of boundary filament initial overlap, the probability that a myosin motor will directly connect the boundary filaments is high, making it possible for the motor to quickly slide the boundary filaments past each other and increase the amount of overlap. On the other hand, if the boundary filaments are in a domain where there is no initial overlap, then it would be impossible for a myosin motor to directly bind to the boundary filament pair. Therefore we introduce the "free" filament network, a constant number of linearly sliding filaments that are not connected to the boundary by a spring and are allowed to experience turn over. The "free" filament network then acts like a ladder for motors to make indirect attachments to the boundary filaments via the "free" filaments. Then the motors are able to slide the boundary filaments based on their connections to "free" filaments to possibly reach a point where the boundary filaments would overlap. There are three possible morphologies: boundary filaments are not pulled toward the center at all (fig 4.4A, stiff), pulled into the center of the domain and slide past each other to bring their plus ends to the same place (fig 4.4A, soft), or pulled only a little toward the center (fig 4.4A, standard). For this model, we

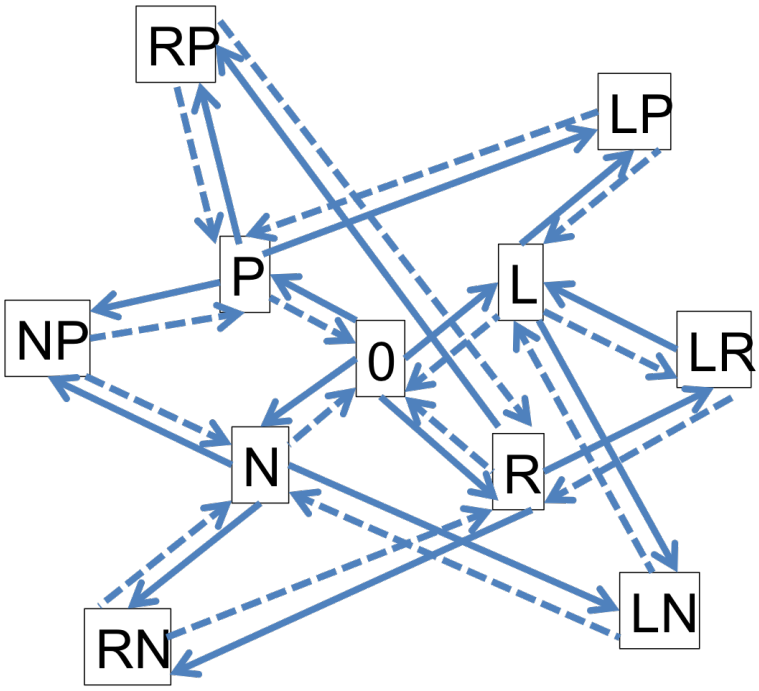

Figure 4.3: **Non-muscle myosin II transition states for the aligned filament model**. The simulation begins with motors unattached, state 0. Motors attach to a filament at a rate of attachment, r_0 (solid arrows). The motor can bind to a left-oriented, spring-bound filament (L), right-oriented, spring-bound filament (R), plus-oriented free filament (P), or negative-oriented free filament (N). A motor can fall off of a filament based on the rate of detachment, r_1 (dotted line). In this case the motor returns to the previous state. All two-letter states are possible combinations of filament pairs which is when the two legs of the motor are attached to two different filaments and can exert a force to slide the filaments. The cases when a motor would bind to two of the same oriented filaments are not shown because the motor would just walk down the filaments and no forces would be exerted to slide these filaments.

consider polymerization as a source of translational noise, analogous to our rotational noise from Chapter 3. So, at a rate of polymerization, only "free" filaments, will disappear and a new one will reappear at a random position along the x-axis, the only dimension we are considering (Movie D.2).

We wanted to be able to assess how varying the model parameters would affect the end morphology for the spring bound ends, so we plotted where the plus ends of the spring bound filaments were over time, averaged over 50 simulations. To see a better idea of the distribution of the plus ends over time, we were also able to average the plus end positions for the last half of the simulation, assuming that was when the initial start up of motors binding to filaments normalized (fig 4.4B). For the standard parameter set, we find that most simulations end up with the plus ends of the boundary, spring-bound filaments in the center of the domain (the middle concentration of white in fig 4.4B at t=20,000), but there are still a few sims with plus ends that have relaxed at the boundary point (evidenced by the time average position plot in fig 4.4C). In essence, this means that the two spring-bound, boundary filaments "lost" their interaction with the inside "free" filaments.

4.2.1 Filament parameters

If we halved the number of filaments to n=10, this meant that 2 filaments were spring-bound, but the remaining 8 were free. In this case, the free filaments were more strongly able to bring the boundary filaments to the center, versus doubling the number of filaments to n=40, when the spring bound filaments were either pulled in towards the center a little bit, or completely relaxed to the boundary (fig 4.5A). The reason for this has to do with the number of potential interactions for the motors.

Some of what dictates how the plus ends of spring-bound filaments moves is the number of opportunities of motors to bind to the spring filaments, via direct connections or linking connections via free filaments. We looked at the effect of shortening or lengthening the filaments. If the filaments are shorter, then we are insuring that there is no initial overlap between the spring bound filaments at the boundary, and the intermediary "free" filaments are also short, decreasing the probability of having a large number of options for motors to

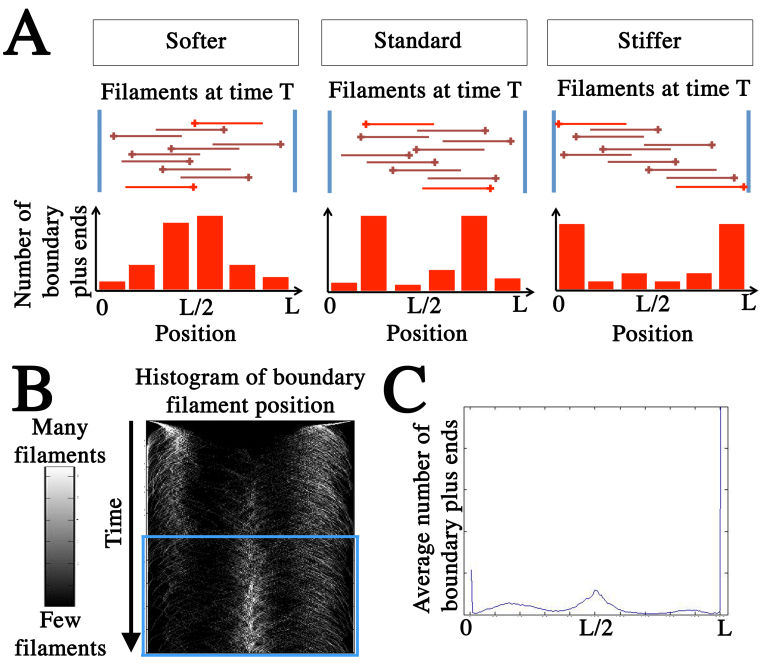

Figure 4.4: **Morphologies and analyzing aligned actin arrays** (A) Examples of filament location for varying boundary filament spring stiffness. In the softer case, boundary filaments (bright red) have plus ends at the center, L/2 position at time T. Below the schematic is a histogram of boundary filament (bright red) plus end location at time T, for 100 different simulations. When the boundary spring stiffness is increased to a standard value, boundary filaments (bright red) are pulled in toward the center (L/2) position, but are not pulled all the way into the center. For 100 different simulations, the sample histogram also shows two peaks off center from the L/2 position. When the boundary spring stiffness is much stiffer, then the boundary filaments (bright red) are not pulled away from the boundaries 0 and L. The same data is captured with the sample histogram for 100 different simulations showing peaks at the 0 and L positions. (B) Time evolution plot of the histograms of the boundary filament positions over 50 sims for 20,000 time steps. In the beginning, plus ends are sharply pulled toward the center from the boundary edges. A large number of simulations ended with the boundary plus ends closely located at the center of the domain. (C) Average number of filament plus ends for the last half of the simulation (shown in the blue box in (B)). The peaks of this histogram show that there is a portion of simulations where filaments ended in the center of the domain, but also simulations where boundary filament plus ends were at the edges.

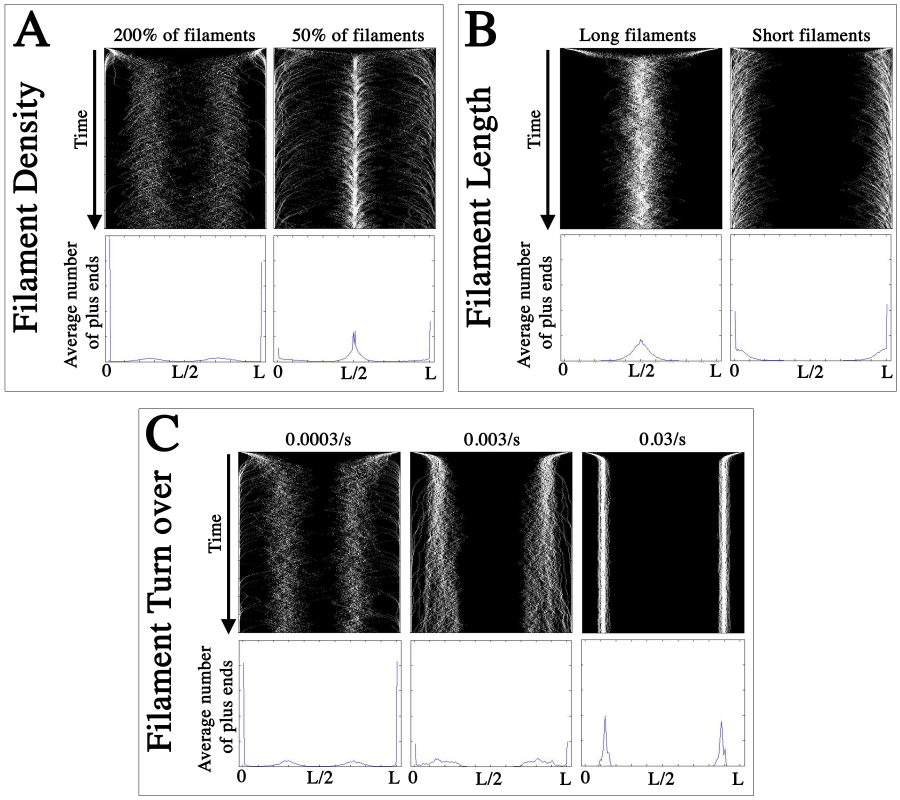

Figure 4.5: **Morphology changes with filament parameters for aligned actin arrays**. (A) Doubling the number of filaments (200%; n=40) results in boundary filaments relaxed back to the boundary edges and another population pulled a little bit into the center, but not all the way. Halving the number of filaments (50%; n=10) results in most simulations with plus ends of boundary filaments at the center of the domain. (B) Longer filaments (l=1.6) means motors have more opportunities to make connections to boundary filaments and bring the plus ends together. Short filaments (l=0.4) mean the motors have less opportunities to make connections to the boundary filaments at the edges. (C) Increasing the rate of turnover ($r_3 = 0.0003$) causes the boundary filament plus ends to spread further out from the center. Increasing the turn over by another order of magnitude ($r_3 = 0.003$) causes the boundary filaments to separate even further. At the fastest rate of turn over ($r_3 = 0.03$), the populations of plus ends pulled away from the edges a little bit but not in the center.

bind, and make linkages between "free" filaments and the spring bound filaments. When we make the filaments longer, then we are starting out with the spring bound filaments overlapped, which means that there is always the possibility of a motor connecting the two spring bound filaments, and more possibilities of linkages via the "free" filaments (fig 4.5B).

Finally, based on our previous research in Chapter 3, we knew that polymerization should be able to disrupt the morphology, and reach a new steady state. Increasing polymerization, increases the noise in position experienced by the free filaments, but since the boundary filaments do not experience polymerization, our graphs will only show how the position of boundary filaments changes over time. With low polymerization (fig 4.4 B), a fraction of the boundary filaments were brought into the center of the domain. We found that as the polymerization rate increases, the boundary filaments move slightly off center, to a steady state position offset from the boundary (fig 4.5C), however there is still a variance in position. As the polymerization rate continues to increase, the variance in plus ends decreases, but the position is slightly pulled in from the boundaries. Because the free filaments are constantly disappearing and reappearing in new positions with new left or right orientations, the connections made between boundary filaments and free filaments are extremely short lived (once a filament polymerizes, all connected motors fall off or disconnect), however connections are made to pull the boundary filaments into the domain, otherwise we would expect to see the boundary filaments at the boundaries.

4.2.2 Motor parameters

If we decrease the number of motors then the number of opportunities for motors to make connections between filament pairs that ultimately results in a connection between the two boundary filaments is less likely. Then the boundary filaments should end at the boundary because the connections from boundary to free to opposite boundary were unable to occur. If we increase the number of motors, then we expect that the motors will be able to quickly relocate the spring bound filaments to the center, or slide filaments past each other (fig 4.6A). As we decrease the spring stiffness constant, motors are unable to exert as much force onto the spring-bound filaments and are unable to bring the plus ends into the center. If the

motor spring stiffness constant is increased, then the motors are able to bring the plus ends of the filaments into the center very quickly (fig 4.6B).

If we decrease the speed of the motor, then the motor spends more time on the filament, except that the chance of the motor falling off (rate of detachment, r_1) is much higher meaning that the motor is doing less work sliding filaments. We observe that the plus ends of the spring bound filaments are mostly congregated at the boundaries in this case. If we increase the speed of the motor, then it is able to go much faster and spend more time on the filaments because it is less likely to fall off. In this case, we see that the plus ends of the filaments are pulled toward the center, although there is some variance in how tightly clustered the plus ends are (fig 4.6C).

If we decrease the spring stiffness of the boundary filaments, then the free filaments and motors are able to bring the spring-bound filaments towards the center. If we increase the spring stiffness of the spring-bound filaments, then the interaction between free filaments and motors will be unable to generate enough force to dislodge the plus ends from the boundaries (fig 4.7).

4.3 CONCLUSIONS

The sliding model had similar conclusions as our rotational model (Chapter 3): polymerization destabilized the contractile geometry with no polymerization, but a steady state morphology was observed even with the addition of polymerization. Varying the filament and motor parameters changed the aligned actin morphology based on the probability and duration of connections between the boundary filaments and the free filaments. Including the boundary filaments gave us a new "tool" for determining forces from the network.

The aligned actin model only addresses part of Aim 1.1.1. We are able to model what might be occurring in *in vivo* aligned actin arrays once they are already established, but we still have questions surrounding how the aligned array arises, and then disassemblies when no longer needed. We are still seeking to understand dynamic, two dimensional *in vivo* filament morphologies. Therefore, we decided to combine the known biophysics of actomyosin

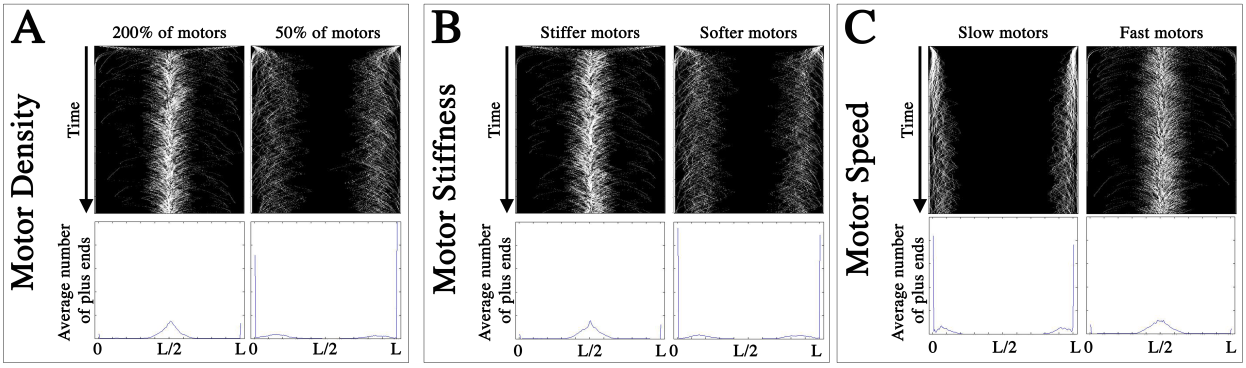

Figure 4.6: **Morphology changes with motor parameters for aligned actin arrays**. (A) Doubling the motors (200%; m=200) results in boundary filaments brought towards the center. Halving the number of motors (50%; m=50) results in the boundary filaments relaxing to the boundary edges. (B) Doubling the stiffness of the motor spring (k2=0.6), the boundary filaments are quickly pulled past each other to the center. Halving the stiffness of the motor spring (k2=0.15), the boundary filaments relax to the boundaries. (C) Decreasing the motor speed (v=0.01) results in the plus ends of the boundary filaments relaxing to the boundary edges because the motors are not spending enough time on the filaments to do the work to slide them past each other and bundle in the center. Increasing the motor speed (v=0.5) means the motors are able to quickly slide the boundary filament plus ends past each other towards the center.

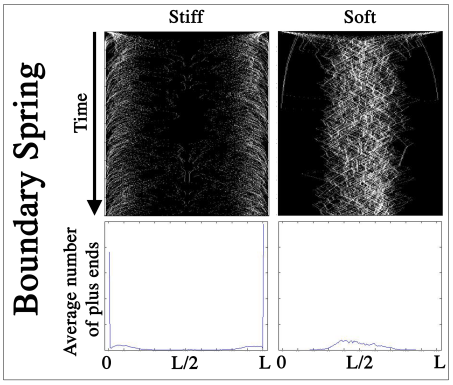

Figure 4.7: **Varying the stiffness of the boundary spring for aligned actin arrays**. Increasing the stiffness of the boundary spring (k1=0.1) results in the plus ends migrating to the boundary edges. Decreasing the stiffness of the boundary spring (k1=0.005) results in the plus ends of the boundary filaments coming towards the center.

networks for rotation from Chapter 3 and sliding from Chapter 4, with the spring-bound force "sensor" boundary filaments developed for this model to create a more realistic 2D model in the next chapter (Chapter 5).

5.0 2D MODEL FOR ACTIN MORPHOLOGY REARRANGEMENT BY MYOSIN MOTORS

In order to fully address Aim 1 (1.1.1), identify how rates of F-actin polymerization and myosin generated forces affect actomyosin dynamic morphology, we have developed a 2D model of actomyosin in the cell cortex, a very thin region of the cell underlying the plasma membrane. Chapters 3 and 4 began to address Aim 1 (1.1.1), but the 2D model will help to simulate experimentally observed actomyosin morphologies, and understand the factors contributing to characteristic geometries of actomyosin contractions.

5.1 INTRODUCTION

Actomyosin plays a critical role in multiple developmental events, such as the contractile actin purse-string located at the margin of the lateral epidermis during dorsal closure in *Drosophila* [Young et al., 1993, Edwards et al., 1997, Jacinto et al., 2002], fusion of the epidermis along the anterior and posterior ends of the epidermis at later stages of dorsal closure in *Drosophila* [Millard and Martin, 2008], bending of the tissue to facilitate invagination during gastrulation in *Drosophila* [Martin et al., 2009], stiffening of the *Xenopus* embryonic tissue during neural tube closure [Zhou et al., 2009], and cell shape changes resulting in convergence and extension of the *Xenopus* embryonic tissue [Kim and Davidson, 2011]. Tools used to examine actomyosin morphology include imaging techniques such as fluorescent speckle [Waterman-Storer and Salmon, 1997], and *in vitro* observations of purified actin and myosin [Kouyama and Mihashi, 1980, Cooper et al., 1983, Amann and Pollard, 2001]. *In vitro* experiments try to determine rates of actin polymerization, branching, bending, breaking,

and annealing, whereas *in vivo* experiments determine locations and frequencies of pulsatile contractions, and actin polymerization, and branching in the thin lamellipodia region [Lecuit et al., 2011]. Although these experiments are essential to understanding the dynamics of the actomyosin complex, a different approach must be taken in order to determine how the network organizes and generates forces based on the network organization.

To investigate cortical actomyosin morphology in embryonic *Xenopus* tissue, our group has developed techniques for quantifying and analyzing actomyosin contractions and used these tools to describe differences in actin morphology in different tissues. For example, we can make a live, time-lapse movie of cortical actin dynamics with fluorescently labeled F-actin (fig 5.1). The concentration of F-actin is recorded using confocal microscopy. Regions of dense F-actin appear as brighter than average pixels. As the F-actin dissipates we observe a drop in pixel intensity (fig 5.2). We can use a kymograph to look at a small patch of the contractile area over time, in addition to plotting the normalized mean intensity of the pixels over time.

We have observed that the basal surface of the epithelium (fig 5.3A) has a different actin morphology than the apical surface (fig 5.3B). Both surfaces, however, have actin contraction dynamics even though the morphologies are different. The apical surface of cells bordering the blastopore lip (fig 5.3C) show highly aligned actin suggesting a unique mechanical role in orienting cells for the involuting tissue. The high frequency of contractions in the apical cortex of the neural epithelium suggests actin dynamics play a role in convergence extension and the creation of the neural folds on the apical, neural epithelia surface (fig 5.3D).

Drugs are used experimentally to modify the biochemistry of actin polymerization and NMM II contractility [Kim and Davidson, 2011]. Jasplakinolide stabilizes F-actin (fig 5.3E), and we observe more stable asters, or high-density concentrations of actin. Latrunculin B depolymerizes actin (fig 5.3F), and the network becomes much more sparse with actin concentrated at the edges of the cells. Y27632 inhibits the contractility of NMM II, leading to a sparser actin network that has lower intensity actin asters (fig 5.3G). Lastly, Calyculin A increases the contractility of NMM II which increases the intensity and concentration of the F-actin network (fig 5.3H).

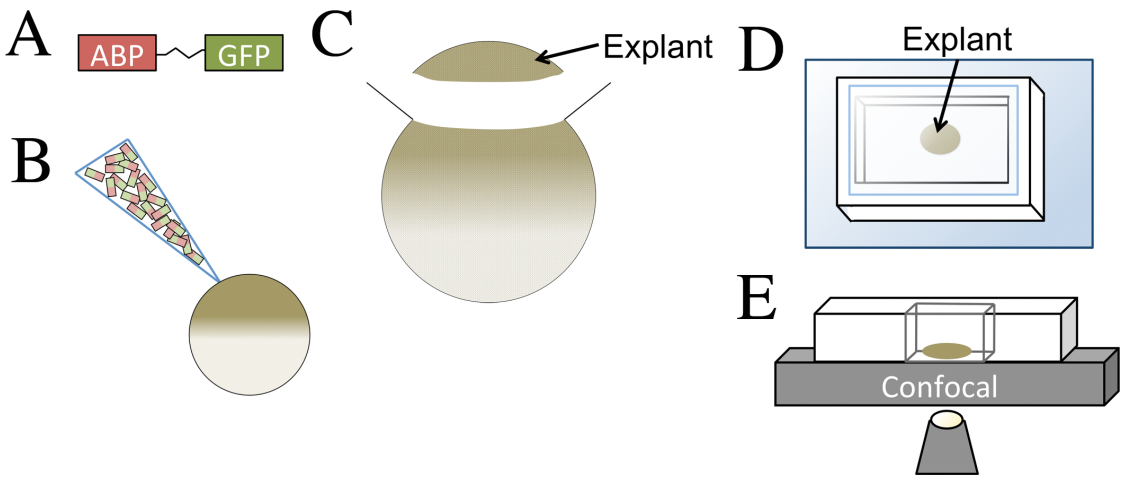

Figure 5.1: **Experimental technique for fluorescently tagging F-actin in *Xenopus*** (A) Our labeling protein is an actin binding protein (ABP) connected to green fluorescent protein (GFP). (B) The protein is injected into the newly fertilized egg in the area of interest. For example, the region of the fertilized egg which will develop into the animal cap. (C) After giving the fertilized egg time to develop, and testing to insure fluorescent expression, the animal cap explant is cut away from the embryo and placed into an imaging chamber. (D) The explant is carefully placed onto a fibronectin coated glass and held in place with a tiny slip of glass (not shown). Media is sealed in the acrylic chamber by placing a smaller glass coverslip onto the top. (E) Actin dynamics are observed with confocal microscopy and time-lapse movies are made of the fluorescent actin.

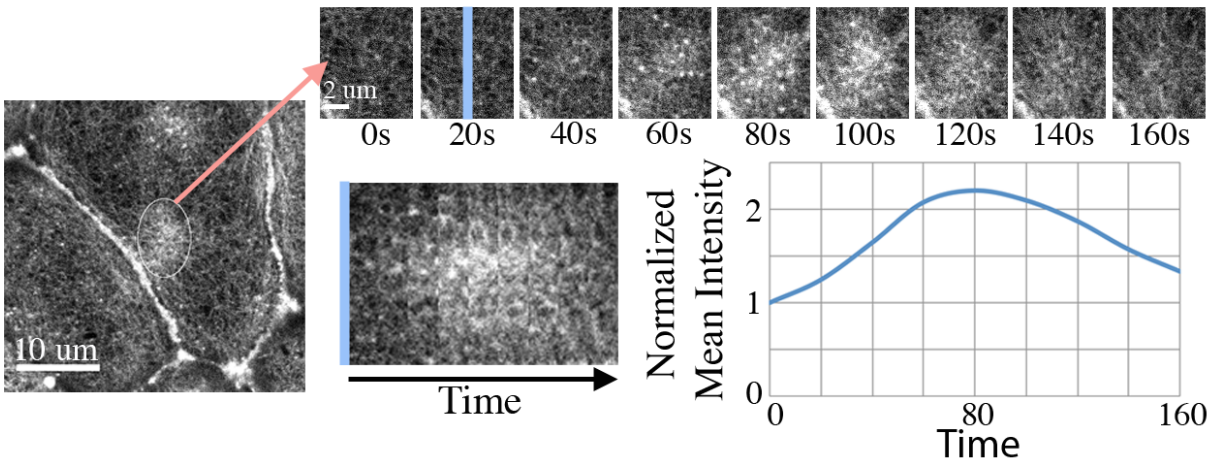

Figure 5.2: **Quantifying actomyosin dynamics**. To the left is the image of a cell from the apical surface of the neural epithelium. The F-actin has been labeled using Utrophin-GFP, and the higher intensity of F-actin is encircled to show the location of a contraction. The pink arrow points toward a zoomed in image of the same contraction area over the period of the time lapse imaging. Another way of examining the contraction is to consider the small blue strip of each frame and piece these strips together over time to create a kymograph of the contraction. Lastly, we can plot the normalized mean intensity of the contraction area over the course of the movie.

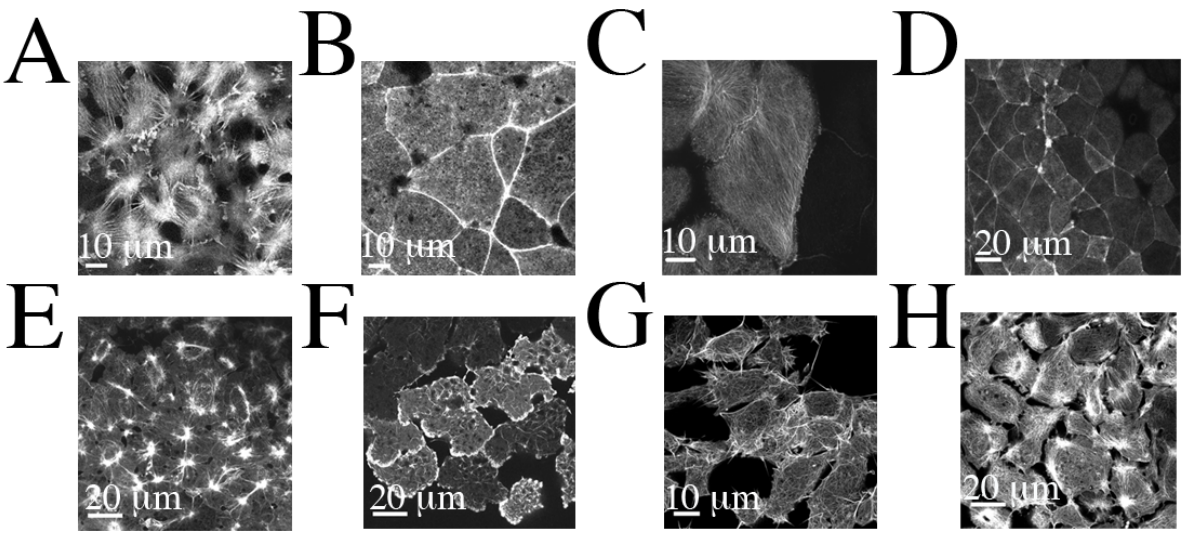

Figure 5.3: **Diverse morphologies of cortical F-actin in *Xenopus***. (A) Utrophin-GFP labeled F-actin on the basal surface of the epithelial tissue of an animal cap explant. The basal surface is placed on a fibronectin coated glass. (B) Utrophin-GFP labeled F-actin on the apical surface of the epithelial tissue of an animal cap explant. This surface is placed on a cleaned glass surface without any fibronectin present. (C) Utrophin-GFP labeled F-actin at the blastopore lip (R. Feroze and J. Shawky). (D) Utrophin-GFP labeled F-actin in the apical surface of the neural epithelium (D. Vijayraghavan). (E) Moesin-GFP labeled F-actin in a dorsal marginal zone explant treated with 5 nM of Jasplakinolide (H.Y. Kim). (F) Moesin-GFP labeled F-actin in mesendoderm tissue treated with 0.6 μM of latrunculin B (H.Y. Kim). (G) Moesin-GFP labeled F-actin in a dorsal marginal zone explant treated with 50 μM of Y27632 (H.Y. Kim). (H) Moesin-GFP labeled F-actin in a dorsal marginal zone explant treated with 50 nM Calyculin A (H.Y. Kim).

Our motivation in developing 2D models is to understand why the F-actin networks adopt different morphologies depending on the tissue or surface of cells, and how these morphologies regulate global force. We will also examine the effects of actin polymerization and myosin contractility in network morphology since these variables experimentally affect actin morphology.

Previous models have examined actomyosin contractions, most notably in sarcomeres where actin and myosin are organized in parallel, sliding arrays to shorten muscles [Hill, 1938]. However, we are interested in cortical actomyosin punctuated contractions that are disorganized compared to sarcomeres. The Gardel group developed a 2D model to investigate disorganized actin networks and how myosin would contract the network [Lenz et al., 2012]. Their model considers the extension and contraction experienced by single F-actin from a tension created by a myosin attached to a different F-actin. They assume that the orientation and strength of the applied tension can cause bending and eventual buckling of the F-actin. Buckling within the network results in a global contraction of the network and they assume this is the same mechanisms of contraction of disorganized F-actin networks *in vivo* and *in vitro*. In a different, but related model, a 2D network of actin filaments was created with stable cross linkers placed at all overlapping filament apices and contractile myosin motors put a contraction stress on the entire network [Dasanayake et al., 2011]. Although both of these recent examples give insight how this complex morphology of "disorganized" actomyosin generates a contractile force to induce tension in the cell cortex, they are not considering the more complex dynamic biophysical aspects of the network.

In addition there are physical models of actomyosin utilizing reconstituted F-actin gels [Falzone et al., 2012]. The idea is that a reconstituted gel represents the cortex of the cell and the mechanical properties of the gel can be determined. Furthermore, researchers can add actin crosslinking proteins and see how the stable actin network changes in morphology and material properties. The limitations with these analog models are that they do not capture the extensive dynamics of actomyosin observed *in vivo*.

To expand on these models, and extend our previous work on the rotational model (chapter 3; [Miller et al., 2012]), and sliding linear arrays (chapter 4), we have created a simple dynamical model for a two-dimensional array of actin filaments containing non

muscle myosin II (NMM II). First, we discuss assumptions made in developing the model. Second, we describe the model and simulation specifics, the modeling assumptions and the rationale behind them. Third, we discuss results arising from this simple model, such as how a contraction arises, how it is possible to disrupt it, and extend our model to simulate *in vitro* experiments. Finally, we conclude with a discussion about our model and our unique approach, and discuss future directions for biophysical models of actomyosin dynamics.

5.2 2D MODEL AND METHODS

In order to understand how actomyosin contractions arise and generate force, we simulated a two dimensional (2D) patch of F-actin and NMM II mini-thick filaments. We picked a hexagonal boundary for the simulation because our previously published image analysis technique breaks the cell into a series of hexagons that are then used to examine differences in pixel intensities between the individual hexagons compared to the mean intensity of the cell [Kim and Davidson, 2011]. Furthermore, the hexagonal domain can be extended to a more generalized polygon domain.

From our experimental studies, we know that the thickness of cortical F-actin, the region of F-actin just below the plasma membrane of the cell, is approximately 2 μm thick, essentially planar when compared to the thickness of the *Xenopus* embryonic cells (40 μm). There could be some 3D aspect to the network which would change the physics of the actomyosin contraction, but we assume that the third dimension is negligible. Furthermore, we assume that F-actin filaments are able to move through and past each other. We have chosen not to include F-actin collisions and entanglements in the model, but these events could be represented by viscous drag. Our model follows the same outline as our rotational model [Miller et al., 2012] where F-actin filaments have polarity (fig 5.4A) and NMM II motors randomly bind to a pair of filaments (fig 5.4B) and walk toward the plus or barbed end of the filament (fig 5.4C).

As with our previous models, F-actin remodeling is driven by the ATP-ase function of myosin II. Cross bridge cycling is the processes by which individual head domains of myosin

change configuration to become activated and able to bind to F-actin. Then through ATP hydrolysis, the bound head domain folds and propels itself towards the F-actin plus end. We assume that the cross bridge cycle is implicitly represented in the myosin motor velocity.

By itself, a NMM II filament is unable to exert a force on F-actin because it consists of only one filament with the head binding domain. Individual NMM II filaments are inactive when they are in a folded configuration and then are activated when they extend their tail domain, which allows multiple NMM II tails to bundle together to form a processive bipolar motor called a mini-thick filament [Lecuit et al., 2011]. Our model assumes the mini-thick filament has already been formed and that NMM II is "active." We can include a switch from inactive to active states for the NMM II by adding in additional rates of activation or inactivation for NMM II.

NMM II exerts a spring-like force while walking, rearranging the filaments. This force is generated from the bipolar arrangement of multiple NMM II filaments into the mini-thick filament arrangement and the action of cross bridge cycling along F-actin at each end of the bipolar mini-thick filament. For simplicity, we assume that our motor, representing a NMM II mini-thick filament, has a rest length of 0 and from the moment it is stretched begins exerting a spring force on the pair of filaments. The maximum force the model's motor is allowed to exert is based on the motor's spring stiffness and the maximum stretch (a parameter set in the beginning of the simulation) of the motor.

Motors have a specific rate of attachment to bind to a random pair of filaments that are located within the motor's threshold of attachment stretch. We assume the radius of attachment for motors is smaller than, or the same size as a single NMM II filament ($\sim$300 nm), and this parametric length also serves as the maximum stretch allowed once the motors bind to a pair of filaments and begin walking (fig 5.4E). Motors fall off of the filaments once they reach the plus end of the filament, but there is also a small rate of detachment where motors fall off before they reach the end of the filament. While motors are waiting to attach to filaments, they diffuse within the domain. If a motor diffuses out of the domain, a new motor appears at a random location within the domain so the population of motors for the simulation remains constant.

Although the dynamics of the model seem straight forward and simple, the model is inherently nonlinear. The polarity of F-actin significantly complicates the polymer models [de Gennes, 1979]. The F-actin array then sorts or sequesters motors, creating heterogeneous patterns.

5.2.1 Setting up the actomyosin network

Our models are created with filaments of the same length, placed at random positions (x_i, y_i) and angles (θ_i) within a hexagonal boundary. We chose a hexagon because it reflects a unit of the cell cortex from our image analysis and allows integration with the microenvironment. Over the course of a simulation, if motors or filaments move past the boundary, then new motors or filaments appear within the hexagonal boundary. For most of the simulations we use a hexagonal boundary and later extend the boundary to polygonal shapes.

If we model polymerization we would need to consider two populations of actin, G-actin the monomer and F-actin the filamentous form. Polymerization would dictate the rate at which G-actin would add to F-actin increasing the F-actin length and depleting the population of G-actin. Depolymerization is the rate of F-actin disassembling and changing back into G-actin, decreasing the population of F-actin and increasing the population of G-actin. For simplicity we use a single turnover rate for polymerization and depolymerization that dictates if a random filament disappears and a new filament appears at the exact same instant in a new spatial position and orientation. The implementation of F-actin turnover introduces spatial noise into our simulations. If there were any motors attached to the filament that polymerized they fall off. Turnover in our rotational and sliding models similarly served to introduce spatial noise into these models (chapter 4 and chapter 3; [Miller et al., 2012]). All of the parameter values for a standard simulation are in table 5.3.

5.2.2 Biophysical theory for actomyosin

Extending our previous rotational and sliding models to a 2D domain requires the addition of biophysical theory to account for free filament movement. All symbols are in table 5.1. We need to consider forces that translate the filament in addition to forces rotating the filament

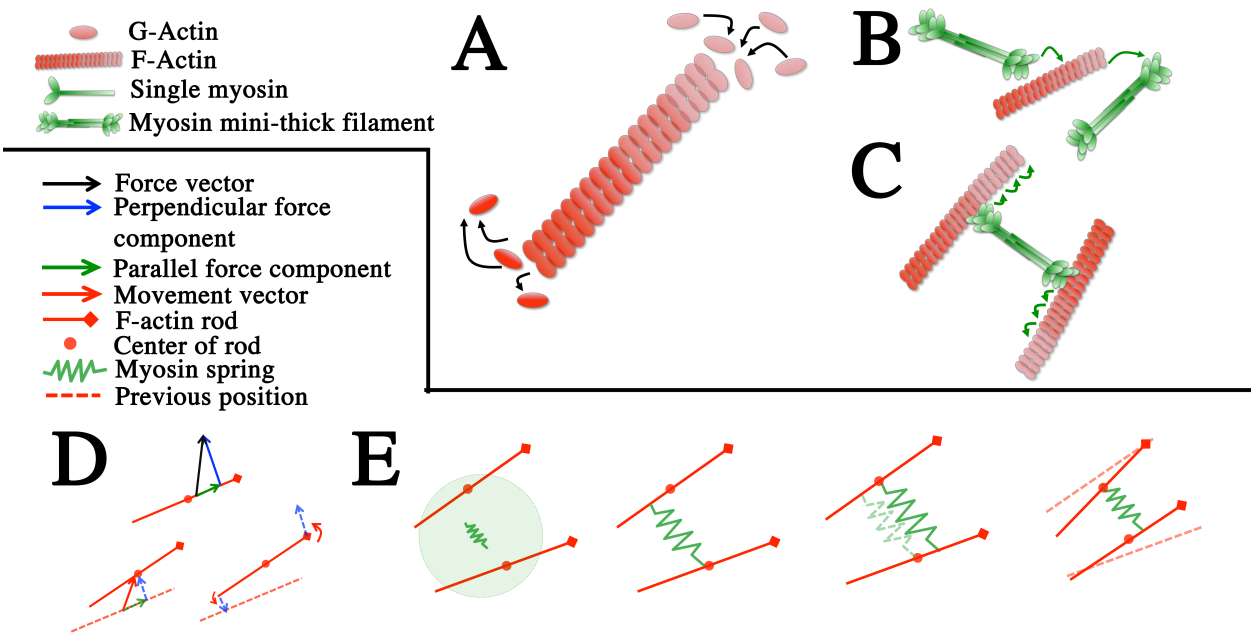

Figure 5.4: **Cartoon of biophysics of actomyosin and simulation dynamics** (A) Depicts the biophysical dynamics of F-actin where the monomer, G-actin, binds to the plus end of the filament in the act of polymerization, and the filament disassembles at the minus end becoming individual monomers in the act of depolymerization. (B) Individual NMM II filaments bundle together into a multi-headed mini-thick filament which can bind to F-actin, or detach from F-actin. (C) The mini-thick filament of NMM II walks to the plus end of F-actin. (D) Pictorial diagram of the break down of forces and movements on an F-actin-like rod. The perpendicular force (blue), is broken into a component that goes towards perpendicular translation of the filament (blue dotted) and a distributed torque (red curved arrows) to the ends of the rod. Translational force goes toward translational movement. (E) Cartoon flow-chart of the simulation where first, a motor searches for a pair of filaments to bind. The motor binds to the pair of filaments, then walks at a certain speed toward the plus ends. After one walking time step, the motor exerts a force on the filaments, contracting, and pulling the filaments together.

(fig 5.4D). In general we know that we can calculate a force vector acting upon a filament and break the force into a parallel and perpendicular component. The parallel component is used to determine how the filament will slide in that direction. The perpendicular component is broken up further into a portion that slides the filament sideways and a portion that applies a torque or rotation to the filament. Furthermore, because we are considering a cylinder moving through a viscous media, we know that the viscosity components for resisting parallel sliding are smaller than for perpendicular sliding, or rotation.

To determine the total force acting upon a filament by motors our algorithm checks each filament to see if there are motors attached and then finds the average motor force vector acting on the filament. We average the positions of all of the attached motors on the actin filament as the starting point for a motor location vector (x, y), then average all the second leg motor positions (which are attached to different filaments) to get an ending point for a motor location vector (xE, yE) (eqn 1, table 5.2). The resulting magnitude of the motor force can then be calculated (eqn 2).

Table 5.1: Symbols for 2D model equations

Symbol	Description
N	Number of filaments
m	Number of motors
(x_p, y_p)	Position of plus end of filament
$(X1_j, Y1_j)$	Position of leg 1 of motor j
$(X2_j, Y2_j)$	Position of leg 2 of motor j
(x, y)	Average position of attached motors to a filament
(xE, yE)	Average end vector position of attached motors to a filament
k	Spring stiffness constant for motors
ϕ	Angle between the filament and the force vector
L	Length of the filament
η	Dynamic viscosity of the media
p	Ratio of length of filament to its diameter
γ_{perp}=0.84, γ_{par}=0.114, and γ_{rot}=-0.662	Constants when $p = \infty$
β	Angle of translational movement
b	Viscous term for cortex filaments
E	Young's modulus
ϵ	Strain

Table 5.2: Equations of 2D motion for filaments from forces generated by motors

Equation	Number	Description
$x = \frac{1}{m}\sum_j X1_j$	1	Determining the resulting stretched motor vector by
$y = \frac{1}{m}\sum_j Y1_j$		summing up all attached motors to a filament
$xE = \frac{1}{m}\sum_j X2_j$		
$yE = \frac{1}{m}\sum_j Y2_j$		
$\|\|F\|\| = k\sqrt{(x-xE)^2 + (y-yE)^2}$	2	Magnitude of motor exerted force
$A = \sqrt{(x-x_p)^2 + (y-y_p)^2}$		
$B = \sqrt{(x-xE)^2 + (y-yE)^2}$		

(continued)

Table 5.2 – *(continued)*

Equation	Number	Description
$C = \sqrt{(x_p - xE)^2 + (y_p - yE)^2}$		
$\cos\phi = \frac{C^2 - A^2 - B^2}{-2AB}$	3	Angle between filament and force vector
$F_{perp} = \|\|F\|\| \sin\phi$	4	Perpendicular force component
$F_{par} = \|\|F\|\| \cos\phi$	5	Parallel force component
$F_{perp1} = F_{perp}\frac{L - l1}{L}$	6	Perpendicular force distributed to plus end (1) and minus end (2)
$F_{perp2} = F_{perp}\frac{L - l2}{L}$		
$F_\tau = \frac{1}{2}(F_{perp1} - F_{perp2})$	7	Torque on the filament
$F_{COM} = \frac{1}{2}(F_{perp1} + F_{perp2})$	8	Perpendicular force to move the center of mass of the filament
$\Gamma_{perp} = \frac{4\pi\eta L}{\log p + \gamma_{perp}}$	9	Drag coefficients
$\Gamma_{par} = \frac{2\pi\eta L}{\log p + \gamma_{par}}$		

(continued)

Table 5.2 – *(continued)*

Equation	Number	Description
$\Gamma_{rot} = \frac{\frac{1}{3}\pi\eta L^3}{\log p + \gamma_r}$		
$v_T = \left\lvert \frac{F_\tau}{\Gamma_{rot}} \right\rvert$	10	Rotational velocity
$\omega = v_T/(L/2)$	11	Angular velocity
$\frac{d\theta}{dt} = \omega$	12	Change in filament angle
$v_{perp} = \frac{F_{perp} - F_{COM}}{\Gamma_{perp}}$	13	Perpendicular translation velocity
$v_{par} = F_{par}/\Gamma_{par}$	14	Parallel translational velocity
$\frac{dx}{dt} = \sqrt{v_{perp}^2 + v_{par}^2}\cos\beta$	15	How the plus end moves over time
$\frac{dy}{dt} = \sqrt{v_{perp}^2 + v_{par}^2}\sin\beta$		
$\sigma_{cortex} + \sigma_{free} = bv$	16	Cortex stress and free filament stress
$\Delta x = \frac{\sigma_{cortex} + \sigma_{free}}{b} dt$	17	Change in cortex filament location
$\sigma_{cortex} = \frac{F_{cortex}}{Area_{cortex}} = E\epsilon$	18	Cortex stress

(continued)

Table 5.2 – *(continued)*

Equation	Number	Description
$F_{cortex} = k_{cortex}\Delta x = \epsilon E Area_{cortex}$	19	Cortex force
$k_{cortex} = Et/N$	20	Cortex spring stiffness constant
$\Delta x = \frac{Edx + F_{motor}}{L_0 b} dt$	21	Simplified change in cortex filament location
$\Delta x = 3\frac{Edx + F_{motor}}{L_0 E} dt$	22	Further simplified, assuming $b = 3 * E$
$F_{avg} = \frac{1}{M}\sum \|\|F\|\|$	23	Average force for all motors.
$var = \frac{1}{N}\sum_i \sqrt{(x_{p_i} - \bar{x_p})^2 + (y_{p_i} - \bar{y_p})^2}$	24	Variance of filament plus ends.

In order to determine the perpendicular (eqn 4) and parallel (eqn 5) components of force acting on the filament, we calculate ϕ, the angle between the filament and the force vector F (eqn 3). The torque (eqn 6) is a portion of the perpendicular force (eqn 4) distributed to each end of the filament, where $l1$ is the distance from the base of the force vector to the filament's plus end, and $l2$ is the distance from the base of the force vector to the filament's minus end ($l1 + l2 = L$). We can then determine the total torque force (eqn 7) and the translational component of the perpendicular force (eqn 8).

Once a set of forces have been applied to a filament we must calculate how it moves. Since filaments are embedded within a viscous cytoplasm, we need to understand how a filament might move using equations that relate the movement of long cylinders in a viscous fluid. We represent viscous drag as a resistance to rotation and translation based on previously established theory for a cylinder moving through a viscous fluid [Hunt et al., 1994]. We use drag constants to represent the three directions of resistance: parallel translation, perpendicular translation, and rotation (eqn 9): p is the ratio of the length (L) to diameter (di) of the cylinder, and γ_{perp}=0.84, γ_{par}=0.114, and γ_{rot}=-0.662 are constants when $p = \infty$ [Tirado and Garcia de la Torre, 1979]. We assume the filaments experience high shear, so the dynamic viscosity, η, is higher than water. From the viscosity terms, we can calculate the tangential velocity (eqn 10) and then determine the angular velocity (eqn 11). Based on the angular velocity, we update the filament's orientation angle (eqn 12). The speed of perpendicular (eqn 13) and parallel (eqn 14) translation are determined similarly. In order to determine how the filament's center of mass moves in the simulation frame of reference, we calculate, β, the angle of the force vector in the simulation frame of reference, and then update the center of mass accordingly (eqn 15).

5.2.3 Analysis techniques

All of the physics of the simulations were calculated in MATLAB and the plotting was done in ImageJ. We can create a movie to let us see how filaments and motors move over the time of the simulation. For most cases, the simulations were run for 1,000 time steps at a step size of 0.01s, which translates to 10 seconds. From the movie we can create a kymograph, just

like we would when analyzing an experimental time-lapse of labeled F-actin. We can also calculate the mean intensity of F-actin, essentially the density of F-actin, within a certain area over the simulation. We found that the F-actin asters consisted of radially oriented F-actin whith all the plus-ends in the center. Because we have data for the locations of filaments and motors, and motor generated forces for each time step, we can determine the mean motor generated force over time, and the variance in the filament plus-ends over time (eqn 24). We can also determine the fraction of filament plus ends that are clustered together by creating a matrix that represents a 2D histogram of plus end locations. We search through the matrix to determine clusters of elements, find the largest cluster, and sum how many plus ends are in that cluster.

5.3 RESULTS

Our first goal was to generate an actomyosin contraction using the simplified 2D model and whether these contractions would produce an aster. Aster is a morphologically defined radial array of F-actin with plus ends at the center and minus ends pointed out. To match the simulation with *in vivo* observations, we are also interested in understanding what parameter cases or additional complexities are necessary in order to deconstruct the aster after it has already formed.

5.3.1 Sparse Network

To validate the biophysics simulated by our model, we simulated a sparse network of F-actin (50 filaments) and NMM II motors (250 motors; table 5.3 parameter values as the standard; fig 5.5A). We observed the network of F-actin contracting into clusters. We can calculate all of the motor generated forces (eqn 23), average them for each time step and observe how force changes over time (fig 5.5B). We can also calculate the morphological features such as the variance in the position of the filament plus ends over time (eqn 24). We observe the system reaches a steady state, a state where variance and force no longer vary over time.

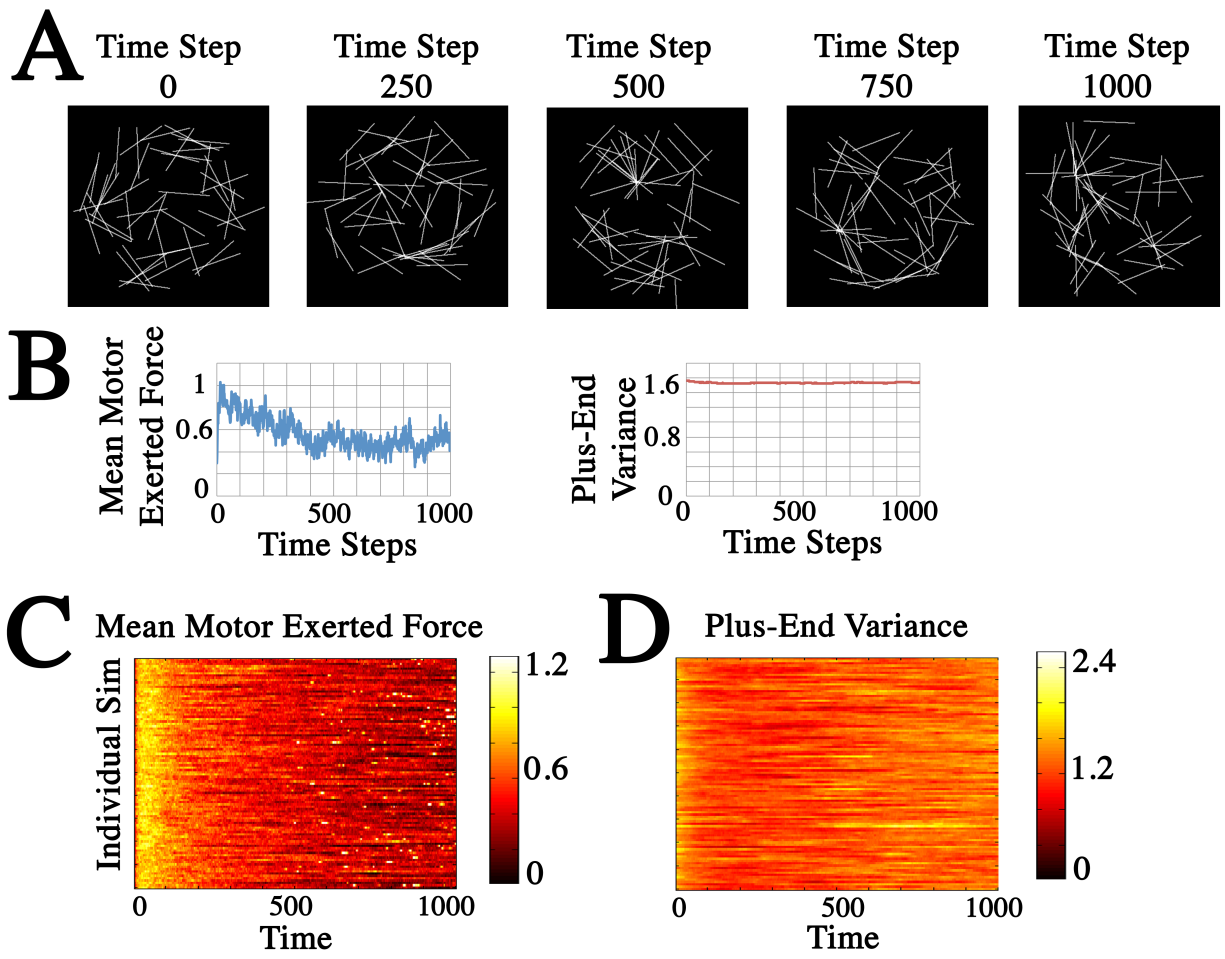

Figure 5.5: **Simulating and analyzing a sparse filament network**. (A) A sparse network simulation for 1,000 time steps, 50 filaments (white) and 250 motors (not shown). (B) The mean motor exerted force (blue) over the time course of the simulation and the variance in the plus ends (red) of the filaments over time. (C) The evolution of mean motor exerted force over time for 100 different simulations (each initial morphology is random). (D) The evolution of the plus end variance over time for the same 100 simulations shown in C.

Because the initial starting location of filaments is random for each simulation, we ran 100 different initial conditions and compared the mean motor exerted forces (fig 5.5C), and plus-end variances (fig 5.5D). The initial randomness of the network does not lead to huge differences in the steady state of force or variance, although some differences do exist. We anticipate that increasing the density of filaments and motors would decrease the observed differences so we assume that the results from one simulation can represent the general results for multiple simulations.

5.3.2 Dense network

In the sparse network simulation (fig 5.4E), we see that the actin network rearranges into an aster. The next step was to consider the dynamics of a denser actin and myosin network (fig 5.6A; Movie F.1). In this case, we consider a network of 1,000 filaments and 5,000 motors. With the denser network we see that the actin network is reorganized by the myosin motors to an intermediary ring structure (time 250, fig 5.6) which continues to contract into a stable aster (time 500-1,000, fig 5.6A). We find that the normalized mean intensity within a small circle at the center of the hexagonal cortex increases over time, and eventually saturates (fig 5.6B). The reason the mean intensity decreases after the maximum is reached is because the aster has moved out of the bounding circle. This is not the same reason for the decrease in intensity for our *in vivo* experimental observations where the actin contractile bundle dissipates. Therefore, we hypothesize that there must be an additional mechanism to break up actin contractions.

We are also able to take a one pixel strip of the merged image of the simulation at each time point to see the kymograph of the contraction over time (fig 5.6C). Again, the contraction has moved away from the kymograph line, which is the reason for the depletion of actin and myosin at the end of the kymograph. Because we are simulating actomyosin, we can plot the mean motor exerted force over time (fig 5.6D) and the variance of the filament plus ends over time (fig 5.6E). Both the force and variance plots show the steady-state reached by the network. The force curve is similar to our rotational model (chapter 3; [Miller et al., 2012]). The variance increases because of the ratio of filaments in the aster to

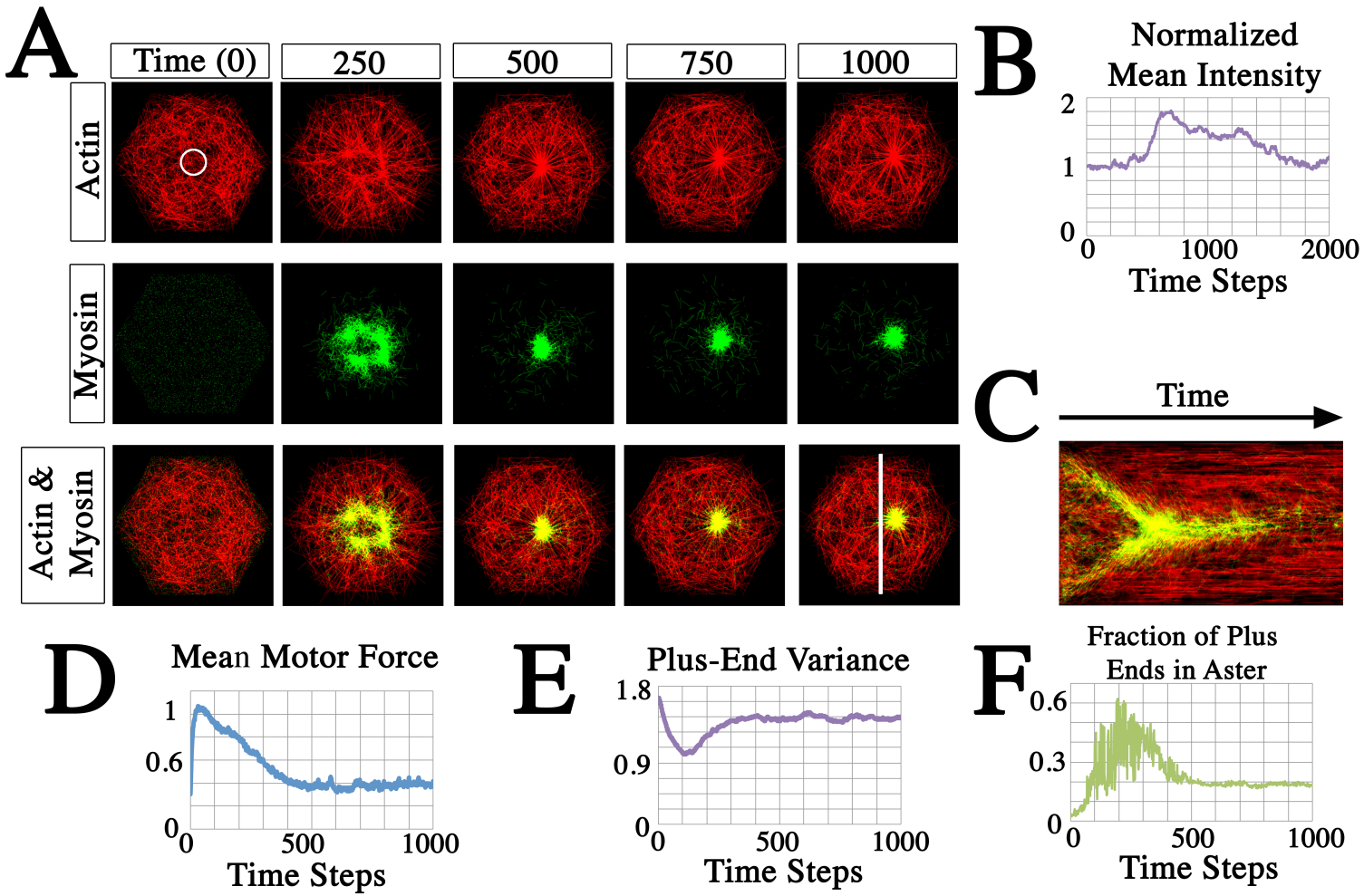

Figure 5.6: **Simulation for a dense network of filaments and motors** (A) 1,000 actin filaments in red, 5,000 myosin motors in green, and a merged image of actin and myosin using an intensity adding calculator in ImageJ. Time is simulation time steps not seconds. (B) The normalized mean intensity of the circle within the actin network shown in A, calculated with ImageJ. *Continued on next page*

Figure 5.6: *Continued from previous page* (C) A strip kymograph of the strip in the merged image in A over time. (D) The mean motor exerted force (blue) over time for the simulation. (E) The centroid variance (purple) over time for the simulation. (F) A plot of the fraction of filament plus ends in the aster over time (green).

filaments outside of the aster (fig 5.6F). More filaments are not a part of the aster because the motors have become trapped by the concentration of plus-end filaments. The polarity of filaments within the aster have laid tracks to direct all walking, bound motors to the center (fig 5.6A, myosin location in green). The density of filaments at the aster location insures that motors are more likely to bind (if rate of attachment is preferable, then there is a huge population of filaments within the motor's search radius), and the motors are not capable of diffusing fast enough to escape this "sink" since every time they bind, they are deposited back into the center of the aster by walking on filaments until they fall off the plus ends.

5.3.3 Changing actin network morphology

Another benefit of modeling is that we can vary the parameters within and outside the physiologically observed ranges and determine how the morphology of the aster changes or stays the same. Our approach in varying parameters is analogous to experimental studies where cells can be incubated with small molecule inhibitors which stabilize or destabilize F-actin, and increase or decrease NMM II contractility (fig 5.2F-I)[Kim and Davidson, 2011]. In each of the following sections we began each simulation with the hexagonal boundary and random initial locations for the actin and myosin. Simulations execute for 1,000 time steps and generate steady state morphology (fig 5.7). The physiological ranges used in our simulations are summarized in Table 5.3.

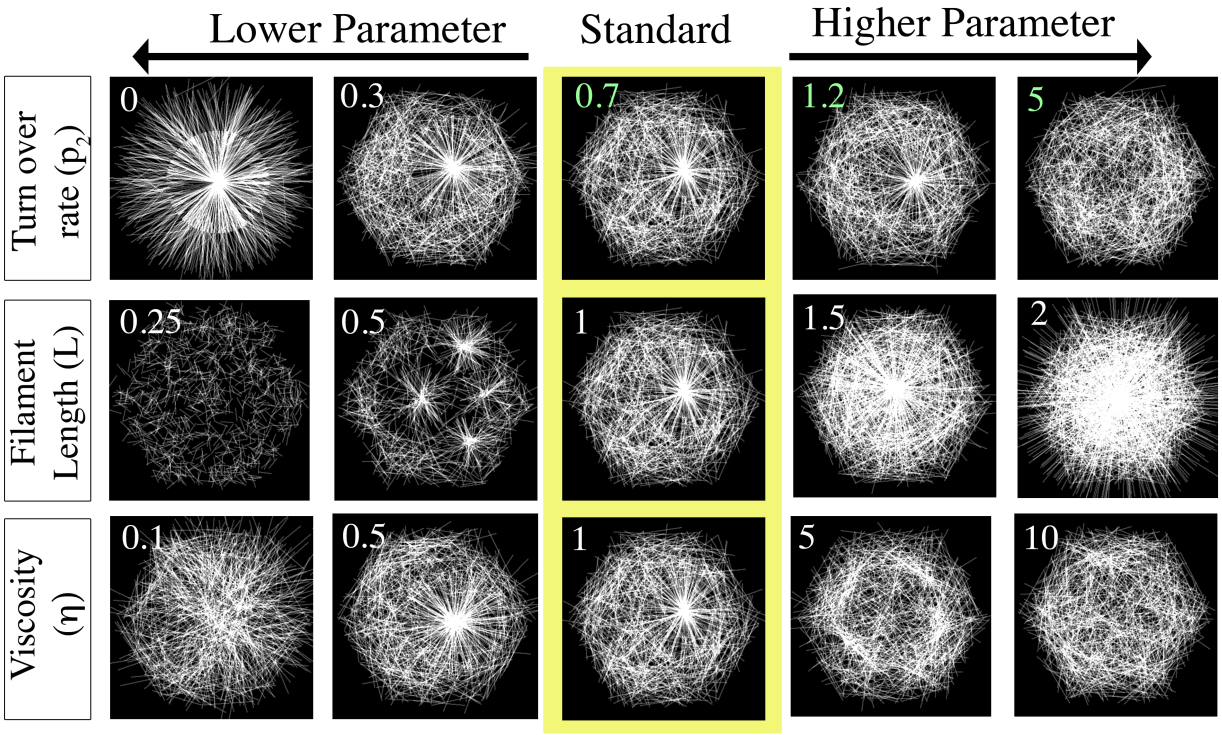

Figure 5.7: **Aster formation as biophysical parameters controlling filaments**. The images are the end actin morphology after 1,000 time steps. The yellow box indicates the same ending image for a simulation with the standard set of parameters, but each row depicts a different parameter variable. Each parameter variable starts at a random initial condition, and the end images at t=1,000 are shown here. All biologically relevant parameters are shown in green text, parameters outside the biological range are in red, and parameters for which we have no reference are in white.

Table 5.3: Parameter values for 2D model with references to *in vitro* values

Parameter name	Symbol	Coding value	*In vitro* value	Reference
Time to run simulation	time	10 s	∼1-2 min	[von Dassow et al., 2014]
Number of filaments	N	1000		
Number of motors	M	5000		
Persistence length of filament	L	1 μm	6nm-10μm	[Murrell and Gardel, 2012]
Rate of motor detachment	p0	1/s		Lower than p1
Rate of motor attachment	p1	10/s		Higher than p0
Rate of filament polymerization	p2	0.7/s	0.7-1.2/s	[Pollard, 1981, Amann and Pollard, 2001]
Time step size	h	0.01s		
Search radius of motor	r	0.3 μm	∼0.3 μm length of a single NMM II	[Shutova et al., 2012]
Motor velocity	v	1 μm/s	1-3 μm/s	[Kron and Spudich, 1986, Murphy et al., 2001]
Dynamic viscosity	eta	0.1 nN s/μm^2	1×10^{-6} nN s/μm^2	[Hunt et al., 1994]

(continued)

Table 5.3 – *(continued)*

Parameter name	Symbol	Coding value	*In vitro* value	Reference
Motor stiffness	k	3 nN/μm	1.875 nN/μm (single myosin)- 1,250 nN/μm (skeletal muscle)	[Kaya and Higuchi, 2010]
Rate of motor diffusion	d	0.02/s		
Mean step size of motor diffusion	mu	0.001 μm		
Diameter of actin filament	di	0.008 μm	0.006-0.008 μm	[Howard, 2001]
Hexagon diameter	cote	2 μm	5 μm in 2D simulation	[Dasanayake et al., 2011]

5.3.3.1 Varying parameters that affect filament properties

Once formed, the aster is a robust, steady state morphology. If F-actin was stable, i.e. no turnover ($p_2 = 0$), the filaments were stabilized with plus ends oriented into the center (see fig E2), but not all of the filaments were bundled into the aster. This configuration depends on parameters that control how large a region is "swept" by searching motors and how long motors dwell in these regions, discussed next in motor parameters section. When the motors are walking at a certain speed and then are quickly deposited into the center of the domain from the actin tracks organizing like asters, the motors are trapped and can't escape. In addition, when motors can only stretch a small distance to bind to filament pairs, they cannot stretch out across the entire domain to grab any additional filaments. In contrast, when the polymerization rate is increased ($p_2 = 5$), the aster can no longer form because the filaments are constantly disappearing and reappearing, destabilizing any work motors are doing.

Changing filament length is similar to changing filament density and results in multi-aster structures ($L = 0.5$), or a single, domain encompassing aster ($L = 2$; fig 5.7). Changing the dynamic viscosity (η) for filament movement tunes the amount of force filaments experience and so can prevent large scale filament movements ($\eta = 5$), trapping filaments at the periphery of the hexagon, or allow filaments to move right past each other, disrupting the density of aster formation ($\eta = 0.1$; fig 5.7).

5.3.3.2 Varying parameters that affect motors

In contrast to the filament parameters, we do not see any changes in the aster for motor detachment rates (p_0). Likewise, the motor attachment rate only disrupts the aster when the rate is small ($p_1 = 1$; fig 5.8). Myosin contractility does affect the aster formation. When we consider extremely soft motors, below physiological range, filaments never congregate into an aster, but are more concentrated at the periphery, if not multi-astered at the periphery ($k = 0.5, 1$; fig 5.8). Varying the motor velocity did not result in a morphological difference in aster formation but did affect how many plus ends were in the aster (see fig E3). As expected, when the motors move fast ($v = 3$), they are unable to spend enough time on filament pairs to pull them into the aster before becoming trapped (fig 5.8). Motor stretch (r) most strongly affected aster formation because this parameter dictates how many possibilities there are for a motor to bind to a

pair of filaments with the range, in addition to the time a motor can spend on a pair of filaments before stretching too far and falling off (although this is not a huge factor, see E4).

5.3.4 Destabilizing and reestablishing the aster

In vivo we see asters form and also dissipate. Since we could simulate their formation we also wanted to know whether we could simulate their assembly. To address this question we turned to studying the stability of asters once a parameter was altered. In practice, we refer to this as a "parameter switch." The theory behind this approach was to begin with a steady-state morphology (use the filament and motor locations at t=1,000 as the initial starting position for a new simulation), change one of the parameters, run the simulation for another 1,000 time steps, and see what the ending morphology of the actin network is. Since there are a few parameter cases that do not show a single aster morphology at t=1,000 (fig 5.7), we consider these parameters in particular to determine if (1) we can deconstruct the single aster from the standard case by switching a parameter and (2) we can reestablish the aster by switching a parameter back to the standard case.

First we considered cases where we would start a simulation with an initial condition for filament and motor locations from the t=1,000 case for our standard parameter set where the stable aster is already well established. Beginning from this morphology, we changed one parameter that we expected to destabilize the aster based on figure 5.7. We ran the new simulation for the same length of time, t=1,000, and saw that the ending morphologies were likewise destabilized, but all still showed small remnants of the initial aster (fig 5.9A).

The next question was if we could "rescue" or reestablish the aster by starting with morphologies at t=1,000 whose parameters did not end up in a single stable aster (fig 5.7). We then switched the abnormal parameter back to the standard value, ran the sim for t=1,000 and found that all ending morphologies resulted in the single, stable aster (fig 5.9B).

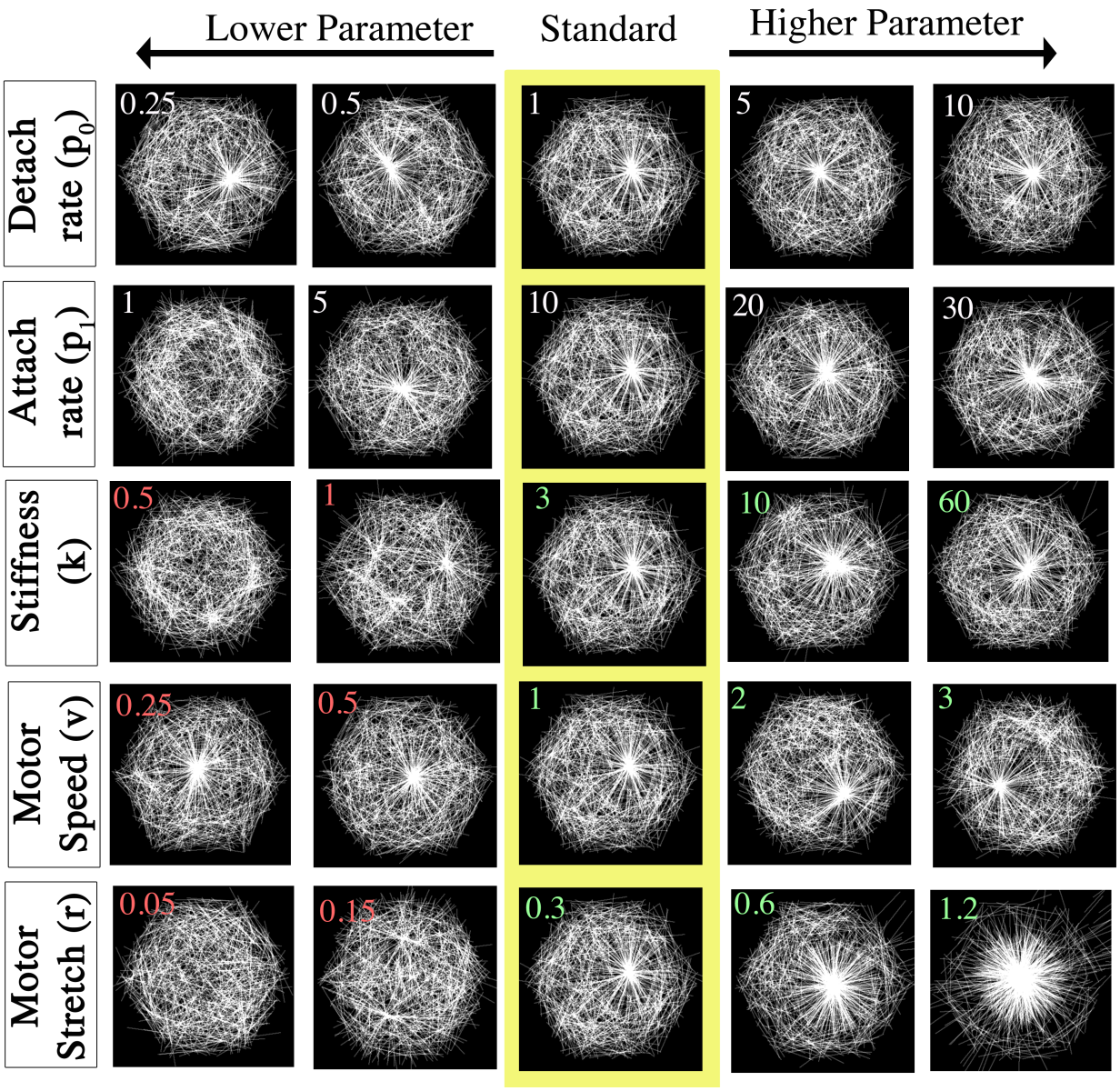

Figure 5.8: **Aster formation as biophysical parameters controlling motors**. The images are the end actin morphology after 1,000 time steps. The yellow box indicates the same ending image for a simulation with the standard set of parameters, but each row depicts a different parameter variable. Each parameter variable starts at a random initial condition, and the end images at t=1,000 are shown here. All biologically relevant parameters are shown in green text, parameters outside the biological range are in red, and parameters for which we have no reference are in white.

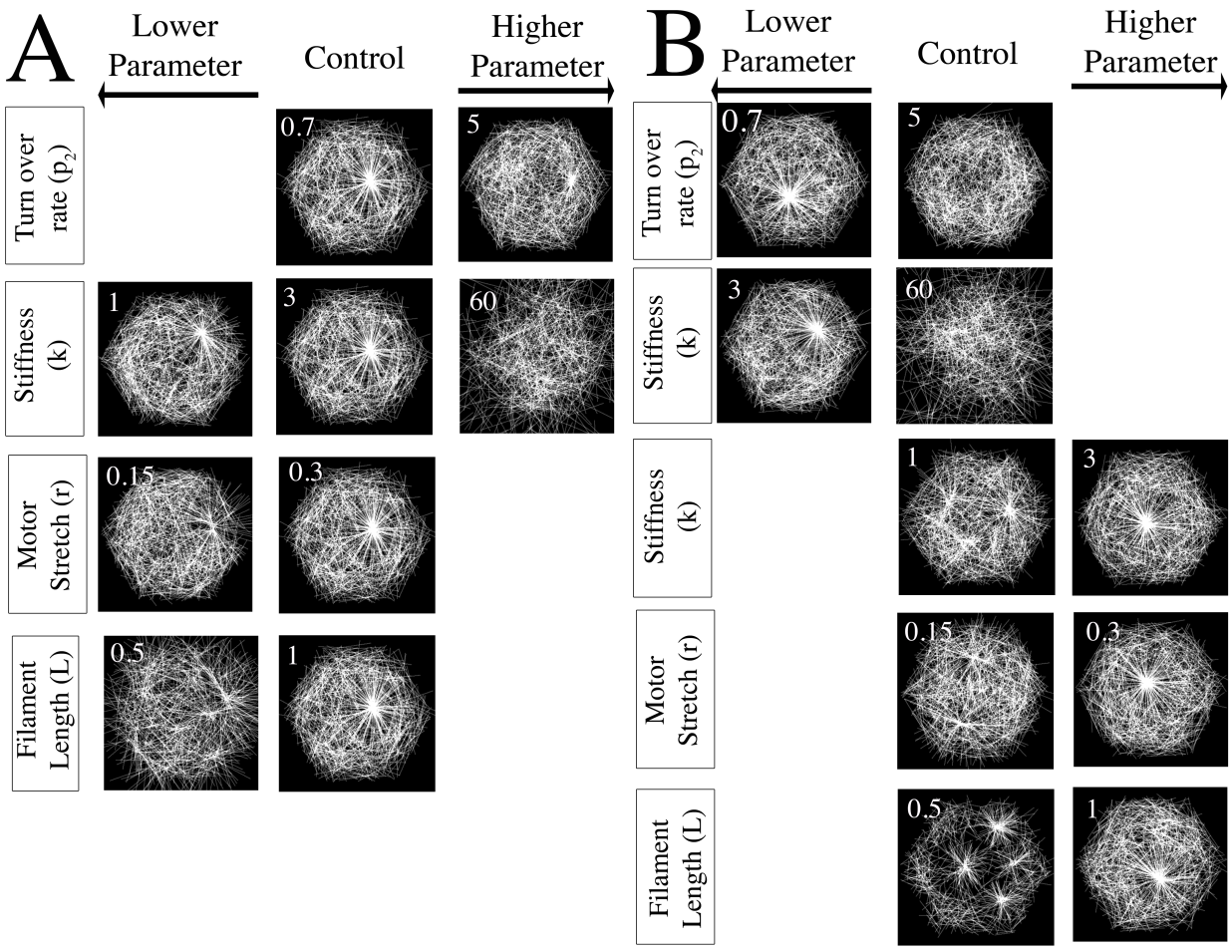

Figure 5.9: **Factors that destabilize or rescue asters**. (A) All simulations started with the morphology for the standard case when t=1,000 (down the center). One parameter was changed, either increasing or decreasing, and the simulation was run for another 1,000 time steps. The ending morphology is shown to the left or right of the center column. (B) Simulations started with the t=1,000 morphology for the center column. The parameter was changed to the standard value in an attempt to rescue the original morphology.

5.3.5 Transmitting force to surrounding cortex

Since the actomyosin contraction correlates to localized changes in cell shape, we wondered if we could incorporate a type of cortex filament (fig 5.10B), similar to the boundary filaments in our sliding model (chapter 4) to act as a type of "sensor" so we could gauge the amount of applied force an aster could generate, and couple the filament to transfer force to a boundary element of the cortical F-actin network to the rest of the cell. We assume that our simulated domain is a small patch of the cell's cortex (fig 5.10A). We simulated sensor filaments whose plus ends are initially placed on the vertices of a polygonal boundary. The sensor filaments are only allowed to slide in or out of the boundary of the polygonal patch based on the forces exerted on them. Motors connect sensor filaments to free filaments in the domain. Therefore, the motor force vector is projected onto the sensor filament so it is parallel to the filament and we assume the cortex filaments do not experience any torque or perpendicular translation. Since sensor filaments should return to the vertices if there are no motors attached, we connect them to the boundary with a spring of stiffness, k_{cortex}. The spring seeks to return the sensor filaments to their initial position. The vector force balance equation for the sensor filament (eqn 16), is simplified from Toyama, et. al [Toyoma et al., 2008] where σ_{cortex} is the stress from the surrounding material around the patch, σ_{free} is the stress from the free filaments inside the patch, b is a viscous term, and v is the speed at which the sensor filament is moving away or toward the vertex point. We can then calculate the change in cortex filament position (eqn 17). Movement of the free F-actin is opposed by viscous drag, b.

The stress within the cortex (eqn 18) is calculated using $Area_{cortex}$, the cross-sectional area of the cortex, or the perimeter of the patch times the thickness (t) of the cortex (fig 5.10A). E is the Young's modulus for reconstituted F-actin gel. Strain is equal to $\frac{\Delta x}{L_0}$, where L_0 is the initial diameter of the free actin domain. If there are N sensor filaments, then the cortex force simplifies (eqn 19) and we can calculate the sensor spring stiffness (eqn 20). If we used a Young's modulus of 100 Pa [Falzone et al., 2012], a cortical thickness of 2 μm, and 6 sensor filaments (hexagonal patch), the stiffness required for a vertex spring is 0.2 nN/μm. The physiological range for k_{cortex} depends on the physiological range of E = 0.03 to 3,000

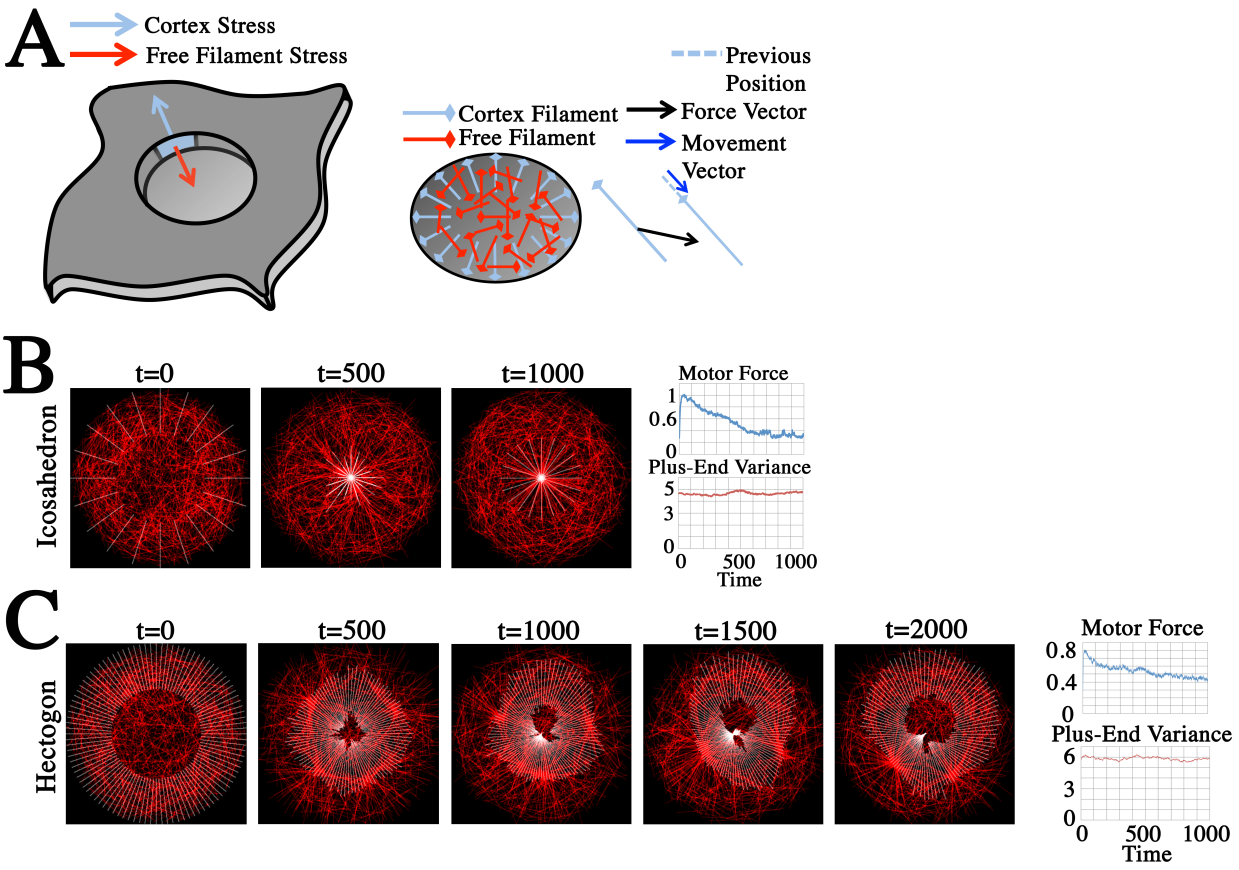

Figure 5.10: **Introducing cortex filaments and multi-sided polygons**. (A) A cartoon explaining the theory behind introducing cortex filaments (blue). The simulation is assumed to be a patch of the entire actomyosin cortex, with cortex filaments (blue) under force conditions analogous to the entire actomyosin cortex. The free filaments (red) are able to move and contract as normal, but the cortex filaments are only allowed to slide in or out when motors exert a force on them. Furthermore, the cortex filaments have plus ends on the boundary, so they are oriented out from the center. (B) Simulating a 20-sided polygon (icosahedron) with 20 cortex filaments (white) simulates a cortex Young's modulus of 1 kPa (table 5.2, eqn 20). (C) Simulating a 100-sided polygon (hectogon) with 100 sensor filaments and a cortex Young's modulus of 1 kPa.

Pa, so the range of stiffness for sensor filaments, k_{cortex}, would need to range from 0.00006 to 6 nN/μm. Since seek to understand how the plus end of the sensor filament moves, we solve for the change in sensor filament plus end from vertex point, Δx (eqn 21), where dx is the current distance from the vertex of the hexagon to the analogous sensor filament's plus end, F_{motor} is the projected force from all attached motors, dt is the change in time step size for the simulation, and L_0 is the initial diameter of the actin domain. We can simplify the equation further using the conclusion from the Gardel group [Falzone et al., 2012], that reconstituted F-actin gels have viscosity, b, 3 fold smaller than the modulus, E (eqn 22). It is not clear if this relation is also true in tissues.

Simulating actomyosin within an icosahedron (20-sided polygon) with a Young's modulus 1 kPa (fig 5.10B), we find actomyosin contracts into a stable aster, with some of the sensor filaments brought into the center with the rest of the free filaments, but not all (fig 5.10B). The force and variance plots appear similar quantitatively to the simulations run without stiff boundaries (fig 5.6D, E). When we increase the number of sides of the polygon and the number of sensor filaments to a hectogon (100-sided polygon), maintaining the same cortex modulus of 1 kPa, we no longer see the stable, single aster (fig 5.10C; Movie F.2). Instead, filaments begin to contract into a ring structure,and bundle. The number of bundles depends on the distance spanned by motors (data not shown) and these bundles align with the plus ends of sensor filaments. We believe we can think of the plus-ends of the sensor filaments as the domain-edge and even the cell-edge if we changed boundary conditions for the free filaments. This observation supports both Rauzi, et al. and Martin, et al.'s observations that the boundary elements can draw asters to the cell edge [Rauzi et al., 2010] and cause the boundary to shorten [Martin et al., 2009].

In our experimental analysis with tissues treated with Latrunculin B (increases F-actin depolymerization), for example, we see filament asters at the boundaries of the cells (fig 5.2F). We see this in our simulation when we reduce the filament length (fig 5.7), which would be analogous to a case when filament depolymerization is high, decreasing the persistence length of F-actin. Furthermore, it suggests that localization of actin binding or stabilizing proteins to specific areas can relocate or even break apart emergent asters.

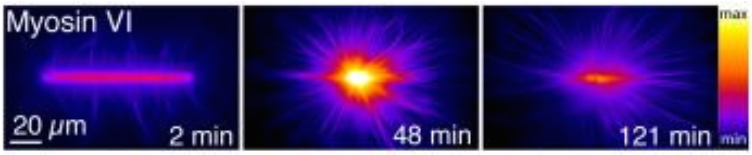

Figure 5.11: **Reconstituted fluorescent actin contracted by myosin VI** Image from Reymann, et al. [Reymann et al., 2012] showing fluorescent actin contracted by myosin VI over time. Actin was micro patterned into a bar shape using an actin nucleating protein stamp. Then a mixture of actin monomers and myosin VI were added. Actin quickly nucleated from the bar pattern, and then myosin VI contracted the actin into an aster structure.

5.3.6 The control of F-actin morphology with patterned substrates

Recent studies examined the dynamic remodeling of F-actin, Myosin VI and II, and actinin within reconstituted gels [Reymann et al., 2012]. They stamped an actin nucleating protein, Wiskot-Aldrich syndrome protein (WASp), onto a micropatterned bar and added G-actin with actin promoting factors to form a dense actin network on the bar with F-actin filaments plus ends on the bar and minus ends off the bar. Then they added myosin and ARP 2/3 to observe the contraction of the bar network. Myosin then contracted the actin network into an aster (fig 5.11). We were able to simulate the experiment and observe similar results (fig 5.12A; Movie F.3). Instead of adding in the complexity of polymerizing F-actin to create the bar geometry, we began with F-actin located within the bar, and a population of filaments with plus ends on the bar and minus ends off of the bar. We then allowed motors to be located over the entire domain (simulating the addition of a myosin solution). We observed that the myosin walks and relocates to the bar area while moving the filaments. Once myosin's were on the bar, they contracted the structure down into an aster.

Reymann, et al. also examined interactions between filaments polymerizing from a rectangular domain of filaments and myosin motors tethered to the substrate. In this case they considered myosin VI. Tethered motors have one "leg" of the motor bound to the substrate

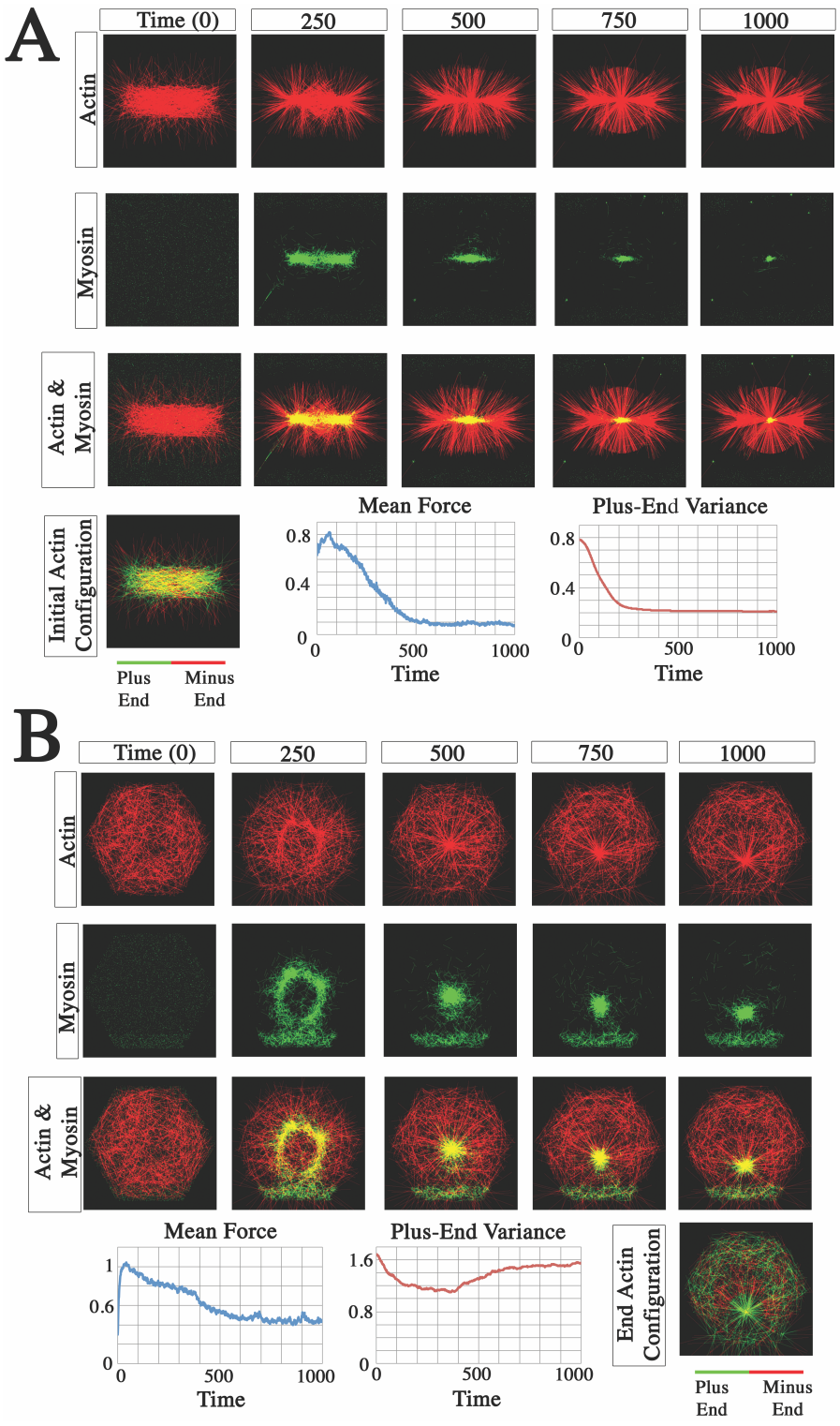

Figure 5.12: **Simulating *in vitro* experiments of purified actin and myosin** (A) A "bar" of actin: The simulation begins with a portion of filaments totally located inside the bar and a portion of filaments with plus ends on the bar and minus ends off of the bar.

Continued on next page

Figure 5.12: *Continued from previous page* Myosin motors begin located over the entire domain. Over time, the myosin motors bind to the filaments and walk towards the plus ends, congregating onto the bar. Once myosin motors are on the bar, they contract the actin network into an aster. (B) Tethered motors: A portion of the motors are "tethered" to the bottom eighth of the hexagon, meaning one leg is fixed into an area in the bottom eight, and the other leg is able to bind to filaments. The rest of the motor population are "loose" across the entire hexagonal domain. Over time, the aster forms as usual, but the tethered motors are able to deplete the bottom portion of the aster, pulling these filaments away.

and the other "leg" free to bind and walk on filaments. They observed that the bar of motors pulled the bar of filaments down to the motor location. We decided to simulate this using our hexagonal boundary, and having a portion of myosin motors tethered (fig 5.12B; Movie F.4). The tethered motors had one leg attached to the substrate in the bottom eighth of the hexagon, and the other leg was free to bind to a filament, move towards the filament plus end, exerting a force, and pulling the filament toward its substrate bound leg. In this case we observe that the free motor network contracts the actin into the characteristic ring and then to the single aster while the tethered motors pull at the actin structure, pulling and depleting the aster at the bottom. This suggests that tethered filaments (e.g. the boundary sensor filaments from fig 5.10) and tethered motors pull and move an aster structure, repositioning the aster to the source of the tether.

5.4 DISCUSSION

Although our simulation implements only simple biophysical interactions of actin and myosin, we are able to capture a range of phenomena observed both *in vivo* and *in vitro*. We demonstrated that by "tuning" parameters for actin and myosin dynamics within their physiological

ranges, we were able to generate different actomyosin morphologies, further supporting the role played by motor activities and F-actin turnover in shaping the actomyosin network.

In vivo, filament movement is primarily due to motors, but filaments can undergo depolymerization. In the cell F-actin can polymerize or depolymerize depending on the concentrations of G-actin and polymerization factors. The structure of the G-actin monomer creates an inherent polarity when the monomers polymerize together and create F-actin. At a critical concentration of G-actin, there is no change in F-actin length. Below critical concentration, F-actin shortens, and above critical concentration F-actin lengthens. In general the polarity of F-actin is defined as a fast growing plus end, and a slow growing minus end [Howard, 2001] (fig 5.4A). *In vitro* experiments have shown that actin monomers experience rapid polymerization at the beginning, but then reach a persistent length once the population of monomers is largely depleted [Alberts, 2008]. The current model assumes the system is at steady state, where G-actin and proteins stabilize the rates of polymerization to maintain filament lengths. We plan to extend the model in the future, however, to include the populations of G-actin monomer and vary filament lengths.

Reconstitued actin gels are able to generate a contraction in the actin network, but the disassembly of the contraction is not understood [Falzone et al., 2012]. Since experimental work for *in vivo* actomyosin show punctuated contractions that assemble and disassemble, understanding the mechanism for disassembly is as important as understanding assembly. Through our simulations of parameter switches (fig 5.9) we have begun to address this question. Running the simulation to a certain point in time, changing a parameter value, restarting the simulation for another period of time demonstrates destabilizing or reestablishing the single aster morphology and occurs on an extremely fast time scale. To consider more physiologically relevant activations of parameter variation, such as increasing the rate of polymerization when myosin density is high, we can extend our model to consider a range of hypotheses concerning filament and motor density activating certain proteins.

By including sensor filaments, we were able to destabilize the single aster, and relocate smaller, bundled asters. Also, we were able to place restrictions on motor location, which causes filaments to be pulled to a different location. Through restrictions placed on filament and motor locations, we were able to disrupt, or relocate the steady state aster morphology.

This result suggests two more mechanisms possibly used by cells *in vivo* to disassemble and relocate the punctuated actin contractions. We would be interested in extending this concept of moving asters to a mechanical regime where an anisotropic force is applied to the cortex boundary and results in a change in steady state morphology. Extending the model in this way would help to address questions of how cells react to externally applied forces and remodel their cytoskeleton accordingly.

Our "steady state" morphology is a radial aster, and although we were able to break apart the aster via parameter changes or different mechanisms, we did not see bundles of parallel arrays of actin, or what we would term co-aligned filaments like we observe experimentally. We can argue that the transitioning ring contraction morphology is a sort of co-aligned structure, like what is observed during the formation and contraction of the cytokinetic furrow, but we did not see a sort of stress-fiber co-alignment. To take this next step in modeling we would need to consider a cross-linking actin binding proteins, such as filamin. We could also consider the nucleating and actin-branching protein ARP 2/3 if we simulated varying filament lengths based on monomer concentrations and (de)polymerization rates. It is reasonable to assume that activation of these proteins (and the rest of the plethora of actin binding proteins) would lead to different, emergent actin morphologies, based on when the activation occurred, how long it lasted, and to what degree it was activated. In the future, we will be considering these additional dynamics and players of the actomyosin system but maintain our philosophy that the addition of these dynamics and proteins will be a simple emergent morphology.

6.0 BIOMECHANICS AND THE THERMOTOLERANCE OF DEVELOPMENT

The purpose of this study was to examine the role that temperature plays in development. Dr. von Dassow began examining the temperature effects on *Xenopus laevis* embryos within the physiological range (16° to 26°C) and observed that the bulk mechanical properties of the embryos did not change, however, the reaction to electrically induced contraction decreased at lower temperature. I was brought onto the project to image and analyze actomyosin contractions at the low, room, and high temperatures. I found that the duration of actomyosin contractions increased at low temperature compared to high, however, there was also a population of short duration contractions at low temperatures that was absent from both room and high temperature data. This study was published in PLoS One in April 2014 [von Dassow et al., 2014].

6.1 ABSTRACT

Successful completion of development requires coordination of patterning events with morphogenetic movements. Environmental variability challenges this coordination. For example, developing organisms encounter varying environmental temperatures that can strongly influence developmental rates. We hypothesized that the mechanics of morphogenesis would have to be finely adjusted to allow for normal morphogenesis across a wide range of developmental rates. We formulated our hypothesis as a simple model incorporating time-dependent application of force to a visoelastic tissue. This model suggested that the capacity to maintain normal morphogenesis across a range of temperatures would depend on how both tissue vis-

coelasticity and the forces that drive deformation vary with temperature. To test this model we investigated how the mechanical behavior of embryonic tissue (*Xenopus laevis*) changed with temperature; we used a combination of micropipette aspiration to measure viscoelasticity, electrically induced contractions to measure cellular force generation, and confocal microscopy to measure endogenous contractility. Contrary to expectations, the viscoelasticity of the tissues and peak contractile tension proved invariant with temperature even as rates of force generation and gastrulation movements varied three-fold. Furthermore, the relative rates of different gastrulation movements varied with temperature: the speed of blastopore closure increased more slowly with temperature than the speed of the dorsal-to-ventral progression of involution. The changes in the relative rates of different tissue movements can be explained by the viscoelastic deformation model given observed viscoelastic properties, but only if morphogenetic forces increase slowly rather than all at once.

6.2 INTRODUCTION

Developing organisms encounter variable environmental conditions. They may be exposed to environmental toxins, limited nutrients, extreme temperatures, etc. We are particularly interested in one of these environmental factors, temperature, since temperature extremes can result in a diverse sent of birth defects [Edwards, 2006, Banhidy et al., 2005, Moretti et al., 2005, Miller and Church, 2013]. High fever is one of the largest risk factors leading to birth defects. Fevers as high as 38.9°C during the first month of pregnancy have been linked to defects observed in animal models [Graham et al., 1998]. Since the timing of exposure correlates to early morphogenetic movements that shape the body plan of the early embryo, we considered the role of temperature in the biomechanics of these early movements in the frog *Xenopus laevis*.

The most surprising aspect of temperature is not that it causes defects, but that many ectothermic animals develop normally across a wide permissive range of temperatures. However, the frequency of developmental defects jumps to 100% above or below this range [Bachmann, 1969, Schirone and Gross, 1968, Bingham et al., 1997, van der Have, 2002]. Within

the permissive range, developmental rates can vary by more than three-fold with temperature, with little change in the frequency of defects. Most studies indicate little or no change in the frequency of defects. Most studies indicate little or no change in the relative timing of morphogenetic events as developmental rate varies [Atlas, 1935, Ryan, 1941, Tyler, 1936, Fujisawa, 1993, Jarosik et al., 2004, Kimmel et al., 1995, Stephens, 1972], although differences in the temperature dependence of cleavage stages and embryo mic morphogenesis have been observed [Schirone and Gross, 1968, Ryan, 1941]. To understand why development fails at high and low temperatures, we need to understand the mechanisms that prevent it from failing, despite dramatic variation in developmental rate, across intermediate temperatures.

Temperature is a key regulator of rates of chemical and biological processes during development. Much of this variation can be understood in the temperature dependence of chemical reaction rates such as the rate of the ATPase activity, the rate of myosin cross bridge cycling [Kawai et al., 2000, Rall and Woledge, 1990] or the rate of exchange of GDP for GTP on actin monomers and the rates of actin polymerization. Temperature dependence of diffusion may also regulate cellular processes such as signaling and the assembly of multi-protein complexes. Rates of simple reaction and diffusion processes vary smoothly with temperature but complex events, such as progression through the cell cycle, often do not [Chan et al., 2010].

We hypothesized that coordinating the biochemical processes of patterning with the mechanical processes of tissue deformation and movement is crucial to maintaining normal morphogenesis across the permissive temperature range [von Dassow and Davidson, 2011]. Since morphogenesis requires both forces to deform tissues and the establishment of stiff tissues to limit or resist deformation [Davidson, 2011], we propose that the rate of morphogenetic movements should depend on the forces driving the movement, the viscoelastic resistance of the embryonic tissue, and the actomyosin contractility underlying these physical processes. Both cellular force generation and viscoelasticity are strongly dependent on temperature [Evans and Yeung, 1989, Liu et al., 2007, Mitchison and Swann, 1954, Norris, 1940, Picard and A., 2009, Rico et al., 2010, Sung et al., 1982, Sunyer et al., 2009, Yoneda, 1976, Kieβling et al., 2013]. For example, cultured human alveolar epithelial cells are much stiffer and more solid-like, while exerting twice the traction forces, at 37°C than at 13°C

[Sunyer et al., 2009]. Therefore, we expected that temperature dependence of developmental rate would require fine control of the mechanics of the embryonic tissue. In this study we formulate biomechanics models of the temperature dependence of morphogenesis and test both the assumptions and consequences of those models within a temperature range that permits normal development.

Gastrulation is one of the earliest and most significant morphogenetic movements in vertebrate development (Movie G.1). In the frog, *Xenopus laevis*, gastrulation integrates the action of multiple cell behaviors, including epiboly, involution, convergent extension, and convergent thickening, to close the blastopore over the endoderm and establish the archetypical body plan consisting of the three primary germ layers [Keller and Shook, 2004]. The stages of gastrulation are marked by: 1) constriction of bottle cells to encircle the yolk plug; 2) formation of a groove at the site of bottle cell contraction, initially at the dorsal-anterior end of the yolk plug, and progressing to the ventral-posterior end of the yolk plug; 3) initial involution at the dorsal anterior end of the blastopore lip spreading to the ventral-posterior lip; and 4) closure of the blastopore [Nieuwkoop and Faber, 1967]. Blastopore closure often fails when cell motility, cell adhesion, or the cytoskeleton are perturbed. We investigate the temperature dependence of blastopore closure because these movements are easily visualized and exhibit clear milestones.

Biomechanical contributions to the temperature dependence of developmental rate appear necessary to explain how tissue movements and deformations are coordinated with molecular patterning processes within the permissive temperature range. Many other molecular and cellular processes may influence the temperature dependence and temperature limits of development. These include the temperature dependence of cell-cycle regulation [van der Have, 2002] or membrane fluidity [Nelson et al., 1982], excessive apoptosis at high temperatures and/or limits to protection by heat shock proteins and other pathways that protect against cell damage [Edwards, 2006, Mirkes et al., 1997, Hosako et al., 2009, Podolsky, 2003]. Here we focus solely on biomechanics and variation in developmental rates over the permissive temperature range.

6.3 RESULTS

6.3.1 Changes in viscoelasticity and force generation

To understand the dependence of morphogenesis on temperature we first developed a simple, generalized model (Model 6.5.5.1; Text G.3.1) to predict expected changes in tissue viscoelasticity and force generation with temperature. We then tested the model's assumptions and predictions using micro aspiration to measure tissue viscoelasticity, and electrically induced contractions to measure force generation (Fig. 6.1A-D) [von Dassow et al., 2010]. Even without considering the complexities of cell adhesion, cell signaling, cytoskeletal dynamics, etc., a three dimensional (3D), non-linear, large-deformation viscoelastic model would involve large numbers of poorly constrained parameters. This would limit its predictive value. A simplified linear, small deformation model allows us to incorporate the essential features (temperature dependence of deformation rates, forces, and viscoelasticity) with a minimum of parameters, all of which can be experimentally constrained.

We formulated our initial model by assuming that the relative timing and magnitude of tissue deformation is identical at different temperatures (Model 6.5.5.1). This is based on the observations that different developmental stages look similar at different temperatures within the permissive range, and that the proportion of time spent in each stage is similar at different temperatures (e.g. [Atlas, 1935]). Thus, we assumed that stages define a temperature-independent "developmental time" that is proportional to clock time through a temperature-dependent constant (see Model 6.5.5.1, eqn.6.5 for definition). For the same reason, we assume that the relative timing of gene expression and protein activation are identical at different temperatures. Furthermore we assume that the timing and magnitude of force generation scales uniformly with temperature: forces exerted by the tissues vary the same way with stage at every temperature, except for possibly a temperature-dependent proportionality factor. This assumption is biologically plausible since we assume force production is controlled by changes in gene expression and protein activity, the timing of which we already assumed varies uniformly with temperature. Furthermore, there are a small number of proteins that contribute to generating force in the embryo (primarily actomyosin

complexes [Lecuit et al., 2011, Zhou et al., 2009]) and it is parsimonious to assume that these proteins are affected by temperature in the same way in every cell. Making these assumptions allows us to predict how the viscoelastic properties should change with temperature over the permissive range (Model 6.5.5.1: eqns. 6.14 & 6.15). Specifically, we predicted that the exponent (β; see Table 6.1 for a list of symbols) in the power law model of viscoelasticity (eqn. 6.13) should be independent of temperature. This parameter indicates whether the tissue behaves more like a solid ($\beta = 0$) or a fluid ($\beta = 1$).

We tested the prediction that β is independent of temperature using microaspiration, and then tested our assumption that deformations during induced contractions (Fig. 6.1) and normal gastrulation are independent of temperature. We performed microaspiration at 16°C and 26°C and fitted the deformations to a power law model of viscoleasticity (eqn. 6.1) to estimate β and $J[1]$ (the compliance- the proportionality between strain and stress - at 1 second after stress is applied). The temperature dependence of cell stiffness and force generation depends on myosin activity in human alveolar epithelial cells [Sunyer et al., 2009]. Therefore we tested for effects of inhibiting myosin contractility by applying blebbistatin at these two temperatures.

Consistent with the prediction of our model, there was little or no change in β with temperature (Fig. 6.1E; Tables 6.2 &6.3), whereas incubation of the embryo in blebbistatin increased β slightly but statistically significantly, indicating that inhibiting myosin contractility made the tissue slightly more fluid-like (Fig. 6.1E, Table 6.2). The interaction between temperature and blebbistatin treatment was not statistically significant for β (Table 6.2).

Our model assumes that the large scale deformations of morphogenesis are independent of temperature (eqn. 6.6). Therefore, we expected that small scale deformations associated with cell contractions should also be independent of temperature. To test this in a controlled manner, we electrically induced contractions of tissues in the channel of the microaspirator. Contrary to our predictions, the magnitudes of contractions were reduced by 44% at 26°C compared to contractions at 16°C (Fig. 6.1A, F; Tables 6.2 & 6.3). Contractions lasted 3.4 times longer at 16°C than at 26°C (Fig. 6.1A & G; Tables 6.2 & 6.3). Blebbistatin did not significantly affect contraction magnitude or duration (Fig. 6.1F-G, Table6.2).

Table 6.1: Symbols

Symbol	Description
c	Proportionality between stress at T_2 and stress at T_1 in generalized model
f	Peak apical tension during contraction
h	Duration of apical tension during contraction
J	Compliance: relates strain and stress as a function of time since stress application
k	Hypothetical constant of proportionality between peak apical tension and stress driving blastopore closure
R_{CP}	Relative duration of blastopore closure to progression of involution: t_C/t_P
t	Clock time
T	Temperature
t_C	Time for blastopore closure
t_P	Time for dorsal-ventral progression of involution
w	Slope of stress in ramp model
α	Proportionality between developmental time and clock time in generalized model
β	Exponent that determines time dependence of compliance
ϵ	Strain ($Ln[L/L_0]$), a non-dimensional measure of deformation
σ	Stress (force/area)
τ	Developmental time in generalized model (Model 6.5.5.1)

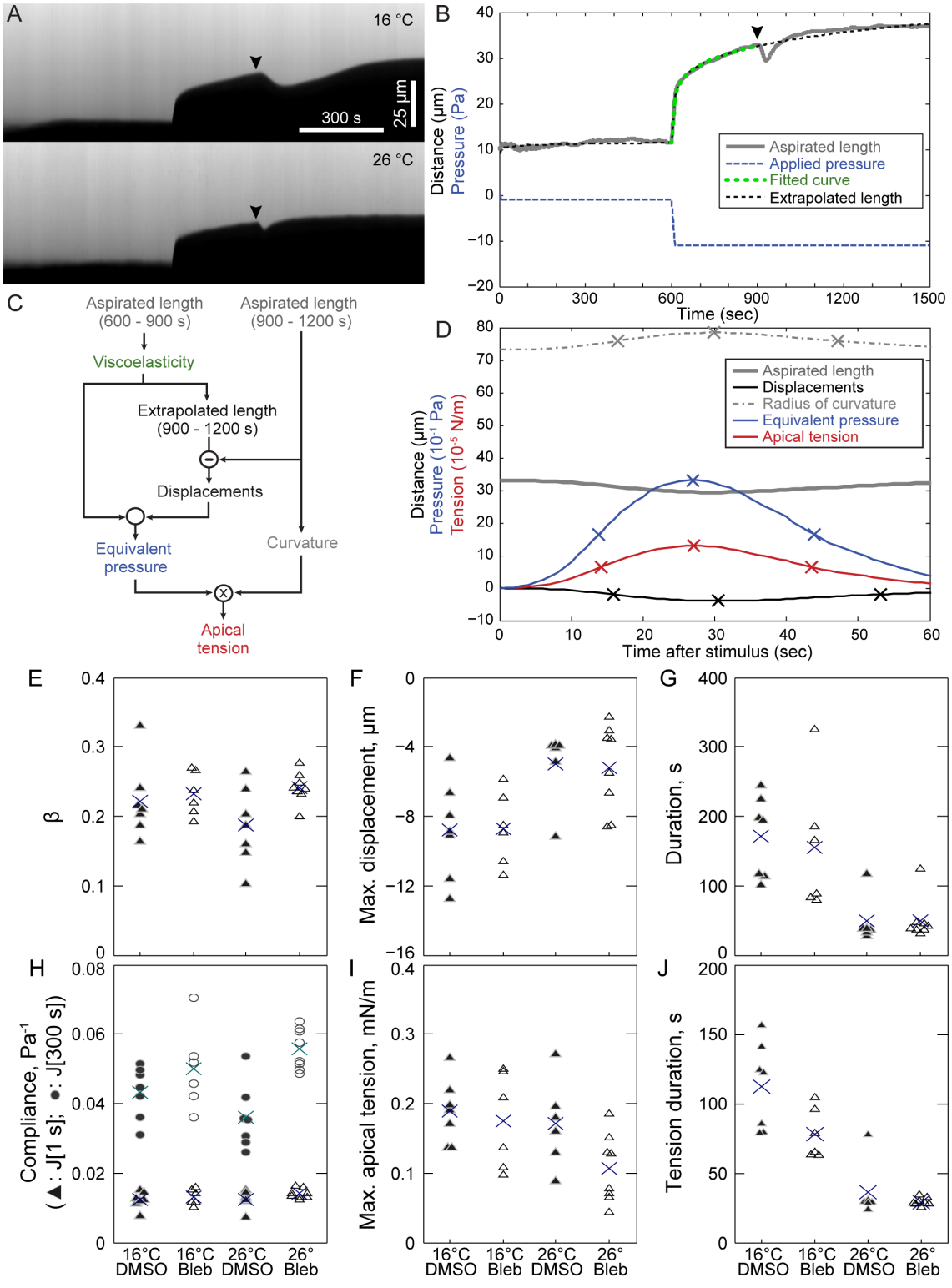

Figure 6.1: **Temperature dependence of compliance and strength of induced contraction** Representative kymographs of microaspiration with electrically induced contractions at 900 seconds at 16°C (upper) and 26°C (lower). *Continued on next page*

Figure 6.1: *Continued from previous page* (B) Fit of power law viscoleastic model to the aspirated length from 600 to 900 s for the 26°C case. (C) Flow chart for analysis of contractions. (D) Contraction analysis. 'X's indicate half-max, max, and return to half-max for each curve. Panels B and D show data from the lower embryo in A. Arrowheads in A and B indicate electrical stimuli. (E) β (F) maximum displacement during induced contraction, (G) duration (half-maximum until return to half-maximum displacement) of contraction, (H) compliance at 1 s (triangles) and at 300 s (circles), (I) maximum apical tension during induced contraction, (J) duration of apical tension. Triangles and circles: individual embryos; X's: means.

In contrast to results from studies with human cells [Sunyer et al., 2009], temperature had little effect on the compliance of the tissue ($J[1]$ or $J[300]$; Fig. 6.1A, H, Tables 6.2 & 6.3). Blebbistatin did not significantly affect the compliance at 1 second, but - due to the change in β- it did increase compliance at 300 s (Fig. 6.1H, Table 6.2). The interaction between temperature and blebbistatin treatment was statistically significant for $J[300]$, though not for $J[1]$ (Table 6.2). Therefore, myosin activity may influence the temperature dependence of stiffness in the system.

From the contraction profiles we can calculate the forces driving induced contractions based on the viscoelastic properties of the tissue (Fig. 6.1B-D; [von Dassow et al., 2010]). Previous results suggest that these forces are best described as apical tensions [von Dassow et al., 2010]. Note that our method for calculating apical tensions assumes that the compliance does not change during contractions. We have been unable to test this so far because contractions are transient. However, neither the calculated tensions nor the viscoelastic parameters varied significantly with temperature. Therefore, it is parsimonious to assume that temperature does not substantially affect the true tension or compliance during contractions.

The peak apical tension was not significantly affected by temperature (Fig. 6.1; Tables 6.2 & 6.3). The higher contraction speed, but unchanged viscoelasticity and unchanged

Table 6.2: ANOVA table for viscoelasticity and contractions.

	temperature	media	clutch	temperature*media	temperature*clutch	media*clutch
β	P=0.7	*P=0.034*	P=0.4	P=0.18	P=0.3	P=0.8
	$F_{1,5,1}$=0.170	$F_{1,5,3}$=8.09	$F_{5,1,8}$=2.16	$F_{1,9}$=2.17	$F_{5,9}$=1.53	$F_{5,9}$=0.511
Max. Contraction	***P=0.029***	P=0.8	P=0.8	P=0.9	P=0.12	P=0.14
	$F_{1,5,0}$=9.107	$F_{1,5,0}$=0.0589	$F_{5,5,9}$=0.434	$F_{1,8}$=0.0378	$F_{5,8}$=2.47	$F_{5,8}$=2.34
Ln[Duration]	***P=0.0025***	P=0.8	P=0.8	P=0.6	P=0.3	P=0.4
	$F_{1,5,0}$=31.0	$F_{1,5,0}$=0.0716	$F_{5,3,2}$=0.496	$F_{1,8}$=0.287	$F_{5,8}$=1.50	$F_{5,8}$=1.13
J[1]	P=0.7	P=0.078	P=0.3	P=0.6	P=0.5	P=0.6
	$F_{1,5,1}$=0.131	$F_{1,5,2}$=4.81	$F_{5,1,4}$=3.39	$F_{1,9}$=0.288	$F_{5,9}$=1.02	$F_{5,9}$=0.762
J[300]	P=0.9	***P=0.020***	P=0.4	**P=0.024**	P=0.3	P=0.080
	$F_{1,5,1}$=0.0075	$F_{1,5,0}$=11.3	$F_{5,5,2}$=1.2	$F_{1,9}$=7.33	$F_{5,9}$=1.52	$F_{5,9}$=2.87
Max. Apical Tension	P=0.14	P=0.3	P=0.8	P=0.21	P=0.3	P=0.15
	$F_{1,5,0}$=3.05	$F_{1,5,0}$=1.64	$F_{5,4,7}$=0.409	$F_{1,8}$=1.83	$F_{5,8}$=1.47	$F_{5,8}$=2.21
Ln[Tension Duration]	***0.0006***	P=0.094	P=0.9	P=0.4	P=0.20	P=0.4
	$F_{1,5,0}$=57.4	$F_{1,5,0}$=4.25	$F_{5,3,6}$=0.297	$F_{1,8}$=0.961	$F_{5,8}$=1.88	$F_{5,8}$=1.08

P values and corresponding F values (with degrees of freedom determined by Matlab). "Temperature" and "media" (blebbistatin vs. DMSO control) were treated as fixed factors; "clutch" was a random factor. Statistically significant entries in bold.

Table 6.3: Temperature dependence of mechanical and morphogenetic parameters

Process	Parameter (X)	X(16°C)/X(26°C) (LB, UB)[1]
Morphogenesis	t_C (time for blastopore closure)	**2.73** (2.29, 3.26)**
	t_P (time for dorsal to ventral progression of involution)	**3.29** (2.75, 3.94)**
	R_{CP} (t_C/t_P)	**0.83** (0.72, 0.94)**
Viscoelasticity	Compliance $J[1]$	0.98 (0.85, 1.13)
	Compliance $J[300]$	1.02 (0.9, 1.16)
	β	1.04 (0.88, 1.24)
Simulated contractions	Contraction Duration	**3.36** (2.23, 5.06)**
	Contraction Magnitude	**1.75* (1.29, 2.38)**
	Tension duration (h)	**2.85** (2.26, 3.6)**
	Peak Apical Tension (f)	1.37 (0.98, 1.94)
Endogenous actin dynamics	Duration[2]	**1.32** (1.10, 1.57)**

$^*P \leq 0.05$; $^{**}P \leq 0.01$; Significant difference between 16 and 26°C for log transformed parameters.

[1]Estimated mean and confidence interval for log-transformed parameters were determined using ANOVA (mechanics and actin) and Tukey's honestly significant difference criterion, or T-tests (morphogenesis).

Values were then transformed back to a linear scale to provide estimates of the lower and upper bounds (LB, UB) on the ratio. To obtain confidence bounds here, we used ANOVA with temperature treatment as a categorical variable, and explant as a random factor; clutch was excluded because it was non-significant.

[2]Comparing 17° and 27°C. Ratios for the durations of actin contractions were 0.9 between 16.9°C and 21.3°C, and 1.5 between 21.3°C and 26.7°C.

peak force, drive the decrease in contraction magnitude at higher temperature. The small reduction in apical tension and tension duration in blebbistatin treated embryos was not statistically significant (Fig. 6.1I-J, Table 6.2). The molecular mechanisms responsible for contraction in response to electrical stimulation in these tissues have not been elucidated, and may depend more on F-actin polymerization-dependent changes in membrane tension [Lieber Arnon et al., 2013] than myosin-mediated contractility.

6.3.2 Temperature dependence of morphogenesis

Given the failure of our prediction that contraction magnitudes would remain unchanged with temperature, we tested our assumption that the relative timing of morphogenetic events is independent of temperature (Model 6.5.5.1, eqn. 6.5). To test this we measured how the ratio of the durations of two morphogenetic processes changed with temperature. While chosen primarily due to the clarity of their beginning and end points, these two processes- blastopore closure, and the dorsal-to-ventral progression of superficial involution (Fig. 6.2A; Movie G.1)- also reflect distinct processes. Blastopore closure involves large scale tissue movements, whereas superficial involution is much more local, and likely represents the timing of signaling events that trigger changes in cell behaviors. Therefore the dorsal-to-ventral progression of involution reflects the difference in timing of cell behaviors between the dorsal and ventral side (Fig. 6.2A).

Contrary to our assumptions, the relative durations of different morphogenetic movements varied with temperature. The time (t_p) between the beginning of involution on the dorsal side and the beginning of involution on the ventral side was 3.3 times longer at 16°C ($n = 8$ clutches) than at 26°C ($n = 7$ clutches). However the time (t_C) between the beginning of dorsal involution and the completion of blastopore closure was only 2.7 times longer at 16° than 26°C. These changes in the timing of developmental events were similar to the changes in duration of induced contractions (Fig.6.1G). The relative duration of blastopore closure (R_{CP}), measured as the ratio of t_C to t_P, was significantly reduced at lower temperature, from 2.55 ±0.29 at 26° to 2.11±0.27 at 16°C (mean ± SD; Fig. 6.2B; $P = 0.01$; t-test; Table 6.3).

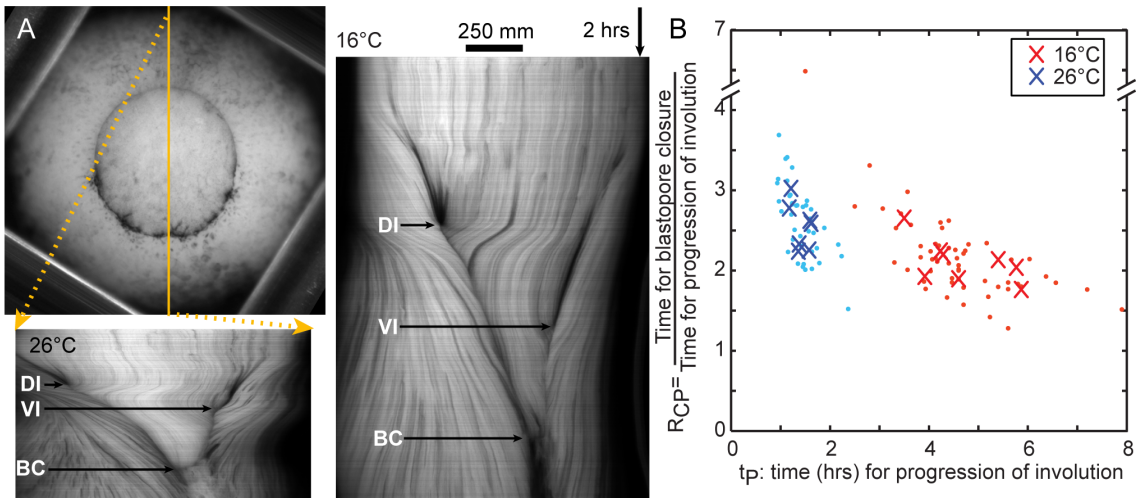

Figure 6.2: **Blastopore closure at high and low temperatures.** (A) Upper: vegetal view of an embryo showing the blastopore soon after the start of dorsal superficial involution. Lower left: kymograph of blastopore cosure at 26°C, taken along the yellow line from the dorsal side to the ventral side, showing the points when dorsal (DI) and ventral (VI) superficial involution begin, and when the blastopore closes (BC). Right: kymograph taken along a line from the dorsal to the ventral side at 16°C. (B) the ratio (R_{CP} of the time for blastopore closure to the time for dorsal-to-ventral progression of involution versus the time (t_P) for dorsal-to-ventral progression of involution. Dots indicate embryos. X's indicate medians for clutches (4 to 8 embryos each).

6.3.3 The role of the time dependence of force generation

We were curious whether the viscoelastic model of morphogenesis could explain the effect of temperature on the relative durations of developmental processes, specifically on R_{CP}. Here we relax the assumption that all developmental processes follow the same clock. We assume instead that "patterning", including all the molecular processes driving changes in cell behaviors, follows one clock, but that large scale morphogenetic movements deviate from the timing of patterning due to tissue viscoelasticity.

To investigate how the dependence of force production on developmental time might alter the temperature dependence of morphogenesis, we compared two specific variants of the linear viscoelastic model (Models 6.5.5.3 & 6.5.5.4). In the step model we assumed the force driving blastopore closure turns on all at once at the beginning of blastopore closure, immediately reaching a peak force and remaining there. In the ramp model we assumed that the forces driving blastopore closure increased gradually with a constant slope, and that the slope was proportional to the rate of patterning. We assume that all cellular responses including gene activation, and cell behaviors, follow the same clock. Blastopore closure is thought to be driven in large part by convergence and extension of the mesoderm, which pulls the ectoderm over the embryo as the mesoderm shortens laterally [Keller and Shook, 2008]. The mediolateral cell intercalation behaviors that drive this do not occur simultaneously throughout the dorsal mesoderm, but instead start and spread progressively [Shih and Keller, 1992]. Therefore we might expect that the forces driving blastopore closure ramp-upwards with time (Fig.6.3A). In both the step and ramp models, we assumed that temperature had the same effect on cell-generated forces driving blastopore closure as it does on the induced contractions.

In these more specific versions of the general model we made the following simplifying assumptions which tie it to our experimental measurements, leaving no free parameters. We assumed that the progression of superficial involution reflects the timing of patterning events rather than mechanical events. Superficial involution is a localized phenomenon and normal dorsal to ventral progression of superficial involution can be reversed by placing embryos in temperature or oxygen gradients [Black, 1989, Black et al., 1996]. These obser-

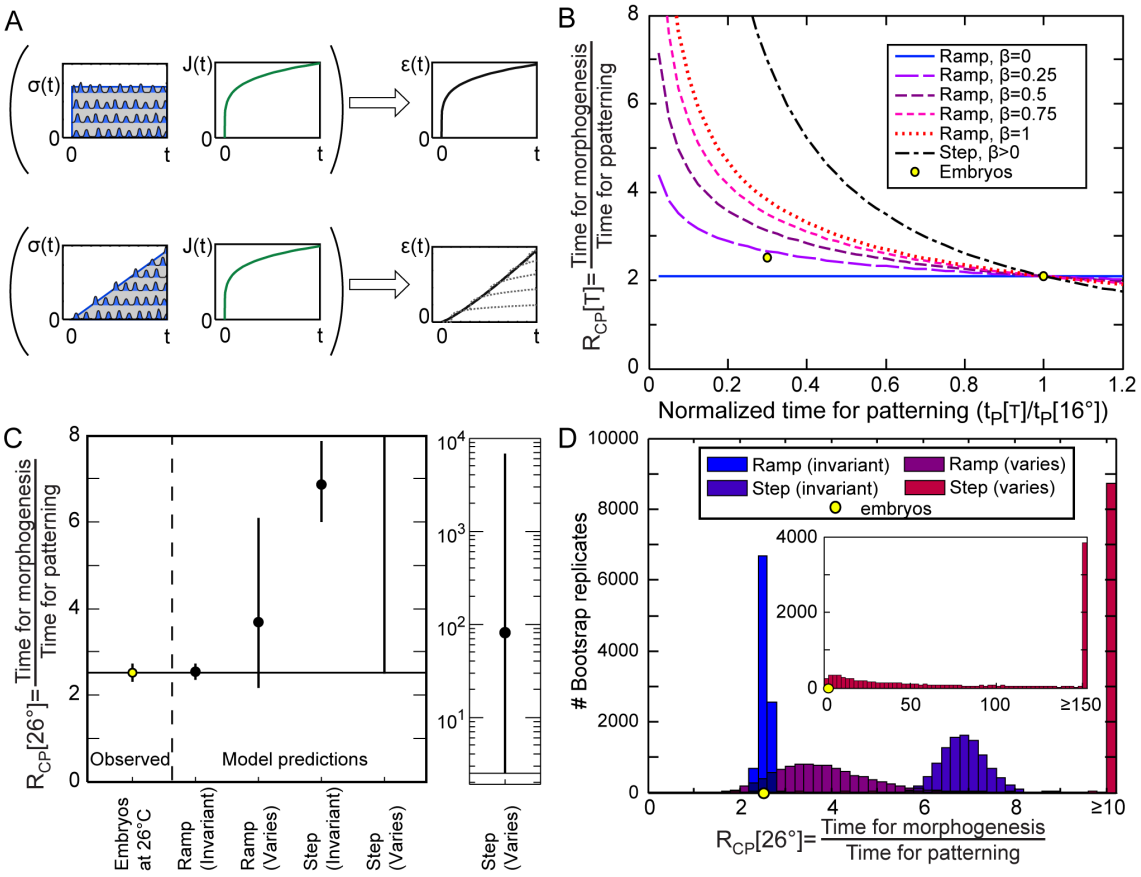

Figure 6.3: **Comparison of viscoelastic models of morphogenesis for ramped versus stepped forces.** (A) Diagram of model. Summed contractions (wavy lines) average out to stepped or ramped stresses (σ) depending on when cells begin contracting. When applied to the viscoelastic material with compliance $J[t]$, the deformations (strains, ϵ) follow the time course of ramped forces more closely than stepped force. This can be visualized as adding up strains due to a series of stepped forces applied over time (dotted lines on right). (B) Predictions for R_{CP}, the ratio of the time for morphogenesis (blastopore closure) to the time for patterning (D-V progression of involution), as a function of the time for patterning at temperature T, normalized to the time for patterning at 16°C, for ramped vs. stepped models for different values of β. Yellow dots: grand mean of experimentally observed values. The curves automatically converge to the right hand dot (at 16°C) where $T_2 = T_1$ since t_C at T_1 is used to calculate R_{CP} at T_2. *Continued on next page*

Figure 6.3: *Continued from previous page* (C) Comparison of the observed R_{CP} at 26°C to the predictions for models with ramped or stepped forces, and with temperature invariant or varying mechanical properties (inset: prediction for stepped force model with temperature dependent mechanical properties on a log scale.) Error bars indicate confidence intervals. (D) Histogram of bootstrap resampling estimates of R_{CP} at 26°C for each model (10,000 resamples total).

vations suggest that progression of involution from the dorsal to the ventral side does not involve large scale mechanical interactions around the embryo, but is tied to the local rate of cellular differentiation. Given this assumption, the rate of patterning (e.g. the timing of when cells begin force-generating behaviors) is inversely proportional to the time for the dorsal-to-ventral progression of involution (t_p). We approximated the complex movements of blastopore closure with a one-dimensional (1D), linear viscoelastic model (Text G.3.1). Additionally, we assumed that the viscoelastic parameters measured by micro aspiration (5 minute time scale) could describe viscoelasticity at the time scales of morphogenesis (2 to 6 hrs). Finally, we assumed, based on the lack of statistically significant effects from our microaspiration and induced contraction experiment, that β, $J[1]$, and the magnitude of cell generated force are unaffected by temperature.

With these assumptions, the step model with invariant mechanical parameters, predicts that the time for blastopore closure (t_C) would be independent of the time for progression of involution (t_P) since neither the force nor the viscoelasticity change. Therefore R_{CP} would increase rapidly as t_P goes down (Fig. 6.3B): at low temperatures the blastopore would close quickly relative to the propagation of cell behaviors driving involution. In addition, R_{CP} would be independent of the how solid or fluid the tissue is (the value of β; Fig. 6.3B). The predicted value of R_{CP} for the step model at 26°C (based on the ratio at 16°C) is much higher than the experimentally observed value (Fig.6.3C).

By contrast, the ramp model predicts a much weaker dependence of R_{CP} on t_P. Because the driving force increases with time more slowly when t_P is larger than when t_P is small, t_C increases with t_P (Fig.6.3B). In addition, the dependence of R_{CP} on t_P varies strongly with the value of β, i.e. with how solid-like or fluid-like the tissue is (Fig. 6.3B). Using the average value of β for the DMSO control embryos at both temperatures (Fig. 6.1E), and the value of R_{CP} at 16°C, the predicted value of R_{CP} at 26°C is surprisingly close to the observed value (Fig. 6.3C).

The absence of statistically significant effects of temperature on mechanical parameters measured by micro aspiration and induced contraction does not mean that the observed differences are not real. Including our observed values of each mechanical parameter for each temperature (From the DMSO controls) substantially changes the outcome of the model. When mechanical parameters vary with temperature, the ramp predicts a higher than observed R_{CP} at 26°C (Fig. 6.3C). However, it is still closer to the observed value than for the step model, and the bootstrap confidence intervals overlap the observed value. When mechanical parameters vary with temperature, the step model predicts an extremely high R_{CP} at 26°C, although the broad confidence interval includes the observed value (Fig. 6.3C). Furthermore, we note that the step model is extremely sensitive to variation in mechanical parameters, much more so than the ramp model (Fig. 6.3C-D). Given observed levels of variation in mechanical parameters, the step model predicts larger variation in R_{CP} at 26°C (Fig. 6.3D) than we observed in live embryos (Fig. 6.2B).

6.3.4 Temperature regulates duration of punctuated F-actin contractions

Recent reports of actomyosin dynamics during morphogenesis (see review [Gorfinkiel and Blanchard, 2011a]) and a previous report by our group that electrically induced contractions are accompanied by a phase of F-actin remodeling [Joshi et al., 2010] suggested that actomyosin dynamics might underlie the complex dependence of morphogenesis on temperature. Furthermore, cortical F-actin dynamics have been implicated in regulating both cell behaviors and biomechanics properties of *Xenopus* embryos at these stages [Zhou et al., 2009, Kim and Davidson, 2011, Zhou et al., 2010b, Skoglund et al., 2008]. Due to technical challenges

in recording actomyosin dynamics during micro aspiration we investigated actin contractions in the basal cell cortex of ectodermal explants (e.g. animal cap explants). To understand how temperature regulates these dynamics we collected time-lapse sequences of punctuated actin contractions within isolated animal cap explants cultured on fibronectin-coated glass (Fig. 6.4A). We confirmed the incidence of actin contractions in animal caps at 21.3°C (room temperature) as well as at 16.9°C and 26.7°C (Fig. 6.4B). Single confocal images did not reveal differences in the qualitative appearance of cortical F-actin across this range of temperatures but time-lapse sequences highlighted consistent retardation of F-actin dynamics at low temperatures and acceleration at high temperatures (see Movie G.2).

Quantitative analysis of the duration of F-actin contractions across three temperatures reveal how dynamics of these contractions change as temperatures either increase or decrease from room temperature. As the temperature was reduced from 26.7 to 21.3°C the average duration of contractions increased from 92 seconds (+/-34 seconds; $n = 113$) to 122 seconds (+/-37; $n = 114$; Fig. 6.4B). Surprisingly, as the temperature was reduced further, from 21.3 to 16.9°C, the average duration remained essentially unchanged (199 +/- 58 seconds; $n = 124$). The non-linear effects of temperature on contraction duration were statistically significant (Table 6.4; clutch- embryos from the same male and female frog). Further analysis of the cumulative distribution for contractions at these three temperatures revealed that the low temperature regime was marked by the addition of many short duration contractions (Fig. 6.4C). By contrast, the distributions of contraction durations at 21 and 26°C were qualitatively similar, albeit time-shifted by a factor of 1.5. We suspected that these short duration contractions might not have been observed at 26.7°C; however, our observations at 21.3°C would have revealed this population had it existed. Confocal observations of actomyosin contractions suggest a redistribution of contraction durations at the lower temperature. Thus, the duration of endogenous F-actin contractions qualitatively paralleled the temperature dependent changes in induced contraction at the high temperature regime but not at the low temperature. The temperature dependence of either morphologies or the duration of stimulated contractions, but was more aligned with the temperature dependence of the tissue viscoelasticity.

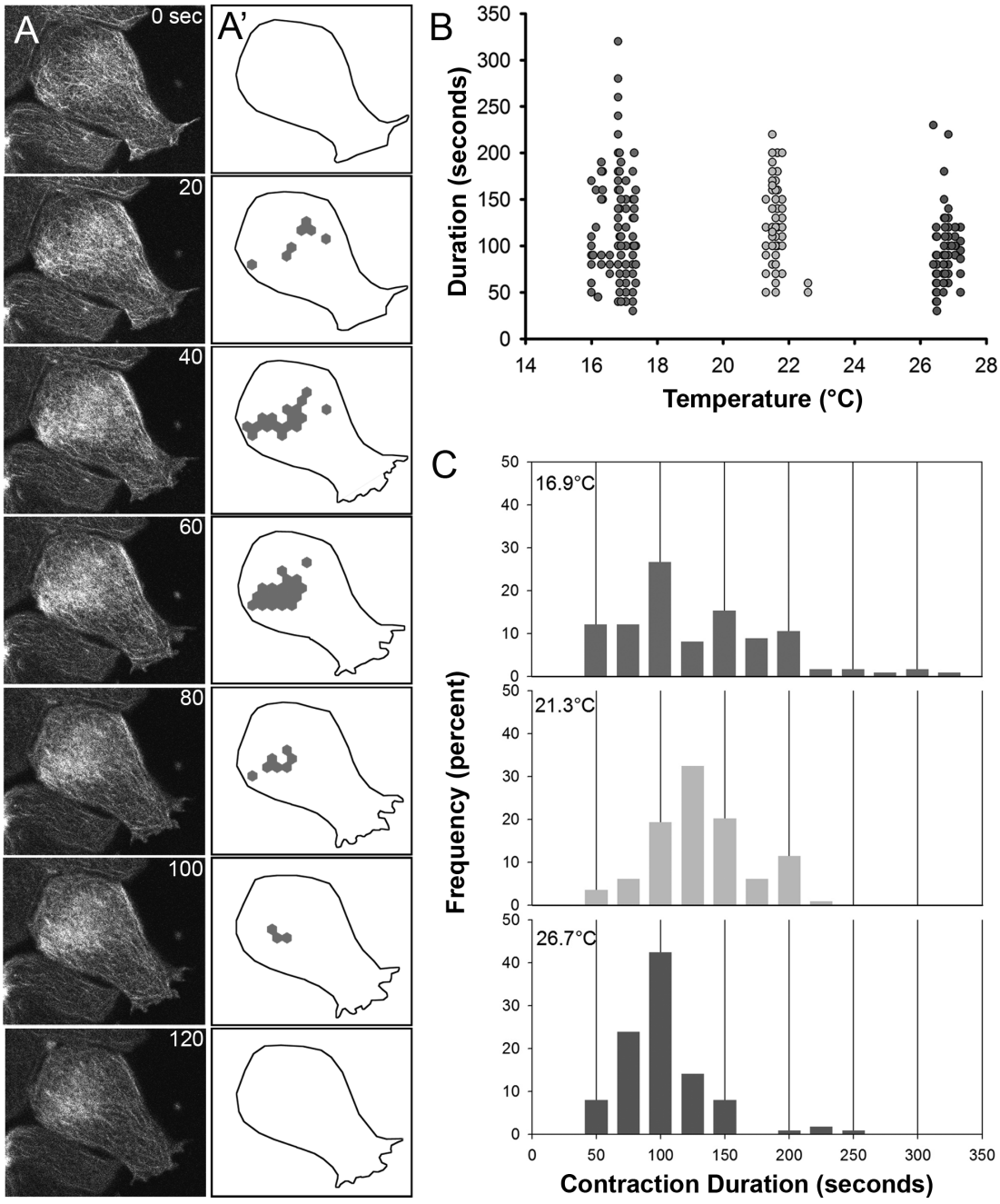

Figure 6.4: **Duration of actomyosin contractions depends on temperature.** (A) Sequential frames from a representative time-lapse sequence collected from the basal cortex of an animal cap ectoderm explant cultured on fibronecyin-coated glass substrate. F-actin dynamics are revealed in cells expressing the actin-binding domain from moesin coupled to EGFP (moe-GFP) (left column). This sample collected at 16°C. *Continued on next page*

Figure 6.4: *Continued from previous page* (A') Schematic of frames matching those in (A) highlighting the cell outline (dotted line) and hexagonal regions of the cell cortex identified as "F-actin contractions." Regions are categorized as contractions when their integrated intensities are 50% greater than the mean intensity of the basal cell cortex. (B) Duration of individual F-actin contractions across the three temperature regimes. (C) Frequency distribution of the duration F-actin contractions at three temperatures. Note abundant short duration contractions at the low temperature regime.

6.4 DISCUSSION

Our simple models suggest that a combination of how solid-like or fluid-like the tissue is, and the precise timing of forces driving morphogenesis (all at once, as in the step model, or gradually, as in the ramp model) are critical to determining how well or how poorly morphogenetic processes remain coordinated across a range of temperatures. In contrast, our experimental results suggest that temperature driven variation in developmental rates does not involve either changes in the viscoelastic properties of the embryo, or the magnitude of cell- generated forces, neither of which change with temperature. Instead, the temperature dependence of developmental rate appears to depend on changes in the timing of force generation, and tolerance of variation in the relative rates of different developmental processes (Table 6.3). The rate of dorsal-to-ventral progression of involution, which we suspect reflects the progression of patterning, increased more quickly with temperature than the rate of blastopore closure, which appears to reflect large scale mechanical interactions [Keller and Shook, 2008, Keller et al., 2008]. One exceptional example of tolerance to variation in development during gastrulation is described in Text G.3.2. This study was conducted within the normal developmental temperature range of *X. laevis*. We hypothesize that developmental defects may result when asynchronies among developmental processes exceed normal tolerance limits.

Table 6.4: ANCOVA table for endogenous F-actin contraction duration*.

T^2	T	clutch	explant(clutch)
P=0.0001	**P=0.0002**	P=0.4	**P=0.02**
$F_{1,345}$=16.6	**$F_{1,345}$=14.2**	$F_{10,3,94}$=1.4	**$F_{7,345}$=2.3**

*P values and corresponding F values. Temperature (T) and T^2 were fixed co-variates; "clutch" and "explant" were random factors, with explant nested within clutch. Statistically significant entries in bold.

Because our models are simplified generalizations of the process of morphogenesis they should be applicable to a wide range of morphogenetic processes. However, to make a generalized model, we had to leave out the complications of the real 3D geometry, large strains, material non-linearity, and plasticity. *Xenopus* embryonic tissue stiffens with increasing strain, although tissues exhibit near linear mechanical properties up to fairly large strain [von Dassow et al., 2010, Zhou et al., 2009]. Most critically, our models treat morphogenesis as a purely viscoelastic deformation, lacking any mechanism that would produce permanent changes in tissue lengths during morphogenesis, e.g. that tissue architecture would remain unchanged by plastic deformation, shear slippage at interfaces, unrecoverable creep, or cell rearrangement. Although Luu et al [Luu et al., 2011] have argued that the *Xenopus* embryonic epithelium displays a long-term "pseudo-elasticity," consistent with our models, we suspect that the apparent long-term elasticity they observe may be an artifact of wound-induced contractions [Joshi et al., 2010]. At present however, mechanical measurements presented here and elsewhere [von Dassow et al., 2010, Zhou et al., 2009, Luu et al., 2011, Wiebe and Brodland, 2005a] do not provide sufficient constraints on plasticity, unrecoverable creep, or the mechanics of cell rearrangement to incorporate these phenomena into our model. Finally, our models invoke several as yet untested assumptions regarding the relationship among the

force of induced contractions, endogenous forces driving blastopore closure, and the time dependence of forces driving blastopore closure. Although such complications would change the quantitative predictions of the models, they would not alter the conclusion that the time-dependence of the forces and the time-dependence of deformation could strongly affect the sensitivity of morphogenesis to variation in developmental rates.

Surprisingly, our viscoelastic deformation model predicts that toxins or mutations which alter cell viscoelasticity or the time dependence of force generation will alter the temperature dependence of morphogenetic rates and the temperature sensitivity for defects in opposite ways. For example, blebbistatin treated embryos have more fluid-like tissues (higher β; Fig. 6.1E). Therefore we would expect that the rate of blastopore closure should increase more slowly with temperature in blebbistatin treated embryos, but the permissive temperature range should be narrower because the reduced temperature sensitivity of tissue movements should lead to great asynchrony between tissue movements and patterning (Fig. 6.3B). The cellular processes driving closure are likely to begin uniformly around dorsalized or ventralized embryos, therefore such embryos should exhibit a more step-like onset of the forces driving blastopore closure than normal embryos. Hence, we would also expect reduced temperature dependence of rates of blastopore closure, but a narrower permissive temperature range, in dorsalized/ventralized embryos than in normal embryos. Future studies should investigate whether the model accurately predicts teratological effects of interactions among temperature and other perturbations.

A surprising finding was that the durations of stochastic actin contractions, whose dynamics are considered major contributors to morphogenesis [Guillot and Lecuit, 2013], were much less sensitive to temperature than either morphogenetic rates or stimulated, force-generating cellular contractions. Therefore we suspect at least two regulatory mechanisms control the temperature dependence of cytoskeletal dynamics. Actomyosin contractility in the cell cortex observed by confocal microscopy correlated qualitatively with the changes in the speed of current-induced contractions in the micro-aspirator. This relationship was best observed in the higher temperature regime; however, at the low temperature regime there appeared to be little correspondence between the duration of F-actin contractions and induced contractions. Large numbers of short duration contractions in the cortex at 16°C suggest

that actomyosin contractility may become decoupled from the long-duration contractions that produce tension in the embryo. Formally, it is possible that we may have under-counted large numbers of short duration contractions at the highest temperature, however, predicted short duration contractions were not observed at intermediate temperatures.

These findings suggest that molecular controls on actomyosin contractility function differently at high and low temperatures. It is unclear how these changes in cytoskeletal dynamics might work to maintain levels of force production and mechanical properties from 16 to 26°C, or whether these dynamics contribute to the failure of morphogenesis outside that range.

By considering how organisms tolerate the forms of environmental variation they have evolved to withstand in nature, we gain new insights into the mechanisms of development. Our models suggest that biomechanics parameters - viscoelasticity and the time dependence of force generation - have a major role in determining the temperature dependence of development. However, it is not the role we first expected. By modulating the synchrony of morphogenesis and patterning, these parameters might influence the evolution of heterochrony and affect the temperature dependence of developmental defects. Our study suggests that embryos tolerate some variation in the relative rates of patterning and mechanical tissue movements, but we hypothesize that increasing levels of asynchrony may lead to gastrulation defects or congenital birth defects. Further work needs to be done to test the predictions of our models, and to test the relationship between short-time scale induced force generation and endogenous forces driving morphogenesis. Additional studies will be needed to extend the experimental work here to temperature ranges that induce developmental defects and develop complimentary models that provide insights into the critical processes that break down under these conditions and increase the risk of birth defects int dal populations of vertebrate embryos.

6.5 METHODS

6.5.1 Ethics statement

Animals used in this study were treated according to an IACUC approved protocol issued to Dr. Davidson(# :0903349; Assurance # : A3187-01) which has been reviewed and approved by the University of Pittsburgh Institutional Animal Care and Use Committee. Embryos were collected and cultured as described previously [von Dassow et al., 2010], and kept at 15°C until late blastula stage (stage 9, [Nieuwkoop and Faber, 1967]).

6.5.2 Micro-aspiration and electrical stimulation

Micro-aspiration was carried out similarly to our previous approach, using a 125 μm diameter channel cast in polydimethylsiloxane [von Dassow et al., 2010], however the chambers were miniaturized (to 23 $\times$ 34 mm) for drug and temperature experiments. Temperature control was done using two aluminum tubes mounted within the polycarbonate body of the micro aspirator. The temperature of fluid running through the tubes was controlled using a recirculating chiller (ThermoCube, Solid State Cooling Systems; Wappingers Falls, NY). Because we could not have metal-media contact, temperature equilibration took up to 10 minutes and had to be adjusted manually to within $\pm$0.25°C. Temperature was monitored using a thermistor (Quality Termistor, Inc. QTMB-14C3) mounted in the media, no further than 5 mm from the embryo. Temperatures were recorded using a USB Thermistor measurement system (Robert Owen Inc., Albertson, NY). Pressures were controlled hydrostatically using a programmable syringe pump (New Era Pump, Pump Systems Inc., Farmingdale, NY) that was controlled through a custom VI in LabView 2009 (National Instruments Inc., Austin, TX). Tissue boundaries were tracked automatically within the LabView VI but had to be manually corrected in videos from two embryos.

For the experiment to test whether temperature or blebbistatin affected viscoelastic properties and contractions, one (or in a few cases two) embryos from each clutch was chosen at random for each treatment combination (16 vs 26°C and Blebbistatin vs. DMSO carrier control). A total of 6 clutches were used, one per day. Blebbistatin (100 μM, racemic;

EMD Millipore, Billerica, MA, USA) and DMSO carrier control media were made fresh each day. Both solutions were made with 1/3-strength Modified Barths Saline [Sive et al., 2000] to which 8 μl/ml antibiotic-antimycotic (A5955; Sigma-Aldrich, St. Louis, MO) and 2 mg/ml bovine serum albumin (Sigma-Aldrich) was added, with a final concentration of 0.2% w/v DMSO (Molecular Biology Grade; Fisher Biotech, Pittsburgh, PA, USA). The order of Blebbistatin or DMSO treatment was randomized on each day, but in the first runs the 26°C treatments were done prior to the 16°C treatments because of the great difference in developmental rates. If an embryo was damaged, or a video was unusable (due to poor imaging or leakage), a new embryo was selected at random. Embryos were cultured at 15°C until late blastula stage (stage 9), after which they were kept at different temperatures so that embryos could be measured at the same developmental stage. We have not seen morphogenetic defects in embryos transferred from 15 to 26°C or vice versa.

Microaspiration measurements were made at stage 11 on the dorsal quadrant between the blastopore and the equator of the embryo (midway between the animal and vegetal pole). The embryos were held at a low baseline suction (-1 Pa) for 10 min to improve the image of the tissue edge; the suction was then dropped to -11 Pa at -0.82 Pa/s for a 5 minute creep test, after which a 4 mx$\times$2.5 μA (channel positive) electrical pulse was applied to stimulate contraction (Fig. 6.1; [von Dassow et al., 2010]).

Analysis of tissue viscoelasticity and contractions was carried out using custom code in Matlab version R2010a (Mathworks, Natick, MA). A linear viscoelastic model with power-law viscoelasticity [von Dassow et al., 2010, Zhou et al., 2010a] was fitted to the aspirated length (L) of the tissue as a function of time (t):

$$L[t] = L_0 - \theta \cdot r \cdot \int_0^t J[1] \cdot (t-\gamma)^{\beta} \cdot \left(\frac{dP[\gamma]}{d\gamma} \right) d\gamma \tag{6.1}$$

L was measured along the channel centerline. L_0 is the initial aspirated length; r is channel radius, $J[1]$ is the compliance at 1 second; β is the exponent of the power law creep compliance; and P is pressure in the channel (negative for suction). θ is a proportionality constant that depends on channel wall thickness, and the ratio of tissue thickness to channel radius. For thick tissues and a very thick walled channel, as used here, θ is approximately 0.97 [von Dassow et al., 2010, Aoki et al., 1997]. This model is based on a viscoelastic

half-space model [Sato et al., 1990], incorporating Boltzmann's superposition principle [von Dassow et al., 2010, Findley et al., 1989, Merryman et al., 2009]. Previous work showed that the tissue thickness in the aspirated region was always greater than 100 μm (1.6*r; typically much greater) in the measured region of the embryo [von Dassow and Davidson, 2009]. Therefore deviations from the half-space model due to finite tissue thickness would be $\leq 17\%$ [Aoki et al., 1997, Boudou et al., 2006].

Because the pressure changes occurred as a series of k ramps, this model takes the following form:

$$L[t] = L[t_s] - \theta \cdot r \cdot J[1] \cdot \sum_{j=0}^{k-1} \left(\frac{P_{j+1} - P_j}{t_{j+1} - t_j} - \frac{P_j - P_{j-1}}{t_j - t_{j-1}} \right) \cdot \left(\frac{H[t - t_j](t - t_j)^{\beta+1} - H[t_s - t_j](t_s - t_j)^{\beta+1}}{\beta + 1} \right) \tag{6.2}$$

Here, times are relative to the baseline suction, t_S is the time at which the creep test began, P_j is the pressure at the end of ramp j ($P_0 = P_{-1} = 0$), and H is a step function.

Previous work suggested that a model in which apical tension drives electrically induced contraction explains effects of suction pressure on contraction magnitude better than a model in which isotropic contraction stresses occur throughout the aspirated tissue [von Dassow et al., 2010]. As described in von Dassow et al 2010, apical tensions are calculated in four steps (Fig. 6.1B-D). First, the viscoelasticity of the tissue is calculated from aspirated lengths prior to the electrical stimulus. Second, we calculate the "displacements" (m) as the difference between the measured aspirated lengths after stimulation, and extrapolated aspirated lengths. The extrapolation is based on applied pressures and measured viscoelasticity. Third, "equivalent pressure" changes at each time point (Q_k) are calculated from the displacements and viscoelasticity. These are the changes in suction one would have to apply to mimic the tissue displacements observed during the contraction. To minimize any effect of the discretization of the contraction forces, a slight refinement to the contraction analysis [von Dassow et al., 2010] was implemented. Instead of treating the equivalent pressures as a series of steps, they were treated as a series of ramps. Therefore, the vector of equivalent

pressure changes $\Delta\mathbf{Q}$ (each component is the change in equivalent pressure at a given time point) can be calculated from a vector of displacements $\mathbf{m}$:

$$\begin{aligned}\Delta Q &= \frac{-1}{\theta r} \cdot C^{-1} \cdot m \\ C_{k,j} &= H[t_k - t_j] \cdot J[1] \cdot \left(\frac{(t_k - t_{j-1})^{\beta+1} - (t_k - t_j)^{\beta+1}}{(\beta+1) \cdot (t_j - t_{j-1})} \right)\end{aligned} \tag{6.3}$$

The elements of the matrix C assume ramped changes in stress applied to material with power-law viscoelasticity between t_j and t_{j+1}. $H[x] = 1$ for $x > 0$, and $H[x] = 0$ for $x \leq 0$. In addition the displacements were smoothed with a 3-point moving average filter before calculating equivalent pressures to reduce noise in tissue positions that can cause spikes in the equivalent pressures. Finally, the equivalent pressure and estimated radius of curvature (R) or the aspirated tissue were used to calculate the apical tension (f) at each time step, based on the Young-Laplace relation:

$$f_k = \frac{R_k}{2} \sum_{i=1}^{k} \Delta Q_i \begin{cases} R_k = \frac{(r^2 + L_k^2)}{2L_k}, & 0 < L_k \leq r \\ R_k = r, & L_k > r \end{cases} \tag{6.4}$$

The radius of curvature of the tissue was estimated assuming the tissue approximates a spherical cap.

Fitted viscoelasticity and contraction parameters were analyzed using ANOVAs (Matlab R2010a) with type 3 sums of squares. Temperature and media (Blebbistatin vs DMSO control) were treated as fixed factors, and clutch was treated as a random factor. Two-way interactions were included in the ANOVA model; however the three-way interaction term was not included because there was only one embryo for each treatment-media-clutch combination in most cases.

6.5.3 Morphogenesis

Time-lapse series of morphogenesis were collected using automated image acquisition software (MicroManager plugin [Stuurman et al., 2007] for Image J [Rueden and Eliceiri, 2007]) to control a motorized stage (Ludl XY and MAC2000 controller, Ludl Electronic Products Ltd., Hawthorne, NY) mounted on a CCD-equipped (Scion Inc, Frederick, MD) inverted microscope (Zeiss Axiovert 100) with a 2.5× lens. Temperatures were maintained using a chamber warmed or chilled by passing fluid through two stainless steel capillary tubes immersed in the media within 1 to 4 mm of that embryos. The temperature was maintained using a recirculating chiller (ThermoCube), and monitored with a thermistor placed in the media as close as possible to the embryos on the bottom coverslip. To minimize temperature variation, a box was placed over the chamber and a thin, closed air space was formed under the chamber using a second coverslip separated from the chamber by a washer. Temperature within the chamber varied by ≤ 0.4°C with time or position, and usually by ≤ 0.2°C.

Blastopore closure was filmed in 6 to 8 embryos from each of several clutches at 16° and 26°C. The ratio of the time for blastopore closure or the time for the dorsal-to-ventral progression of involution was measured for each embryo. Because there may be clutch-to-clutch variation in the timing of morphogenesis, the medians of these two parameters were calculated for each clutch. Those embryos which rolled out of view before the completion of blastopore closure were not analyzed. Excluding these embryos did not have a substantial effect on the results. We used t-tests (comparing the set of clutch medians) to test whether clutches incubated at different temperatures differed in the timing of morphogenesis. Data analysis of the timing of morphogenesis was carried out in Microsoft Excel 2010.

Bootstrap analysis [Efron and Tibshirani, 1993] of the predictions of the ramp and step models was carried out with custom code (Matlab R2010a). Because the variables in the model come from two experiments, data from the two sets was resampled separately and entered into the equations in Models 2A & B (below, 6.5.5.3 & 6.5.5.4). $J[1]$, f, and h always appear together as a product in those equations, so the product of these variables was calculated for each embryo and resampled. Confidence intervals were estimated using the percentile method.

6.5.4 Actin dynamics

In order to track F-actin dynamics, fertilized *Xenopus laevis* eggs were injected at the 1-cell stage with synthetically transcribed mRNA encoding the actin binding domain of moesin coupled to EGFP (moeGFP) [Kim and Davidson, 2011, Litman et al., 2000]. Embryos were cultured to late blastula or early gastrula stages in 1/3-strength Modified Barths Saline [Sive et al., 2000]. Animal cap ectoderm was dissected from staged embryos and gently compressed under glass cover-slip fragments so that the basolateral surface of deep cells faced fibronecyin-coated glass mounted in a custom chamber designed for stable temperature control. The chamber and connected temperature controlled circulating water bath was identical to the one used for time-lapse imaging of whole embryos. Fluorescence images were optimized [Joshi et al., 2012] and time-lapse sequences were collected using a laser scanning confocal microscope mounted on an inverted compound microscope (Leica TCS SP5; Leica Microsystems, Bannockburn, IL). Time-lapse sequences were subsequently analyzed within image processing software (ImageJ) where the starting and ending frame of each contraction were identified. Contraction durations were analyzed using ANCOVA in Matlab R2010a. Temperature was included as a continuous variable incorporating linear and quadratic terms in the ANCOVA [Zar, 1999]. To account for the possibility of embryo-to-embryo and clutch-to-clutch differences, clutch and explant were included in the ANCOVA as random factors (explant nested within clutch; [Zar, 1999]). Data was plotted using SigmaPlot (SPSS Inc., Chicago, IL).

6.5.5 Models

In each of the following models (Models 6.5.5.1 and 6.5.5.2) we approximate the complex, non-linear, three dimensional (3D) deformations of morphogenesis as a one-dimensional (1D), spatially homogenous, linear viscoelastic process to focus on the effect of temperature (Figure 6.5; Text G.3.1).

6.5.5.1 Model 1: Generalized model We started by assuming that the process of development is identical at different temperatures except that every process is accelerated

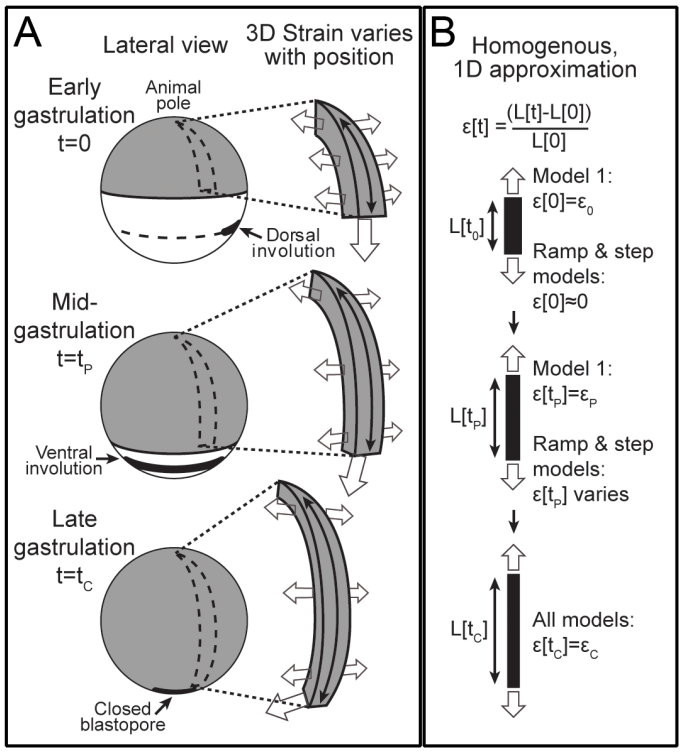

Figure 6.5: **Model schematic.** (A) Diagrams of blastopore closure from the lateral side. The ectoderm and neurectoderm (gray) spreads over the embryo during gastrulation. Involution begins on the dorsal side at $t = 0$, and begins on the ventral side at t_P; the blastopore closes at t_C. In the generalized model (Model 6.5.5.1) we assumed all morphogenetic durations (t_P, t_C, etc) changed by the same proportion with temperature. In the step and ramp models (Models 6.5.5.3 & 6.5.5.4) t_P is used, as an estimate of the timing of cell behaviors that exert morphogenetic forces, to predict t_C. A strip of tissue (A, to right of each whole embryo schematic) experiences spatially and temporally varying stresses (open arrow; stresses from deep tissues not shown), which elongate it and change its shape. We approximate this deformation as uniform stretching of a strip of material (B). The generalized model (Model 6.5.5.1) assumes temperature only affects the speed of morphogenesis, therefore each morphogenetic event occurs at fixed, but unspecified strains (ϵ_P, ϵ_C, ...). In the step and ramp models (Models 6.5.5.3 & 6.5.5.4) the main forces driving blastopore closure begin near the start of ventral involution (so $\epsilon[0] \approx 0$), and blastopore closure occurs at a fixed strain ($\epsilon[t_C] = \epsilon_C$); however, the strain at t_P varies with temperature.

or decelerated by the same amount for a given change in temperature. This implies that we can define a time scale- developmental time (τ)- that is proportional to clock time (t) via a factor (α) that is a function of temperature (T) so that a developmental event occurring at developmental time τ at temperature T_1 would occur at the same developmental time at all other temperatures:

$$\tau = t/\alpha[T] \tag{6.5}$$

Strain is a non-dimensional measure of deformation. For extension or compression, strain can be measured as $Ln[L/L_0]$, where L is the deformed length of the material, and L_0 is the undeformed length. Since all deformations are identical at a given developmental time τ, all strains (ϵ^*) are identical at a given developmental time:

$$\epsilon^*[\tau, T_1] = \epsilon^*[\tau, T_2] \tag{6.6}$$

For a highly simplified linear, small deformation, one dimensional model [Findley et al., 1989], this implies:

$$\begin{aligned} \epsilon^*[\tau] &= \int_0^\tau J^*[\tau - \xi, T_1] \cdot \frac{d\sigma^*[\xi, T_1]}{d\xi} d\xi \\ &= \int_0^\tau J^*[\tau - \xi, T_2] \cdot \frac{d\sigma^*[\xi, T_2]}{d\xi} d\xi \end{aligned} \tag{6.7}$$

Here, J^* and σ^* are the creep compliance and stress as functions of developmental time (eqn. 6.5). Creep compliance is a material property that relates the applied stress (force per unit area to strain. For an elastic (spring-like) material, compliance is the inverse of the elastic modulus (Young's modulus for tension or compression).

We further assume that the stress at any developmental time T_2 is proportional to the stress at the same developmental time at T_1:

$$\sigma^*[\tau, T_2] = c[T_2, T_1] \cdot \sigma^*[\tau, T_1] \tag{6.8}$$

This implies:

$$\begin{aligned} \epsilon^*[\tau] &= \int_0^\tau J^*[\tau - \xi, T_1] \cdot \frac{d\sigma^*[\xi, T_1]}{d\xi} d\xi \\ &= \int_0^\tau J^*[\tau - \xi, T_2] \cdot c[T_2, T_2] \cdot \frac{d\sigma^*[\xi, T_1]}{d\xi} d\xi \end{aligned} \tag{6.9}$$

The Laplace transform of equation 6.9 gives:

$$\begin{aligned}&\mathcal{L}\{J^*[s,T_1]\}\cdot(-\sigma^*[0,T_1]+s\cdot\mathcal{L}\{\sigma^*[t,T_1]\})\\&=\mathcal{L}\{J^*[t,T_2]\}\cdot c[T_2,T_1]\cdot(-\sigma^*[0,T_1]+s\cdot\mathcal{L}\{\sigma^*[t,T_1]\})\end{aligned}\tag{6.10}$$

This expression simplifies to:

$$\mathcal{L}\{J^*[t,T_1]\}/c[T_2,T_1]=\mathcal{L}\{J^*[t,T_2]\}\tag{6.11}$$

Taking the inverse Laplace transform gives:

$$J^*[\tau,T_1]/c[T_2,T_1]=J^*[\tau,T_2]\tag{6.12}$$

Given our definition of developmental time, the creep compliance, and the temperature dependence of force generation: it exhibits time-temperature superposition [Kieβling et al., 2013], with identical time scaling as morphogenesis.

The *Xenopus laevis* gastrula epithelium exhibits power law creep compliance [von Dassow et al., 2010]:

$$J[t,T]=J[1,T]t^{\beta[T]}\tag{6.13}$$

Substituting the developmental time into equation 6.13, putting it into equation 6.12 and rearranging gives:

$$\left(J[1,T_1]\cdot(\alpha[T_1]\tau)^{\beta[T_1]}\right)/\left(J[1,T_2]\cdot(\alpha[T_2]\tau)^{\beta[T_2]}\right)=c[T_2,T_1]\tag{6.14}$$

Since $J[1,T]$ and $\alpha[T]$ are independent of time (time is fixed at 1 in $J[1,T]$), the only way for this expression to be independent of time is if β is independent of temperature. Therefore, this simplified model predicts that β is independent of temperature.

In addition, the coefficient, $J[1,T]$, the stress ratio c, and the temperature dependence of morphogenesis are related by:

$$\frac{J[1,T_1]}{J[1,T_2]}\cdot\left(\frac{\alpha[T_1]}{\alpha[T_2]}\right)^{\beta}=c[T_2,T_1]\tag{6.15}$$

This predicts that if development slows down at lower temperatures, and the coefficient $J[1,T]$ does not change with temperature, then morphogenetic forces should be weaker at

lower temperatures. For $T_2 = 16°C$, and $T_1 = 26°C$, the ratio of α's approximately was 1/3, the ratio of $J[1]$'s was 1, and β is approximately 0.2. Therefore for contractions, we would expect c, the ratio of the peak apical tension at 16°C to the peak tension at 26°C, to be approximately 0.8, rather than the observed value of approximately 1.4.

6.5.5.2 Models 2A and 2B: Specific models These models retain the simplifying assumption that the complex 3D, large deformation process of morphogenesis can be approximated by a simplified 1D, linear viscoelastic model (Fig. 6.5; Text G.3.1 includes a justification for this approximation). One outcome of our approximation approach is that we characterize the progress of blastopore closure by a single parameter that scales approximately with the strain field throughout the whole system. This parameter, ϵ, behaves as the strain in the linear 1 dimensional models below. Because all of the complex deformations during blastopore closure are indexed to this parameter, blastopore closure occurs at a particular value of this "strain," ϵ_C.

6.5.5.3 Model2A: Step model A step of stress starting at $t = 0$ would give strain (ϵ) as follows, where σ is the step stress, and the other variables are as described for model 6.5.5.1:

$$\epsilon[t] = \sigma \cdot J[1]t^{\beta} \tag{6.16}$$

Solving of the time, t_C, to reach the level of strain, ϵ_C, needed to close the blastopore gives:

$$t_C = \left(\frac{\epsilon_C}{(\sigma \cdot J[1])}\right)^{1/\beta} \tag{6.17}$$

With ϵ_C the same at each temperature, we can substitute 6.16 back into 6.17 to determine how t_C varies with temperature.

$$t_C[T_2] = \left(\frac{\sigma[T_1] \cdot J[1, T_1] \cdot t_C[T_1]^{\beta[T_1]}}{\sigma[T_2] \cdot J[1, T_2]}\right)^{1/\beta[T_2]} \tag{6.18}$$

We assume we can express σ in terms of the measured contraction forces. We assume that blastopore closure is driven by pulses of force produced as individual cells intercalate. The average force will be proportional to the force per pulse (f), multiplied by the average

number of pulses occurring at a time. The average number of pulses occurring at a time equals the pulse duration (h) multiplied by the rate of pulse initiation. We assume that the pulse duration (h) and force (f) change with temperature in the same way that duration and force of induced contractions change. Because involution involves localized deformations, its dorsal-to-ventral progression should closely follow the initiation times of the cell behaviors that drive it. Therefore, the time (t_P) it takes for dorsal-to-ventral progression of involution should scale with temperature similarly to the timing of cell behaviors, such as force pulses. Therefore, we assume the rate of force pulses scales inversely with t_P. These assumptions imply the following, with k a constant of proportionality:

$$\sigma = k \cdot h \cdot f / t_P \tag{6.19}$$

Substituting this into equation 6.18 and dividing by t_P gives an expression predicting how R_{CP} (the ratio t_C to t_P) varies with t_P, which changes with temperature:

$$\begin{aligned} R_{CP}[T_2] &= \left(\frac{t_C[T_2]}{t_P[T_2]}\right) \\ &= \left(\frac{J[1,T_1]h[T_1]f[T_1]t_P[T_2](t_C[T_1])^{\beta[T_1]}}{J[1,T_2]h[T_2]f[T_2]t_P[T_1]}\right)^{1/\beta[T_2]} / t_P[T_2] \end{aligned} \tag{6.20}$$

If we assume that f, $J[1]$, and β are independent of temperature (based on the lack of statistically significant effects), and that h is proportional to t_P (both biochemcially-controlled durations change the same way with temperature), this simplifies to the following:

$$R_{CP}[T_2] = t_C[T_1]/t_P[T_2] \tag{6.21}$$

6.5.5.4 Model 2B: Ramp model A ramp of stress starting at $t = 0$ would give strain (ϵ) as follows, where w is the slope of the ramp in stress, and the other variables are as described before:

$$\epsilon[t] = \frac{w \cdot J[1] \cdot t^{\beta+1}}{\beta + 1} \tag{6.22}$$

We make the same assumptions regarding the force as in the step model, but with the addition that the frequency of force pulses increases with developmental time with a constant slope. As in the step model, the rate of pulses at any given developmental stage should vary inversely with t_P. In addition, the time it takes to get to that stage varies directly with t_P. Therefore, slope of the ramp in stress should be as follows:

$$w = k \cdot h \cdot f / t_P^2 \tag{6.23}$$

Substituting and rearranging as in the step model gives the following expression for R_{CP}, where each parameter is assumed to be a function of temperature:

$$R_{CP}[T_2] = \left(\frac{(\beta[T_2]+1) J[1,T_1] h[T_1] f T_1] t_P[T_2]^2 t_C[T_1]^{\beta[T_1]+1}}{(\beta[T_1]+1) J[1,T_2] h[T_2] f[T_2] t_P[T_1]^2} \right)^{1/(\beta[T_2]+1)} / t_P[T_2] \tag{6.24}$$

If we assume that f, $J[1]$, and β are independent of temperature, and that h is proportional to t_P, this simplifies to the following:

$$R_{CP}[T_2] = R_{CP}[T_1] \cdot (t_P[T_1]/t_P[T_2])^{\beta/(\beta+1)} \tag{6.25}$$

In summary, differences among the models are illustrated graphically in Figure6.6. The generalized model (Model 6.5.5.1) makes *no* assumptions about the time course of morphogenetic forces; the step and ramp models *assume* specific time courses of morphogenetic forces (stepped or ramped; Models 6.5.5.3 & 6.5.5.4). The generalized model *assumes* that the relative durations of morphogenetic events (e.g. the ratio, R_{CP}, of t_C to t_P) do not vary with temperature; the step and ramp models *predicts* the changes in relative durations (R_{CP}) with temperature. The generalized model *predicts* the temperature dependence of compliance and stress magnitude; the step and ramp models take these as inputs.

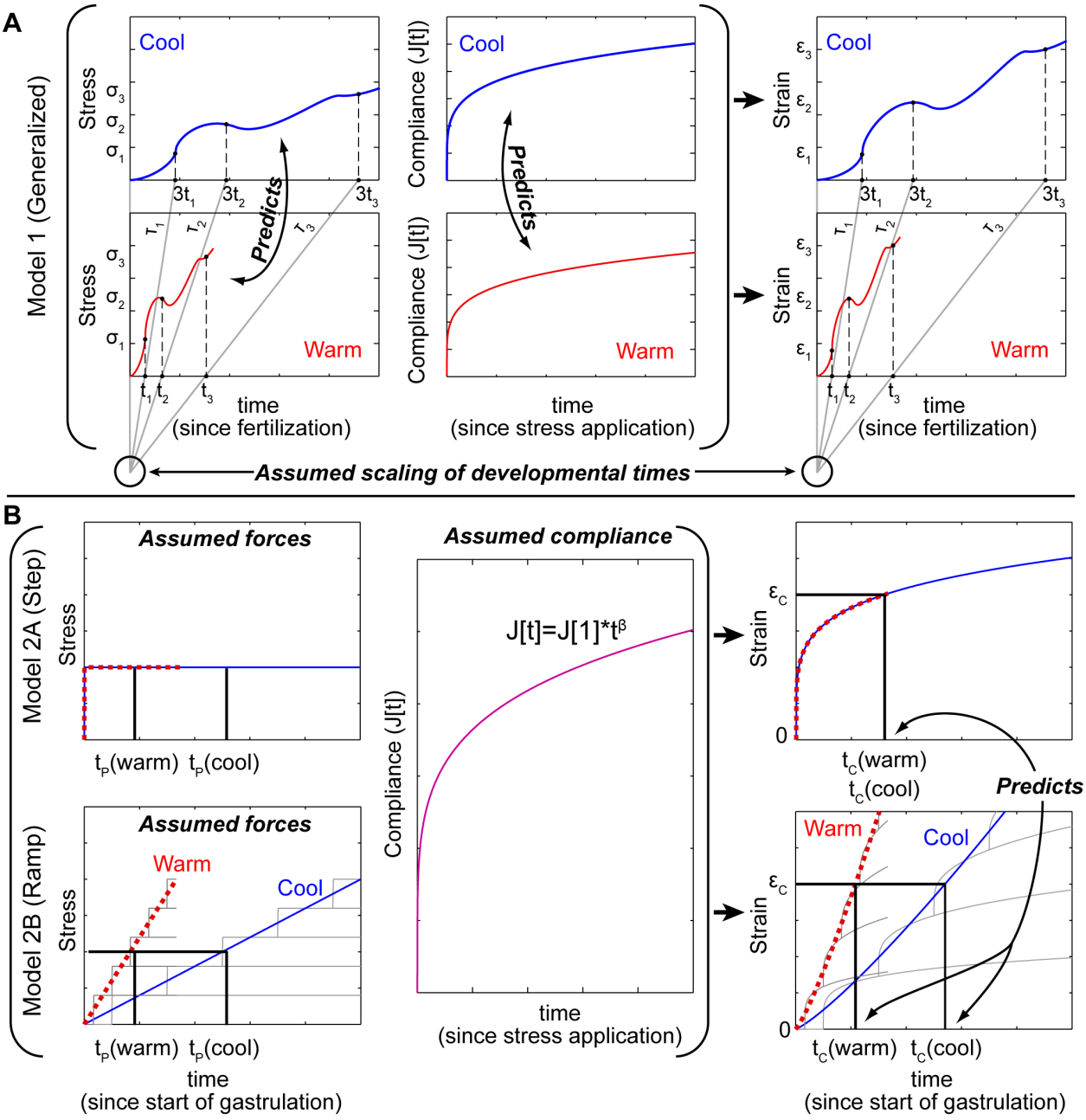

Figure 6.6: **Differences among models.** Hypothetical stress (left), creep compliance (middle), and deformation (strain, ϵ; right) in the tissue. (A) The generalized model (Model 6.5.5.1) assumes the relative timing and the strains, of all events (1,2,3,...) are independent of temperature (cool (blue) vs warm (red)), as in a movie played faster. The generalized model does not specify the developmental course of strain or stress, only that timing scales with temperature. The generalized model predicts how stress and compliance vary together as temperature changes (Model 6.5.5.1, eqn. 6.15). *Continued on next page*

Figure 6.6: *Continued from previous page* (B) Step and ramp models (Models 6.5.5.3 & 6.5.5.4). The step and ramp models assume morphogenetic stresses are stepped (top) or ramped (bottom) with time. For a step stress (upper), the change in t_P with temperature does not affect the time t_C to reach strain ϵ_C (when the blastopore closes) because peak stress and compliance are unchanged (Model 6.5.5.3, eqns. 6.20-6.21). A ramp is the sum of stress increments (gray lines; bottom left). Stress timing (hence the slope of the ramp) scales with t_P, and therefore with temperature (red, warm; blue, cool). The time t_C varies with t_P (and therefore temperature) for the ramp model (upper; Model 6.5.5.4, eqns. 6.24-6.25), because train increments follow the change in timing of stress increments (gray lines).

7.0 CONCLUSIONS

The goal of this dissertation was to develop the tools to examine force generated by the actomyosin cytoskeleton in cells. The project involved a thorough understanding of the multi-scale feedback mechanism that exists between molecular, cellular, and tissue level mechanics and signals. We needed an understanding of the current techniques and challenges researchers face when trying to experimentally determine the role of the cytoskeleton during development and other model systems, as well as understand how to build computational models and simulations that would answer these questions. The project addressed two specific aims (1.1.1 and 1.1.2). Aim 1.1.1 extensively investigated modeling and understanding of actomyosin networks (Chapter 3,4,5) and led to further motivation for understanding the role of actin crosslinking proteins addressed in Aim 1.1.2. The role of cross linkers was addressed in discussions for each of the models in Chapters 3, 4, and 5, but preliminary studies into crosslinking proteins are presented here as a foundation for future work with the novel modeling technique.

My contributions to the project investigating the effects of temperature on development (Chapter 6) served to expose me to the challenges of experimental set up, gathering data, and data analysis for biological tissues. It also led to the question of why the actin network had short and long duration contractions at low temperature only, when bulk mechanical properties of the embryo remained the same. Although the model and simulation were not utilized in this paper, the 2D model (Chapter 5) has been set up to help understand this phenomenon. With the cortex filaments around the hexagonal boundary serving as a type of force sensor for the hexagonal patch, they can be used to perform *in situ* mechanical testing on the hexagonal patch. The mechanical testing will tell us the range (because each simulation is random) of mechanical properties for the patch of actin cortex. We can then

tune the parameters based on the expected behavior of the proteins in various temperature conditions. Another approach would be to tune parameters in order to slow down the duration of contraction of the aster to analogous times as experimentally observed [von Dassow et al., 2014]. We hypothesize that the short duration contractions with the long duration contractions at low temperature are a remodeling response to maintain mechanics at lower temperature. Knowing the mechanical properties of the simulation patch, and tuning the contraction to match the data will allow us to investigate the mechanisms by which the short and long duration contractions are helping the embryo to maintain its bulk mechanical properties across a range of temperatures and how these mechanisms might fail outside the range of developmentally permissive temperatures.

Working on the review of mechanically sensing proteins in development (Chapter 2; [Miller and Davidson, 2013]) challenged me to narrow the communication gap between geneticists, biologists, and engineers. It also helped to solidify my understanding of the extremely complex feedback that exists between actomyosin and force sensing proteins, for example at cell junctions. Once researchers discover mechanically activated proteins or genes, the exact role they play in the local environment is only hypothesized because of limited testing strategies. Because my model has started out extremely simplified, it is easy to build upon the simple actomyosin interactions and add specific mechanical sensing proteins or gene activation. Furthermore, we can use the model to explore conditions within the external mechanical environment that might trigger mechanosensors in the patch that could in turn trigger protein or gene activation. Simulating feedback may offer a quicker solution than biologically testing knock downs or over expression, and would direct researchers in more efficient experimental design.

The simplified rotational model of actomyosin (Chapter 3; [Miller et al., 2012]) helped us gain an initial understanding of the interactions between actin and myosin. It also laid the foundation for building more complex simulations. Because of its simplified structure, we were able to develop continuum solutions for the computed Monte Carlo sims. From the continuum solutions, we arrived at a very interesting hypothesis that there is a region where the actomyosin system can be generating the same amount of force, but two different morphologies are possible just by turning up or down the polymerization rate of the actin

(fig 3.8B). Our experimental observations of actin behavior at various stages of development in specific tissues also point towards this hypothesis. The best way to test this hypothesis would involve selecting a specific tissue system with well defined actomyosin dynamics over a time course of development, for example mesoderm during convergent extension, then test for genes that are activated or differences in protein expression over that period of time. Our model suggests that the greatest differences in morphology may be driven by actin polymerization rates, so the genes and proteins of interest should be ones that would affect actin polymerization.

The sliding model of actomyosin (Chapter 4) built upon the rotational model and helped to lay the ground work for the 2D model and the intuition behind the boundary filaments (Chapter 5). We found that morphologies where boundary filaments were pulled into the center depended on the probability of interactions between boundary and free filaments. Aligned actin filaments can be found in muscle cells, the cytokinetic furrow, stress fibers, circumapical ring at cell-cell junctions, and cells along the blastopore lip in *Xenopus laevis* (fig 4.1). Several forms are thought to be a consequence of the external mechanical environment. The sliding model identifies what happens once actin is already in this arrangement, but image analysis might help identify cases of sliding F-actin in specific tissues and times. The model can then be used to predict how the cell boundary edges perpendicular to the parallel arrays will remodel.

Finally, our 2D model of actomyosin (Chapter 5) closely captures several features of actomyosin behaviors observed *in vitro*, as well as the events leading to formation of a contractile F-actin aster. The simplified approach we took to develop our model opens the doors for many opportunities for extending its use as an experimental tool in the future. I will specifically focus on these ideas in the following sections.

7.1 IMAGE ANALYSIS TECHNIQUES

Our lab has begun investigating the complicated process of neural tube development in *Xenopus laevis*. Preliminary studies have found the existence of rosettes which are correlated

with the process of convergent extension [Pohl et al., 2012, Vijayraghavan and Davidson, prep]. Thus we have the ability to quantify the changes in cell shape over this time period. Furthermore, we found that we see a similarly dynamic, more dense actomyosin network at the apical surface of the neural epithelium. We are able to quantify the duration of these contractions, but in order to relate these data to the 2D model, we need to improve quantifications and identification of actomyosin. Since the 2D model represents a small patch of the actin cortex within a cell, we can parallelize the code to make it more efficient and piece multiple hexagons together using mean field analysis or homogenization. Then the boundary filaments act as the sensors between neighboring hexagons to build a "cell." We would then expect to see similar actin contractions as observed experimentally. Furthermore, we know how a cell changes shape through development, so we can use the model to determine what actomyosin morphologies and forces would be necessary to reshape a simulated cell accordingly.

Building a model cell would bridge the molecular and cellular scales. In order to improve the connection to the experiments, we can analyze the experiments by considering where peaks of actin intensity are occurring and quantify where these peaks are in terms of distances from the cell boundary toward the center of the cell, and even where they are in the direction of tissue convergent extension. Once we are able to build the 2D model into a representative cell, we can then consider neighboring cells with localized areas of contractions to better understand rosette formation and their mechanical role in development. This level would extend the model up to the tissue level.

7.2 ACTIN BINDING PROTEINS

As we have discussed, there are other proteins that contribute to shaping actomyosin morphology and keep it dynamic (see review [Lee and Anderson, 2008]). We began to investigate ways of destabilizing the steady state aster in Chapter 5, by fixing filament location or fixing motor location (figs 5.10 and 5.12). This observation brings us to Aim 1.1.2 where we want to consider actin crosslinking proteins that might serve to localize F-actin or bind F-actin

to other cytoskeletal scaffolds. The key to adding in additional complexity into our model lies with understanding the biophysics of these proteins and how these properties can be translated into our model framework.

The three major categories of actin binding proteins are capping proteins, bundling proteins, and membrane proteins [Pollard and Cooper, 1986]. Capping proteins are responsible for affecting the rates of polymerization and depolymerization of F-actin by sequestering monomers of actin (G-actin), or binding to an end of F-actin [Cooper, 2000]. Two examples of capping proteins are profilin and cofilin [Alberts, 2008]. Profilin binds to free actin monomers to stimulate the exchange of ADP to ATP. ATP G-actin is then allowed to bind to the plus end of F-actin, but not to the minus end. The profilin-actin complex then caps the plus end of the filament, not allowing anymore monomers to bind, and prevents the monomer from detaching from the filament. Cofilin on the other hand, binds to the ADP actin and keeps it in ADP form so the monomers can no longer bind to the filament which halts polymerization of F-actin [Cooper, 2000]. Capping proteins are also able to stabilize filament length (effectively shortening them through the aforementioned mechanisms), sever the filament to create shorter filaments with new plus/minus ends for new binding cites, and possibly bind the plus end of the filament to the membrane [Pollard and Cooper, 1986].

Bundling proteins are cross-linking proteins that have properties based on how they bind and bundle actin filaments. Fimbrin and Fascin, for example, bind to a pair of co-aligned filaments with one cross-linker every 3.5-5 actin monomers, and keep the F-actin 10 nm apart, oriented with the same polarity [Pollard and Cooper, 1986]. Fimbrin and Fascin limit the ability of NMM II to interact with the filaments. α-actinin, on the other hand, binds to a pair of filaments, orienting their polarity, and maintains a spacing of 40 nm. α-actinin also allows NMM II to continue to interact and contract the network [Cooper, 2000]. Filamin is a v-shaped molecule which binds at the cross-over point between orthogonal filaments and is flexible allowing the network to deform [Cooper, 2000].

To model a "universal" cross linker, we allowed cross linkers to bind to a filament pair within 40 nm and $\pi/8$ radians of each other (fig 7.1). We do not observe parallel alignment of filaments, but we have halted the single aster from forming. Since we saw the "ring" alignment of filaments versus parallel stress-fiber-like parallel alignment, we hypothesize

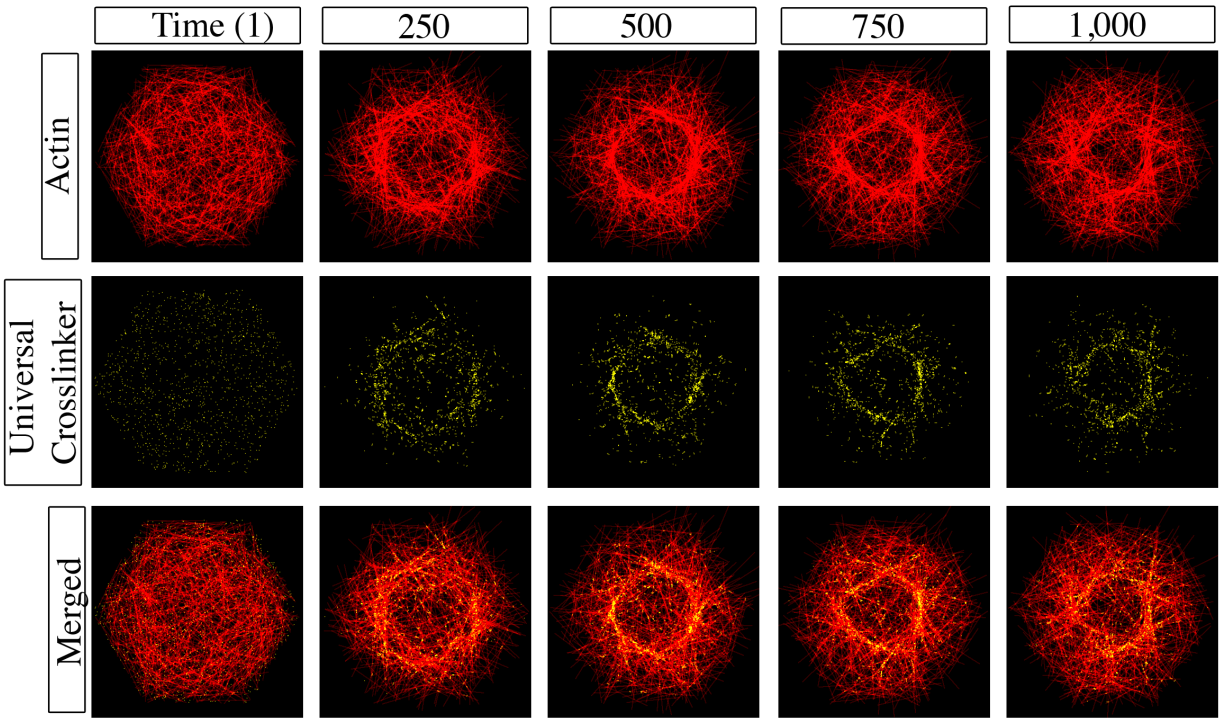

Figure 7.1: **Testing a "universal" actin crosslinker**. Red "actin" filaments are across the top row for t=1 to t=1,000. In yellow are the actin crosslinking proteins (1,250) which are only allowed to bind at the same rate as the myosin motors (p_0), to filaments that are within $\pi/8$ degrees of each other, and 0.04 μm apart. The cross linkers bind to the shortest distance between candidate filament pairs. The bottom row are the merged images for the time course of the simulation.

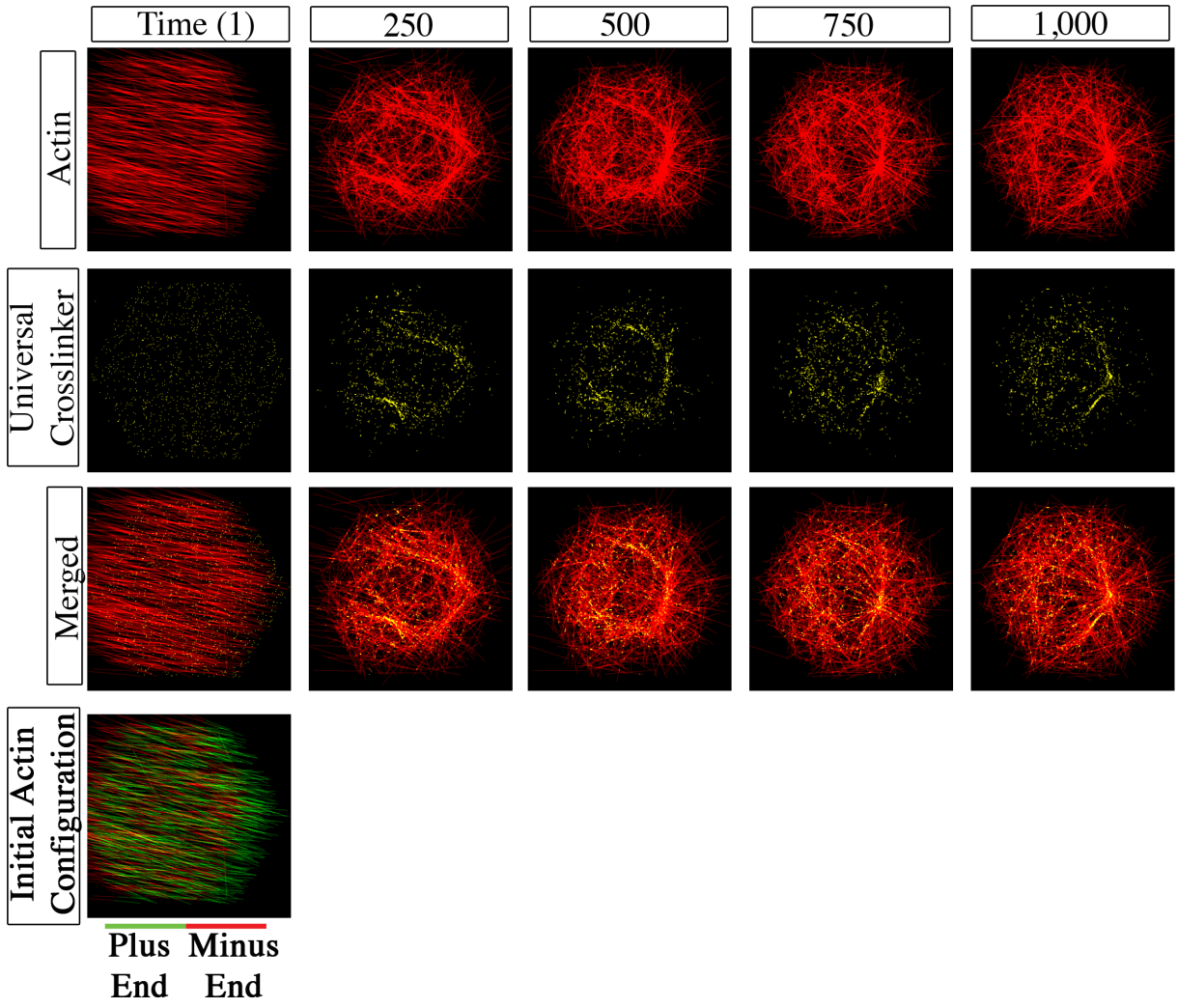

Figure 7.2: **Restricting the initial condition of filaments**. To begin, we assumed that all plus ends of the filaments were within the hexagon. Then filament (red) orientation was chosen to be a random number between 0 and $\pi/8$. Therefore the minus ends of the filaments can be out of the hexagon. Crosslinkers (yellow) follow the same rules as in figure 7.1 where filament pairs must be within 0.04 μm and $\pi/8$.

that filaments *in vivo* are acted upon by other actin binding proteins to begin to form parallel arrays and then the bundling proteins move in and stabilize the morphology. As a preliminary test, we ran a simulation where the initial orientation of randomly placed filaments were all within $\pi/8$ of each other (fig 7.2). The motors continue to act upon the filaments, contracting toward an aster, but it appears that the aster has formed where most plus ends of the initial array were oriented.

The best way to incorporate actin binding proteins is to include G-actin monomers to serve as a pool for polymerization of F-actin filaments. Capping proteins would then affect the rates of length increase (polymerization) and decrease (depolymerization). In this case we would consider the G-actin monomer population as a constant rather than conserving the number of already established filaments (current model). Then we can consider cofilin/profilin as one molecule, which has a parameter of probability of either being cofilin (increasing the rate of polymerization), or profilin (decreasing the rate of polymerization). The rate of attachment of cofilin/profilin to a filament should be 1 /s (from [Mogilner and Edelstein-Keshet, 2002]). Once the filament has a capping protein attached, profilin will activate at a rate of 20/s, and coffin will activate at a rate of 10/s [Mogilner and Edelstein-Keshet, 2002]. If the filament is in the "profilin-active" state, then it will have a rate of polymerization lower than the standard value. If the filament is in the "cofilin-active" state, then it will have a rate of polymerization higher than the standard value. If profilin and cofilin are bound to the filament but not "active", then nothing changes for the polymerization rate. There will also be a rate of detachment for the capping protein. The population of profilin/cofilin will be the same as the number of filaments based on the idea that every filament can have a capping protein [Pollard and Cooper, 1986]. Extending the model to incorporate monomeric G-actin and capping proteins would involve a few extra sections of bookkeeping code, but otherwise would be fairly easy.

7.3 CONCLUDING REMARKS

We were able to take a very simple rotational model and build upon it to create a model that mimics *in vitro* experiments with purified actin and myosin. Furthermore, we have laid the foundation for using the 2D model in the future to gain valuable insight into the localized mechanics of cells. Our model has addressed the dynamic remodeling property of *in vivo* cortical actomyosin and has the theory behind its inception which will drive researchers to predict actomyosin network remodeling in response to externally applied forces.

Even though the current model is extremely simplified and we are able to apply the results to experimental observations, I hope that the model could be extended into something more directly related to experimental observations. For example, the most powerful application for the model would be to have a short experimental time-lapse movie of actin in a tissue or cell of interest, and by using the positional information of the actin over the time-lapse, the model can then be used to predict how the network morphology would change in the next time step. Being able to directly simulate and accurately predict the "next step" in the future would allow us to do *in silico* testing with the model to determine how we could mechanically perturb the "next step." We could then use this intuition to drive experiments, testing how external mechanical environments would affect the tissue. We would have all the molecular level understanding of protein location and force generation, and the model extends this molecular level to the cellular level of shape change and rearrangements.

APPENDIX A

NATURE REVIEWS GENETICS SUPPLEMENT

A.1 DEFINITIONS

gastrulation- Stage of embryonic development when large cell rearrangements occur and the three germ layers - endoderm, mesoderm and ectoderm - of the embryo are established.

Vegetal plate- The columnar epithelium at the vegetal pole of an echinoderm embryo. The thickened vegetal plate forms a pocket and tube by invagination during gastrulation to form the archenteron, or primitive gut, of the embryo.

Blastula- The early stage of a developing embryo after rapid cell divisions have created a sphere, sometimes hollow, of many cells.

Ectoderm- The outermost germ layer of the embryo. Cells from this layer differentiate into skin and neural tissues.

Dorsal closure- A step in *Drosphila melanogaster* development in which the epidermis closes over the exposed amnioserosa

Amnioserosa- A layer of epithelial cells that covers dorsal regions of the early *Drosophila melanogaster* embryo

Epidermis- The outermost epithelial layer of an embryo

Anterior- The axis of the embryo defined by the tissues fated to form the head.

Posterior- The axis of the embryo defined by the tissues fated to form the tail.

Invagination- The 'in-folding' of an epithelium.

Apical- Surfaces that face the 'outside' or lumen.

Basal- Surfaces that face in the opposite direction to apical surfaces; that is, away from the 'outside'.

Traction force microscopy- A method used to determine the force that a cell or tissue exerts on a substrate to which it is adhered.

Focal adhesion complex- A dynamic protein complex that connects the cytoskeleton of the cell to the extracellular matrix.

Desmosomes- A spot-like junctional complex for cell-cell adhesion that is distinct from adherents junctions (which connect epithelial cells to neighbors at their apical ends).

Cell cortex- A layer of cytoplasm just inside the plasma membrane. Cytoskeletal proteins in the cell cortex maintain the shape of the cell.

Stomodeal primordium- A tissue fated to give rise to the *Drosophila melanogaster* foregut.

A.2 BOXES

A.3 ENGINEERING PRINCIPLES AND TERMS

Translation and rotation

An object can move or translate by moving up, down, left or right. Rotation can be described by the angle of change the object experiences; see the figure A1, part a, where the object before translation at time t_0 moves to its final location at t_f after translation.

Tension and stretch

Tension(T) (see the figure A1, part b, where T is a pair of forces applied to the object) is an engineering term for the forces that tend to stretch an object from t_0 to t_f. Stretch can be measured as a normalized engineering strain (see the figure A1, part b, where l_0 represents the initial length and l_f the final length).

Deformation and strain

Deformations of cells and tissues are changes in the shape of the cells and tissues over time or in response to an applied force, normally measured using live cell time-lapse imaging.

Engineers use the term strain, which is a measure of deformation normalized to the size of the structure, to quantify deformations. Also, from a measure of deformation over time, a strain rate can be determined. The units of deformation are in units of length (l) (see the figure A1, part b). Strain is generally dimensionless but is sometimes noted as length/length (for example, mm/mm), and strain rate is given per a measurement of time.

Force and stress

Force is any influence that causes an object to undergo a change such as translation, rotation or deformation. Stress is a measure of force applied over a surface, either perpendicular to the surface (for example, tension or compression) or within the plane of the surface (shear). The units of force are mass times acceleration and the units of stress are force per unit area. See the figure A1, part c, for an illustration of its physical definition, where F is force and A is area.

Fluids and solids

In addition to the ability to generate force, biological tissues all exhibit some resistance to mechanical force. If they flow in response to force, they are considered to be a viscous fluid. If they deform in proportion to the applied force and recover their original shape when the force is removed, they are considered to be an elastic solid (by contrast, a fluid will not recoil once the applied force, or load, is removed).

Viscoelastic

In practice, cells and tissues typically exhibit behaviors of both solids and fluids, and are considered to be viscoelastic: they deform slowly under a load or adopt a new shape after the load is removed. Often, viscoelastic behaviors of a tissue are reported in terms of a combination of springs (elastic elements) and dashpots (viscous elements), but these are only convenient mathematical representations and do not necessarily mean that the tissue consists of microscopic springs and fluids. The behavior of the material to a constant force or stress applied between time points '1' and '2' (see the figure A1, part d) shows whether it is considered to be elastic (material deforms immediately once force is applied or removed), viscous (material slowly deforms once force is applied and does not return to original shape once force is removed) or viscoelastic (material slowly deforms once force is applied but returns to the original shape once the force is removed).

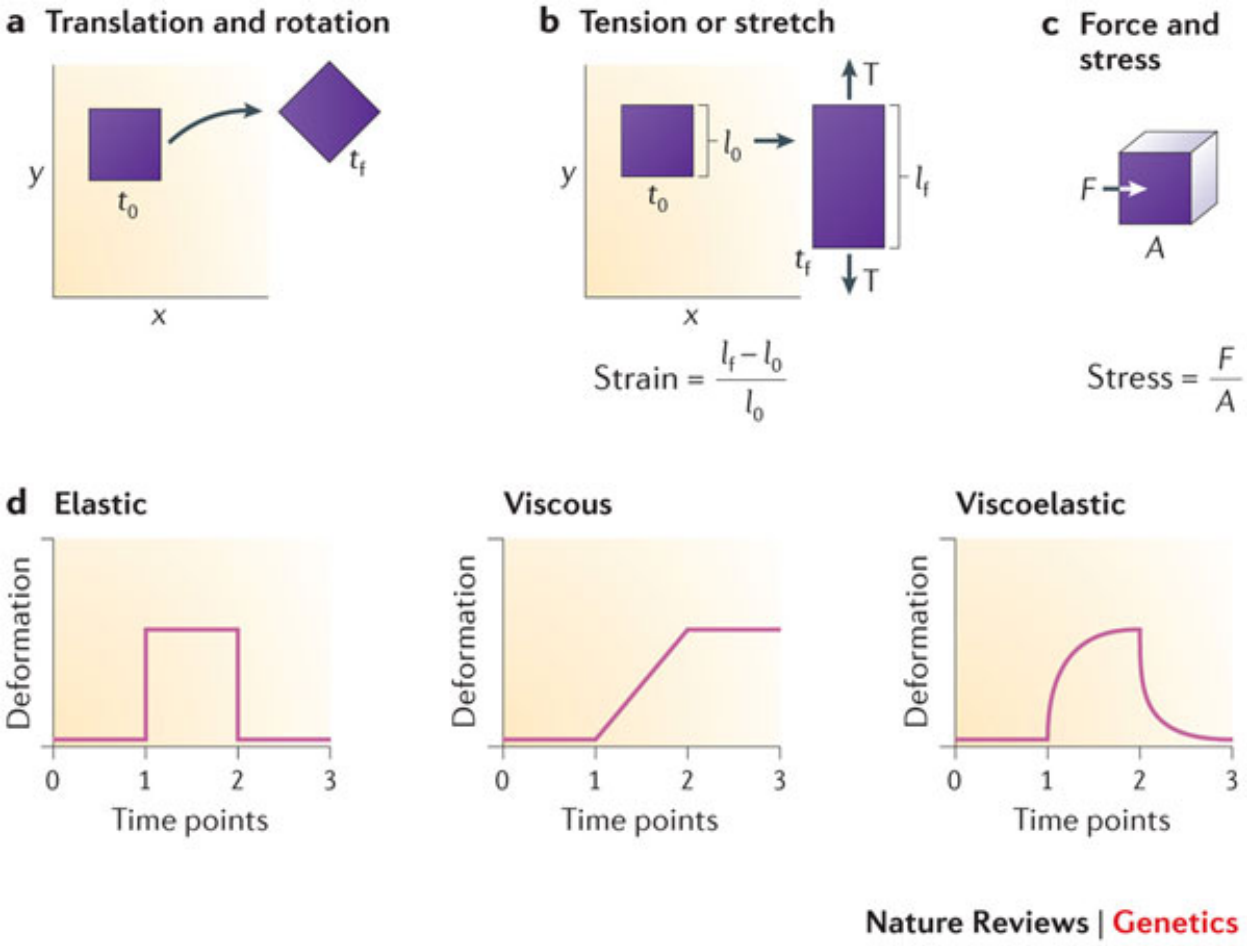

Figure A1: Engineering Principles and Terms

A.4 TOOLS USED TO MEASURE AND DETERMINE MECHANICAL PROPERTIES

Cutting tissue to determine stresses

One cannot easily 'see' stress in tissues, so to determine the mechanical stresses within a tissue early experimentalists turned to physically cutting tissues or attaching them to deformable substrates. Laser cutting allows for a specific area of the tissue, such as a portion of the epithelial layer, to be targeted and ablated with a high-powered laser. After laser ablation, measurements are taken of the recoil of the surrounding cells and tissue within the first few seconds to infer the mechanical state of the tissue, including the forces, such as tension, that were present in order to hold the tissue together before ablation [Beloussov et al., 1990, Ma et al., 2009, Rodriguez-Diaz et al., 2008, Benazeraf et al., 2010, Varner et al., 2010]. Another strategy involves fixing a tissue to a deformable substrate, such as a silicone membrane, that can be mechanically manipulated [Eisenhoffer et al., 2012, Beloussov et al., 1988]. This approach allows precise control over the magnitude and rate at which local mechanical conditions are changed. Investigation of the stress at the cellular and tissue scales, however, involves two different approaches: laser cutting and microsurgery. Similarly to laser cutting, microsurgery can be used to investigate the local mechanics of a tissue, but it can also be used to isolate tissue-specific mechanical processes without the influence of the surroundings of the tissue, which greatly simplifies the system.

Measuring deformation and strain

Because mechanical properties are a measure of the ratio of deformation under externally or internally applied forces, quantifying the deformation and calculating the strain is the first step in estimating the stresses and forces that are present in the tissue. Live cell and tissue imaging plays a key part in these measurements. Confocal time-lapse microscopy allows quantitative analysis of cell movements and shape changes that can be related to deformation and engineering strain. Because the big questions are how tissues and cells generate forces and what forces are acting on cells and tissues during morphogenesis, analysis must be framed by assumptions about the basic mechanical nature of the cells and surrounding tissues [Beloussov et al., 1975, Sokolow et al., 2012, Peralta et al., 2008]. Other crucial as-

pects of measuring and quantifying deformations involve deducing additional principles that guide moving tissues and developing new models and methods to test these new principles. Examples of such methods include measuring the gradient velocities of moving cells [Blanchard et al., 2009] and identifying geometries that are common to developing tissues and deducing the reason behind these emergent geometries [Gibson et al., 2006].

Engineering-based tensile and compression tests

The physiologically relevant mechanical properties of the tissue or embryo can be determined using micro indentation compression tests or micro aspiration tensile tests. From these tests, the stiffness of the tissue can be calculated and can be used in conjunction with cutting experiments to complete the mechanical profile of morphogenic tissues. There are many different tools available for carrying out tensile or compression tests, such as the nanoNewton Force Measuring Device (nNFMD [Zhou et al., 2009, Zhou et al., 2010b]), glass or metal needles [Wiebe and Brodland, 2005b, Zamir and Taber, 2004], parallel plate compression [Davidson et al., 1999, Foty et al., 1996, Forgacs et al., 1998], and microaspiration [von Dassow et al., 2010]. Furthermore, tools designed to measure mechanical properties of the whole embryo can be combined with tools that perturb mechanics such as electrical stimulation [von Dassow et al., 2010], laser activation of proteins or nano-perfusion to reveal ways in which electrophysiological and biochemical pathways might interface with mechanical pathways [Joshi et al., 2010].

A.5 COMPUTATIONAL APPROACHES TO MODELING MECHANICS IN DEVELOPMENT

Theory and computer simulation are routinely used in mechanical engineering and developmental mechanics to test the plausibility of new hypotheses and to aid the interpretation of complex mechanical experiments. Modeling allows one to assess the contribution of specific aspects of an experiment that are difficult to control experimentally: for example, the rates of actin polymerization. Furthermore, because the models are explicitly defined, *in silico* experiments and the resulting kinematic can provide insights into which aspects of the biology

are most important. These tools can suggest new research directions by identifying aspects of the biology that most affect the overall mechanics and behavior of the cells and tissue.

Theoretical and computational tools can take many forms, but the process of creating the models is mostly uniform. For example, when observing the formation of the heart tube, one study began by characterizing the *in vivo* folding and then creating a model that describes the necessary stresses the tube would experience in order to replicate the same folding. The researchers further validated the theoretical model by creating computational simulations with finite element techniques that they used to match their model to the experimental results [Zamir and Taber, 2004, Voronov and Taber, 2002, Zamir et al., 2003]. Other notable models include those of sea urchin primary invagination [Davidson et al., 1995, Davidson et al., 1999], head-fold formation in the avian embryo [Varner et al., 2010], coordination of cell behaviors during ascidian gastrulation [Sherrard et al., 2010], ventral furrow formation in *Drosophila melanogaster* [Odell et al., 1981, Brodland et al., 2010] and looping of the gut [Savin et al., 2011].

Computer simulation is a common strategy for dealing with an 'ill-posed' problem, in which there is incomplete understanding of the biology of a particular mechanical process. For example, in trying to understand which cellular behaviors contribute to the mechanical morphogenetic event of convergent extension, one group created a cellular finite element model in which the different cellular behaviors could be implemented (see the figure A2). This allowed them to determine which emergent behavior of the model (that is, external force-driven reshaping (see the figure A2, part a), lamellipodium-driven reshaping (see the figure A2, part b); the white tubes indicate the lamellipodia which are membrane-like extensions seen at the leading edge of motile cells) or mitosis-driven reshaping (see the figure A2, part c)) was most closely correlated to experimentally observed tissue shape and behavior [Brodland and Veldhuis, 2012]. Computer simulations can be used to test the basic plausibility of a hypothesis. The best simulations and models are ones in which the behavior is emergent and predictive on the basis of a few fundamental facts about cell and tissue behavior, and in which the outcome that emerges closely correlates with both existing observations and those from new experiments.

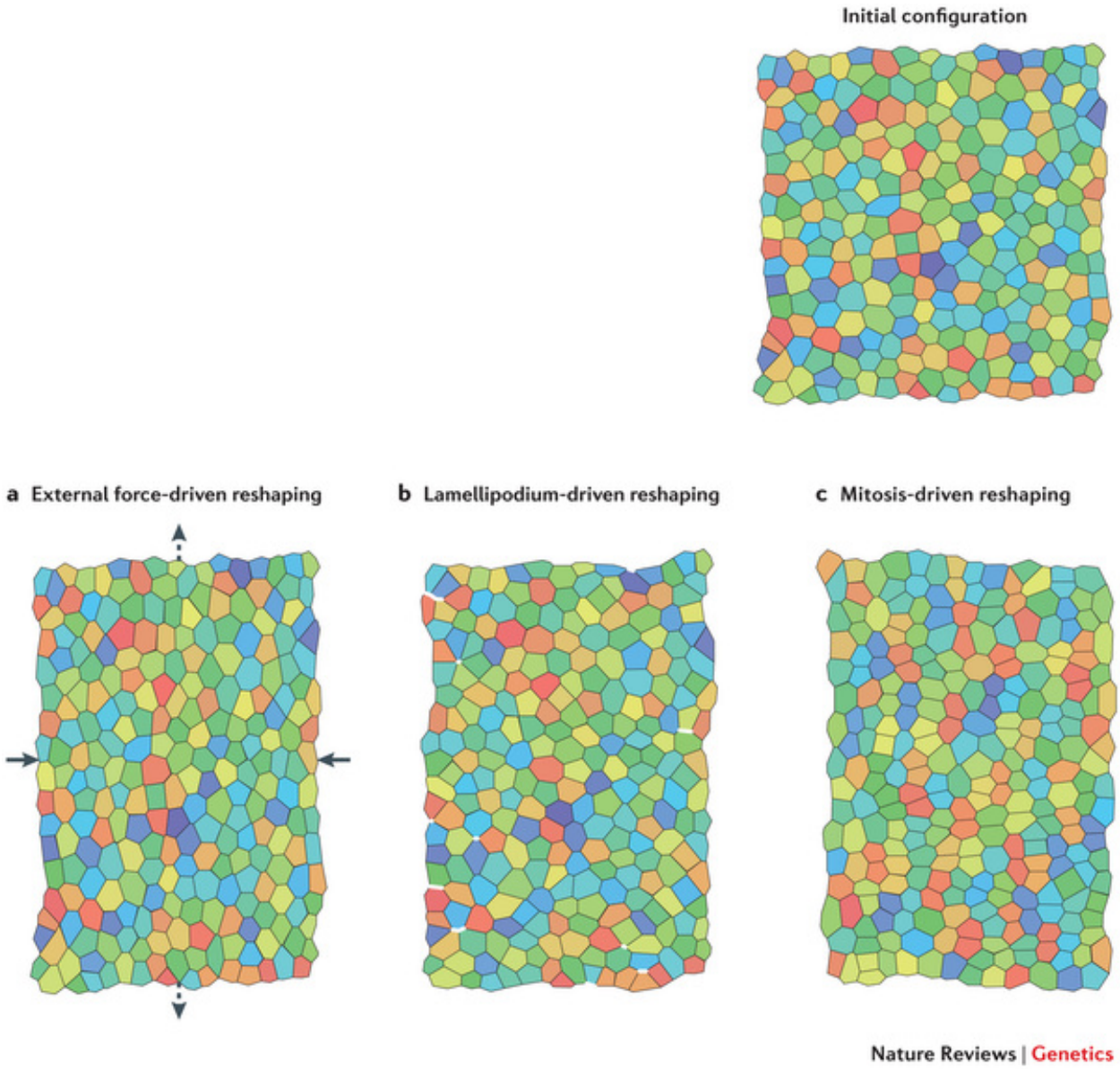

Figure A2: Computational modeling of convergent extension [Brodland and Veldhuis, 2012]

APPENDIX B

ROTATIONAL MODEL APPENDICES AND SUPPLEMENT

B.1 DERIVING THE EQUATIONS OF MOTION

We begin with the vector defining the position of the motor along filament j ($x_j = s(\cos\theta_j, \sin\theta_j)$ for $j = 1, 2$), and derive the potential and kinetic energy for the system (Equation B.1), where k is the spring constant and m is the mass of the motor.

$$\begin{aligned} \text{P.E.} &= k||\vec{x}_1 - \vec{x}_2||^2 = ks^2[1 - \cos(\theta_2 - \theta_1)] \\ \text{K.E.} &= \frac{1}{2}m\left(||\dot{\vec{x}}_1(t)||^2 + ||\dot{\vec{x}}_2(t)||^2\right) = \frac{1}{2}ms^2[\dot{\theta}_1^2 + \dot{\theta}_2^2] + \frac{1}{2}mv^2. \end{aligned} \tag{B.1}$$

In order to obtain equations of motion from the potential and kinetic energy equations, we consider the Lagrangian equations (Equation B.2).

$$\frac{\partial}{\partial t}\left(\frac{\partial \text{K.E.}}{\partial \dot{\theta}_i}\right) - \frac{\partial \text{K.E.}}{\partial \theta_i} = \frac{\partial \text{P.E.}}{\partial \theta_i} \tag{B.2}$$

We assume that motors operate without a drag force, based on the known sizes of myosin. However, we do consider a viscous damping term (μ) which opposes the movement of actin filaments and is analogous to the friction the filaments might experience when moved through water. Substituting into the potential and kinetic energies equations for filaments 1 and 2, we can explicitly derive our Lagrangian equations (Equation B.3).

$$\begin{aligned} ms^2\ddot{\theta}_1 + \mu\dot{\theta}_1 &= ks^2\sin(\theta_2 - \theta_1) \\ ms^2\ddot{\theta}_2 + \mu\dot{\theta}_2 &= ks^2\sin(\theta_1 - \theta_2) \end{aligned} \tag{B.3}$$

Since the masses of the motor and filaments are small, we ignore the momentum term and solve for the equations of motion for the change in filament angle (Equation B.4; Equation 3.1 in the main text).

$$\begin{aligned} \dot{\theta}_1 &= \frac{k}{\mu} s^2 \sin(\theta_2 - \theta_1) \\ \dot{\theta}_2 &= \frac{k}{\mu} s^2 \sin(\theta_1 - \theta_2). \end{aligned} \tag{B.4}$$

B.2 SOLVING THE COUPLED INTEGRO-PARTIAL DIFFERENTIAL EQUATIONS

For the distribution Q_j which denotes a stationary solution, we can write an equation for force ($\langle s^2 \rangle$) and the order parameter (Z):

$$\langle s^2 \rangle = \int_{-\pi}^{\pi} \int_0^L Q_1(\phi, s) s^2 ds$$

$$Z = \int_{-\pi/2}^{\pi} \cos\phi/2 \left(\int_0^L Q_1(\phi, s) ds + Q_0(\phi) ds \right) d\phi$$

The histogram of the values of the angle difference, ϕ, is a plot of $Q_M(\phi) = Q_0(\phi) + \int_0^L Q_1(\phi, s) ds$, the marginal distribution of the angles. These stationary solutions are represented by a pair of coupled integro-partial-differential equations and are generally difficult to solve numerically or analytically. However, in this case we can get a closed expression for the filament distributions and thus an exact expression for our torque-like term, $\langle s^2 \rangle$ (Equation 10). We can then use this distribution to approximate the dependence on the difference in angles, ϕ, and estimate the order parameter Z.

The marginal densities with respect to the motor distance down the filament pair, s, is found by integrating $Q_{0,1}$ with respect to ϕ:

$$\begin{aligned} 0 &= \int_{-\pi}^{\pi} \left(-v \partial_s Q_1(\phi, s) + \frac{k}{\mu} \partial_\phi [\sin\phi Q_1(\phi, s)] - (r_1 + r_2) Q_1(\phi, s) \right) d\phi \\ 0 &= \int_{-\pi}^{\pi} \left(v Q_1(\phi, s) + \int_0^L \left[r_1 Q_1(\phi, s) + \frac{1}{2\pi} \int_{-\pi}^{\pi} Q_1(\theta, s) \, d\theta \right] ds - r_0 Q_0(\phi) \right) d\phi. \end{aligned} \tag{B.5}$$

Let

$$W_1(s) = \int_{-\pi}^{\pi} Q_1(\phi, s)\ d\phi$$
$$W_0(s) = \int_{-\pi}^{\pi} Q_0(\phi)\ d\phi$$

denote the marginal densities. Then from Equation B.5, we see that

$$0 = -vW_1' - (r_1 + r_2)W_1 \tag{B.6}$$
$$0 = vW_1(L) - r_0 W_0 + (r_1 + r_2)\int_0^L W_1(s)\ ds \tag{B.7}$$
$$W_1(0) = \frac{r_0}{v} W_0. \tag{B.8}$$

Finally, we must have the normalization:

$$W_0 + \int_0^L W_1(s)\ ds = 1.$$

Remarkably, the marginal density for the motor position involves no unknown integrals with respect to ϕ and so we can solve it exactly. Furthermore, we can easily compute $\langle s^2 \rangle$. To save on some notational headaches, we set $L = 1$ without loss in generality. We also note that as far as the marginal motor position is concerned, r_1 and r_2 serve only to dislodge the motors; this is evident by the observation that they always appear as a sum $r_1 + r_2$. For the moment, we absorb the effects of r_2 into an effective r_1 to simplify the algebra. That is, if $r_1 = 0.1$ and $r_2 = 0.05$, as was the case in Figure 3.3 from the paper, then the effective r_1 is 0.15, the sum. Equation (B.6) and the boundary condition in Equation B.8 imply

$$W_1(s) = \frac{r_0}{v} W_0 \exp\left(-\frac{r_1}{v} s\right).$$

Normalization allows us to solve for W_0:

$$W_0 = \frac{r_1}{v(r_1 + r_0(1 - e^{-r_1/v}))},$$

So that

$$W_1(s) = \frac{r_0 r_1}{v} \frac{e^{-r_1 s/v}}{r_1 + r_0(1 - e^{-r_1/v})}. \tag{B.9}$$

We can now integrate Equation B.9 against s^2 to compute:

$$\langle s^2 \rangle = \frac{r_0}{r_1^2} \frac{2v^2 - e^{-r_1/v}(2v^2 + 2vr_1 + r_1^2)}{r_1 + r_0(1 - e^{-r_1/v})}. \tag{B.10}$$

Equation B.10 allows us to see how the optimal velocity depends on the parameters. If we set the derivative of Equation B.10 to zero, we get an expression to determine the maximum. It is not possible to solve the resulting derivative for v since the equation involves a mix of exponentials and rational functions. However, we can solve the resulting equation for r_0 and thus we obtain an expression, $r_0 = \rho_0(v, r_1)$ such that Equation B.10 is maximal. Figure B1 shows plots of this expression for three different values of r_1. The way to interpret this plot is to, say, fix $r_0 = 1$, $r_1 = 1$ then observe that this corresponds to a value of $v \simeq 0.8$ on the red curve (which corresponds to $r_1 = 1$). As $r_0 \to 0$, the three curves appear to intersect the v-axis at values which depend on r_1. In the loglog plot (Figure B1), all three curves asymptote with the same slope, the translation depends only on r_1. The intersection with the v-axis can be found by letting r_0 tend to zero in the expression for $\partial F/\partial v$; we find that this expression vanishes when

$$\exp(r_1/v) = 1 + r_1 v + (1/2)(r_1/v)^2 + (1/4)(r_1/v)^3.$$

There is a unique positive root, $r_1/v \simeq 1.45$, so we see that for r_0 small, the optimal velocity is linearly proportional to r_1. We can also understand this intuitively. As r_0 tends to zero, this means we spend a great deal of time with the motor unattached to the filaments. We thus want to choose v to maximize the amount of time spent on the filaments and in particular, we want to choose v so that we get as far out as possible toward the ends of the filaments where the most work is done. Since the expected time to remain on the filament is $1/r_1$, then by choosing $v \simeq r_1$, we can get to the end of the filament before falling off while at the same time, not going so fast that we reach the ends. The linear asymptotes in the loglog plot can also be easily found by letting $v \to \infty$ whence, we find that $v \sim \sqrt{r_1 r_0}/2$. This is satisfying since it says that for large rates, the optimal velocity is the geometric mean of the rate of falling off and the rate of attaching.

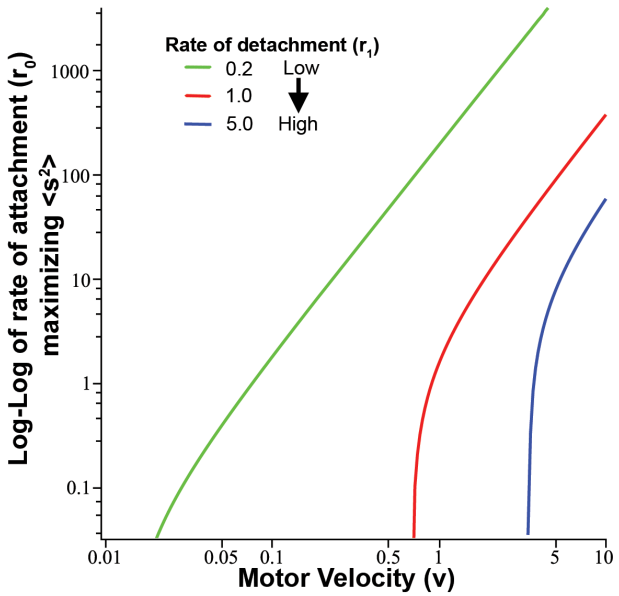

Figure B1: **Examining the relationship between attachment and detachment rates on optimal motor velocity for maximizing force.** The curves depict the maximal values of force for two filaments and one motor with varying rates of detachment and attachment, and the resulting optimal motor velocity. The green curve depicts a small rate of detachment ($r_1 = 0.2/s$), the red curve a medium rate of detachment ($r_1 = 1.0/s$), and the blue curve a high rate of detachment ($r_1 = 5/s$). For the curves we do not consider the rate of polymerization, but we are able to deduce the relationship between all the variables that affect force.

B.3 CALCULATING THE MARGINAL DENSITY OF THE ANGLE DIFFERENCES

We now turn to the marginal density of the angle differences. To obtain an equation for this, we integrate Equation B.5 with respect to s. Let $S_0(\phi) = Q_0(\phi)$ and let $S_1(\phi) = \int_0^L Q_1(\phi, s)\, ds$. Note that $S_{0,1}(\phi)$ are the densities for the angle between the filaments when the motors are off, on respectively and independent of the motor position. $S_1(\phi)$ satisfies

$$0 = v[Q_1(\phi, 0) - Q_1(\phi, L)] + \int_0^L s^2 \frac{k}{\mu} \frac{\partial \sin\phi Q_1(\phi, s)}{\partial \phi}\, ds - (r_1 + r_2) S_1(\phi).$$

Unfortunately, this expression does not just involve S_1, but also requires knowledge of the joint distribution, $Q_1(\phi, s)$. We now make an approximation; we suppose that $Q_1(\phi, s) = S_1(\phi) W_1(s)$. That is, we assume that the variables s and ϕ are independent.While it is true that the value of s is independent of ϕ (which is why we could solve for the marginal density, $W_1(s)$), the angle difference, ϕ should depend on s as this governs the effective strength of the spring. With this approximation, we get

$$\begin{aligned} 0 &= v[W_1(0) - W_1(L)] S_1(\phi) + \frac{k\langle s^2 \rangle}{\mu} [\sin\phi S_1(\phi)]' \\ &\quad -(r_1 + r_2) S_1(\phi) \qquad \text{(B.11)} \\ 0 &= v W_1(L) S_1(\phi) + r_1 S_1(\phi) - r_0 S_0(\phi) \\ &\quad + r_2 \frac{1}{2\pi} \int_{-\pi}^{\pi} S_1(\psi)\, d\psi \qquad \text{(B.12)} \\ v S_1(\phi) W_1(0) &= r_0 S_0(\phi) \qquad \text{(B.13)} \end{aligned}$$

Equation B.13 is the approximate boundary condition. Let $\bar{S}_1 = 1/(2\pi) \int_{-\pi}^{\pi} S_1(\phi) d\phi$ and $X_2 := \langle s^2 \rangle$. Then we can solve Equation B.12 to get

$$r_0 S_0 = v W_1(L) S_1(\phi) + r_1 S_1(\phi) + r_2 \bar{S}_1$$

and use Equation B.13 to obtain a single equation for $S_1(\phi)$:

$$\frac{d}{d\phi}[\sin\phi S_1] = \frac{\mu r_2}{k X_2} [S_1 - \bar{S}_1] \qquad \text{(B.14)}$$

For notational simplicity, let $r = (\mu r_2)/(kX_2)$. In order to solve Equation B.14, we observe that it is symmetric about zero, and singular at $-\pi$, 0, and π. So we just have to solve it in the interval $(0, \pi)$, and then can reflect this solution about zero to obtain the solution for the interval $(-\pi, 0)$. Then, we must take appropriate limits. We remark that it is not necessary that $S_1(\phi)$ has a well-defined limit as $\phi \to 0$; we only require integrability. For simplicity we let $S_1(\pi/2) = 1$, which we can always scale later since Equation B.14 is linear and homogeneous in S_1. (The actual value will come about from normalization). Solving the ODE, we obtain

$$S_1(\phi) = \left[1 - r\bar{S}_1 \int_{\frac{\pi}{2}}^{\phi} \left(\frac{1-\cos\psi}{\sin\psi}\right)^{-r} d\psi\right] \left[\frac{1-\cos\phi}{\sin\phi}\right]^r \frac{1}{\sin\phi} \tag{B.15}$$

We rewrite the expression for S_1 as

$$\begin{aligned} S_1(\phi) &= F(\phi)\left(\tan\frac{\phi}{2}\right)^r \frac{1}{\sin\phi} \\ F(\phi) &= 1 - ra\int_{\frac{\pi}{2}}^{\phi} (\cot\frac{\psi}{2})^r d\psi \\ m &= \bar{S}_1 \end{aligned}$$

We notice that $\left(\tan\frac{\phi}{2}\right)^r \frac{1}{\sin\phi}$ goes towards infinity like the function $(\pi-\phi)^{-(r+1)}$ as ϕ goes to π, which is not integrable on our interval of $(0, \pi)$. So in order for $S_1(\phi)$ to be integrable on the interval of $(0, \pi)$, $F(\pi)$ must go to zero as ϕ goes to π. We choose a to make $F(\phi) \to 0$. Then, applying L'Hopital's rule it is easy to show that $\lim_{\phi\to\pi} S_1(\phi)$ is finite. Next, we need to address the case of ϕ going to zero. We can approximate the behavior of $F(\phi)$ as $\phi \to 0$ as the function $k_1\phi^{1-r}+k_2$, and $\tan(\phi/2)^r/\sin\phi$ as the function ϕ^{r-1}. Then $S_1(\phi) \approx k_1+k_2\phi^{r-1}$, which is singular for $0 < r < 1$ near $\phi = 0$, but is integrable. So if we integrate $S_1(\phi)$ from zero to π, we find, using integration by parts the following:

$$\begin{aligned} \int_0^{\pi} S_1(\phi)\, d\phi &= \frac{1}{r}\left[\left(\tan\frac{\phi}{2}\right)^r \left(1 - ra\int_{\pi/2}^{\phi} \cot\left(\frac{\psi}{2}\right)^r d\psi\right)\right]_0^{\pi} \\ &- \frac{1}{r}\int_0^{\pi} \frac{\left(\tan\frac{\phi}{2}\right)^r}{r}\left(-ra\cot\left(\frac{\phi}{2}\right)^r\right) d\phi \\ &= 0 + a\pi = a\pi. \end{aligned}$$

We use L'Hopital's rule to show the first expression is zero. This integration shows that $\int_{-\pi}^{\pi} S_1(\phi) = 2\pi a$ so that $\bar{S}_1 = a$ as required for self-consistency. We can rewrite the expression and use Equation B.12 to write:

$$S_1(\phi) = \frac{1}{\sin\phi} \tan^r \frac{\phi}{2} \int_{\phi}^{\pi} \cot^r \frac{\psi}{2}\, d\psi \tag{B.16}$$

$$S_0(\phi) = \frac{1}{r_0} \left[(vW_1(L) + r_1)\, S_1(\phi) + r_2 a \right]. \tag{B.17}$$

B.4 DETERMINING THE STABILITY OF THE TRIVIAL STATE

We write $P_1(\theta, s, t) = (1/2\pi)W_1(s) + p_1(\theta, s, t)$ and $P_0(\theta, t) = (1/2\pi)W_0 + p_0(\theta, s, t)$ and find that to linear order:

$$\frac{\partial p_1}{\partial t} = -v\frac{\partial p_1}{\partial s} - K\frac{W_1(s)}{2\pi}\frac{\partial}{\partial\theta}\left(\int_0^L \int_{-\pi}^{\pi} \sin(\theta' - \theta) s^2 p_1(\theta', s, t)\; ds\; d\theta'\right) - (r_1 + r_2)p_1 \tag{B.18}$$

$$\frac{\partial p_0}{\partial t} = vp_1(\theta, L, t) - r_0 p_0 + \int_0^L \left(r_1 p_1(\theta, s', t) + \frac{1}{2\pi}\int_{-\pi}^{\pi} r_2 p_1(\theta', s', t)\; d\theta' \right)\; ds' \tag{B.19}$$

$$p_1(\theta, 0, t) = \frac{r_0}{v} p_0(\theta, t). \tag{B.20}$$

Where $K = \frac{kM}{\mu N}$, M is the number of motors and N is the number of filaments. In addition, we must have the normalization of the perturbation

$$\int_0^L \int_{-\pi}^{\pi} p_1(\theta, s, t) + p_0(\theta, t)\; d\theta\; ds = 0.$$

Equation B.18 is a convolution in θ and is homogeneous with respect to t and θ, so that we can look for solutions of the form

$$p_1(\theta, s, t) = \psi_1(s) e^{im\theta} e^{\lambda t}$$

$$p_0(\theta, t) = \psi_0 e^{im\theta} e^{\lambda t}$$

where m is an integer and ψ_j are unknown. If, for some m, the real part of λ is positive, then solutions will grow with respect to that mode, m, and the completely disordered state

will be unstable. We plug this form into Equations B.18-B.20 to get a sequence of linear eigenvalue problems. We consider three distinct cases: $m = 0$, $m = 1$, and $m \geq 2$. First, we will address the first and last cases, and then turn to the more difficult $m = 1$ case. The cases for which $m \neq 1$ are simplest because the integral term in Equation B.18 vanishes since the convolution over θ involves only $\sin\theta$.

B.4.1 Case 1: $m = 0$

When $m = 0$, the eigenvalue problem is

$$\begin{aligned} \lambda\psi_1 &= -v\psi_1' - (r_1 + r_2)\psi_1 \\ \lambda\psi_0 &= v\psi_1(L) - r_0\psi_0 + (r_1 + r_2)\int_0^L \psi_1(s')\, ds'. \end{aligned}$$

The solution to the first equation along with the boundary condition implies

$$\psi_1(s) = \frac{r_0\psi_0}{v} e^{-(\lambda + r_1 + r_2)s/v}.$$

We exploit a special property of $m = 0$. The normalization implies that

$$\psi_0 + \int_0^L \psi_1(s')\, ds' = 0.$$

Plugging the formula for $\psi_1(s)$ into the normalization yields

$$\psi_0 + \psi_0 \frac{r_0}{\lambda + r_1 + r_2}\left[1 - \exp(-[\lambda + r_1 + r_2]L/v)\right] = 0.$$

Dividing by ψ_0 and rearranging, we get

$$(\lambda + r_1 + r_2 + r_0)e^{\lambda L/v} = r_0 e^{-(r_1 + r_2)L/v}$$

Multiply both sides by L/v and call $z = \lambda L/v$ to obtain

$$e^z z + a e^z = b$$

where $a = (r_1 + r_2 + r_0)L/v$ and $b = r_0(L/v)\exp(-(r_1 + r_2)L/v)$. We rewrite one more time as

$$-ae^z + b - ze^z = 0.$$

Bellman and Cooke [Bellman and Cooke, 1963] prove that all roots, z to this equation have negative real parts if and only if $-a < 1$, $-a < -b$, and one more condition that requires that $-b$ be less than a positive number. Clearly all three conditions hold since $a > b > 0$. Thus, we conclude that with respect to perturbations with $m = 0$, the trivial state is stable.

B.4.2 Case 2: $m > 1$

When $m > 1$, then the eigenvalue equation is

$$\begin{aligned} \lambda\psi_1 &= -v\psi_1' - (r_1 + r_2)\psi_1 \\ \lambda\psi_0 &= v\psi_1(L) - r_0\psi_0 + r_1 \int_0^L \psi_1(s')\, ds'. \end{aligned}$$

As in the $m = 0$ case, we have

$$\psi_1(s) = \frac{r_0\psi_0}{v} e^{-(\lambda + r_1 + r_2)s/v}.$$

Unfortunately, we can no longer make use of the normalization condition since $\int_{-\pi}^{\pi} e^{im\theta}\, d\theta = 0$ for $m \neq 0$. We now plug this into the second equation to obtain

$$\lambda = -r_0 \left(1 - \frac{r_1}{\lambda + r_1 + r_2}\right) \left(1 - e^{-(\lambda + r_1 + r_2)L/v}\right).$$

There are no positive values of λ that satisfy this equation since the right-hand side will be negative. We can rewrite the equation as

$$\frac{\lambda(\lambda + r_1 + r_2)}{\lambda + r_2} = -r_0 \left(1 - e^{-\lambda L/v} e^{-(r_1 + r_2)L/v}\right). \tag{B.21}$$

For L/v large enough, there can be no roots with positive real parts since the right-hand side goes to $-r_0$ and thus, we must have

$$\lambda(\lambda + r_1 + r_2) + r_0(\lambda + r_2) = 0$$

which has only roots with negative real parts. Thus, as L/v gets smaller, the only way to get positive real parts is that a root must have a zero real part. Since we have eliminated any

possible real zero roots, we must then have an imaginary root, $i\omega$. In this case we substitute $\lambda = i\omega$ into Equation B.21 and obtain

$$\frac{r_1\omega^2}{r_2^2+\omega^2} + i\frac{\omega(r_2r_1+r_2^2+\omega^2)}{r)2^2+\omega^2} = -r_0\left(1-e^{-(r_1+r_2)L/v}e^{i\omega L/v}\right).$$

As ω varies, the right-hand side traces out a circle centered on the real axis and entirely in the left-half plane. The left-hand side traces out a curve that is in the right-half plane. Thus, there can never be an intersection so that there can never be an imaginary root. Thus there is no way to get roots with a positive real part as L/v varies and we conclude that all roots to Equation B.21 must have negative real parts.

B.4.3 Case 3: $m = 1$

We finally turn to the most interesting case. So far, we have seen that perturbations in modes of the form $\exp(im\theta)$ where $m \neq 1$ decay exponentially. For $m = 1$, the linear equation is

$$\begin{aligned}
\lambda\psi_1 &= -v\psi_1' - (r_1+r_2)\psi_1 + \frac{K}{2}W_1(s)\int_0^L s'^2\psi_1(s')\,ds'. \\
\lambda\psi_0 &= v\psi_1(L) - r_0\psi_0 + r_1\int_0^L \psi_1(s')\,ds' \\
\psi_1(0) &= \frac{r_0}{v}\psi_0.
\end{aligned}$$

One could solve these linear equations explicitly to find an equation for the eigenvalues, λ. However, the resulting equation is very complicated and offers little analytic insight. Thus, rather take the difficult approach, we make the following observations. First, if $K = 0$, then the eigenvalue equations are the same as for the $m \geq 2$ case and we know that there are no eigenvalues with positive real parts. Thus, we can ask if increasing K can cause some of these "stable" eigenvalues to cross the imaginary axis. There are two ways that this can happen: (i) a negative real eigenvalue becomes a positive real eigenvalue; or (ii) a pair of complex conjugate eigenvalues crosses at an imaginary eigenvalue. Our numerical simulations show that the alignment seems to always produce a *stationary* peak rather than a peak that rotates at a constant velocity. This empirical fact suggests that the loss of stability of the uniform state occurs through a *real* eigenvalue crossing zero as in the second

case, time periodic (rotating) solutions would be expected. Thus, we will ask if there is a value of K such that there is a zero eigenvalue. Hence we must solve

$$\begin{aligned} 0 &= -v\psi_1' - (r_1 + r_2)\psi_1 + \frac{K}{2} W_1(s) \int_0^L s'^2 \psi_1(s')\, ds'. \\ 0 &= v\psi_1(L) - r_0\psi_0 + r_1 \int_0^L \psi_1(s')\, ds' \\ \psi_1(0) &= \frac{r_0}{v}\psi_0. \end{aligned}$$

There is one differential equation and two algebraic conditions, so we cannot expect there to be a nonzero solution for any K. However, picking the correct K will tell us the critical value, K above which there will be alignment and below which there will be a uniform distribution of filament angles. For notational simplicity, we write $\psi_1(s) = \psi_0\phi(s)$, $\sigma := (r_1 + r_2)/v$, and $W_1(s) = A\exp(-\sigma s)$. Let

$$D := \int_0^L s^2\phi(s)\, ds.$$

Then $\phi(s)$ satisfies

$$\frac{d\phi}{ds} = -\sigma\phi + \frac{KAD}{2v} e^{-\sigma s}$$

which with the boundary condition yields

$$\phi(s) = \left(\frac{r_0}{v} + \frac{KAD}{2v} s \right) e^{-\sigma s}.$$

Let

$$\mu_n := \int_0^L s^n e^{-\sigma s}\, ds.$$

Then the unknown constant, D satisfies

$$D = \int_0^L s^2\phi(s)\, ds = \frac{r_0\mu_2}{v} + D\frac{KA\mu_3}{2v}$$

or

$$D = \frac{2r_0\mu_2}{2v - KA\mu_3}.$$

We finally use the equation for ψ_0 to obtain:

$$0 = -r_0\psi_0 + v\psi_0\phi(L) + r_1 \int_0^L \psi_0\phi(s)\, ds.$$

Dividing this by ϕ_0, we obtain an equation of the form:

$$0 = -r_0 + r_0 e^{-\sigma L} + \frac{r_0 r_1}{r_1 + r_2}\left(1 - \exp(-\sigma L)\right) + \frac{KAD}{2v}\left(vLe^{-\sigma L} + r_1\mu_1\right).$$

A final bit of rearranging and use of the definition of D yields

$$\frac{r_0 r_2}{(r_1 + r_2)(Lve^{-\sigma L} + r_1\mu_1)}\left(1 - e^{-\sigma L}\right) = \frac{KAr_0\mu_2}{v(2v - KA\mu_3)}. \tag{B.22}$$

The lefthand side is strictly positive. The righthand side is a function of K which vanishes when $K = 0$ and tends to infinity as K tends to $2v/(A\mu_3)$. Thus, for any parameters, we can find a unique value of K, call it K_{crit} solving Equation B.22:

$$K_{crit} = \frac{2zv^2}{A(zv\mu_3 + r_0\mu_2)} \tag{B.23}$$

where the lefthand side of Equation B.22 is abbreviated as z. Since all of these functions and constants are known, we can plot K_{crit} as a function of any parameter, in particular, v.

Figure B2 shows the value of K_{crit} as the velocity of the motors varies. If $K > K_{crit}$, then there is a real positive eigenvalue and the uniformly distributed orientation is unstable. That is, we expect to see the beginnings of alignment along a single direction. First, note that in all cases the curve has a single minimum value at a particular velocity. K_{crit} goes to infinity as v goes to both 0 and infinity. We can interpret the curves as follows. Suppose for example, that $K = 0.6, r_0 = 0.7, r_1 = 0.1, r_2 = 0.1$. Then for a band of velocities between 0.05 and 0.35, $K > K_{crit}$ so that we expect to see alignment only when the velocity is in this narrow band.

The position of the minimum of K_{crit} is most dependent on $r_1 + r_2$ (compare black, green, and blue curves). The parameter r_0 tends to pull down the right part of the curve; large r_0 makes K_{crit} independent of v for large velocities. This is because, when r_0 is large, you spend almost all your time on the filaments so the velocity doesn't matter so much, there is no "penalty" for going fast.

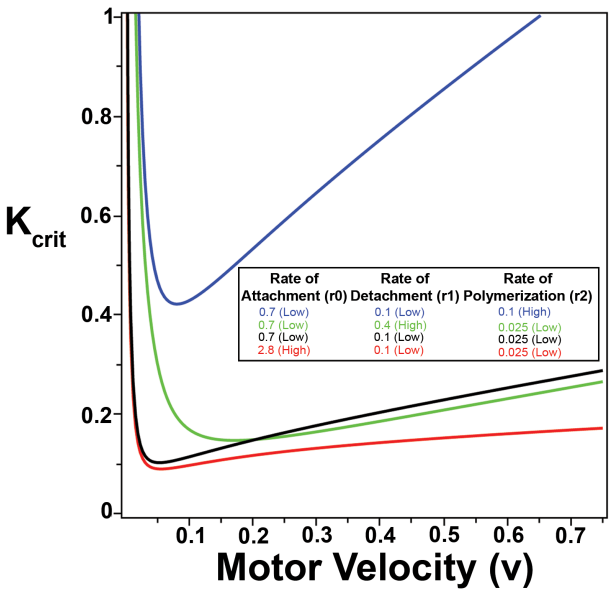

Figure B2: **Determining how K_{crit} is a function of motor velocity** K_{crit} depends on all the variables of the model: motor velocity, and rates of attachment, detachment, and polymerization. The curves specifically show how K_crit depends on motor velocity, but also how it depends on the three variable rates. The blue curve shows a low rate of attachment ($r_0 = 0.7$), a low rate of detachment ($r_1 = 0.1$), and a high rate of polymerization ($r_2 = 0.1$). The rest of the curves are as follows: green ($r_0 = 0.7$ (low), $r_1 = 0.4$ (high), $r_2 = 0.025$ (low)), black ($r_0 = 0.7$ (low), $r_1 = 0.1$ (low), $r_2 = 0.025$ (low)), and red ($r_0 = 2.8$ (high), $r_1 = 0.1$ (low), $r_2 = 0.025$ (low)). Notice that the minimum value of K_crit depends most on the sum of the rate of detachment and polymerization. The asymptotic approximation yields the range of motor velocities for which maximal alignment is expected.

We can use MAPLE to compute an asymptotic approximation for K_{crit} at the extremes of $v \to 0$ and $v \to \infty$. We find that as $v \to 0$,

$$K_{crit} \sim \frac{r_2(r_2 + r_1)(r_2 + r_1 + r_0)}{r_0} \frac{1}{v},$$

and as $v \to \infty$,

$$K_{crit} \sim \frac{6r_2}{r_0} v.$$

The latter is independent of r_1, which makes sense for when v is very large, the probability of ever falling off the filament is virtually zero and the key parameters are the waiting time r_0 and the depolymerization, r_2. We note that for small r_2, both of the asymptotic expressions are proportional to r_2; the more orientation "noise", the larger is the spring strength needed to overcome it. The asymptotic expansions can be added together to get a qualitatively good approximation of the true curve:

$$K_{approx} = \frac{r_2(r_2 + r_1)(r_2 + r_1 + r_0)}{r_0} \frac{1}{v} + \frac{6r_2}{r_0} v.$$

This simple function has a minimum at

$$v = v_{min} := \sqrt{(r_1 + r_2)(r_0 + r_1 + r_2)/6}$$

which is a reasonable approximation of the minimum of K_{crit}. What the minimum tells us is the velocity for which the weakest motors (lowest value of K) could cause some alignment. We emphasize that the analysis here is a linearized analysis, so that it does not necessarily tell us about what happens far from the onset of the alignment instability. Thus, we cannot necessarily infer the optimal velocity from this calculation; we can only determine the range of velocities for which alignment is possible.

B.5 KURAMOTO MODEL SIMILARITIES

$$\frac{\partial P_1(s,\phi,t)}{\partial t} = -v\frac{\partial P_1(s,\phi,t)}{\partial s} - \frac{\partial}{\partial \theta}\left(P_1(s,\phi,t)f(\theta)\right) - (r_1+r_2)P_1(s,\phi,t) \tag{B.24}$$

$$\begin{aligned}\frac{\partial P_0(s,t)}{\partial t} &= vP_1(L,\theta,t) - r_0P_0 + \int_0^L r_1P_1(s',\theta,t)ds' \\ &\quad + \frac{1}{2\pi}\int_0^L\int_{-\pi}^{\pi} r_2P_1(s',\theta',t)\ d\theta' ds'\end{aligned} \tag{B.25}$$

Equations B.24 and B.25 bear a close resemblance to the well-studied Kuramoto model for synchronization of a pool of globally coupled oscillators.

$$\frac{d\theta_i}{dt} = \omega_i + \frac{K}{N}\sum_{j=1}^{N}\sin(\theta_j - \theta_i) + \omega\xi_i$$

In the Kuramoto model, θ_i represents the phase of the ith oscillator, K the coupling strength, ω_i, the uncoupled frequencies of the oscillators and $\sigma\xi_i$ the external noise. In the limit as N goes to infinity, we write an equation for the density, $\rho(\theta,\omega,t)$ of the oscillators:

$$\begin{aligned}\frac{\partial \rho}{\partial t} &= -\frac{\partial}{\partial\theta}\left(\rho(\theta,\omega,t)\left[\omega + K\int_{-\infty}^{\infty} g(\omega)\int_0^{2\pi}\sin(\phi-\theta)\rho(\phi,\omega t)d\phi d\omega\right]\right) \\ &\quad + \frac{\sigma^2}{2}\frac{\partial^2\rho}{\partial\theta^2}\end{aligned}$$

Here $g(\omega)$ is the density for the distribution of oscillator frequencies. There are two sources of disorder in the Kuramoto model, extrinsic noise, σ, and the heterogeneity of the frequencies. In our model, the noise comes from the de/polymerization of the filaments and since the new filaments occur at any angle, the noise does not appear locally as phase diffusion as in the Kuramoto model. Both our equations and the Kuramoto equations have a similar nonlinearity and both equations admit a completely disordered state as a solution. In our analysis and the Kuramoto analysis, the key to the onset of order (synchronization in the Kuramoto model) is that this disorder state becomes unstable as some parameter increases. Thus, while the two equations come from completely different motivating systems, they bear a close resemblance simply because they both describe dynamics of systems which lie on the circle.

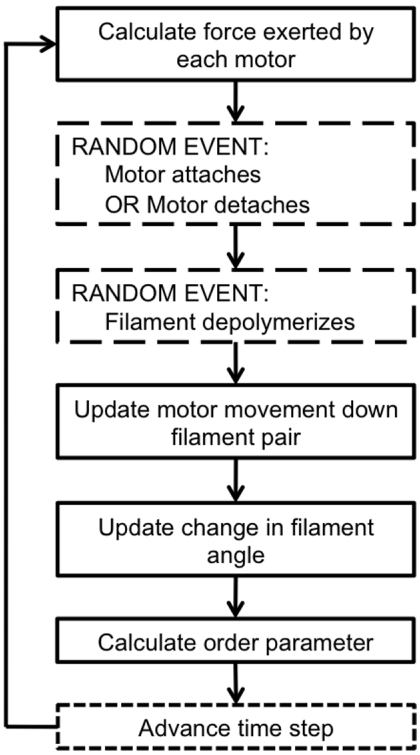

Figure B3: **Algorithm flow chart for Monte Carlo simulations.** Pictorial flow chart describing the Monte Carlo simulation code used in the paper.

Table B1: Parameters and values most often used in the code

Parameter Symbol	Description	Default Value	Units
k	Motor's spring stiffness	1	pg/s^2
μ	Viscous term	1	μm^2/s
L	Filament length	1	μm
r_0	Rate of motor attachment	0.7	1/s
r_1	Rate of motor detachment	0.1	1/s
r_2	Rate of filament polymerization	0.025	1/s

Table B2: Variables for the code

Variable Symbol	Description	Units
T	Time	s
N	Number of filaments	
M	Number of motors	
v	Motor velocity	μm/s
s_j	Motor j's position along the filament	μm
θ_i	Orientation angle of filament i	rad
ϕ	Difference in angle between motor bound filament pair	rad

APPENDIX C

ROTATIONAL MOVIES

C.1 NO POLYMERIZATION

This movie is from a Matlab simulation of the rotation of F-actin-type-rods from processive, non-muscle myosin II-like-springs. Blue lines are the filaments with minus ends pinned at the origin. Red lines are motors attached to two filaments. The green * are motors that have both legs attached to the same filament.

C.2 POLYMERIZATION

This movie is from a Matlab simulation demonstrating our concept of polymerization as a source of angular noise. Blue lines are filaments with minus ends pinned at the origin. Red lines are motors attached to two filaments. The green * are motors that have both legs attached to the same filament. The thick black filaments that flash are new filaments that have reappeared after a polymerization event has occurred.

APPENDIX D

SLIDING MODEL SUPPLEMENT

D.1 SLIDING MODEL: STEADY STATE EQUATIONS

In order to determine how the linear array of filaments will move, we have a series of equations to dictate how the filaments will move based on connected motors, and how the pools of motors are related to each other at steady state. For simplicity, we have included equations for a set of four filaments: two boundary filaments with left and right orientations, and two free filaments with left and right orientations. x_L is the position of the plus end for the left oriented boundary filament, x_R is the position of the plus end for the right oriented boundary filament, x_P is the position of the plus end for a "plus" or right oriented free filament, and x_N is the position of the plus end for a "negative" or left oriented free filament. The left and right boundary filaments will move based on the forces from the boundary spring with stiffness k_0, and attached motors with motor stiffness k_m. The plus and negative free filaments will move only from the influence of attached motors. We sum all attached motors and calculate the motor generated force by considering the stretch of a motor $(y_j - y)$, where y_j is the location of the other "leg" of the attached motor, and y is the location of the attached leg on the filament.

Equations of motion

$$\dot{x}_L = -k_0 x_L + \sum_j k_m(y_j - y_L) \tag{D.1}$$

$$\dot{x}_N = \sum_j k_m(y_j - y_N) \tag{D.2}$$

$$\dot{x}_P = \sum_j k_m(y_j - y_P) \tag{D.3}$$

$$\dot{x}_R = -k_0 x_R + \sum_j k_m(y_j - y_R) \tag{D.4}$$

To determine where motors will be at steady state, we consider the various pools of motors based on their "state" (q): waiting to attach (q_0), one leg on a left boundary filament (q_L), one leg on a plus oriented free filament (q_P), one leg on a negative oriented free filament (q_N), one leg on a right boundary filament (q_R), attached to a pair of left and right boundary filaments (q_{LR}), attached to a left boundary filament and a plus oriented free filament (q_{LP}), attached to a left boundary filament and a negative oriented free filament (q_{LN}), attached to a right boundary filament and a negative oriented free filament (q_{RN}), attached to a pair of free filaments with negative and positive orientations (q_{NP}), and attached to a right boundary filament and a plus oriented free filament (q_{RP}). Motors attach to a filament one leg at a time with an attachment rate of r_1. They detach from a filament one leg at a time with a detachment rate of r_0.

Steady State Equations

$$\dot{q}_0 = -4r_0 q_0 + r_1[q_p + q_N + q_L + q_R] \tag{D.5}$$

$$\dot{q}_L = -4r_1 q_L + r_0[q_0 + q_{LP} + q_{LR} + q_{LN}] \tag{D.6}$$

$$\dot{q}_P = -4r_1 q_P + r_0[q_0 + q_{RP} + q_{NP} + q_{LP}] \tag{D.7}$$

$$\dot{q}_N = -4r_1 q_N + r_0[q_0 + q_{RN} + q_{NP} + q_{LN}] \tag{D.8}$$

$$\dot{q}_R = -4r_1 q_R + r_0[q_0 + q_{RN} + q_{LR} + q_{RP}] \tag{D.9}$$

$$\dot{q}_{LR} = -2r_1 q_{LR} + r_0[q_L + q_R] \tag{D.10}$$

$$\dot{q}_{LP} = -2r_1 q_{LP} + r_0[q_L + q_P] \tag{D.11}$$

$$\dot{q}_{LN} = -2r_1 q_{LN} + r_0[q_L + q_N] \tag{D.12}$$

$$\dot{q}_{RN} = -2r_1 q_{RN} + r_0[q_R + q_N] \tag{D.13}$$

$$\dot{q}_{NP} = -2r_1 q_{NP} + r_0[q_N + q_P] \tag{D.14}$$

$$\dot{q}_{RP} = -2r_1 q_{RP} + r_0[q_R + q_P] \tag{D.15}$$

D.2 SLIDING MODEL EXAMPLE

This movie shows left oriented filaments in blue, and right oriented filaments in red. Motors are shown in black lines and the black * denote motors that only have one leg attached to a filament. The top blue filament and the bottom red filament are the spring-bound filaments (springs to boundaries not shown). When a "free" filament disappears, a new one reappears in the same y-position in the ladder, but has a randomly selected orientation (left or right with equal probability), and a random x-placement.

APPENDIX E

2D MODEL SUPPLEMENT

E.1 SQUARE BOUNDARY CONDITION

To determine whether the single asters observed in our simulations developed as an artifact of a hexagonal boundary, we ran simulations in a square boundary instead of a hexagon (fig E1). We still observed the single, stable contraction, although the geometry of contraction begins as a square ring instead of the circular ring we saw before (fig 5.6) as it transitioned to the final aster structure. The filament plus-end variance increased, but the domain area is likewise larger even though the radius of the square and hexagon are the same. Nevertheless, force and variance still reach a steady state, as quickly as they did for our hexagonal sim.

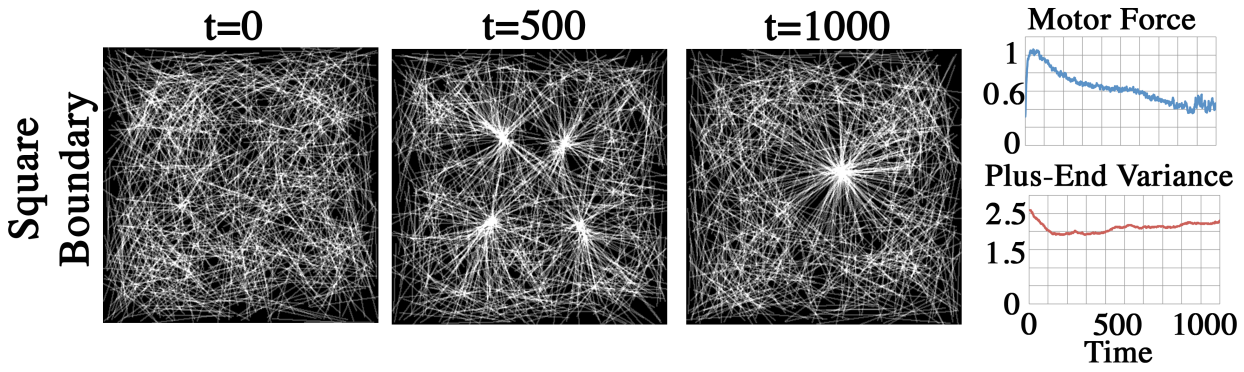

Figure E1: **Testing a square boundary condition**. Simultaion run within a square boundary. The actin still forms an aster structure, with similar force (blue) and variance (red) plots as hexagonal boundary controls.

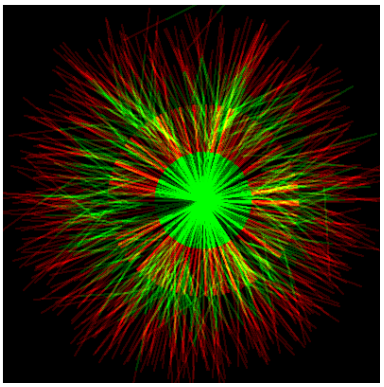

Figure E2: Filaments are color coded so the plus end half is green, and the minus end half is red. This is the case where there is no polymerization ($p_2 = 0$), and the ending morphology at t=1,000.

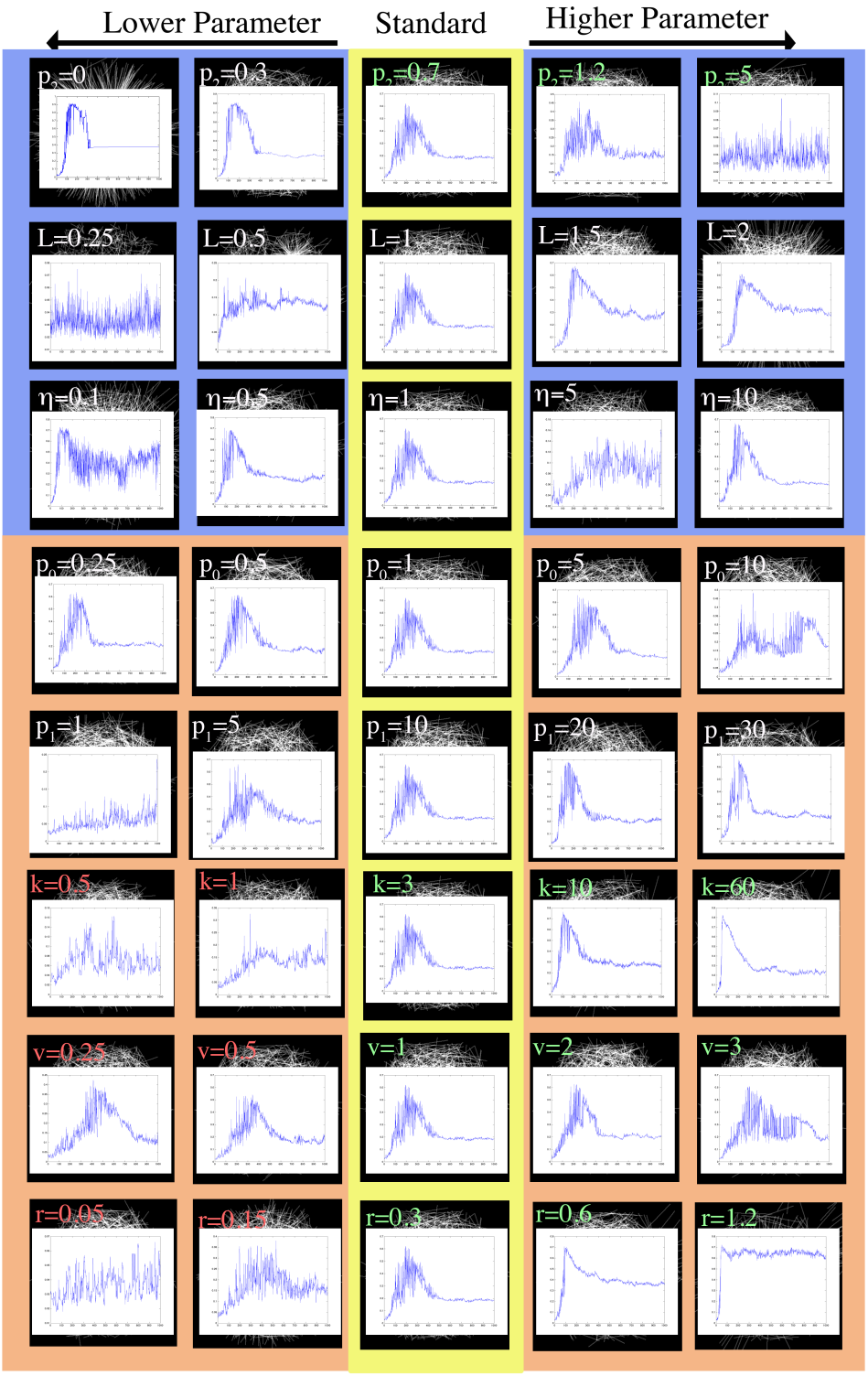

Figure E3: **Parametric analysis of the fraction of plus ends in aster** We calculated the fraction of plus ends in the aster in each of the parameter cases.

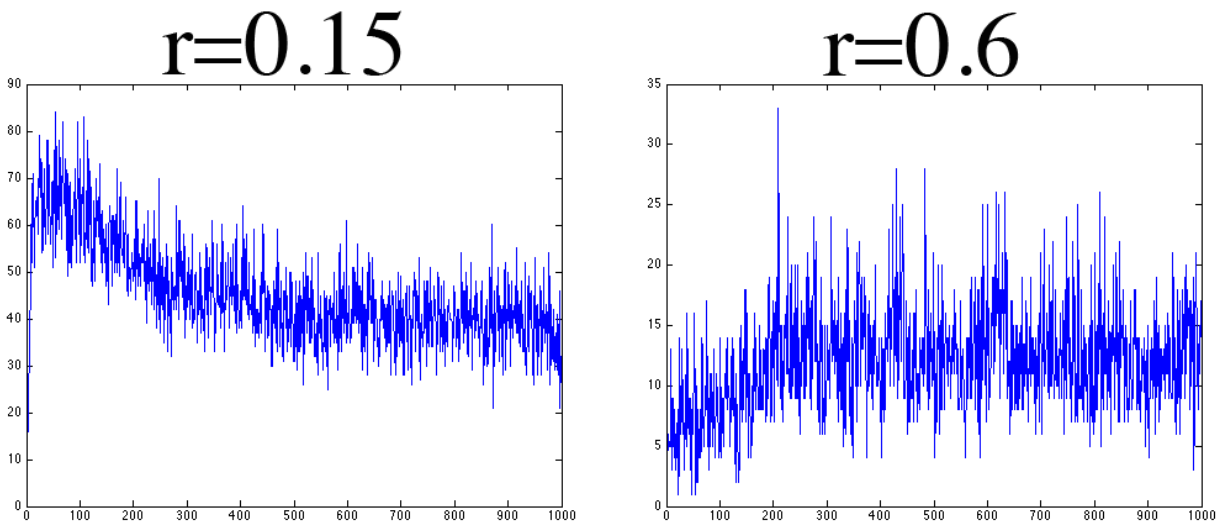

Figure E4: We counted how many motors fell off at each time step due to stretching too far. As expected, when the motors are not allowed to stretch very far, then there are more that fall off, however, the difference between the stretch thresholds does not significantly affect the number of motors stretching too far.

APPENDIX F

2D MOVIES

F.1 2D SIMULATION FOR STANDARD CASE

On the left in red are the filaments, and on the right in green are the motors. Motors are shown if they are unattached or attached. When they are unattached they diffuse within the hexagonal boundary. The movie runs for 1,000 time steps at a rate of 20 frames per second.

F.2 2D SIMULATION FOR 100-SIDED POLYGON

On the left in red are the free filaments, and white shows the sensor filaments. Sensor filaments are attached to the vertices of the 100-sided polygon by a spring. Motors are on the right in green. The movie runs for 2,000 time steps at a rate of 20 frames per second.

F.3 2D SIMULATION FOR AN *IN VITRO* BAR OF FILAMENTS

On the left in red are the filaments which are placed so that they are within a rectangle region, or plus ends are on the rectangle with minus ends off of the bar. On the right in green are the myosin motors which are assumed to initially cover the entire domain of the simulation. The movie runs for 1,000 time steps at a rate of 20 frames per second.

F.4 2D SIMULATION FOR MOTORS THAT ARE TETHERED TO THE SUBSTRATE AND SOME THAT ARE FREE

On the left in red are the filaments which are randomly placed within the hexagonal region. On the right in green are motors. The lower eighth of the hexagon contain the population of

tethered motors which have one "leg" anchoring them to the substrate, and the other "leg" is free to interact with filaments within its stretch threshold.

APPENDIX G

THERMOTOLERANCE SUPPLEMENT

G.1 GASTRULATION AT 16° AND 26°C

This movie shows gastrulation at 16°C (left) and 26°C (right) starting at the late blastula stage, ending after blastopore closure, as the neural plate converges on the dorsal side (top). Embryos are in a vegetal pole view. Movies were rotated so that the dorsal side is towards the top of the image, cropped to fit, and contrast was adjusted to optimize the image. Note that the embryo at 16°C was filmed at 2 minutes per frame, while the embryo at 26°C was filmed at 1 minute per frame. For this combined movie their playback rates were adjusted to match, and they were synchronized to the beginning of involution on the dorsal side. Early on in each embryo, the apices of bottle cells contract strongly. This begins on the dorsal side of the embryo, eventually forming a dark ring of cells with narrowed apices around the blastopore. Soon after the ring fully forms, the superficial layer of tissue outside the blastopore on the dorsal side begins to involute ("dorsal involution"), appearing to roll inwards over the blastopore lip and inside the embryo. Involution progresses around the blastopore, until it occurs on the ventral side as well ("ventral involution"). This time difference is t_P. The blastopore finally closes ("blastopore closure") sometime after involution begins on the ventral side, but involution continues after blastopore closure. Note that the ectoderm and mesoderm move vegetal while the ring of bottle cells contracts, before superficial involution begins. However, we defined the time for blastopore closure (t_C) based on the beginning of involution because it is a much more clearly marked time point.

G.2 F-ACTIN DYNAMICS AT LOW (16°C) AND HIGH (26°C) PERMISSIVE TEMPERATURES

Confocal time lapse sequences of moe-GFP within the basal cell cortex of deep ectodermal cells from gastrula stage embryos. Both sequences were collected with the same confocal settings and magnification at 10 second intervals. Sequences appear to fade at times due to thermal drift which was corrected manually during the collection. The scale-bar indicates 10μm.

G.3 SUPPORTING TEXT

The supplemental text includes a justification for using a linear, one dimensional approximation in models of blastopore closure (G.3.1) and a description of an unusual example of tolerance to variation in gastrulation (G.3.2).

G.3.1 1D, small deformation approximation

Blastopore closure is a complex, large-deformation problem (hence geometrically non-linear), involving materials that are likely to display non-linear material properties at sufficiently large deformations [von Dassow et al., 2010, Zhou et al., 2009]. Furthermore material properties and force generation vary spatially [Zhou et al., 2009]. A full model would require a very large number of parameters, many of which are unknown, and most of which are poorly characterized. Those parameters that have been measured are highly variable [von Dassow et al., 2010, Zhou et al., 2009, von Dassow and Davidson, 2009, Kalantarian et al., 2009]. We seek a simplified model, with as few parameters as possible, to explore the effects of variation in viscoelasticity and timing of force generation on the temperature dependence of morphogenesis.

Here we argue that a simple linear, scalar (1D) model is a reasonable first approximation given the number of unknown parameters, and high levels of mechanical variation. This model captures expected behaviors such as: 1) increased forces lead to increased deformation; 2) usually (though not always) the rate of deformation declines with time after application of a load; and 3) compliance measured in the micro aspirator should correlate with tissue responses to stresses driving blastopore closure (i.e. tissues that appear softer in micro aspiration should behave as through they are softer during blastopore closure). We also expect that if the tissue behaves like a solid in the micro aspirator, it will behave like a solid during blastopore closure. Similarly if it behaves like a fluid in the micro aspirator, it should also behave like a fluid during blastopore closure.

Consider the full 3D, non-linear, large-deformation model. The strain tensor (μ_{ij}) at time t and position $X = \{x, y, z\}$ is a function of the stress tensor σ and compliance tensor C:

$$\mu_{ij}[X,t] = f[C_{ijkl}[X,\gamma], \sigma_{kl}[X,\gamma], t] \tag{G.1}$$

We assume zero strain at the beginning of gastrulation. C and σ are functions of both time and position in the embryo, and f is a function of C and σ over all points in time prior to t (represented by γ). Let us take $\sigma_{kl} = s_{kl} * \Theta$, where Θ is a scalar, with f going to zero as Θ goes to zero (i.e. when stress is zero at all times). Then approximating with a Taylor series around $\Theta = 0$,

$$\mu_{ij}[X,t] = \frac{df}{d\theta}\theta + \omega[\theta] \tag{G.2}$$

Where $\omega[\theta]$ are higher order terms in the series. The term $(df/d\theta)\theta$ is the linear, small deformation viscoelastic model. So we can write:

$$\mu_{ij}[X,t] = \theta\left(\int_0^t C_{ijkl}[X, t-\gamma]\frac{ds_{kl}[X,\gamma]}{d\gamma}d\gamma\right) + \omega[\theta] \tag{G.3}$$

Furthermore, we can split s_{kl} into two terms:

$$s_{kl}[X,t] = z_{kl}[X]v[t] + y_{kl}[X,t] \tag{G.4}$$

Here $z_{kl}[X]$ is the time averaged value of s_{kl} at position X, $v[t]$ is a scalar function of time, and $y_{kl}[X,t]$ are the deviations from $z_{kl}[X]v[t]$. We can choose $v[t]$ in a way that minimizes the contribution of $y[X,t]_{kl}$ to the strain (it is not important how to do this, only that there exists a choice of y and v that would maximize the contribution of z). Hence,

$$\mu_{ij}[X,t] = \theta\left(z_{kl}[X]\int_0^t C_{ijkl}[X, t-\gamma]\frac{dv[\gamma]}{d\gamma}d\gamma + \int_0^t C_{ijkl}[X, t-\gamma]\frac{dy_{kl}[X,\gamma]}{d\gamma}d\gamma\right) + \omega[\theta] \tag{G.5}$$

Both ω and y are unknown even to sign, and y is chose so that its contribution is as small as possible. Therefore, it is reasonable to take as a first approximation, the linear model:

$$\mu_{ij}[X,t] \approx \theta z_{kl}[X]\int_0^t C_{ijkl}[X, t-\gamma]\frac{dv[\gamma]}{d\gamma}d\gamma \tag{G.6}$$

The compliance and strain are still 2nd and 4th order tensors. If we assume that C_{ijkl} can be approximated as the product of a scalar valued term (J) dependent on time, and a tensor (c_{ijkl}), we get:

$$\mu_{ij}[X,t] \approx c_{ijkl}[X]\theta z_{kl}[X] \int_0^t J[t-\gamma]\frac{dv[\gamma]}{d\gamma}d\gamma \tag{G.7}$$

(Alternatively one could use a similar division into the sum of two tensors as used for s_{ij}). This means that $\mu_{ij}[X,t]$ must also be approximately separable into products of a spatially varying term ($g_{ij}[X]$) and a temporally varying term ($\epsilon[t]$) in the same way. All the spatial variation can be separated into one set of terms, and we can simplify to a scalar equation equivalent to our linear model. The unknown proportionality term (K) cancels out of the final model:

$$\epsilon[t] \approx K \int_0^t J[t-\gamma]\frac{dv[X,\gamma]}{d\gamma}d\gamma \tag{G.8}$$

The scalar ϵ is not the only parameter that characterizes the progression of gastrulation, so we can map morphogenetic events (deformation states) to $\epsilon[t]$. Hence, blastopore closure begins and ends at a particular values of ϵ (0 and ϵ_C respectively).

Clearly, we have cut out a lot of important processes and parameters to get to this point. Furthermore, we have not accounted for changes in compliance over development [Zhou et al., 2009, von Dassow and Davidson, 2009]. However, given the unknowns, and the variation in the known parameters, this linear, scalar-valued model is a reasonable first approximation. It is also minimal: all parameters other than those that whose importance we wish to determine ($v[t]$), can be tied to measurements ($J[t]$), or cancel out (K).

G.3.2 An example of tolerance to variation in gastrulation

A remarkable illustration of embryos' capacity to tolerate morphogenetic variation occurred in one clutch (a batch of embryos collected from the same female at the same time). In this clutch (Figure G1) gastrulation took a very different path than in others (7 of 8 embryos). Bottle cell formation began normally. However, at the point when superficial involution would normally begin at the dorsal blastopore edge, a tongue of material (most likely presumptive notochord) extended out across the blastopore from the dorsal side. Superficial

involution then began at a point further up the dorsal side, and blastopore closure occurred over the tongue of material. Despite its abnormal trajectory, blastopore closure completed successfully and the resulting embryos looked essentially normal at later stages (neural and early tadpole). Because blastopore closure was so unusual in this clutch, these results were not analyzed for shifts in developmental timing, yet they provide a clear example of how robust morphogenesis can be.

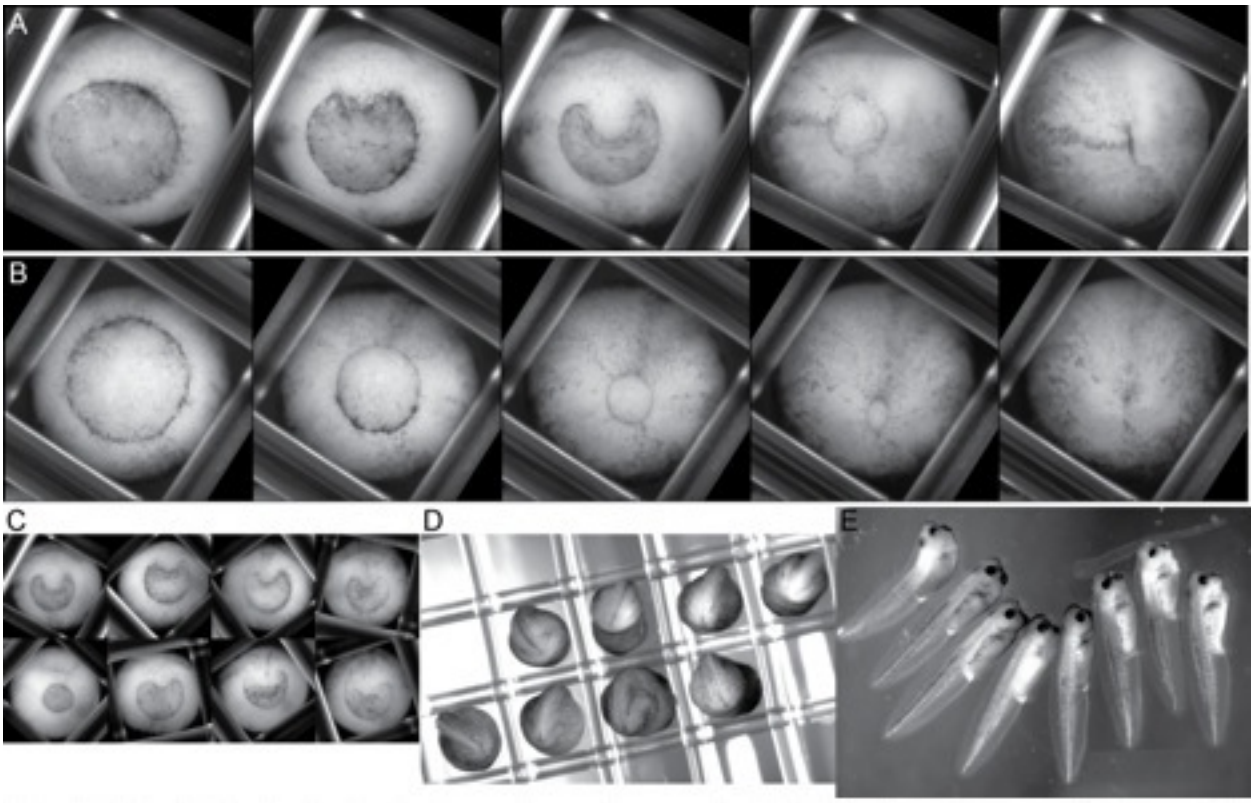

Figure G1: **Variation in the trajectory of morphogenesis.** (A) Time lapse images of the vegetal side of an embryo in a clutch with an unusual trajectory of morphogenesis. A tongue of material extended over the blastopore from the dorsal side at the time when normal embryos (B) would be undergoing dorsal superficial involution. Images in A and B are at hourly intervals from bottle cell contraction (left) to blastopore closure (right) at 26°C. (C) The same time point midway through blastopore closure in all 8 embryos from this unusual clutch. (D) Posterior ends of the same eight embryos at neural stages had completed blastopore closure. (D) The same eight embryos at tadpole stages showed only minor defects. Contrast and brightness were adjusted to optimize images; images in A-C were rotated dorsal side up. B shows embryo from Figure 6.2A.

BIBLIOGRAPHY

[Alberts, 2008] Alberts, B. (2008). *Molecular biology of the cell*. Garland Science, New York.

[Alberts and Odell, 2004] Alberts, J. B. and Odell, G. M. (2004). *In silico* reconstitution of listeria propulsion exhibits nano-saltation. *PLoS Biology*, 2 (12). e412.

[Alvarez and Schoenwolf, 1992] Alvarez, I. S. and Schoenwolf, G. C. (1992). Expansion of surface epithelium provides the major extrinsic force for bending of the neural plate. *Journal of Experimental Zoology*, 261:340–8.

[Amann and Pollard, 2001] Amann, K. J. and Pollard, T. D. (2001). Direct real-time observation of actin filament branching mediated by arp 2/3 complex using total internal reflection fluorescence microscopy. *Proc Natl Acad Sci U S A*, pages 15009–13.

[Aoki et al., 1997] Aoki, T., Ohashi, T., Matsumoto, T., and Sato, M. (1997). The pipette aspiration applied to the local stiffness measurement of soft tissues. *Annals of Biomedical Engineering*, 25:581–587.

[Atlas, 1935] Atlas, M. (1935). The effect of temperature on the development of rana pipiens. *Physiological Zoology*, 8:290–310.

[Bachmann, 1969] Bachmann, K. (1969). Temperature adaptations of amphibian embryos. *The American Naturalist*, 103:115–130.

[Baneyx et al., 2002] Baneyx, G., Baugh, L., and Vogel, V. (2002). Fibronectin extension and unfolding within cell matrix fibrils controlled by cytoskeletal tension. *Proc Natl Acad Sci U S A*, 99:5139–43.

[Banhidy et al., 2005] Banhidy, F., Puho, E., and Czeizel, A. (2005). Maternal influenza during pregnancy and risk of congenital abnormalities in offspring. *Birth Defects Research Part A: Clinical and Molecular Teratology*, 73:989–996.

[Bellman and Cooke, 1963] Bellman, R. and Cooke, K. (1963). *Differential- Difference Equations*. Academic Press, NY.

[Beloussov et al., 2006] Beloussov, L., Luchinskaya, N., Ermakov, A., and Glagoleva, N. (2006). Gastrulation in amphibian embryos, regarded as a succession of biomechanics feedback events. *International Journal of Developmental Biology*, 50:113–22.

[Beloussov et al., 1975] Beloussov, L. V., Dorfman, J. G., and Cherdantzev, V. G. (1975). Mechanical stresses and morphological patterns in amphibian embryos. *Journal of Embryology and Experimental Morphology*, 34:559–74.

[Beloussov et al., 1988] Beloussov, L. V., Lakirev, A. V., and Naumidi, I. (1988). The role of external tensions in differentiation of *Xenopus laevis* embryonic tissues. *Cell Differentiation and Development*, 25:165–76.

[Beloussov et al., 1990] Beloussov, L. V., Lakirev, A. V., Naumidi, I., and Novoselov, V. V. (1990). Effects of relaxation of mechanical tensions upon the early morphogenesis of *Xenopus laevis* embryos. *International Journal of Developmental Biology*, 34:409–19.

[Benazeraf et al., 2010] Benazeraf, B., Francois, P., Baker, R. E., Denans, N., Little, C. D., and Pourquie, O. (2010). A random cell motility gradient downstream of fgf controls elongation of an amniote embryo. *Nature*, 466:248–52.

[Bingham et al., 1997] Bingham, B., Bacigalupi, M., and Johnson, L. (1997). Temperature adaptations of embryos from intertidal and sub tidal sand dollars (dendraster eccentrics, eschscholtz. *Northwest Science*, 71:108–114.

[Black, 1989] Black, S. (1989). Experimental reversal of the normal dorsal-ventral timing of blastopore formation does not reverse axis polarity in *Xenopus laevis* embryos. *Developmental Biology*, 134:376–381.

[Black et al., 1996] Black, S., Hawk, S., and Larkin, K. (1996). Restricting oxygen supply to the prospective dorsal side does not reverse axis polarity in embryos of *Xenopus laevis*. *Development Genes and Evolution*, 206:147–152.

[Blanchard et al., 2009] Blanchard, G., Kabla, A., Schultz, N., Butler, L., Sanson, B., Gorfinkiel, N., Mahadevan, L., and Adams, R. (2009). Tissue tectonics: morphogenetic strain rates, cell shape change and intercalation. *Nature Methods*, 6:458–464.

[Blanchard et al., 2010] Blanchard, G. B., Murugesu, S., Adams, R. J., Martinez-Arias, A., and Gorfinkiel, N. (2010). Cytoskeletal dynamics and supracellular organisation of cell shape fluctuations during dorsal closure. *Development*, pages 2743–52.

[Bonder et al., 1988] Bonder, E. M., Fishkind, D. J., Henson, J. H., Cotran, N. M., and Begg, D. A. (1988). Actin in cytokinesis: formation of the contractile apparatus. *Zoological Science*, pages 699–711.

[Boudou et al., 2006] Boudou, T., Ohayon, J., Arntz, Y., Finet, G., Picart, C., and Tracqui, P. (2006). An extended modeling of the micropipette aspiration experiment for the characterization of the young's modulus and poisson's ratio of adherent thin biological samples: numerical and experimental studies. *Journal of Biomechanics*, 39:1677–85.

[Brodland et al., 1994] Brodland, G., Scott, M., Bjorklund, N., Luchka, K., Martin, C., Matuga, C., Globus, M., Vethamany-Globus, S., and Shu, D. (1994). Furrowing surface

contraction wave coincident with primary neural induction in amphibian embryos. *Journal of Morphology*, 219:131–42.

[Brodland and Veldhuis, 2012] Brodland, G. and Veldhuis, J. (2012). Assessing the mechanical energy costs of various tissue reshaping mechanisms. *Biomechanics and Modeling in Mechanobiology*, 11:1137–1147.

[Brodland et al., 2010] Brodland, G. W., Conte, V., Cranston, P. G., Veldhuis, J., Narasimhan, S., Hutson, M. S., Jacinto, A., Ulrich, F., Baum, B., and Miodownik, M. (2010). Video force microscopy reveals the mechanics of ventral furrow invagination in *Drosophila*. *Proc Natl Acad Sci U S A*, 107:22111–6.

[Burbank et al., 2007] Burbank, K., Mitchison, T. J., and Fisher, D. (2007). Slide-and-cluster models for spindle assembly. *Current Biology*, 17:1373–83.

[Burnette et al., 2011] Burnette, D. T., Manley, S., Sengupta, P., Sougrat, R., Davidson, M. W., Kachar, B., and Lippincott-Schwartz, J. (2011). A role for actin arcs in the leading-edge advance of migrating cells. *Nature Cell Biology*.

[Chan and Odde, 2008] Chan, C. E. and Odde, D. J. (2008). Traction dynamics of filopodia on compliant substrates. *Science*, 322:1687–91.

[Chan et al., 2010] Chan, K., Goldmark, J., and Roth, M. (2010). Suspended animation extends survival limits of caenorhabditis elegant and saccharomyces cerevisiae at low temperature. *Molecular Biology of the Cell*, 21:2161–2171.

[Chen et al., 1997] Chen, C., Mrksick, M., Huang, S., Whitesides, G., and Ingber, D. (1997). Geometric control of cell life and death. *Science*, 276:1425–8.

[Chiu et al., 2012] Chiu, C., Chou, C., Takada, S., and Liu, Y. (2012). Development and fibronectin signaling requirements of the zebrafish interrenal vessel. *PLoS One*, 7.

[Condeelis, 1993] Condeelis, J. (1993). Life at the leading edge: The formation of cell protrusions. *Annual Review Cell Biology*, 9:411–44.

[Cooper, 2000] Cooper, G. (2000). *The Cell: A Molecular Approach*. Sunderland (MA): Sinauer Associates, 2nd edition.

[Cooper et al., 1983] Cooper, J. A., Walker, S. B., and Pollard, T. D. (1983). Pyrene actin: Documentation of the validity of a sensitive assay for actin polymerization. *Journal Muscle Research and Cell Motility*, pages 253–262.

[Cosens and Manning, 1969] Cosens, D. and Manning, A. (1969). Abnormal electroretinogram from a drosophilia mutant. *Nature*, 224:285–7.

[Coste et al., 2012] Coste, B., B., X., Santos, J., Syeda, R., Grandl, J., Spencer, K., Kim, S., Schmidt, M., Mathur, J., Dubin, A., Montal, M., and Patapoutian, A. (2012). Piezo proteins are pore-forming subunits of mechanically activated channels. *Nature*, 483:176–81.

[Coste et al., 2010] Coste, B., Mathur, J., Schmidt, M., Earley, T., Ranade, S., Petrus, M., Dubin, A., and Patapoutian, A. (2010). Piezo1 and piezo2 are essential components of distinct mechanically activated cation channels. *Science*, 330:55–60.

[Craig et al., 2011] Craig, E., Dey, S., and Mogilner, A. (2011). The emergence of sarcomeric, graded-polarity and spindle-like patterns in bundles of short cytoskeletal polymers and two opposite molecular motors. *Journal of Physics: Condensed Matter*, 23.

[Dasanayake et al., 2011] Dasanayake, N., Michalski, P., and Anders, E. (2011). General mechanism of actomyosin contractility. *Physical Review Letters*, 107.

[David et al., 2010] David, D., Tishkina, A., and Harris, T. (2010). The par complex regulates pulsed actomyosin contractions during amnioserosa apical constriction in *Drosophila*. *Development*, 137:1645–1655.

[Davidson, 2011] Davidson, L. (2011). Embryo mechanics: balancing force production with elastic resistance during morphogenesis. *Current Topics in Developmental Biology*, 95:215–241.

[Davidson et al., 2006] Davidson, L., Marsden, M., Keller, R., and DeSimone, D. (2006). Integrin alpha5beta1 and fibronectin regulate polarized cell protrusions required for xenopus convergence and extension. *Current Biology*, 16:833–44.

[Davidson et al., 2009] Davidson, L., von Dassow, M., and Zhou, J. (2009). Multi-scale mechanics from molecules to morphogenesis. *International Journal of Biochemistry and Cell Biology*, 41:2147–62.

[Davidson et al., 2010] Davidson, L. A., Joshi, S. D., Kim, H. Y., von Dassow, M., Zhang, L., and Zhou, J. (2010). Emergent morphogenesis: elastic mechanics of a self-deforming tissue. *Journal of Biomechanics*, 43:63–70.

[Davidson et al., 1995] Davidson, L. A., Koehl, M. A., Keller, R., and Oster, G. F. (1995). How do sea urchins invaginate? using biomechanics to distinguish between mechanisms of primary invagination. *Development*, 121:2005–28.

[Davidson et al., 1999] Davidson, L. A., Oster, G. F., Keller, R. E., and Koehl, M. A. (1999). Measurements of mechanical properties of the blastula wall reveal which hypothesized mechanisms of primary invagination are physically plausible in the sea urchin *Strongylocentrotus purpuratus*. *Development Biology*, 209:221–38.

[de Gennes, 1979] de Gennes, P.-G. (1979). *Scaling Concepts in Polymer Physics*. Cornell University Press.

[del Rio et al., 2009] del Rio, A., Perez-Jimenez, R., Liu, R., Roca-Cusachs, P., Fernandez, J., and Sheetz, M. (2009). Stretching single talon rod molecules activates vinculin binding. *Science*, 323:638–41.

[Dembo and Wang, 1990] Dembo, M. and Wang, Y. (1990). Stresses at the cell-to-substrate interface during locomotion of fibroblasts. *Biophysical Journal*, 76:2307–16.

[Desprat et al., 2008] Desprat, N., Supatto, W., Pouille, P. A., Beaurepaire, E., and Farge, E. (2008). Tissue deformation modulates twist expression to determine anterior midgut differentiation in *Drosophila* embryos. *Developmental Cell*, 15:470–7.

[Dos Remedios et al., 2003] Dos Remedios, C., Chhabra, D., Kekic, M., Dedova, I., Tsubakihara, M., Berry, D. A., and Nosworthy, N. (2003). Actin binding proteins: Regulation of cytoskeletal microfilaments. *Physiological Reviews*, 83:433–473.

[Dunaway et al., 2002] Dunaway, D., Fauver, M., and Pollack, G. (2002). Direct measurement of single synthetic vertebrate thick filament elasticity using nanofabricated cantilevers. *Biophysical Journal*, 82:3128–33.

[Dupont et al., 2011] Dupont, S., Morsut, L., Aragona, M., Enzo, E., Giulitti, S., Cordenonsi, M., Zanconato, F., Le Digabel, J., Forcato, M., Bicciato, S., Elvassore, N., and Piccolo, S. (2011). Role of yap/taz in mechanotransduction. *Nature*, 474:179–183.

[Edwards et al., 1997] Edwards, K., Demsky, M., Montague, R., Weymouth, N., and Kiehart, D. (1997). Gfp-moesin illuminates actin cytoskeleton dynamics in living tissue and demonstrates cell shape changes during morphogenesis in *Drosophila*. *Development Biology*, 191:103–117.

[Edwards, 2006] Edwards, M. (2006). Review: Hyperthermia and fever during pregnancy. *Birth Defects Research Part A: Clinical and Molecular Teratology*, 76:507–516.

[Efron and Tibshirani, 1993] Efron, B. and Tibshirani, R. (1993). *An introduction to the bootstrap*. New York: Chapman & Hall.

[Eisenhoffer et al., 2012] Eisenhoffer, G., Loftus, P., Yoshigi, M., Otsuna, H., Chien, C., Morcos, P., and Rosenblatt, J. (2012). Crowding induces live cell extrusion to maintain homeostatic numbers in epithelia. *Nature*, 484:546–9.

[Engler et al., 2006] Engler, A. J., Sen, S., Sweeney, H. L., and Discher, D. E. (2006). Matrix elasticity directs stem cell lineage specification. *Cell*, 126:677–89.

[Ettensohn, 1985] Ettensohn, C. A. (1985). Mechanisms of epithelial invagination. *Quarterly Review of Biology*, 60:289–307.

[Evans and Yeung, 1989] Evans, E. and Yeung, A. (1989). Apparent viscosity and cortical tension of blood granulocytes determined by micro pipet aspiration. *Biophysical Journal*, 56:151–160.

[Falzone et al., 2012] Falzone, T., Lenz, M., Kovar, D., and Gardel, M. (2012). Assembly kinetics determine the architecture of α-actinin cross linked f-actin networks. *Nature Communications*, 3.

[Farge, 2003] Farge, E. (2003). Mechanical induction of twist in the drosophila foregut/stomodeal primordium. *Current Biology*, 13:1365–77.

[Farge, 2011] Farge, E. (2011). Mechanotransduction in development. *Current Topics in Developmental Biology*, 95:243–265.

[Fernandez-Gonzalez et al., 2009] Fernandez-Gonzalez, R., Simoes Sde, M., Roper, J. C., S., E., and Zallen, J. A. (2009). Myosin ii dynamics are regulated by tension in intercalating cells. *Developmental Cell*, 17:736–43.

[Feroze et al., tted] Feroze, R., Shawky, J., von Dassow, M., and Davidson, L. (*submitted*). Mechanics of blastopore closure during amphibian gastrulation. *Developmental Biology*.

[Findley et al., 1989] Findley, W., Lai, J., and Onaran, K. (1989). *Creep and relaxation of nonlinear viscoelastic materials*. New York: Dover Publications, Inc.

[Forgacs et al., 1998] Forgacs, G., Foty, R., Shafrir, Y., and Steinberg, M. (1998). Viscoelastic properties of living embryonic tissues: a quantitative study. *Biophysical Journal*, 74:2227–2234.

[Foty et al., 1996] Foty, R., Pfleger, C., Forgacs, G., and Steinberg, M. (1996). Surface tensions of embryonic tissues predict their mutual envelopment behavior. *Development*, 122:1611–1620.

[Fu et al., 2010] Fu, J., Wang, Y., Desai, R., Yu, X., Liu, Z., and Chen, C. (2010). Mechanical regulation of cell function with geometrically modulated elastomeric substrates. *Nature Methods*, 7:733–736.

[Fujisawa, 1993] Fujisawa, H. (1993). Temperature sensitivity of a hybrid between two species of sea urchin differing in thermotolerance. *Development, Growth and Differentiation*, 35:395–401.

[Garcia et al., 1999] Garcia, A., Vega, M., and Boettiger, D. (1999). Modulation of cell proliferation and differentiation through substrate-dependent changes in fibronectin conformation. *Molecular Biology of the Cell*, 10:785–98.

[Gee et al., 2011] Gee, S., Milgram, S., Kramer, K., Conlon, F., and Moody, S. (2011). Yes-associated protein 65 (yap) expands neural progenitors and regulates pax3 expression in the neural plate border zone. *PLoS ONE*, 6.

[Ghosh et al., 2004] Ghosh, M., Song, X., Mouneimne, G., Sidani, M., Lawrence, D., and Condeelis, J. (2004). Cofilin promotes actin polymerization and defines the direction of cell motility. *Science*, 304:743–746.

[Gibson et al., 2006] Gibson, M. C., Patel, A. B., Nagpal, R., and Perrimon, N. (2006). The emergence of geometric order in proliferating metazoan epithelia. *Nature*, 442:1038–41.

[Gorfinkiel and Blanchard, 2011a] Gorfinkiel, N. and Blanchard, G. (2011a). Dynamics of actomyosin contractile activity during epithelial morphogenesis. *Current Opinion in Cell Biology*, 23:531–539.

[Gorfinkiel et al., 2009] Gorfinkiel, N., Blanchard, G., Adams, R., and Martinez Arias, A. (2009). Mechanical control of global cell behavior during dorsal closure in *Drosophila*. *Development*, 136:1889–1898.

[Gorfinkiel and Blanchard, 2011b] Gorfinkiel, N. and Blanchard, G. B. (2011b). Dynamics of actomyosin contractile activity during epithelial morphogenesis. *Current Opinion in Cell Biology*, 23:531–9.

[Graham et al., 1998] Graham, J., Edwards, M., and Edwards, M. (1998). Teratogen update: gestational effects of maternal hypothermia due to febrile illness and resultant patterns of defects in humans. *Teratology*, 58:209–221.

[Grashoff et al., 2010] Grashoff, C., Hoffman, B., Brenner, M., Zhou, R., Parsons, M., Yang, M., McLean, M., Sligar, S., Chen, C., Ha, T., and Schwartz, M. (2010). Measuring mechanical tension across vinculin reveals regulation of focal adhesion dynamics. *Nature*, 466:263–6.

[Groenendijk et al., 2004] Groenendijk, B., Hierck, B., Gittenberger-De Groot, A., and Poelmann, R. (2004). Development related changes in the expression of shear stress responsive genes klf-2, et-1, and nos-3 in the developing cardiovascular system of chicken embryos. *Developmental Dynamics*, 230:57–68.

[Guillot and Lecuit, 2013] Guillot, C. and Lecuit, T. (2013). Mechanics of epithelial tissue homeostasis and morphogenesis. *Science*, 340:1185–1189.

[Gustafson and Wolpert, 1963] Gustafson, T. and Wolpert, L. (1963). The cellular basis of morphogenesis and sea urchin development. *International Review of Cytology*, 15:139–214.

[Harris et al., 1980] Harris, A., Wild, P., and Stopak, D. (1980). Silicone rubber substrata: a new wrinkle in the study of cell locomotion. *Science*, 208:177–9.

[Hill, 1938] Hill, A. (1938). The heat shortening and dynamics constants of muscles. *Proc Roy Soc B*, 126:136–195.

[Hill et al., 1996] Hill, K., Catlett, N., and Weisman, L. (1996). Actin and myosin function in directed vacuole movement during cell division in *Saccharomyces cerevisiae*. *Journal of Cell Biology*, 135:1535–49.

[His, 1888] His, W. (1888). On the principles of animal morphology. *Proc. R. Soc. Edinburgh*, 15:287–298.

[Ho et al., 2012] Ho, T., Horn, N., Huynh, T., Kelava, L., and Lansman, J. (2012). Evidence trpv4 contributes to mechanosensitive ion channels in mouse skeletal muscle fibers. *Channels (Austin)*, 6:246–54.

[Hodge et al., 2000] Hodge, T., Jamie, M., and Cope, T. (2000). A myosin family tree. *Journal of Cell Science*, 113:33.

[Hosako et al., 2009] Hosako, H., Francisco, L., Martin, G., and Mirkes, P. (2009). The roles of p53 and p21 in normal development and hyperthermia-induced malformations. *Birth Defects Res B Dev Reprod Toxicol*, 86:40–47.

[Houk et al., 2012] Houk, A., Jilkine, A., Mejean, C., Boltyanskiy, R., Dufresne, E., Angenent, S., Altschuler, S., Wu, L., and Weiner, O. (2012). Membrane tension maintains cell polarity by confining signals to the leading edge during neutrophil migration. *Cell*, 148:175–188.

[Howard, 2001] Howard, J. (2001). *Mechanisms of Motor Proteins and the Cytoskeleton*. Sinauer Associates, Sunderland, MA.

[Howard et al., 1993] Howard, P., Sefton, B., and Firtel, R. (1993). Tyrosine phosphorylation of actin in *Dictyostelium* associated with cell-shape changes. *Science*, 259:241–244.

[Humphries et al., 2007] Humphries, J., Wang, P., Streuli, C., Geiger, B., Humphries, M., and Ballestrem, C. (2007). Vinculin controls focal adhesion formation by direct interactions with talin and actin. *Journal of Cell Biology*, 179:1043–57.

[Hunt et al., 1994] Hunt, A. J., Gittes, F., and Howard, J. (1994). The force exerted by a single kinesin molecule against a viscous load. *Biophysical Journal*, 67:766–781.

[Hutson et al., 2003] Hutson, M., Tokutake, Y., Chang, M., Bloor, J., Venakides, S., Kiehart, D., and Edwards, G. (2003). Forces for morphogenesis investigated with laser microsurgery and quantitative modeling. *Science*, 300:145–9.

[Itoh et al., 2005] Itoh, T., Erdmann, K., Roux, A., Habermann, B., Werner, H., and De Camilli, P. (2005). Dynamin and the actin cytoskeleton cooperatively regulate plasma membrane invagination by bar and f-bar proteins. *Developmental Cell*, 9:791–804.

[Jacinto et al., 2002] Jacinto, A., Wood, W., Balayo, T., Turmaine, M., Martinez-Arias, A., and Martin, P. (2002). Dynamic actin-based epithelial adhesion and cell matching during *Drosophila* dorsal closure. *Current Biology*, 12:1245–1250.

[Jarosik et al., 2004] Jarosik, V., Kratochvil, L., Honek, A., and Dixon, A. (2004). A general rule for the dependence of developmental rate on temperature in ectothermic animals. *Proc Biol Sci*, 271:219–221.

[Jiang et al., 2005] Jiang, X., Bruzewicz, D., Wong, A., Piel, M., and Whitesides, G. (2005). Directing cell migration with asymmetric micro patterns. *Proc Natl Acad Sci U S A*, 102:975–978.

[Joshi et al., 2012] Joshi, S., Kim, H., and Davidson, L. (2012). Microscopy tools for quantifying developmental dynamics in xenopus embryos. *Methods Molecular Biology*, 917:477–493.

[Joshi et al., 2010] Joshi, S. D., von Dassow, M., and Davidson, L. A. (2010). Experimental control of excitable embryonic tissues: three stimuli induce rapid epithelial contraction. *Experimental Cell Research*, 216:103–14.

[Kalantarian et al., 2009] Kalantarian, A., Ninomiya, H., Saad, S., David, R., Winklbauer, R., and Neumann, A. (2009). Axisymmetric drop shape analysis for estimating the surface tension of cell aggregates by centrifugation. *Biophysical Journal*, 96:1606–1616.

[Kamasaki et al., 2007] Kamasaki, T., Osumi, M., and Mabuchi, I. (2007). Three-dimensional arrangement of f-actin in the contractile ring of fission yeast. *Journal of Cell Biology*, 178:765–771.

[Karsenti et al., 2006] Karsenti, E., Nedelec, F., and Surrey, T. (2006). Modeling microtubule patterns. *Nature Cell Biology*, 8:1204–11.

[Kawai et al., 2000] Kawai, M., Kawaguchi, K., Saito, M., and Ishiwata, S. (2000). Temperature change does not affect force between single actin filaments and hmm from rabbit muscles. *Biophysical Journal*, 78:3112–3119.

[Kaya and Higuchi, 2010] Kaya, M. and Higuchi, H. (2010). Nonlinear elasticity and an 8-nm working stroke of single myosin molecules in myofilaments. *Science*, 329(5992):686–689.

[Keller et al., 2000] Keller, R., Davidson, L., Edlund, A., Elul, T., Ezin, M., Shook, D., and Skoglund, P. (2000). Mechanisms of convergence and extension by cell intercalation. *Philosophical Transactions of the Royal Society B: Biological Sciences*, 355:897–922.

[Keller et al., 2003] Keller, R., Davidson, L., and Shook, D. R. (2003). How we are shaped: the biomechanics of gastrulation. *Differentiation*, 71:171–205.

[Keller and Shook, 2004] Keller, R. and Shook, D. (2004). *Gastrulation: From Cells to Embryos*. New York: Cold Spring Harber Press.

[Keller and Shook, 2008] Keller, R. and Shook, D. (2008). Dynamic determinations: patterning the cell behaviors that close the amphibian blastopore. *Philos Trans R Soc Lond B Biol Sci*, 363:1317–1332.

[Keller et al., 2008] Keller, R., Shook, D., and Skoglund, P. (2008). The forces that shape embryos: physical aspects of convergent extension by cell intercalation. *Physical biology*, 5.

[Kieβling et al., 2013] Kieβling, T., Stange, R., Kas, J., and Fritsch, A. (2013). Thermorheology of living cells- impact of temperature variations on cell mechanics. *New Journal of Physics*, 15.

[Kiehart et al., 2000] Kiehart, D., Galbraith, C., Edwards, K., Rickoll, W., and Montague, R. (2000). Multiple forces contribute to cell sheet morphogenesis for dorsal closure in *Drosophila*. *Journal of Cell Biology*, 149:471–490.

[Kim and Davidson, 2011] Kim, H. and Davidson, L. (2011). Punctuated actin contractions during convergent extension and their permissive regulation by the non-canonical wnt-signaling pathway. *Journal of Cell Science*, 124:635–646.

[Kim et al., 2012] Kim, S., Coste, B., Chadha, A., Cook, B., and Patapoutian, A. (2012). The role of drosophila piezo in mechanical nociception. *Nature*, 483:209–12.

[Kimmel et al., 1995] Kimmel, C., Ballard, W., Kimmel, S., Ullmann, B., and Schilling, T. (1995). Stages of embryonic development of the zebrafish. *Developmental Dynamics*, 203:253–310.

[Klotzsch et al., 2009] Klotzsch, E., Smith, M., Kubow, K., Muntwyler, S., Little, W., Beyeler, F., Gourdon, D., Nelson, B., and Vogel, V. (2009). Fibronectin forms the most extensible biological fibers displaying switchable force-exposed cryptic binding sites. *Proc Natl Acad Sci U S A*, 106:18267–72.

[Koehl, 1990] Koehl, M. (1990). Biomechanical approaches to morphogenesis. *Seminars in Developmental Biology*, 1:367–78.

[Kong et al., 2013] Kong, F., Li, Z., Parks, W., Dumbauld, D., Garcia, A., Mould, A., Humphries, M., and Zhu, C. (2013). Cyclic mechanical reinforcement of integrin-ligand interactions. *Molecular Cell*, 49:1060–8.

[Kottgen et al., 2008] Kottgen, M., Buchholz, B., Garcia-Gonzalez, M., Kotsis, F., Fu, X., Doerken, M., Boehlke, C., Steffl, D., Tauber, R., Wegierski, T., Nitschke, R., Suzuki, M., Kramer-Zucker, A., Germino, G. G., Watnick, T., Prenen, J., Nilius, B., Kuehn, E., and Walz, G. (2008). Trpp2 and trpv4 form a polymodal sensory channel complex. *Journal of Cellular Biology*, 182:437–47.

[Kouyama and Mihashi, 1980] Kouyama, T. and Mihashi, K. (1980). Pulse-fluorometry study on actin and heavy meromyosin using f-actin labelled with n-(1-pyrene)maleimide. *European Journal of Biochemistry*, pages 279–287.

[Krammer et al., 1999] Krammer, A., Lu, H., Isralewitz, B., Shulten, K., and Vogel, V. (1999). Forced unfolding of the fibronectin type iii module reveals a tensile molecular recognition switch. *Proc Natl Acad Sci U S A*, 96:1351–6.

[Kron and Spudich, 1986] Kron, S. J. and Spudich, J. A. (1986). Fluorescent actin filaments move on myosin fixed to a glass surface. *Proc Natl Acad Sci U S A*, pages 6272–6.

[Kruse et al., 2004] Kruse, K., Joanny, J. G., Jülicher, F., Prost, J., and Sekimoto, K. (2004). Asters, vortices, and rotating spirals in active gels of polar filaments. *Physical Review Letters*, 92.

[Kruse and Jülicher, 2006] Kruse, K. and Jülicher, F. (2006). Dynamics and mechanics of motor-filament systems. *The European Physical Journal E- Soft Matter*, 20:459–65.

[Kumar and Shivashankar, 2012] Kumar, A. and Shivashankar, G. (2012). Mechanical force alters morphogenetic movements and segmental gene expression patterns during *Drosophila* embryogenesis. *PLoS ONE*, 7.

[Kuramoto, 1984] Kuramoto, Y. (1984). *Chemical Oscillations, Waves, and Turbulence*. Springer.

[Lang et al., 1986] Lang, I., Scholtz, M., and Peters, R. (1986). Molecular mobility and nucleocytoplasmic flux in hepatoma cells. *Journal of Cell Biology*, 102:1183–1190.

[Lauffenburger and Horwitz, 1996] Lauffenburger, D. A. and Horwitz, A. F. (1996). Cell migration: a physically integrated molecular process. *Cell*, 84:359–69.

[le Duc et al., 2010] le Duc, Q., Shi, Q., Blonk, I., Sonnenberg, A., Wang, N., Leckband, D., and de Rooij, J. (2010). Vinculin potentiates e-cadherin mechanosensing and is recruited to actin-anchored sites within adherens junctions in a myosin ii-dependent manner. *Journal of Cell Biology*, 189:1107–15.

[Lecuit et al., 2011] Lecuit, T., Lenne, P., and Munro, E. (2011). Force generation, transmission, and integration during cell and tissue morphogenesis. *Annual Review of Cell Developmental Biology*, 27:157–184.

[Lee and Anderson, 2008] Lee, J. and Anderson, K. (2008). Morphogenesis of the node and notochord: The cellular basis for the establishment and maintenance of left-right asymmetry in the mouse. *Developmental Dynamics*, 237:3464–76.

[Lee et al., 2006] Lee, J., Yu, Q., Shin, J., Sebzda, E., Bertozzi, C., Chen, M., Mericko, P., Stadtfeld, M., Zhou, D., Cheng, L., Graf, T., MacRae, C., Lepore, J., Lo, C., and Kahn, M. (2006). Klf2 is an essential regulator of vascular hemodynamic forces *in vivo*. *Developmental Cell*, 11:845–857.

[Lehenkari and Horton, 1990] Lehenkari, P. and Horton, M. (1990). Single integrin molecule adhesion forces in intact cells measured by atomic force microscopy. *Biochemical Biophysical Research Communications*, 259:645–50.

[Lenz et al., 2012] Lenz, M., Gardel, M., and Dinner, A. (2012). Requirements for contractility in disordered cytoskeletal bundles. *New Journal of Physics*, 14.

[Lewis, 1947] Lewis, W. (1947). Mechanics of invagination. *Anatom. Record*, 97:139–156.

[Lieber Arnon et al., 2013] Lieber Arnon, D., Yehudai-Resheff, S., Barnhart, E., Theroit, J., and Keren, K. (2013). Membrane tension in rapidly moving cells is determined by cytoskeletal forces. *Current Biology*, 23:1409–1417.

[Liedtke et al., 2003] Liedtke, W., Tobin, D., Bargmann, C., and Friedman, J. (2003). Mammalian trpv4 (vr-oac) directs behavioral responses to osmotic and mechanical stimuli in *Caenorhabditis elegans*. *Proc Natl Acad Sci U S A*, 100:14531–14536.

[Litman et al., 2000] Litman, P., Amieva, M., and Furthmayr, H. (2000). Imaging of dynamic changes of the actin cytoskeleton in micro extensions of live nih3t3 cells with a gfp fusion of the f-actin binding domain of moesin. *BMC Cell Biol*, 1:1.

[Littlefield et al., 2001] Littlefield, R., Almenar-Queralt, A., and Fowler, V. (2001). Actin dynamics at pointed ends regulates thin filament length in striated muscle. *Nature Cell Biology*, 3:544–551.

[Liu et al., 2007] Liu, B., Goergen, C., and Shao, J. (2007). Effect of temperature on tether extraction, surface protrusion, and cortical tension of human neutrophils. *Biophysical Journal*, 93:2923–2933.

[Loughlin et al., 2010] Loughlin, R., Heald, R., and Nedelec, F. (2010). A computational model predicts *Xenopus* meiotic spindle organization. *Journal of Cell Biology*, 191:1239–49.

[Luby-Phelps, 2000] Luby-Phelps, K. (2000). Cytoarchitecture and physical properties of cytoplasm: volume, viscosity, diffusion, intracellular surface area. *International Review of Cytology*, 192:189–221.

[Luu et al., 2011] Luu, O., David, R., Ninomiya, H., and Winklbauer, R. (2011). Large-scale mechanical properties of xenopus embryonic epithelium. *Proc Natl Acad Sci U S A*, 108:4000–4005.

[Ma et al., 2009] Ma, X., Lynch, H. E., Scully, P. C., and Hutson, M. S. (2009). Probing embryonic tissue mechanics with laser hole drilling. *Physical Biology*, 6.

[Manu et al., 2009] Manu, Surkova, S., Spirov, A., Gursky, V., Janssens, H., Kim, A., Radulescu, O., Vanario-Alonso, C., Sharp, D., Samsonova, M., and Reinitz, J. (2009). Canalization of gene expression in the *Drosophila* blastoderm by gap gene cross regulation. *PLoS Biology*, 7.

[Marsden and DeSimone, 2001] Marsden, M. and DeSimone, D. (2001). Regulation of cell polarity, radial intercalation and epiboly in *Xenopus*: novel roles for integrin and fibronectin. *Development*, 128:3635–3647.

[Martin, 2010] Martin, A. C. (2010). Pulsation and stabilization: contractile forces that underlie morphogenesis. *Development Biology*, 341:114–25.

[Martin et al., 2009] Martin, A. C., Kaschube, M., and Wieschaus, E. F. (2009). Pulsed contractions of an actin-myosin network drive apical constriction. *Nature*, pages 495–9.

[Mason et al., 2013] Mason, F., Tworoger, M., and Martin, A. (2013). Apical domain polarization localized actin-myosin activity to drive ratchet-like apical constriction. *Nature Cell Biology*, 15:926–939.

[McBeath et al., 2004] McBeath, R., Pirone, D., Nelson, C., Bhadriraju, K., and Chen, C. (2004). Cell shape, cytoskeletal tension, and rhoa regulate stem cell lineage commitment. *Developmental Cell*, 6:483–495.

[Merryman et al., 2009] Merryman, W., Bieniek, P., Guilak, F., and Sacks, M. (2009). Viscoelastic properties of the aortic valve interstitial cell. *Journal of Biomechanical Engineering*, 131.

[Mierke et al., 2008] Mierke, C., Kollmannsberger, P., Zitterbart, D., Smith, J., Fabry, B., and Goldmann, W. (2008). Mechano-coupling and regulation of contractility by the vinculin tail domain. *Biophysical Journal*, 94:661–70.

[Millard and Martin, 2008] Millard, T. and Martin, P. (2008). Dynamic analysis of filopodial interactions during the zippering phase of *Drosophila* dorsal closure. *Development*, 135:621–626.

[Miller and Davidson, 2013] Miller, C. and Davidson, L. (2013). The interplay between cell signaling and mechanics in developmental processes. *Nature Reviews Genetics*, 14:733–44.

[Miller et al., 2012] Miller, C., Ermentrout, G., and Davidson, L. (2012). Rotational model for actin filament alignment by myosin. *Journal of Theoretical Biology*, 300:344–59.

[Miller and Church, 2013] Miller, M. and Church, C. (2013). Arrhenius thermodynamics and birth defects: Chemical teratogen synergy. *Untested, testable, and projected relevance. Birth Defects Research Part C: Embryo Today: Reviews*, 99:50–60.

[Mirkes et al., 1997] Mirkes, P., Cornel, L., Park, H., and Cunningham, M. (1997). Induction of thermotolerance in early post implantation rat embryos is associated with increased resistance to hyperthermia-induced apoptosis. *Teratology*, 56:210–219.

[Mitchison and Swann, 1954] Mitchison, J. and Swann, M. (1954). The mechanical properties of the cell surface. ii. the unfertilized sea-urchin egg. *Journal of Experimental Biology*, 31:461–472.

[Mogilner and Edelstein-Keshet, 2002] Mogilner, A. and Edelstein-Keshet, L. (2002). Regulation of actin dynamics in rapidly moving cells: a quantitative analysis. *Biophysical Journal*, 83:1237–58.

[Mogilner and Oster, 1996] Mogilner, A. and Oster, G. (1996). Cell motility driven by actin polymerization. *Biophysical Journal*, 71:3030–45.

[Mogilner and Rubinstein, 2010] Mogilner, A. and Rubinstein, B. (2010). Actin disassembly 'clock' and membrane tension determine cell shape and turning: a mathematical model. *Journal of Physics: Condensed Matter*, 22.

[Moore and Burt, 1939] Moore, A. and Burt, A. (1939). On the locus and nature of the forces causing gastrulation in the embryos of *Dendraster excentricus*. *Journal of Experimental Zoology*, 82:159–71.

[Moretti et al., 2005] Moretti, M., Bar-Oz, B., Fried, S., and Koren, G. (2005). Maternal hyperthermia and the risk for neural tube defects in offspring: systematic review and meta-analysis. *Epidemiology*, 16:216–219.

[Morgan, 1927] Morgan, T. (1927). *Experimental Embryology*. Columbia University Press.

[Morin-Kensicki et al., 2006] Morin-Kensicki, E., Boone, B., Howell, M., Stonebraker, J., Teed, J., Alb, J., Magnuson, T., O'Neal, W., and Milgram, S. (2006). Defects in yolk sac vasculogenesis, chorioallantoic fusion, and embryonic axis elongation in mice with targeted disruption of yap65. *Molecular Cell Biology*, 26:77–87.

[Murphy et al., 2001] Murphy, C. T., Rock, R. S., and Spudich, J. A. (2001). A myosin ll mutation uncouples atpase activity from motility and shortens step size. *Nature Cell Biology*, pages 311–5.

[Murrell and Gardel, 2012] Murrell, M. and Gardel, M. (2012). F-actin buckling coordinates contractility and severing in a biomimetic actomyosin cortex. *Proc Natl Acad Sci U S A*, 109.

[Nagornyak et al., 2005] Nagornyak, E., Blyakhman, F., and Pollack, G. (2005). Stepwise length changes in single invertebrate thick filaments. *Biophysical Journal*, 89:3269–76.

[Nedelec et al., 2003] Nedelec, F., Surrey, T., and Karsenti, E. (2003). Self-organisation and forces in the microtubule cytoskeleton. *Current Opinion in Cell Biology*, 15:118–24.

[Nelson et al., 1982] Nelson, L., Mild, K., and Lovtrup, S. (1982). Changes in temperature tolerance during the development of *Xenopus laevis* embryos. *Journal of Experimental Zoology*, 222:103–104.

[Neumann et al., 1998] Neumann, T., Fauver, M., and Pollack, G. (1998). Elastic properties of isolated thick filaments measured by nanofabricated cantilevers. *Biophysical Journal*, 75:938–47.

[Niederman and Pollard, 1975] Niederman, R. and Pollard, T. D. (1975). Human platelet myosin ll *In vitro* assembly and structure of myosin filaments. *Journal of Cell Biology*, pages 72–79.

[Nieuwkoop and Faber, 1967] Nieuwkoop, P. and Faber, J. (1967). *Normal tables of Xenopus laevis*. Amsterdam: Elsevier North-Holland Biomedical Press.

[Norris, 1940] Norris, C. (1940). Elasticity studies on the myxomycete, *Physarum polycephalum*. *Journal of Cellular and Comparative Physiology*, 16:313–322.

[Odell et al., 1981] Odell, G. M., Oster, G., Alberch, P., and Burnside, B. (1981). The mechanical basis of morphogenesis. *Development Biology*, 85:446–462.

[Parmar et al., 2013] Parmar, K., Larman, H., Dai, G., Zhang, Y., Wang, E., Moorthy, S., Kratz, J., Lin, Z., Jain, M., Gimbrone, M. J., and Garcia-Cardena, G. (2013). Integration

of flow-dependent endothelial phenotypes by kruppel-like factor 2. *Journal of Clinical Investigation*, 116:196–208.

[Pearson et al., 2008] Pearson, R., Fleetwood, J., Eaton, S., Crossley, M., and Bao, S. (2008). Kruppel-like transcription factors: a functional family. *International Journal of Biochemistry and Cell Biology*, 40:1996–2001.

[Peralta et al., 2007] Peralta, X., Touama, Y., Hutson, M., Montague, R., Venakides, S., Kiehart, D., and Edwards, G. (2007). Upregulation of forces and morphogenic asymmetries in dorsal closure during drosophila development. *Biophysical Journal*, 92:2583–96.

[Peralta et al., 2008] Peralta, X. G., Toyama, Y., Kiehart, D. P., and Edwards, G. S. (2008). Emergent properties during dorsal closure in *Drosophila* morphogenesis. *Physical Biology*, 5.

[Perrin and Ervasti, 2010] Perrin, B. and Ervasti, J. (2010). The actin gene family: Function follows isoform. *Cytoskeleton*, 67:630–634.

[Picard and A., 2009] Picard, C. and A., D. (2009). The impact of environmental changes upon the microrheological response of adherent cells. *European Physical Journal E Soft Matter*, 30:127–134.

[Podolsky, 2003] Podolsky, R. (2003). Integrating development and environment to model reproductive performance in natural populations of an intertidal gastropod. *Integrative and Comparative Biology*, 43:450–458.

[Pohl et al., 2012] Pohl, C., Tiongson, M., Moore, J., Santella, A., and Bao, Z. (2012). Actomyosin-based self-organization of cell internalization during *C. elegant* gastrulation. *BMC Biology*, 94.

[Pollard, 1981] Pollard, T. (1981). Purification of a calcium-sensitive actin gelation protein from *Acanthamoeba*. *Journal of Biological Chemistry*, 256:7666–7670.

[Pollard and Cooper, 1986] Pollard, T. and Cooper, J. (1986). Actin and actin-binding proteins. a critical evaluation of mechanisms and functions. *Annual Review of Biochemistry*, 55:987–1035.

[Pollard and Borisy, 2003] Pollard, T. D. and Borisy, G. G. (2003). Cellular motility driven by assembly and disassembly of actin filaments. *Cell*, 112:453–65.

[Ponte et al., 2000] Ponte, E., Rivero, F., Fechheimer, M., Noegel, A., and Bozzaro, S. (2000). Severe developmental defects in *Dictyostelim* numb mutants for actin-binding proteins. *Mechanisms of Development*, 91:153–161.

[Ponti et al., 2004a] Ponti, A., Machacek, M., Gupton, S., Waterman-Storer, C., and Danuser, G. (2004a). Two distinct actin networks drive the protrusion of migrating cells. *Science*, 305:1782–6.

[Ponti et al., 2004b] Ponti, A., Matov, A., Adams, M., Gupton, S., Waterman-Storer, C. M., and Danuser, G. (2004b). Periodic patterns of actin turnover in lamellipodia and lamellae of migrating epithelial cells analyzed by quantitative fluorescent speckle microscopy. *Biophysical Journal*, pages 3456–69.

[Pouille et al., 2009] Pouille, P., Ahmadi, P., Brunet, A., and Farge, E. (2009). Mechanical signals trigger myosin ii redistribution and mesoderm invagination in drosophila embryos. *Science Signaling*, 2.

[Pulina et al., 2011] Pulina, M., Hou, S., Mittal, A., Julich, D., Whittaker, C., Holley, S., Hynes, R., and Astrof, S. (2011). Essential roles of fibronectin in the development of the left-right embryonic body plan. *Development Biology*, 354:208–20.

[Rafelski et al., 2009] Rafelski, S. M., Alberts, J. B., and Odell, G. M. (2009). An experimental and computational study of the effect of acta polarity on the speed of *Listeria monocytogenes* actin-based motility. *PLoS Computational Biology*, 5.

[Raich et al., 1999] Raich, W., Agbunag, C., and Hardin, J. (1999). Rapid epithelial-sheet sealing in the *Caenorhabditis elegans* embryo requires cadherin-dependent filopodial priming. *Current Biology*, 9:1139=1146.

[Rall and Woledge, 1990] Rall, J. and Woledge, R. (1990). Influence of temperature on mechanics and energetics of muscle contraction. *The American journal of physiology*, 259:R197–203.

[Rauzi et al., 2010] Rauzi, M., Lenne, P. F., and Lecuit, T. (2010). Planar polarized actomyosin contractile flows control epithelial junction remodeling. *Nature*, pages 1110–4.

[Reisler, 1993] Reisler, E. (1993). Actin molecular structure and function. *Current Opinion in Cell Biology*, 5:41–47.

[Reymann et al., 2012] Reymann, A.-C., Boujemaa-Paterski, R., Martiel, J.-L., Guerin, C., Cao, W., Chin, H., De La Cruz, E. M., Thery, M., and Blanchoin, L. (2012). Actin network architecture can determine myosin motor activity. *Science*, 336:1310–1314.

[Rhumbler, 1902] Rhumbler, L. (1902). Zur mechanik der invagination. *Archiv fur Entwicklungsmechanik der Organismen*, 14:401–476.

[Rico et al., 2010] Rico, F., Chu, C., Abdulreda, M., Qin, Y., and Moy, V. (2010). Temperature modulation of integrin-mediated cell adhesion. *Biophysical Journal*, 99:1387–1396.

[Rodriguez-Diaz et al., 2008] Rodriguez-Diaz, A., Toyama, Y., Abravanel, D. L., Wiemann, J. M., Wells, A. R., Tulu, U. S., Edwards, G. S., and Kiehart, D. P. (2008). Actomyosin purse strings: renewable resources that make morphogenesis robust and resilient. *HFSP Journal*, 2:220–37.

[Rueden and Eliceiri, 2007] Rueden, C. and Eliceiri, K. (2007). Visualization approaches for multidimensional biological image data. *Biotechniques*, 43:33–36.

[Ryan, 1941] Ryan, F. (1941). The time-temperature relation of different stages of development. *The Biological Bulletin*, 81:432–440.

[Saarikangas et al., 2009] Saarikangas, J., Zhao, H., Pykalainen, A., Laurinmaki, P., Mattila, P., Butcher, S., and Lappalainen, P. (2009). Molecular mechanisms of membrane deformation by i-bar domain proteins. *Current Biology*, 19:95–107.

[Sampath et al., 1998] Sampath, K., Rubinstein, A., Cheng, A., Liang, J., Fekany, K., Solnica-Krezel, L., Korzh, V., Halpern, M., and C.V., W. (1998). Induction of the zebrafish ventral brain and floor plate requires cyclops/nodal signaling. *Nature*, 395:185–189.

[Sandmann et al., 2007] Sandmann, T., Girardot, C., Brehme, M., Tongprasit, W., Stolc, V., and Furlong, E. (2007). A core transcriptional network for early mesoderm development in *Drosophila melanogaster*. *Genes Development*, 21:436–449.

[Sato et al., 1990] Sato, M., Theret, D., Wheeler, L., Ohshima, N., and Nerem, R. (1990). Application of the micropipette technique to the measurement of cultured porcine aortic endothelial cell viscoelastic properties. *Journal of Biomechanical Engineering*, 112:263–268.

[Savin et al., 2011] Savin, T., Kurpios, N., Shyer, A., Florescu, P., Liang, H., Mahadevan, L., and Tabin, C. (2011). On the growth and form of the gut. *Nature*, 476:57–62.

[Schaub et al., 2007] Schaub, S., Bohnet, S., Laurent, V. M., Meister, J. J., and Verkhovsky, A. B. (2007). Comparative maps of motion and assembly of filamentous actin and myosin ii in migrating cells. *Molecular Biology of the Cell*, 18:3723–32.

[Schirone and Gross, 1968] Schirone, R. and Gross, L. (1968). Effect of temperature on early embryological development of the zebra fish, brachydanio rerio. *Journal of Experimental Zoology*, 169:43–52.

[Schler et al., 2013] Schler, S., Hauptmann, J., Perner, B., Kessels, M. M., Englert, C., and Qualmann, B. (2013). Ciliated sensory hair cell formation and function require the f-bar protein syndapin i and the wh2 domain-based actin nucleator cobl. *Journal of Cell Science*, 126:196–208.

[Selman, 1955] Selman, G. G. (1955). Studies on the forces producing neural closure in amphibia. *Proceedings of the Royal Physical Society of Edinburgh*, 24:24–27.

[Selman, 1958] Selman, G. G. (1958). The forces producing neural closure in amphibia. *Journal of Embryology and Experimental Morphology*, 6:448–465.

[Sherrard et al., 2010] Sherrard, K., Robin, F., Lemaire, P., and Munro, E. (2010). Sequential activation of apical and basolateral contractility drives ascidian endoderm invagination. *Current Biology*, 20:1499–510.

[Shih and Keller, 1992] Shih, J. and Keller, R. (1992). Patterns of cell motility in the organizer and dorsal mesoderm of *Xenopus laevis*. *Development*, 116:915–930.

[Shook and Keller, 2008] Shook, D. and Keller, R. (2008). Morphogenic machines evolve more rapidly than the signals that pattern then: lessons from amphibians. *Journal of Experimental Zoology Part B: Molecular and Developmental Evolution*, 310:111–135.

[Shutova et al., 2012] Shutova, M., Yang, C., Vasiliev, J., and Svitkina, T. (2012). Functions of nonmuscle myosin ii in assembly of the cellular contractile system. *PLoS ONE*, 7.

[Sive et al., 2000] Sive, H., Grainger, R., and Harland, R. (2000). *Early development of Xenopus laevis: a laboratory manual*. Cold Spring Harbor, New York: Cold Spring Harbor Laboratory Press.

[Skoglund et al., 2008] Skoglund, P., Rolo, A., Chen, X., Gumbiner, B., and Keller, R. (2008). Convergence and extension at gastrulation require a myosin iib-dependent cortical actin network. *Development*, 135:2435–2444.

[Smith et al., 2007] Smith, D., Ziebert, F., Humphrey, D., Duggan, C., Steinbeck, M., Zimmermann, W., and Kas, J. (2007). Molecular motor-induced instabilities and cross linkers determine biopolymer organization. *Biophysical Journal*, 93:4445–52.

[Smith and Schoenwolf, 1991] Smith, J. L. and Schoenwolf, G. C. (1991). Further evidence of extrinsic forces in bending of the neural plate. *Journal of Computational Neurology*, 307:225–36.

[Smith and Schoenwolf, 1997] Smith, J. L. and Schoenwolf, G. C. (1997). Neurulation: coming to closure. *Trends in Neuroscience*, 20:510–7.

[Smith et al., 1994] Smith, J. L., Schoenwolf, G. C., and Quan, J. (1994). Quantitative analyses of neuroepithelial cell shapes during bending of the mouse neural plate. *Journal of Computational Neurology*, 342:144–51.

[Snider et al., 2004] Snider, J., Lin, F., Zahedi, N., Rodionov, V., Yu, C. C., and Gross, S. P. (2004). Intracellular actin-based transport: How far you go depends on how often you switch. *Proc Natl Acad Sci U S A*, 101:13204–209.

[Soares e Silva et al., 2011] Soares e Silva, M., Depken, M., Stuhrmann, B., Korsten, M., MacKintosh, F., and Koenderink, G. H. (2011). Active multistage coarsening of actin networks driven by myosin motors. *Proc Natl Acad Sci U S A*, 23:9408–13.

[Sobol, 1994] Sobol, I. (1994). *A Primer for the Monte Carlo Method*. CRC Press.

[Sokolow et al., 2012] Sokolow, A., Toyama, Y., Kiehart, D. P., and Edwards, G. S. (2012). Cell ingression and apical shape oscillations during dorsal closure in *Drosophila*. *Biophysical Journal*, 102:969–79.

[Solon et al., 2009] Solon, J., Kaya-Copur, A., Colombelli, J., and Brunner, D. (2009). Pulsed forces timed by a ratchet-like mechanism drive directed tissue movement during dorsal closure. *Cell*, pages 1331–42.

[Sommi et al., 2011] Sommi, P., Cheerambathur, D., Brust-Mascher, I., and Mogilner, A. (2011). Actomyosin-dependent cortical dynamics contributes to the prophase force-balance in the early drosophila embryo. *PLoS One*, 6.

[Somogyi and Rorth, 2004] Somogyi, K. and Rorth, P. (2004). Evidence for tension-based regulation of *Drosophila* mal and srf during invasive cell migration. *Developmental Cell*, 7:85–93.

[Spiros and Edlestein-Keshet, 1998] Spiros, A. and Edlestein-Keshet, L. (1998). Testing a model for the dynamics of actin structures with biological parameter values. *Bulletin of Mathematical Biology*, 60:275–305.

[Stephens, 1972] Stephens, R. (1972). Studies on the development of the sea urchin strongylocentrotus droebachiensis. i. ecology and normal development. *The Biological Bulletin*, 142:132–144.

[Stuurman et al., 2007] Stuurman, N., Amdodaj, N., and Vale, R. (2007). Micro-manager: Open source software for light microscope imaging. *Microscopy Today*, 15:42–43.

[Suetsugu, 2010] Suetsugu, S. (2010). The proposed functions of membrane curvatures mediated by the bar domain superfamily proteins. *Journal of Biochemistry*, 148:1–12.

[Sung et al., 1982] Sung, K., Schmid-Schobien, G., Skalak, R., Schuessler, G., Usami, S., and Chien, S. (1982). Influence of physicochemical factors on rheology of human neutrophils. *Biophysical Journal*, 39:101–106.

[Sunyer et al., 2009] Sunyer, R., Trepat, X., Fredberg, J., Farre, R., and Navajas, D. (2009). The temperature dependence of cell mechanics measured by atomic force microscopy. *Physical Biology*, 6.

[Sweeney and Houdusse, 2010] Sweeney, H. and Houdusse, A. (2010). Structural and functional insights into the myosin motor mechanism. *Annual Review of Biophysics*, 39:539–557.

[Thievessen et al., 2013] Thievessen, I., Thompson, P., Berlemont, S., Plevock, K., Plotnikov, S., Zemljic-Harpf, A., Ross, R., Davidson, M., Danuser, G., Campbell, S., and Waterman, C. (2013). Vinculin-actin interaction couples actin retrograde flow to focal adhesions, but is dispensable for focal adhesion growth. *Journal of Cell Biology*, 202:163–177.

[Thodeti et al., 2009] Thodeti, C., Matthews, B., Ravi, A., Mammoto, A., Ghosh, K., Bracha, A., and Ingber, D. (2009). Trpv4 channels mediate cyclic strain-induced endothelial cell reorientation through integrin-to-integrin signaling. *Circulation Research*, 104:1123–30.

[Tirado and Garcia de la Torre, 1979] Tirado, M. M. and Garcia de la Torre, J. (1979). Translational friction coefficients of rigid symmetric top macromolecules. application to circular cylinders. *Journal of Chemical Physics*, 71:2581–2587.

[Toyoma et al., 2008] Toyoma, Y., Peralta, X., Wells, A., Kiehart, D., and Edwards, G. (2008). Apoptotic force and tissue dynamics during drosophila embryogenesis. *Science*, 321:1683–6.

[Trappmann et al., 2012] Trappmann, B., Gautrot, J. E., Connelly, J. T., Strange, D. G., Li, Y., Oyen, M. L., Cohen Stuart, M. A., Boehm, H., Li, B., Vogel, V., Spatz, J. P., Watt, F. M., and Huck, W. T. (2012). Extracellular-matrix tethering regulates stem-cell fate. *Nature Materials*, 11:642–9.

[Trinh and Stainier, 2004] Trinh, L. and Stainier, D. (2004). Fibronectin regulates epithelial organization during myocardial migration in zebrafish. *Developmental Cell*, 6:371–82.

[Trinkaus, 1984] Trinkaus, J. (1984). *Cells into Organs: the forces that shape the embryo.* Prentice-Hall Inc., Englewood Cliffs.

[Tyler, 1936] Tyler, A. (1936). On the energetics of differentiation. iii: Comparison of the temperature coefficients for cleavage and later stages in the development of the eggs of some marine animals. *The Biological Bulletin*, 71:59–81.

[Tyszka et al., 2005] Tyszka, J., Ewald, A., Wallingford, J., and Fraser, S. (2005). New tools for visualization and analysis of morphogenesis in spherical embryos. *Developmental Dynamics*, 234:974–983.

[Vallotton et al., 2004] Vallotton, P., Gupton, S. L., Waterman-Storer, C. M., and Danuser, G. (2004). Simultaneous mapping of filamentous actin flow and turnover in migrating cells by quantitative fluorescent speckle microscopy. *Proc Natl Acad Sci U S A*, pages 9660–5.

[van der Have, 2002] van der Have, T. (2002). A proximate model for thermal tolerance in ectotherms. *Oikos*, 98:141–155.

[Varner et al., 2010] Varner, V. D., Voronov, D. A., and Taber, L. A. (2010). Mechanics of head fold formation: investigating tissue-level forces during early development. *Development*, 137:3801–11.

[Vavylonis et al., 2008] Vavylonis, D., Wu, J. Q., Hao, S., O'Shaughnessy, B., and Pollard, T. D. (2008). Assembly mechanism of the contractile ring for cytokinesis by fission yeast. *Science*, pages 97–100.

[Vicente-Manzanares et al., 2009] Vicente-Manzanares, M., Ma, X., Adelstein, R., and Horwitz, A. (2009). Non-muslce myosin ii takes centre stage in cell adhesion and migration. *Nature Reviews Molecular Cell Biology*, 10:778–790.

[Vijayraghavan and Davidson, prep] Vijayraghavan, D. and Davidson, L. (*in prep*). Actin dynamics and apical protrusivity in xenopus laevis neural tube epithelial morphogenesis. Cellular and Molecular Bioengineering Special Interest Group, La Jolla, CA.

[von Dassow and Davidson, 2009] von Dassow, M. and Davidson, L. (2009). Natural variation in embryo mechanics: gastrulation in *Xenopus laevis* is highly robust to variation in tissue stiffness. *Developmental Dynamics*, 238:2–18.

[von Dassow and Davidson, 2011] von Dassow, M. and Davidson, L. (2011). Physics and the canalization of morphogenesis: a grand challenge in organismal biology. *Physical Biology*, 8:17.

[von Dassow et al., 2014] von Dassow, M., Miller, C., and Davidson, L. (2014). Biomechanics and the thermotolerance of development. *PLoS One*, 9:16.

[von Dassow et al., 2010] von Dassow, M., Strother, J. A., and Davidson, L. A. (2010). Surprisingly simple mechanical behavior of a complex embryonic tissue. *PLoS One*, 5:12.

[Voronov and Taber, 2002] Voronov, D. A. and Taber, L. A. (2002). Cardiac looping in experimental conditions: effects of extraembryonic forces. *Developmental Dynamics*, 224:413–21.

[Wang et al., 2001] Wang, H., Dembo, M., Hanks, S., and Wang, Y. (2001). Focal adhesion kinase is involved in mechanosensing during fibroblast migration. *Proc Natl Acad Sci U S A*, 98:11295–300.

[Wang et al., 2006] Wang, N., Miao, H., Li, Y., Zhang, P., Haga, J., Hu, Y., Young, A., Yuan, S., Nguyen, P., Wu, C., and Chien, S. (2006). Shear stress regulation of kruppel-like factor 2 expression is flow pattern specific. *Biochemical and Biophysical Research Communications*, 341:1244–51.

[Waterman-Storer and Salmon, 1997] Waterman-Storer, C. and Salmon, E. (1997). Actomyosin-based retrograde flow of microtubules in the lamella of migrating epithelial cells influences microtubule dynamic instability and turnover and is associated with microtubule breakage and treadmilling. *Journal of Cell Biology*, 139:417–434.

[Weber et al., 2012] Weber, G., Bjerke, M., and DeSimone, D. (2012). A mechanoresponsive cadherin-keratin complex directs polarized protrusive behavior and collective cell migration. *Developmental Cell*, 22:104–15.

[Wiebe and Brodland, 2005a] Wiebe, C. and Brodland, G. (2005a). Tensile properties of embryonic epithelia measured using a novel instrument. *Journal of Biomechanics*, 38:2087–2094.

[Wiebe and Brodland, 2005b] Wiebe, C. and Brodland, G. (2005b). Tensile properties of embryonic epithelia measured using a novel instrument. *Journal of Biomechanics*, 38:2087–2094.

[Wozniak and Chen, 2009] Wozniak, M. A. and Chen, C. S. (2009). Mechanotransduction in development: a growing role for contractility. *Nature Reviews Molecular Cell Biology*, 10:34–43.

[Xu et al., 1998] Xu, W., Baribault, H., and Adamson, E. (1998). Vinculin knockout results in heart and brain defects during embryonic development. *Development*, 125:327–37.

[Yam et al., 2007] Yam, P. T., Wilson, C. A., Ji, L., Herbert, B., Barnhart, E. L., Dye, N. A., Wiseman, P. W., Danuser, G., and Theriot, J. A. (2007). Actin-myosin network reorganization breaks symmetry at the cell rear to spontaneously initiate polarized cell motility. *Journal of Cell Biology*, 178:1207–21.

[Yamaguchi et al., 2006] Yamaguchi, H., Pixley, F., and Condeelis, J. (2006). Invadopodia and podosomes in tumor invasion. *Journal of Cell Biology*, 85:213–18.

[Yoneda, 1976] Yoneda, M. (1976). Temperature-dependence of the tension at the surface of sea-urchin eggs. *Development, Growth & Differentiation*, 18:387–389.

[Yonemura et al., 2010] Yonemura, S., Wada, Y., Watanable, T., Nagafuchi, A., and Shibata, M. (2010). α-catenin as a tension transducer that induces adherents junction development. *Nature Cell Biology*, 12:533–542.

[Young et al., 1993] Young, P., Richman, A., Ketchum, A., and Kiehart, D. (1993). Morphogenesis in *Drosophila* requires nonmuscle myosin heavy chain function. *Genes Dev.*, 7:29–41.

[Zamir et al., 2003] Zamir, E. A., Srinivasan, V., Perucchio, R., and Taber, L. A. (2003). Mechanical asymmetry in the embryonic chick heart during looping. *Annual Biomedical Engineering*, 31:1327–36.

[Zamir and Taber, 2004] Zamir, E. A. and Taber, L. A. (2004). Material properties and residual stress in the stage 12 chick heart during cardiac looping. *Journal of Biomedical Engineering*, 126:823–30.

[Zar, 1999] Zar, J. (1999). *Biostatistical analysis*. Prentice Hall, 4 edition.

[Zemel and Mogilner, 2009] Zemel, A. and Mogilner, A. (2009). Motor-induced sliding of microtubule and actin bundles. *Physical Chemistry Chemical Physics*, 11:4821–33.

[Zemel et al., 2010] Zemel, A., Rehfeldt, F., Brown, A., Discher, D., and Safran, S. (2010). Optimal matrix rigidity for stress fiber polarization in stem cells. *Nature Physics*, 6:468–473.

[Zhou et al., 2010a] Zhou, E., Quek, S., and Lim, C. (2010a). Power-law rheology analysis of cells undergoing micropipette aspiration. *Biomechanics and Modeling in Mechanobiology*, 9:563–572.

[Zhou et al., 2009] Zhou, J., Kim, H. Y., and Davidson, L. A. (2009). Actomyosin stiffens the vertebrate embryo during crucial stages of elongation and neural tube closure. *Development*, 136:677–88.

[Zhou et al., 2010b] Zhou, J., Kim, H. Y., Wang, J. H., and Davidson, L. A. (2010b). Macroscopic stiffening of embryonic tissues via microtubules, rhogef and the assembly of contractile bundles of actomyosin. *Development*, 137:2785–94.

[Ziebert et al., 2009] Ziebert, F., Vershinin, M., Gross, S., and Aranson, I. (2009). Collective alignment of polar filaments by molecular motors. *Eur Phys J E Soft Matter*, 28:401–409.

[Zohn et al., 2005] Zohn, I., Anderson, K., and Niswander, L. (2005). Using genome wide mutagenesis screens to identify the genes required for neural tube closure in the mouse. *Birth Defects Res A Clin Mol Teratol*, 73:583–90.

[Zumdieck et al., 2007] Zumdieck, A., Kruse, K., Bringmann, H., Hyman, A., and Julicher, F. (2007). Stress generation and filament turnover during actin ring constriction. *PLoS ONE*, 2.